PROBING CHARGE MOTION IN NEXT-GENERATION SEMICONDUCTORS WITH SCANNED PROBE MICROSCOPY

A Dissertation
Presented to the Faculty of the Graduate School
of Cornell University
in Partial Fulfillment of the Requirements for the Degree of
Doctor of Philosophy

by
Ryan Patrick Dwyer
August 2017

PROBING CHARGE MOTION IN NEXT-GENERATION SEMICONDUCTORS WITH SCANNED PROBE MICROSCOPY

Ryan Patrick Dwyer, Ph.D.

Cornell University 2017

Scanned probe microscopy has allowed researchers to explore spatial variations in charge generation and transport in solar-cell films prepared on a conductive substrate with a best-case resolution of 2 nanometers. In this thesis, we introduce new scanned probe measurements to measure light- and voltage-induced changes to capacitance, surface potential, and electric fields with better time resolution. We demonstrate the measurements on organic and perovskite semiconductors.

First, we present a new method for measuring photocapacitance transients. We demonstrate the ability of this indirect, "phase kick" technique to record multi-exponential photocapacitance transients on timescales ranging from 40 microseconds to 10 milliseconds in the organic donor:acceptor blend PFB:F8BT. The technique's ability to measure subcycle, nanosecond charge dynamics is demonstrated by measuring the 34 nanosecond sample electrical charging time. Along with the measurement, we present an accurate approximate model for the cantilever dynamics during the photocapacitance measurement. We use the model to explain the origin of the signal in our new phasekick electric force microscopy measurement and the alternative feedback-free time-resolved electric force microscopy. We show that for sample time constants faster than the inverse cantilever angular frequency, feedback-free time-resolved electric force microscopy is sensitive mainly to the size of the abrupt phase shift induced by the abrupt step change in the tip-sample capacitive force.

Second, we present a new method for measuring the vector electric field using frequency-modulated Kelvin probe force microscopy. During a Kelvin probe force microscopy linescan, we sinusoidally modulate the cantilever position along the direction perpendicular to the linescan. We determine the electric field along both the linescan direction and the modulation direction simultaneously by numerical differentiation and lock-in detection respectively. We demonstrate the technique by recording linescans of the in-plane electric field vector in the vicinity of a patch of trapped charge in a DPh-BTBT organic field-effect transistor. The measured electric field depends strongly on experimental parameters: the Kelvin probe force microscopy feedback loop bandwidth, the linescan speed, the position modulation amplitude, and the position modulation frequency. We demonstrate how to optimally choose these experimental parameters for our new vector electric field measurement.

BIOGRAPHICAL SKETCH

Ryan Dwyer was born in Waukesha, Wisconsin on September 28, 1989. He went to college at the University of Notre Dame in South Bend, Indiana. During college, he performed undergraduate research on quantum dot solar cell counter electrode materials with Professor Prashant V. Kamat and graduate student James Radich. Ryan graduated from the University of Notre Dame in 2011 with a Bachelor of Science degree in Chemistry. In the Fall of 2011, he started graduate school at Cornell University in the Department of Chemistry and Chemical Biology. He completed his doctoral research under the supervision of Professor John Marohn in 2017.

To my parents.

ACKNOWLEDGEMENTS

I would like to thank my family for their support and encouragement, especially my parents. I also thank my grandmother for encouraging and cultivating my curiosity at a young age.

I thank John Marohn for being a great, supportive advisor and teaching me so much about how to be a scientist. I thank Roger Loring for many useful discussions about sample-induced cantilever frequency noise and dissipation. I thank Stephen Lee for a great teaching assistant experience and serving on my committee.

The work in this thesis would not have been possible without the collaboration of many others. I thank Nicholas Hoepker for training me in scanned probe microscopy and nanofabrication. Nik's upbeat attitude and perseverance when parts of the microscope broke set a great example.

I thank Lee Harrell for collaborating on the simulations and theory presented in Chapters 2 and 3. I thank Sarah Nathan for putting in the years of work to develop the measurements presented in Chapter 2. I thank Dr. Brandon Wenning and Sarah Nathan for preparing the sample studied in Chapter 2. I thank Louisa Smieska for designing and implementing the collaborative measurement presented in Chapters 4 and 5.

I thank Ali Tirmzi for implementing many of the measurements described in Chapter 6, preparing the sample and performing AFM and transfer curve measurements for the sample described in Chapter 4 and collecting so much interesting perovskite data to puzzle over the last year and a half. I have learned and been motivated by your comprehensive knowledge of the literature and focus on what scanned probe microscopy measurements can contribute to the knowledge of perovskites. The EFM side of the group is in great hands!

Thanks to the rest of the Marohn group for making it such an enjoyable place to work and do research the last 6 years.

I thank Ryo Wakabayashi for being a great roommate, friend and intramural team captain, all of which made my time in graduate school much more enjoyable. I thank my wife Laura for all her support, assistance and encouragement over the last 6 years.

This work was supported by Cornell University and the U.S. National Science Foundation, through Grants NSF-DMR 1309540, NSF-DMR 1602951, and an NSF GK–12 Teaching Fellowship. This work was performed in part at the Cornell NanoScale Facility, a member of the National Nanotechnology Coordinated Infrastructure (NNCI), which is supported by the National Science Foundation (Grant ECCS-1542081). This work made use of the Cornell Center for Materials Research Shared Facilities which are supported through the NSF MRSEC program (DMR-1120296).

TABLE OF CONTENTS

LIST OF FIGURES

CHAPTER 1

INTRODUCTION

Organic semiconductors are promising materials for electro-optical devices. In particular, solar cells made from blends of organic semiconductors have achieved efficiencies of over 10 percent. The highest performance blends use a bulk heterojunction structure, which combine a donor and acceptor material into a film with nanometer- to micrometer-scale majority-donor and majority-acceptor domains. Compared to commercial silicon solar cells, bulk heterojunction organic solar cells offer a number of advantages: they have the potential to be lower-cost and less-energy intensive to manufacture and produce; offer chemical tune-ability to optimize performance for a variety of different applications, such as transparent solar cells and indoor solar cells; and have high absorption coefficients, which would allow thin organic solar cell layers to be integrated into other materials, such as windows or roofing materials.

Despite these potential advantages, the design of higher efficiency organic solar cells has proven challenging. There is still ongoing controversy concerning the operating principles of organic solar cells built from donor-acceptor blends. It is widely accepted that an energy-level offset between donor and acceptor molecules provides the driving force to dissociate the exciton in an organic bulk-heterojunction solar cell [1]. Recent data and simulations have led to a more involved picture of charge generation [2, 3, 4, 5, 6, 7, 8, 9, 10, 11, 12, 13] in which the photoexcited state S_1 transitions to either a bound charge-transfer (CT) state or, alternatively, proceeds directly to the desired charge-separated (CS) state. Once formed, the CS state can exhibit a lifetime exceeding 100s of nanoseconds — 10s to 1000s of times longer than one would estimate from a Langevin model of diffusion-limited charge recombination [14, 15, 4, 10]. In this revised view, champion materials have a special ability to efficiently generate charge by sidestepping the low-energy CT state while, at the same time, exhibiting slow, sub-Langevin charge recombination that facilitates extraction of free charge into metallic electrodes.

Rumbles has proposed that these favorable rates can be explained by the hypothesis that the S_1-to-CT-state and CS-to-ground-state electron-transfer reactions both operate in the Marcus inverted regime [16]. Evidence in favor of this hypothesis has so far been obtained using time-resolved microwave conductivity [17, 4]. These studies probed charge generation with nanosecond time resolution in a series of dilute organic donor-acceptor blends prepared on electrode-free substrates. Time-resolved optical spectroscopy studies of electron transfer carried out on completed organic solar cells, in contrast, show no evidence of inverted-regime electron transfer [7]. This is likely due to the multiple interfering electron-transfer processes taking place in a completed device. Scanned probe microscopy has been used to independently probe charge generation, transport, trapping, and injection/extraction processes in heterogeneous solar-cell films through spatially resolved measurements of electrostatic potential and sample capacitance. To date, scanned probe microscopy has been used to study charge generation in organic solar-cell films by measuring photocapacitance, but only with millisecond to microsecond time resolution. To test the Rumbles hypothesis, we must improve the time resolution of scanned-probe photocapacitance measurements by three orders of magnitude.

In this thesis, we present experimental and theoretical results that significantly extend the ability of scanned probe microscopy to study time-resolved charge dynamics in semiconductor samples. In scanned probe microscopy, a nanometer-scale tip is brought near a sample. By measuring the displacement x of the cantilever tip, researchers obtain information about the tip-sample force F_{ts}, which is linked to the cantilever displacement by Newton's second law. The tip-sample force F_{ts} can be used to infer a variety of sample mechanical [18], electrical [19], and magnetic properties [20] with nanometer spatial resolution. In this thesis, we measure sample topography using atomic force microscopy and sample electrical properties by applying a bias voltage between the tip and sample and measuring the attractive electrostatic force, a method we call electric force microscopy [21, 22].

The electrostatic force between a metal scanned probe tip and semiconductor sample depends on two distinct properties of the tip-sample system: the contact potential difference, or surface potential ϕ; and the capacitance C. When the tip-sample voltage V_{ts} is equal to ϕ, the attractive force between the tip and sample is minimized. The surface potential is a sensitive probe of the semiconductor charge density because the sample chemical potential, and therefore the measured surface potential [23], depends on the charge density n: $\Delta\mu \approx k_{\mathrm{B}}T \log n/n_0$, where $\Delta\mu$ is the change in chemical potential, n is the charge density, and n_0 is the initial charge density. Scanned probe images of the surface potential have been used to acquire a wealth of information about the spatial distribution of mobile and trapped charge carriers in organic semiconductor devices such as field-effect transistors, light-emitting electrochemical cells, and organic solar cells.

The tip-sample capacitance C provides complementary information about the sample dielectric constant, impedance, and charge density. As the tip-sample voltage is varied, charge flows onto the cantilever tip and the tip-sample force increases. The capacitance C is a measure of how much charge q flows onto the cantilever tip: $C = dq/dV_{\mathrm{ts}}$. For a metal sample, the capacitance C is purely geometric; if the tip-sample system is approximated as a vacuum-gap parallel plate capacitor, $C = \epsilon_0 A/d$ with A the area and d the tip-sample distance. This geometric capacitance is independent of the applied tip-sample voltage and the frequency at which the capacitance is measured. Physically, the tip and sample charges reside on the tip and sample surface. All of the applied tip-sample bias drops in the vacuum gap between the two electrodes and the specific properties of the tip and sample metals do not affect the charge flow. For a semiconductor sample, in contrast, there may be a surface charge q_{surf}, but there also may be a significant charge density distribution below the sample surface $\rho_{\mathrm{s}}(x)$ [24]. In this case, the flow of tip charge q will depend on $\rho_{\mathrm{s}}(x)$. In turn, the sample charge density depends sensitively on properties of the semiconductor, such as the sample dielectric constant (as a function of frequency), band-bending, the charge mobility or resistance to charge flow, and light exposure which may affect these sample properties. The analysis of the metal-tip, air, semiconductor-sample structure is analogous to the analysis of the well-studied bulk metal-insulator-semiconductor (MIS) structure [25, 26, 27, 28].

In this thesis, we present new experimental techniques and theoretical results that enable electric force microscopy measurements to probe semiconductor charge motion (1) through changes in sample capacitance C with a time resolution improved from microseconds to nanoseconds, (2) through direct measurements of the vector electric field $\boldsymbol{E}$ with significantly improved time resolution and fidelity, and (3) using an improved theoretical framework for relating cantilever frequency shift and dissipation to changes in the sample impedance as a function of the applied frequency.

In Chapter 2, we employ a charged microcantilever as a gated mechanical integrator to record photocapacitance indirectly by measuring the accumulated change in cantilever phase as a function of the time delay between precisely synchronized voltage and light pulses. In contrast with prior time-resolved scanned-probe photocapacitance measurements [29, 30, 31, 32], the time resolution of this method is set by the rise and fall time of the voltage and light pulses and not by the inverse detection bandwidth. We demonstrate the ability of this indirect, "phase kick" technique to record multi-exponential photocapacitance transients on timescales ranging from 40 microseconds to 10 milliseconds in the organic donor:acceptor blend PFB:F8BT. The technique's ability to measure subcycle, nanosecond charge dynamics is demonstrated by measuring the 34 nanosecond sample electrical charging time.

Chapter 3 uses and extends the theory developed in Chapter 2. The theory is extended to clearly cover feedback-free time-resolved electric force microscopy (FF-trEFM) [30, 31, 32]. We show that the FF-trEFM experiment is only sensitive to the total magnitude of the force-induced phase shift for photocapacitance risetimes τ_{s} much less than the inverse cantilever frequency ω_0^{-1}. To extract a specific time constant in the limit that $\tau_{\mathrm{s}} \ll \omega_0^{-1}$, an assumption must be made about the magnitude of the abrupt change in the tip-sample force.

In Chapter 4, we present position-modulated Kelvin probe force microscopy (PM-KPFM) which enables the improved measurement of the vector electric field. High-quality spatially-resolved measurements of electric fields are critical to understanding charge injection, charge transport, and charge trapping in semiconducting materials. In the new technique, electric field components are measured along multiple directions simultaneously by employing position modulation and lock-in detection instead of numeric differentiation of the surface potential. We demonstrate the technique by using it to record linescans of the in-plane electric field vector in the vicinity of a patch of trapped charge in a DPh-BTBT organic field-effect transistor.

Chapter 5 presents a theory that explains the measured signal in PM-KPFM. We determine how the measured electric field depends on experimental parameters and noise sources. We discuss the precise relationship between experimental settings necessary to achieve high spatial resolution and low noise measurements of the vector electric field with PM-KPFM.

Chapter 6 presents a description of scanned probe microscopy as a measure of the sample impedance which aids the interpretation and analysis of a variety of electric force microscopy measurements of the capacitance C. We analyze the scanned probe microscopy measurements performed in Ref. 33 using this theory and describe in detail how our custom scanned probe microscope was modified to perform the experiments described in this thesis. We close by outlining opportunities for future measurements of semiconductor properties with improved spatial and temporal resolution. These future measurements could contribute to an improved understanding of the mechanism underlying efficient charge generation in organic solar cells.

CHAPTER 2

PHASE-KICK ELECTRIC FORCE MICROSCOPY

The text and figures in this chapter are reproduced, with minor modifications (a corrected sign error in Eq. 2.7 and expanded explanations of the pk-EFM theory in Sec. 2.1.1) from Ref. 34 "Microsecond photocapacitance transients observed using a charged microcantilever as a gated mechanical integrator', by Ryan Dwyer, Sarah Nathan and John Marohn. The text and figures are used under a https://creativecommons.org/licenses/by-nc/4.0/ license.

2.1 Introduction

We introduce a method that significantly improves the time resolution of electric force microscopy, enabling the rapid acquisition of photocapacitance transients in solar-cell films. A light pulse generates free carriers in the sample while a nearby charged microcantilever is used as a voltage-gated mechanical integrator to encode the time evolution of the subsequent carrier recombination as a change in the cantilever's phase of oscillation. We illustrate the method by using it to reveal a biexponential photocapacitance buildup in a polymer-blend solar-cell film, with the fast component having a risetime of $40\,\mu\mathrm{s}$ at high light intensity. We demonstrate the method's time resolution in a control experiment in which we measure a tip-charging time of $35\,\mathrm{ns}$.

Scanned probe microscopy has allowed researchers to explore spatial variations in charge generation and transport in solar-cell films prepared on a conductive substrate [35, 36, 37, 38] with a best-case resolution of $2\,\mathrm{nm}$ [39]. Ginger and coworkers introduced time-resolved electric force microscopy (tr-EFM) which enabled the study of photocapacitance transients on the microsecond timescale in bulk heterojunction organic blends

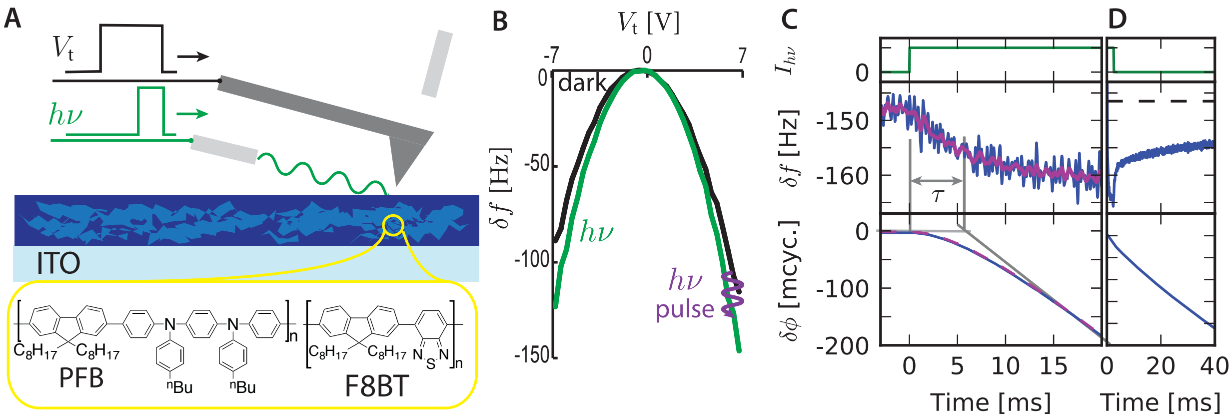

Figure 2.1: **Experimental overview**. (**A**) The experimental setup and sample, a spin-coated PFB:F8BT film on indium tin oxide. (**B**) The increased curvature of the frequency shift δf *vs.* tip voltage V_t parabola under illumination reflects the increased tip-sample capacitance. (**C**) Photocapacitance charging measured via the cantilever frequency and phase. Data demodulated with 3 dB bandwidth $1.92\,\mathrm{kHz}$ (blue) and $0.96\,\mathrm{kHz}$ (purple). (**D**) When the light is turned off, but the voltage is still on, light-induced capacitance remains elevated for tens of seconds to minutes. The dashed line shows the frequency shift before the start of the light pulse. Average of 100 traces shown, each demodulated with 3 dB bandwidth $1.92\,\mathrm{kHz}$. Experimental parameters: tip-sample distance $h = 250\,\mathrm{nm}$; tip-sample voltage $V_t = 10\,\mathrm{V}$; light intensity $I_{h\nu} = 0.1\,\mathrm{kW\,m^{-2}}$ in (C) and $I_{h\nu} = 20\,\mathrm{kW\,m^{-2}}$ in (D); light pulse time $50\,\mathrm{ms}$ in (C), $2.5\,\mathrm{ms}$ in (D). Adapted from Ref. 34, licensed under https://creativecommons.org/licenses/by-nc/4.0/.

[29, 30, 31, 32]. These studies revealed that photocapacitance charging rates were proportional to external quantum efficiency in prototypical organic bulk heterojunction blends, raising the exciting possibility of using scanned-probe microscope measurements to help rationally optimize the processing of organic semiconductor donor-acceptor blends.

We seek to extend the time resolution of EFM in order to study fundamental processes like photoinduced electron transfer, charge recombination, charge trapping, photocatalysis, and ferroelectric switching at the single-molecule or single-domain level. The mechanism of charge generation [2, 3, 4, 5, 6, 7, 8, 9, 10, 11, 12, 13] and recombination [14, 15, 4, 10] in organic donor-acceptor blends, for example, is a topic of intense debate. Nanosecond-resolution microwave conductivity measurements of charge generation have recently revealed tantalizing evidence that Marcus theory can be applied to understand charge generation in an organic donor-acceptor photovoltaic film [17, 4]. The ability to perform analogous EFM measurements at high spatial resolution on conductive substrates is therefore an extremely exciting possibility. Frustratingly, the tr-EFM experiment's time resolution is set by the detector and demodulation bandwidth; achieving nanosecond time resolution would seem to require using radiofrequency oscillators digitized at GHz sampling rates, which is impractical.

To impart EFM with nanosecond resolution we must rethink the experiment from first principles. Ultrafast indirect scanning tunneling microscopy (STM) measurements have demonstrated ns to ps time resolution on gallium arsenide, but lack the clear connection to organic solar cell performance demonstrated by Ginger with tr-EFM [40, 41, 42, 43, 44, 45, 46, 47]. Indirect Kelvin probe force microscopy (KPFM) methods can measure surface potential changes with picosecond time resolution [48, 49, 50, 51, 52, 52], but these measurements exploit the nonlinear dependence of photovoltage on light intensity and/or the nonlinear dependence of the cantilever frequency f_{c} on photovoltage or assume the tip voltage passively observes sample properties. Unfortunately, because photocapacitance generally depends linearly on light intensity, produces a linear change in f_{c}, and depends *strongly* on tip voltage, the ultrafast methods of Refs. 48–52 are not applicable to the donor-acceptor blends studied here.

In this work, we demonstrate a new method to measure the photocapacitance charging rate — "phase-kick" electric force microscopy (pk-EFM). The pk-EFM measurement is sensitive to the same underlying photocapacitance dynamics as Ginger's tr-EFM measurement. Our measurement employs an indirect, non-linear detection protocol that enables the reconstruction of the full photocapacitance transient while sidestepping detector-noise and demodulator-bandwidth limitations to the achievable time resolution.

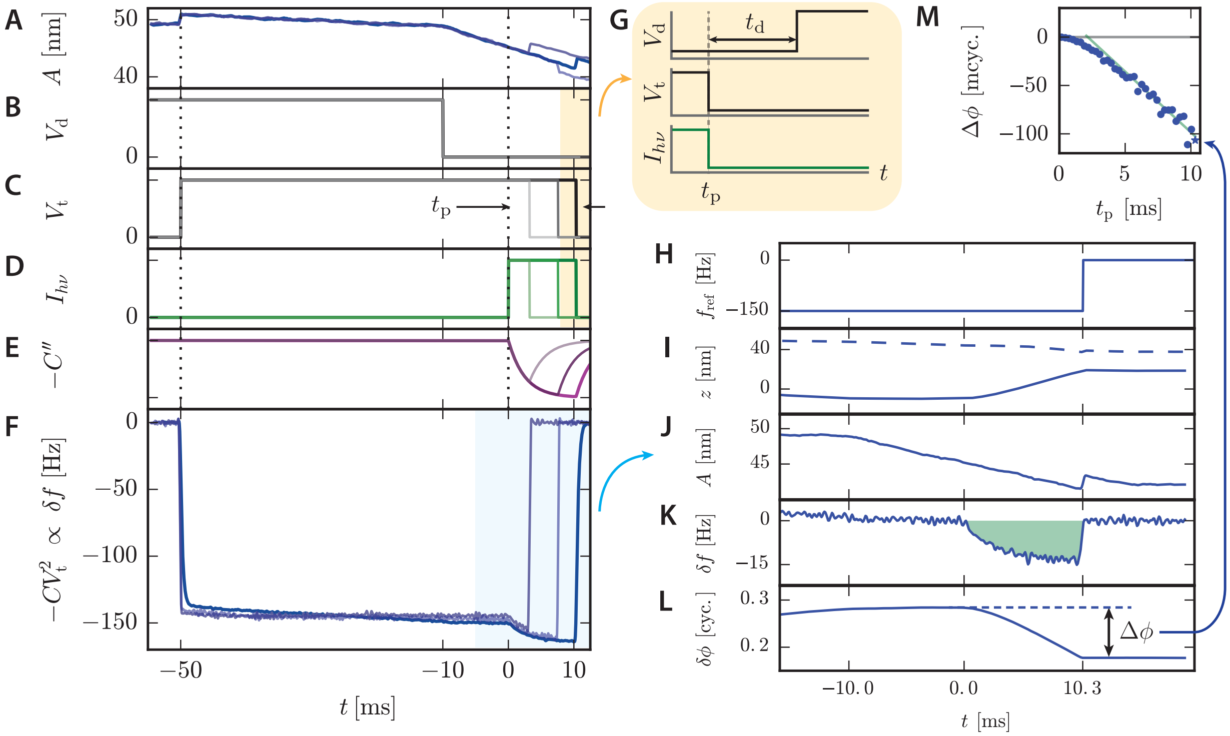

Figure 2.2: **The pk-EFM experiment.** For three representative pulse times, we plot (**A**) cantilever amplitude; (**B**) cantilever drive voltage, turned off at $t = -10\,\mathrm{ms}$; (**C**) tip voltage, with the pulse time t_{p}; (**D**) sample illumination intensity, turned on at $t = 0$; (**E**) sample capacitance; and (**F**) cantilever frequency shift. (**G**) Precise experimental timing for applied voltages and light pulses. The voltage and light turn off simultaneously at $t = t_{\mathrm{p}}$. After a delay t_{d} (typically 5 to $15\,\mathrm{ms}$), the cantilever drive voltage is turned back on. Next we illustrate how the phase shift $\Delta\phi$ is calculated using the $t_{\mathrm{p}} = 10.3\,\mathrm{ms}$ data. We process the cantilever displacement data using a software lock-in amplifier. (**H**) The software lock-in amplifier reference frequency changes at $t = t_{\mathrm{p}}$. The software lock-in amplifier outputs (**I**) the in-phase, real (solid), and out-out-phase, imaginary (dashed) components of the cantilever displacement; (**J**) cantilever amplitude; (**K**) cantilever frequency shift; and (**L**) cantilever phase shift. The total phase shift $\Delta\phi$ is equal to the area under the cantilever frequency shift curve. (**M**) The voltage- and light-induced phase shift $\Delta\phi$ is measured as a function of the pulse time t_{p}. We show only every other data point for clarity. The $t_{\mathrm{p}} = 10.3\,\mathrm{ms}$ data point is denoted with a star. Experimental parameters: PFB:F8BT-on-ITO film, $h = 250\,\mathrm{nm}$, $V_{\mathrm{t}} = 10\,\mathrm{V}$, $I_{h\nu} = 0.3\,\mathrm{kW\,m^{-2}}$, delay time between pulses = $1.5\,\mathrm{s}$. Adapted from Ref. 34, licensed under https://creativecommons.org/licenses/by-nc/4.0/.

Photocapacitance measurements — We bring a conductive cantilever near an organic donor-acceptor semiconductor film (PFB:F8BT, see Fig. 2.1A). A voltage pulse is applied to the cantilever while a carefully timed light pulse is applied to the sample.

Due to the electrostatic interactions with the sample, the cantilever's resonance frequency is shifted by

$$\delta f(t) = -\frac{f_0}{4k_0} C_{\mathrm{t}}''(t, h\nu)\big(V_{\mathrm{t}} - \Phi(t, h\nu)\big)^2, \tag{2.1}$$

where f_0 and k_0 are the cantilever resonance frequency and spring constant, respectively; V_{t} is the tip voltage; Φ is the sample's surface potential; and C_{t}'' is the second derivative of the tip-sample capacitance with respect to the vertical direction. We write $C_{\mathrm{t}}''(t, h\nu)$ and $\Phi(t, h\nu)$ to indicate that these quantities depend on time and light through the sample's photocapacitance and photopotential, respectively. The change in the curvature of the δf *vs.* V_{t} parabola apparent in Fig. 2.1B indicates that, in the PFB:F8BT sample, light primarily affects C'' and not Φ.

To measure the time evolution of the sample's photocapacitance in Fig. 2.1, the tip voltage was fixed at $V_{\mathrm{t}} = 10\,\mathrm{V}$ and the cantilever frequency shift was recorded following the application of a light pulse. The large tip-sample voltage $V_{\mathrm{ts}} - \phi$ makes the measurement relatively insensitive to light-induced changes in Φ. In the representative data of Fig. 2.1C, the photocapacitance charging time is $\tau \sim 5\,\mathrm{ms}$. In Fig. 2.1D we show that photoinduced changes in C_{t}'' persist for many seconds, making it difficult or impossible to collect reproducible data and implement signal averaging. As previously observed by Coffey and Ginger [29, 53], we found that C_{t}'' could be induced to recover quickly by returning the tip voltage to zero, which sweeps out charge accumulated below the tip (Section 2.5, Fig. 2.8).

Experimental protocol — Figure 2.2 shows our new, indirect photocapacitance measurement. We oscillate the cantilever at its resonance frequency using a commercial phase-locked loop controller (Fig 2.2A). Since the cantilever resonance peak in vacuum is narrow (Δf_{FWHM} = $2.5\,\mathrm{Hz}$), we turn off the cantilever drive at $t = -10\,\mathrm{ms}$ so that analysis of the photocapacitance transients is not complicated by phase-locked-loop phase errors (Fig 2.2B). We apply precisely timed voltage steps and light pulses using a commercial pulse and delay generator. To begin the experiment, we step the tip-sample voltage from $V_{\mathrm{t}} = \Phi$ to $V_{\mathrm{t}} = \Phi + 10\,\mathrm{V}$ (Fig 2.2C). Over the next $50\,\mathrm{ms}$, tip-sample charge equilibrates as additional electrons flow to the sample surface. The additional electrons increase the magnitude of the cantilever frequency shift from approximately $\delta f(-50\,\mathrm{ms}) = -133\,\mathrm{Hz}$ to $\delta f(0) = -150\,\mathrm{Hz}$ (Fig. 2.2D).

At $t = 0$, we apply a light pulse synchronized to the cantilever oscillation (Fig. 2.2D). The light pulse initiates charge generation, which causes a change in the capacitance derivative C_{t}'' (Fig. 2.2E). This change induces a small shift in the cantilever's frequency of oscillation (Fig. 2.2F). The frequency shift concomitantly advances the cantilever's *phase* of oscillation (Fig. 2.2E). At a time $t = t_{\mathrm{p}}$, we arrest the photo-induced advance of the cantilever phase by abruptly switching the tip voltage to zero:

$$V_{\mathrm{t}}(t) = \begin{cases} V & \text{for } \; t < \; t_{\mathrm{p}} \\ 0 & \text{for } \; t \geq t_{\mathrm{p}}. \end{cases} \tag{2.2}$$

In these experiments, we end the light pulse simultaneous with the voltage step to limit the sample's exposure to high light intensities (Fig. 2.2G). This is not critical for the measurement, however. No matter when the light pulse ends, $\delta f \approx 0$ after the voltage turns off because $V_{\mathrm{ts}} \approx \Phi$. The end of the light and voltage pulses are not synchronized to the cantilever oscillator cycle. After the voltage turns off, we wait a delay time t_{d} to turn the cantilever drive signal back on. We wait at least $5\,\mathrm{ms}$ so that the data used to determine the cantilever phase at the end of the light pulse is not complicated by phase-locked-loop phase errors ($t_{\mathrm{d}} = 5$ to $15\,\mathrm{ms}$).

Figure 2.2H–M shows how we calculate the phase shift $\Delta\phi = \phi(t_{\mathrm{p}}) - \phi(0)$. The cantilever displacement is detected with a fiber interferometer, digitized at $1\,\mathrm{MHz}$ and saved for later analysis. We first process the cantilever displacement data using a software lock-in amplifier and determine the cantilever frequency before the beginning of the pulse and after the end of the pulse using $5\,\mathrm{ms}$ of data (highlighted region of Fig. 2.2F, section 2.6–2.7). We use these frequencies to construct a second software lock-in amplifier with a variable reference frequency set to match the cantilever frequency before and after the pulse (H). From the in-phase and out-of-phase channels of the lock-in amplifier (I), we determine the cantilever amplitude (J), phase (L), and frequency (K).

The net phase shift $\Delta\phi$ is the time integral of the light-induced change in the cantilever frequency (Fig. 2.2K, shaded region). The frequency shift, and hence the phase shift, depends on the product of the sample's capacitance and the square of the tip voltage (Eq. 2.1). By pulsing the tip voltage we turn the cantilever into a *gated mechanical integrator* of the photocapacitance transient. We step the time t_{p}, repeat the experiment, and plot the net cantilever phase shift $\Delta\phi$ versus t_{p} (Fig. 2.2M). The measured phase shift is proportional to the integrated photocapacitance transient,

$$\Delta\phi = \int_0^{t_{\mathrm{p}}} \delta f(t)\, dt = -\frac{f_0}{4k_0} V^2 \int_0^{t_{\mathrm{p}}} C_{\mathrm{t}}''(t, h\nu)\, dt \tag{2.3}$$

We fit the measured $\Delta\phi$ *versus* t_{p} curve to obtain sample photocapacitance rise time information.

Comparison of photocapacitance measurements — In contrast, tr-EFM measures the photocapacitance rise time constant *directly* by demodulating the cantilever oscillation *versus* time data using a lock-in amplifier filter with bandwidth b_{L} and fitting the resulting frequency shift *versus* time data. The lock-in filter bandwidth limits the time resolution of the measurement since the measured frequency shift convolves the cantilever frequency shift with the lock-in's filter function (Fig. 2.7(A and B)). The wide filter bandwidth nec-

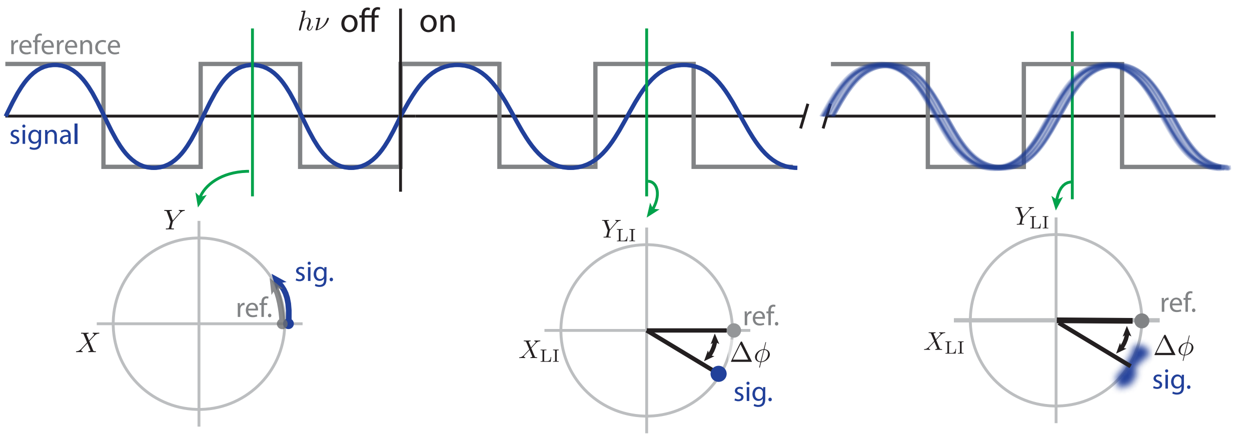

Figure 2.3: **Phase memory and noise.** Illustration of phase memory and phase noise, in the time domain (top), or displayed as $X_{\mathrm{LI}} - Y_{\mathrm{LI}}$ lock-in channel components, or equivalently, in position-momentum state space (bottom).

essary to obtain improved time resolution also increases noise, as shown in Fig. 2.7B and Fig. 2.1C. Any such *direct* measurement faces the same trade-off: detector bandwidth b_{L} determines the time resolution $t_{\mathrm{r}} = 1/2\pi b_{\mathrm{L}}$; increasing b_{L} to reduce t_{r} leads to a larger mean-square frequency noise.

Like ultrafast STM and KPFM photovoltage measurements, pk-EFM is an *indirect* measurement. Indirect measurements record only the *average* detector signal. To build up a picture of the sample's fast dynamics, the average detector signal is measured for a series of different time-offset electrical or optical pulses. The time resolution is limited only by the duration or jitter of the pulses. Crucially, indirect measurements require a system non-linearity so that the average detector signal responds to changes in pulse length, delay, or frequency. In pk-EFM, phase shift $\Delta\phi$ depends on the product of C_{t}'' and V_{t}, so the limited-duration tip-voltage pulses provide the necessary non-linearity.

To detect sub-microsecond photocapacitance changes, Ginger *et al.* introduced *fixed-frequency* and *fast-free time-resolved electrostatic force microscopy* (FF-trEFM) [30, 32]. In both FF-trEFM experiments, the cantilever oscillation is digitized, filtered and demodulated to extract t_{FP}, the time at which the cantilever frequency reaches a minimum. An empirical calibration step is required to relate the measured t_{FP} to the sample's underlying photocapacitance rise time. This empirical calibration step reduces the entire photocapacitance transient to a single number, t_{FP}. Moreover, time resolution is still limited by the detector bandwidth since FF-trEFM is not a true *indirect* measurement.

In contrast, pk-EFM is sensitive to arbitrarily fast changes in photocapacitance during the pulse time t_{p}. Time resolution is obtained by using short pulse times t_{p}. The ultimate time resolution is limited only by the ability to modulate the tip voltage, which can be as fast as ps [54, 55, 56]. We are free to employ a phase filter to minimize the effect of surface and detection noise (Fig. 2.7D and Sections 2.6 and A.1). Figure 2.7E plots the power spectrum of the filtered phase fluctuations. The Fig. 2.7D filter successfully rejects both low frequency surface-induced noise and high frequency detector noise. The Fig. 2.7D filter — and therefore the mean-square phase noise — is essentially independent of the pulse time t_{p} for short pulse times.

2.1.1 pk-EFM Theory

To demonstrate that our new technique is sensitive to subcycle, nanosecond dynamics, we model the cantilever as an oscillator with position x, momentum p, mass m, and spring constant k_0,

$$\dot{x} = p/m \tag{2.4}$$

$$\dot{p} = -(k_0 + \delta k(t))\, x + F(t) \tag{2.5}$$

with,

$$F(t) = \frac{1}{2} C_{\mathrm{t}}'(t) V_{\mathrm{t}}(t)^2 \tag{2.6}$$

$$\delta k(t) = -\frac{1}{2} C_{\mathrm{t}}''(t) V_{\mathrm{t}}(t)^2, \tag{2.7}$$

a time-dependent force and spring-constant shift, respectively, caused by the capacitive tip-sample interaction. In Eq. 2.7, C_{t}' and C_{t}'' are the first and second derivatives of the tip-sample capacitance with respect to height and V_{t} is the tip voltage. We neglect dissipation because the experiments described here occur on a timescale much shorter than the cantilever ringdown time. Equations 2.4 and 2.5 are two coupled linear equations with time-dependent coefficients.

Magnus expansion — While there is no general analytic solution to Eqs. 2.4 and 2.5, we can use the Magnus expansion to obtain a highly accurate approximate solution [57, 58]. The cantilever's evolution can be written in terms of the state vector $\boldsymbol{x} = (x \; p)^T$,

$$\dot{\boldsymbol{x}} = \boldsymbol{A}(t)\boldsymbol{x} + \boldsymbol{b}(t), \tag{2.8}$$

with a state matrix

$$\boldsymbol{A}(t) = \begin{pmatrix} 0 & 1/m \\ -m\omega_0^2 \left(1 + \kappa(t)\right) & 0 \end{pmatrix} \tag{2.9}$$

and generalized force

$$\boldsymbol{b}(t) = \begin{pmatrix} 0 \\ F(t) \end{pmatrix}. \tag{2.10}$$

We write $\boldsymbol{A}$ using the cantilever resonance frequency $\omega_0 = \sqrt{k_0/m}$ and the normalized spring-constant shift

$$\kappa(t) \equiv \delta k(t)/k_0. \tag{2.11}$$

The exact solution for the time evolution of the state vector in Eq. 2.8 can be written in terms of the system's propagator $\boldsymbol{U}$,

$$\boldsymbol{x}(t) = \boldsymbol{U}(t, t_0)\, \boldsymbol{x}(t_0) + \int_{t_0}^{t} \boldsymbol{U}(t, t')\, \boldsymbol{b}(t')\, dt'. \tag{2.12}$$

The Magnus expansion writes the propagator as the exponential of a certain matrix $\boldsymbol{\Omega}$, $\boldsymbol{U}(t, t_0) \equiv \exp \boldsymbol{\Omega}(t, t_0)$. The first-order Magnus approximation for $\boldsymbol{\Omega}$ is

$$\boldsymbol{\Omega}(t, t_0) \approx \int_{t_0}^{t} \boldsymbol{A}(t') dt'. \tag{2.13}$$

This gives the approximate propagator

$$\boldsymbol{U}(t, t_0) \approx \begin{pmatrix} \cos\left(\bar{\omega}\,(t - t_0)\right) & (m\,\bar{\omega})^{-1} \sin\left(\bar{\omega}\,(t - t_0)\right) \\ -m\,\bar{\omega} \sin\left(\bar{\omega}\,(t - t_0)\right) & \cos\left(\bar{\omega}\,(t - t_0)\right) \end{pmatrix}, \tag{2.14}$$

where $\bar{\omega}(t, t_0)$ is a *time-dependent frequency* representing the average cantilever frequency between the time t_0 and t,

$$\bar{\omega}(t, t_0) = \omega_0 \left(1 + \frac{1}{t - t_0} \int_{t_0}^{t} \kappa(t')\, dt'\right)^{1/2}. \tag{2.15}$$

Likewise, $\theta(t, t_0) = \bar{\omega}\,(t - t_0)$ is the cantilever phase accumulated between t_0 and t. Typically $\kappa \ll 1$ so the phase is well-approximated by

$$\theta(t, t_0) \approx \omega_0\,(t - t_0) + \frac{\omega_0}{2} \int_{t_0}^{t} \kappa(t')\, dt'. \tag{2.16}$$

If $\kappa(t)$ is equal to a constant, the first order Magnus expansion is exactly equal to the propagator $\boldsymbol{U}$. For a time varying $\kappa(t)$, corrections to the exponent $\boldsymbol{\Omega}$ will be on the order of the *change* in the normalized spring constant shift $\Delta\kappa$. We typically observe light-induced frequency shifts $\Delta f \leq 62\,\mathrm{Hz}$ for a $f_0 = 62\,\mathrm{kHz}$ resonance frquency cantilever. This corresponds to a maximum change in the normalized spring constant $\Delta\kappa_{\max} = 2\Delta f / f_0 = 2 \times 10^{-3}$. We are justified in neglecting higher-order terms of the Magnus expansion because $\Delta\kappa_{\max} \ll 1$. Equation 2.1, the usual KPFM expression for the cantilever's frequency, is recovered by defining an instantaneous frequency $2\pi f(t) = d\theta/dt$.

Experimental protocol — Consider the experiment of Fig. 2.2. We abruptly initiate sample illumination at time $t = 0$, and the sample's capacitance begins evolving to a new steady-state value. Simultaneously, both C_{t}' and C_{t}'' will likewise evolve to new values, following the same dynamics. The key to extracting the photocapacitance transient is that we can independently control the tip voltage $V_{\mathrm{t}}(t)$. At a subsequent time $t = t_{\mathrm{p}}$, we abruptly turn the tip voltage to zero as in Eq. 2.2. Inserting Eqs. 2.2 and 2.7 into Eq. 2.11 and inserting the result into Eq. 2.16 with $t_0 = 0$, we obtain

$$\theta \approx \omega_0 \, t - \frac{\omega_0 V^2}{4 k_0} \int_0^{t_{\mathrm{p}}} C_{\mathrm{t}}''(t') \, dt', \tag{2.17}$$

which agrees with the phase shift given in Eq. 2.3.

Long time response — For simplicity let us model the photocapacitance dynamics as single-exponential with a rise time of τ. In this approximation $C_{\mathrm{t}}''(t) = C_{\mathrm{t}}''(0) + \Delta C_{h\nu}''(1 - e^{-t/\tau})$ for $t > 0$. Inserting this $C_{\mathrm{t}}''(t)$ into Eq. 2.17, we obtain the cantilever phase measured at $t \geq t_{\mathrm{p}}$,

$$\theta(t) \approx \omega_0 \, t - \frac{\omega_0 V^2}{4 k_0} \Delta C_{\mathrm{t}}''(0) \, t_{\mathrm{p}} + \Delta\phi \tag{2.18}$$

$$\Delta\phi = -\frac{\omega_0 V^2}{4 k_0} \Delta C_{h\nu}'' \left\{ t_{\mathrm{p}} - \tau + \tau \, e^{-t_{\mathrm{p}}/\tau} \right\}. \tag{2.19}$$

The first term in this equation, $\omega_0 \, t$, is the expected time-dependent phase arising from free evolution of the cantilever. The second term is a pulse-time-dependent phase shift arising from the voltage-dependent force gradient. Since both ω_0 and $\Delta C_{\mathrm{t}}''(0)$ are easily measured, it is straightforward to extract from θ the additional phase shift $\Delta\phi$ arising from the transient photocapacitance. The slope of the $\Delta\phi$ *versus* t_{p} line is $-\omega_0 V^2 \Delta C_{h\nu}''/(4 k_0)$ and the intercept is τ, the sample's sought-after photocapacitance rise time.

Short time response — At short times, the forcing term $\boldsymbol{b}(t)$ in Eq. 2.8 also contributes significantly to the cantilever's subsequent motion. We model the C_{t}' photocapacitance dynamics with the same single-exponential rise time τ: $C_{\mathrm{t}}'(t) = C_{\mathrm{t}}'(0) + \Delta C_{h\nu}'(1 - e^{-t/\tau})$. For reference, consider the effect of this force in the absence of photocapacitance ($\Delta C_{h\nu}' = 0$). The electrostatic force vanishes abruptly at time $t = t_{\mathrm{p}}$, so that the cantilever's position and momentum evolve according to the equations

$$\begin{aligned}\begin{pmatrix} x(t \geq t_{\mathrm{p}}) \\ p(t \geq t_{\mathrm{p}}) \end{pmatrix} &= \begin{pmatrix} A_0 \cos\left(\omega_0(t - t_{\mathrm{p}}) + \phi_{\mathrm{p}}\right) + \delta x_0 \cos\left(\omega_0(t - t_{\mathrm{p}})\right) \\ -m\omega_0 A_0 \sin\left(\omega_0(t - t_{\mathrm{p}}) + \phi_{\mathrm{p}}\right) \end{pmatrix} \\ &= \boldsymbol{U}(t, t_{\mathrm{p}}) \begin{pmatrix} A_0 \cos\phi_{\mathrm{p}} + \delta x_0 \\ -m\omega_0 A_0 \sin\phi_{\mathrm{p}} \end{pmatrix} \end{aligned} \tag{2.20}$$

with $\delta x_0 = V^2 C_{\mathrm{t}}'(0)/(2k_0)$ the DC deflection of the cantilever due to the electrostatic force on the tip and $\phi_{\mathrm{p}} = \theta(t_{\mathrm{p}})$ the cantilever's phase at t_{p}, given by Eq. 2.18. For $\delta x_0 \ll A_0$, the effect of δx_0 on x in a voltage-only reference experiment can be written in terms of an equivalent shift in amplitude and phase given by, respectively,

$$\Delta A_{\mathrm{ref}} = \delta x_0 \cos\phi_{\mathrm{p}} \tag{2.21}$$

$$\Delta\phi_{\mathrm{ref}} = -\frac{\delta x_0}{A_0} \sin\phi_{\mathrm{p}}. \tag{2.22}$$

In words, the $V_{\mathrm{t}} \to 0$ step leads to either an amplitude or phase shift depending on the cantilever's absolute phase of oscillation at the moment when the voltage is returned to zero.

The photocapacitance term $\Delta C_{h\nu}'$ adds an additional shift to the cantilever position and momentum

$$\begin{pmatrix} \Delta x_{h\nu}(t \geq t_{\mathrm{p}}) \\ \Delta p_{h\nu}(t \geq t_{\mathrm{p}}) \end{pmatrix} \simeq \delta x_{h\nu} \frac{\omega_0}{1 + \tau^2\omega_0^2} \left\{ t_{\mathrm{p}} - \tau + \tau e^{-t_{\mathrm{p}}/\tau} \right\} \boldsymbol{U}(t, t_{\mathrm{p}}) \begin{pmatrix} \tau\omega_0 \\ -m\omega_0 \end{pmatrix}. \tag{2.23}$$

with $\delta x_{h\nu} = V^2 \, \Delta C_{h\nu}'/(2k_0)$ the DC deflection arising from the photocapacitance-related force. In writing Eq. 2.23, we have used the approximation that we are working in a short-time limit where $t_{\mathrm{p}} \ll 1/\omega_0$ and $\tau \ll 1/\omega_0$. The shifts in position and momentum in Eq. 2.23 should be added to Eq. 2.20. The resulting change in cantilever position can be written in terms of an additional amplitude and phase shift. For $\tau\omega_0 \ll 1$, the effect of $\Delta x_{h\nu}$ on the amplitude and phase is small compared to the effect of $\Delta p_{h\nu}$. In this limit,

$$\Delta A \simeq -\frac{\Delta p_{h\nu}}{m\omega_0} \sin\phi_{\mathrm{p}} \tag{2.24}$$

$$\Delta\phi \simeq -\frac{\Delta p_{h\nu}}{A_0 m\omega_0} \cos\phi_{\mathrm{p}}. \tag{2.25}$$

Writing the amplitude and phase shifts out, we have

$$\Delta A \simeq \delta x_{h\nu} \frac{\omega_0}{1+\tau^2\omega_0^2} \left\{ t_{\mathrm{p}} - \tau + \tau e^{-t_{\mathrm{p}}/\tau} \right\} \sin\phi_{\mathrm{p}} \tag{2.26}$$

$$\Delta\phi \simeq \frac{\delta x_{h\nu}}{A_0} \frac{\omega_0}{1+\tau^2\omega_0^2} \left\{ t_{\mathrm{p}} - \tau + \tau e^{-t_{\mathrm{p}}/\tau} \right\} \cos\phi_{\mathrm{p}}. \tag{2.27}$$

Remarkably, the braced terms in Eqs. 2.23, 2.26 and 2.27 show the same characteristic dependence on τ seen in the long-time phase-shift experiment, Eq. 2.19. By controlling the timing of the voltage pulse we can arrange for ϕ_{p} to be $\pi/2$; in this case the short-time photocapacitance leads to a phase shift. We can instead encode the short-time photocapacitance as an amplitude shift by adjusting the pulse time so $\phi_{\mathrm{p}} = 0$ or π. Below we demonstrate the use of an amplitude shift to verify the effect of short ($< 1\,\mu\mathrm{s}$) duration voltage pulses on the cantilever. The slope of the $\Delta\phi$ *versus* t_{p} line is $\omega_0 V^2 \Delta C'_{h\nu}/(2A_0 k_0)$. We observe that $\Delta C'_{h\nu}/A_0 \gg \Delta C''_{h\nu}$, making the accumulated phase per unit time in the short-time experiment an order of magnitude larger than one would expect from extrapolating Eq. 2.18. This fortuitous finding partially mitigates the challenge of observing the small total phase shift accumulated in a sample with submicrosecond photocapacitance dynamics.

2.2 Results

See the Materials and Methods section for a description of sample-fabrication, measurement, and data-analysis protocols.

We directly compared the new phase-kick technique to tr-EFM by performing both experiments consecutively, under identical illumination and sample conditions ($I_{h\nu} = 100\,\mathrm{kW\,m^{-2}}$, PFB:F8BT on ITO). For the pk-EFM experiment, we measured phase shift $\Delta\phi$ *vs*. pulse time t_{p} for $N = 768$ data points with the pulse time varied from 0 to $1.4\,\mathrm{ms}$. For each pulse time, we also collected a control data point with the light off. For the tr-EFM experiment, we calculated the mean and standard error of the frequency shift δf *vs*. time t from $N = 384$ repetitions. For both experiments, an $87\,\mathrm{ms}$ delay (with $V_{\mathrm{t}} = 0\,\mathrm{V}$) was included between repetitions to ensure the sample's photocapacitance was fully recovered. We operate at a tip-sample separation of $h = 250\,\mathrm{nm}$ to limit the effects of tip-sample drift over the course of the 20 minute measurement. To compare the two experiments, we modeled the cantilever's frequency shift under illumination as the sum of two exponentials,

$$\delta f(t) = \Delta f_1(1 - e^{-t/\tau_1}) + \Delta f_2(1 - e^{-t/\tau_2}). \tag{2.28}$$

The tr-EFM mean frequency shift data was fit directly to Equation 2.28. Since the phase shift during the pulse is the integral of the frequency shift (Eq. 2.3), we fit the phase to the integral of Equation 2.28.

We fit to a biexponential model because the data fits a single exponential model poorly (Section 2.8, Fig. 2.12). A biexponential model offers enough degrees of freedom to adequately fit our data. Since we have no clear microscopic model for photocapacitance, we do not speculate on the physical origin of the two components. We conclude only that the measured frequency shift has both a fast and slow component. If a microscopic model

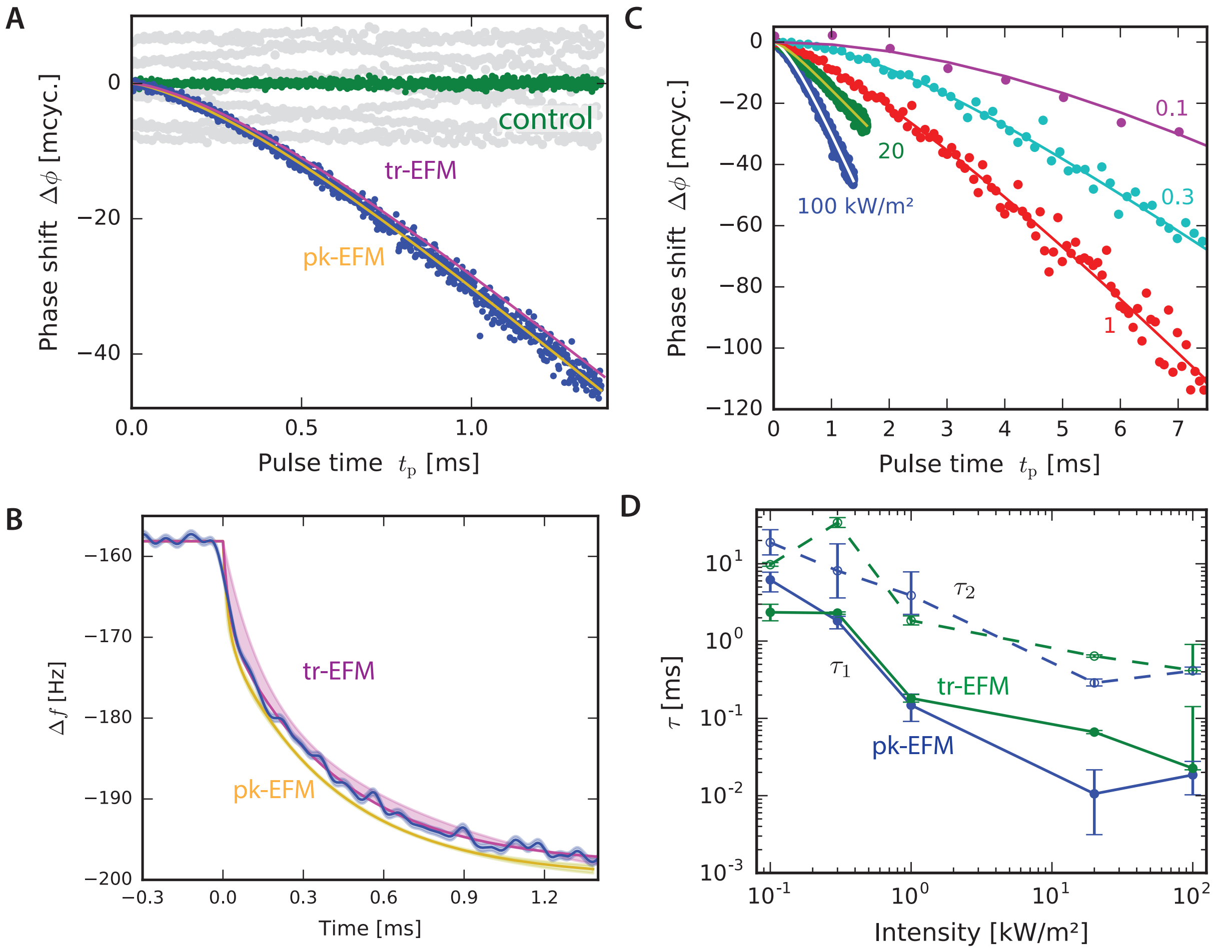

Figure 2.4: **Comparison of pk-EFM and tr-EFM signals** (PFB:F8BT on ITO, $h = 250\,\mathrm{nm}$, and $V_\mathrm{t} = 10\,\mathrm{V}$). (**A**) pk-EFM phase shift *versus* pulse time data, collected at $100\,\mathrm{kW\,m^{-2}}$ intensity, overlaid with best-fit pk-EFM and tr-EFM phase shift curves. The control dataset (green) shows the observed phase shift with the light off. The gray points show the control data before correcting for the phase shift caused by the abrupt change in tip-sample voltage at the end of the pulse. (**B**) tr-EFM frequency shift *versus* time data, overlaid with best-fit tr-EFM and pk-EFM frequency shift curves. (**C**) Phase shift data collected across a range of light intensities. The photocapacitance transient rises more quickly at higher light intensities. Solid curves are a biexponential fit. The delay time between pulses was at least $87\,\mathrm{ms}$. (**D**) Time constants for biexponential fits of photocapacitance transients measured using pk-EFM and tr-EFM show a consistent trend. Adapted from Ref. 34, licensed under https://creativecommons.org/licenses/by-nc/4.0/.

were developed or proposed, it would have to be consistent with our observation of a fast initial change in capacitance and continued slow changes in capacitance that extend for much longer than a single exponential model would predict.

We rule out several other possibilities for the observed biexponential frequency and phase transients. At the highest light intensities, the changes in photocapacitance are fast enough to potentially involve the short time response theory (Eqs. 2.20–2.27). We do see evidence that light-induced changes in the tip-sample force $F \propto C_{\mathrm{t}}'$ affect the cantilever phase, but the size of the neglected phase shift is only $\sim 0.2\,\mathrm{mcyc}$, small compared to the total measured phase shift (Sections 2.9 and 2.10, figure 2.13). The cantilever's displacement power spectral density shows no evidence that higher cantilever eigenmodes are excited in our experiment (section A.2 and figure A.1). The cantilever's surface potential Φ changes by $+160$ to $+440\,\mathrm{mV}$ under illumination (from $0.1\,\mathrm{kW\,m^{-2}}$ to $100\,\mathrm{kW\,m^{-2}}$ intensity). We operate at a tip-sample voltage of $V_{\mathrm{ts}} = \Phi_{\mathrm{dark}} + 10\,\mathrm{V}$, so on its own, the light-induced change in surface potential would result in a *positive* cantilever frequency or phase shift, which we do not observe.

In Fig. 2.4A, we compare the datasets by plotting the pk-EFM phase shift experimental and control data along with the integrated biexponential best fit calculated from both the pk-EFM and tr-EFM experiments. The gray points show the control data before correcting for the phase shift caused by the abrupt change in tip-sample voltage at the end of the pulse (Eq. 2.22, see section 2.7). In Fig. 2.4B, the raw tr-EFM data is compared to the biexponential best fit calculated from both the phasekick and tr-EFM experiments. Even though the two fits come from different datasets, they are quite consistent. The agreement between the plots in Fig. 2.4A and B establishes that both techniques measure the same photocapacitance information.

To further demonstrate the equivalent information obtained with the two techniques,

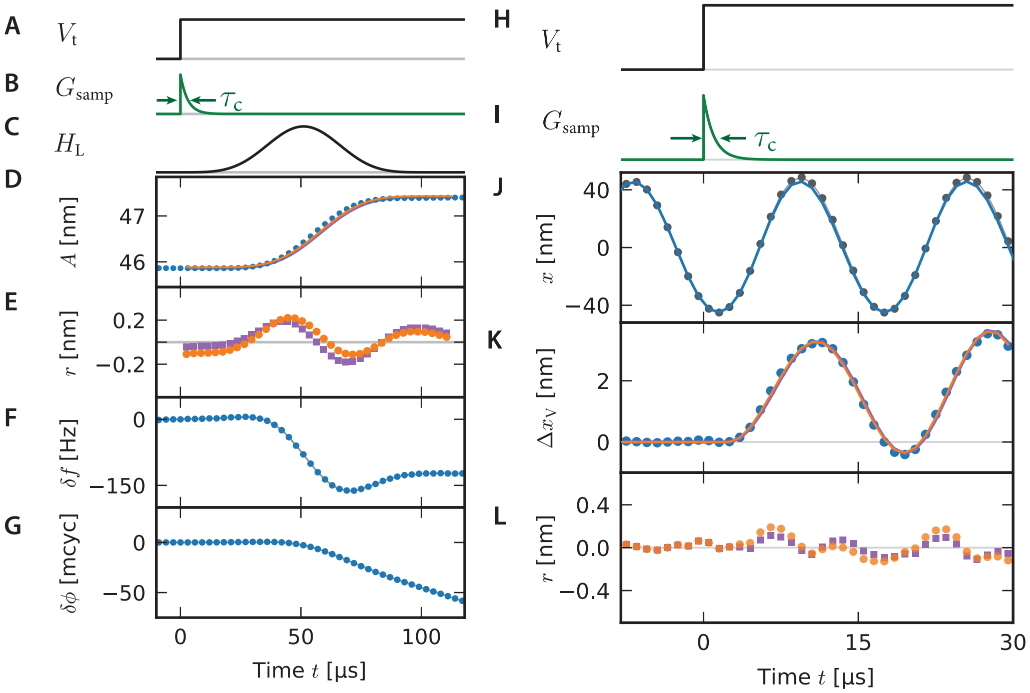

Figure 2.5: **Direct measurements insensitive to fast sample dynamics**. Inferring the charging time *via* the cantilever frequency and phase. (**A**) Cantilever tip voltage; (**B**) sample response function, with charging time constant τ_c; (**C**) lock-in amplifier response function; (**D**) measured cantilever amplitude with modeled, best-fit response for $\tau_c = 0.1\,\mathrm{ns}$ (orange) and $\tau_c = 1000\,\mathrm{ns}$ (purple) (**E**) Fit residuals: $0.1\,\mathrm{ns}$ orange circles, $1000\,\mathrm{ns}$ purple squares. (**F**) Measured cantilever frequency; and (**G**) measured cantilever phase. Inferring the charging time *via* the cantilever displacement. (**H**) Cantilever tip voltage; (**I**) Sample response function; (**J**) Cantilever displacement, with best-fit sinusoid from the data before the voltage step ($t < 0$); (**K**) Change in cantilever displacement Δx_V induced by the voltage pulse, along with best-fit responses for $\tau_c = 10\,\mathrm{ns}$ (orange) and $\tau_c = 350\,\mathrm{ns}$ (purple). (**L**) Fit residuals: $10\,\mathrm{ns}$ orange circles, $350\,\mathrm{ns}$ purple squares. Adapted from Ref. 34, licensed under https://creativecommons.org/licenses/by-nc/4.0/.

we repeated this direct comparison at light intensities ranging from 0.1 to $100\,\mathrm{kW\,m^{-2}}$. The pk-EFM results are shown in Fig. 2.4C. The time constant is different at each light intensity. The best-fit time constants τ_1, τ_2 are found to be comparable for the two methods across the full range of intensities (Fig. 2.4D). For the fast τ_1 time constants measured at $20\,\mathrm{kW\,m^{-2}}$ and $100\,\mathrm{kW\,m^{-2}}$, the time constants and error bars are less directly comparable. The tr-EFM model does not account for the fact that the measured $f_c(t)$ is a convolution of the cantilever's actual frequency shift with the lock-in filter (see Fig. 2.7A), which explains

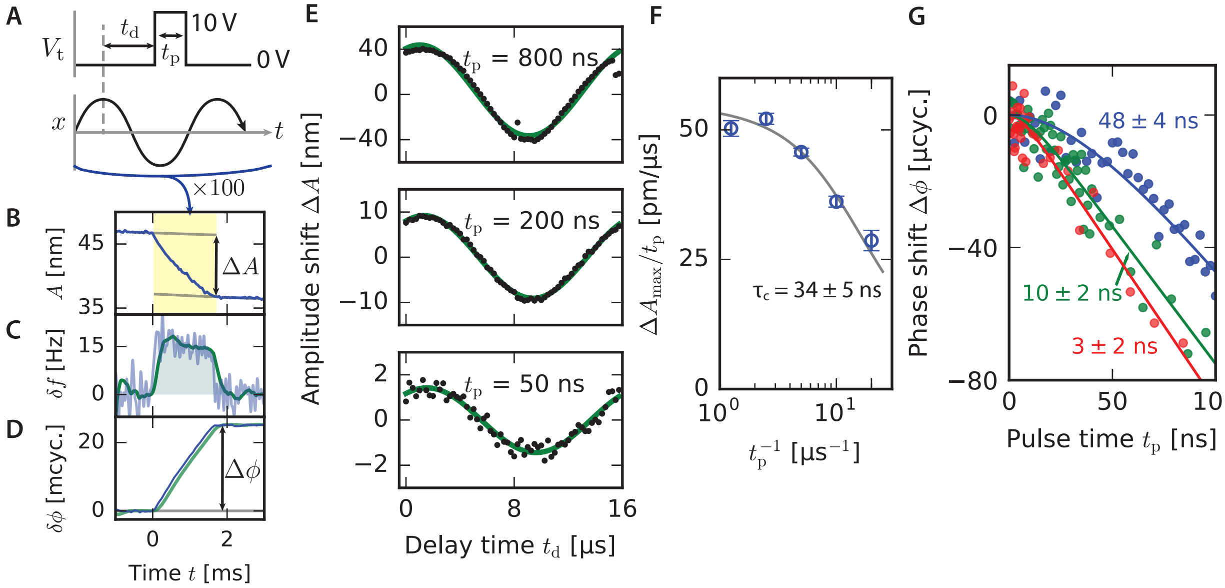

Figure 2.6: **Experimental and simulated evidence for subcycle time resolution in pk-EFM**. (**A**) Subcycle voltage-pulse control experiment (PFB:F8BT on ITO, $h = 250\,\mathrm{nm}$). A voltage pulse of length t_p is applied to the cantilever tip (top) at a delay of t_d relative to the cantilever oscillation (middle) for 100 consecutive cantilever oscillations. (**B**) The pulses shift the cantilever amplitude by ΔA. (**C**) Measured frequency shift; and (**D**) phase shift, demodulated with 3 dB bandwidth $4.8\,\mathrm{kHz}$ (blue) and $1.5\,\mathrm{kHz}$ (green). (**E**) The amplitude shift ΔA *vs*. delay time t_d for three representative pulse lengths. (**F**) The normalized response $\Delta A_{max}/t_p$ obtained by fitting data in (E) shows the cantilever wiring attenuating the response at short pulse times. The gray line is a fit to a single-exponential cantilever charging transient. (**G**) Numerically simulated phase shift in microcycles *vs*. t_p for a sample with a photocapacitance charging time of $50\,\mathrm{ns}$ (blue), $10\,\mathrm{ns}$ (green), and $2\,\mathrm{ns}$ (red). Solid lines are a fit to a single-exponential rise time model. Simulations include detector noise, thermomechanical cantilever position fluctuations, and sample-related frequency noise at levels comparable to those observed in the experiments of Fig. 2.4 (Section A.4). The simulated data assumed 1600 averages per point ($16\,\mathrm{s/pt} = 1600 \times (2\,\mathrm{ms\ acq./pt} + 8\,\mathrm{ms\ delay/pt})$; total acquisition time = 30 minutes). Adapted from Ref. 34, licensed under https://creativecommons.org/licenses/by-nc/4.0/.

why it measures longer time constants. The pk-EFM error bars are also highly dependent on the pulse times used; to better measure the very fast component of the $20\,\mathrm{kW\,m^{-2}}$ data set, for example, more data points could be taken for pulse times from 0 to $100\,\mathrm{\mu s}$. Consistent with Coffey *et al.*, the time constants decrease with increasing intensity [29].

Coffey *et al.* only employed intensities up to $2.5\,\mathrm{kW\,m^{-2}}$. In agreement with Coffey *et al.*, we see very little dependence of Δf_{∞} on intensity at low intensities ($< 2.5\,\mathrm{kW\,m^{-2}}$). At higher intensities, we find that Δf_{∞} increases with increasing intensity (Fig. A.3). The light-induced surface potential change ($\Delta\Phi_{h\nu}$ increasing from $+160$ at $0.1\,\mathrm{kW\,m^{-2}}$ to $+440\,\mathrm{mV}$ at $100\,\mathrm{kW\,m^{-2}}$) would, on its own, lead to a decrease in Δf_{∞} with increasing light intensity. The change in Δf_{∞} is also unlikely to be due to photothermal effects; we estimate that sample heating caused by the laser at $I_{h\nu} = 100\,\mathrm{kW\,m^{-2}}$ is $2\,\mathrm{K}$ during the $1.5\,\mathrm{ms}$ pulse time (section A.3). Even if the sample temperature change were significantly larger, the tip-sample separation h would have to decrease by an implausibly large amount ($\sim 100\,\mathrm{nm}$) to account for the additional frequency shift.

Figure 2.4 shows that we can measure sample dynamics down to the very edge of the long-time response limit with pk-EFM. In the long-time response limit, the difference between pk-EFM and tr-EFM is not dramatic. Before proceeding to the short-time response limit, it is helpful to write a simple model of the measurement. When we turn on the light, the cantilever's *actual* frequency δf_{cant} changes as a function of time. The changes in the cantilever's actual frequency are related to the sample's response function G_{samp}. We write the *actual* cantilever frequency shift δf_{cant} as a convolution (denoted by $*$) of the sample response function G_{samp} and a dummy variable u representing the light intensity:

$$\delta f_{\mathrm{cant}}(t) \propto (u * G_{\mathrm{samp}})(t). \tag{2.29}$$

In tr-EFM or pk-EFM, we attempt to infer information about sample properties (G_{samp}) from the cantilever's *measured* frequency (or phase) shift δf_{meas}. The measured frequency shift δf_{meas} or phase shift $\delta\phi_{\mathrm{meas}}$ is the convolution of the lock-in amplifier response function H_{L} and the cantilever's actual frequency shift:

$$\delta f_{\mathrm{meas}}(t) = (H_{\mathrm{L}} * \delta f_{\mathrm{cant}})(t). \tag{2.30}$$

In a typical direct measurement, it is assumed that sample dynamics are significantly slower than the time scale of the lock-in amplifier response, so that $\delta f_{\mathrm{meas}}(t) \approx \delta f_{\mathrm{cant}}(t)$.

In Figure 2.5, we attempt to use tr-EFM to measure the sample's fast charging time τ_{c}. We step the cantilever tip voltage from $V_{\mathrm{t}} = \Phi$ to $V_{\mathrm{t}} = \Phi + 10\,\mathrm{V}$ (A). The sought-after charging time τ_{c} is a property of the sample response function G_{samp} (B). We expect that the cantilever's actual frequency δf_{cant} quickly changes as the sample charges on the microsecond or faster timescale. However, the measured frequency shift δf_{meas} (F) and phase (E) evolve over a timescale of 10s of microseconds, reflecting the time scale of the lock-in amplifier filter H_{L} (C). We can tell that the force on the cantilever changes much more quickly than the 10s of microsecond timescale by noting that the voltage step changes the cantilever amplitude (D), as described by the abrupt theory of Equation 2.21. The timescale of the change in the cantilever's measured amplitude is dominated by the response of the lock-in amplifier filter. To demonstrate the difficulty of inferring information about sample properties from the measured amplitude and frequency, we model the expected cantilever amplitude for sample charging time constants of $\tau_{\mathrm{c}} = 0.1\,\mathrm{ns}$ (orange) and $\tau_{\mathrm{c}} = 1000\,\mathrm{ns}$ (purple). The residuals for the two models are shown in Figure 2.5E. Since $\tau_{\mathrm{c}} \ll \tau_{\mathrm{L}}$, there is essentially no difference in the cantilever's measured amplitude *versus* time even for a 4 order of magnitude change in the sample charging time. Using the demodulated phase $\delta\phi_{\mathrm{meas}}$ is no improvement; the phase exhibits the same characteristic broadening due to the convolution of the actual phase $\delta\phi_{\mathrm{cant}}$ with the lock-in amplifier filter.

The bandwidth of the lock-in amplifier measurement $b_{\mathrm{L}} = 8\,\mathrm{kHz}$ is much lower than the bandwidth of our detector $b_{\mathrm{det}} = 200\,\mathrm{kHz}$. With the results of our short time response theory (Eqs.2.20–2.27), it is natural to consider measuring the light-induced shifts in cantilever position directly in the time domain. We fit the signal-averaged displacement *versus* time data for $t < 0$ (J, blue curve). In Figure 2.5K, we plot the difference between the measured displacement data and the blue curve fit. This difference corresponds to the additional cantilever displacement caused by the abrupt change in tip-sample force F. We model the charging-induced oscillation and plot the fits and residuals (L) for $\tau_{\mathrm{c}} = 10\,\mathrm{ns}$ (orange, circles) and $\tau_{\mathrm{c}} = 350\,\mathrm{ns}$ (purple, squares). Again, there is almost no difference between the resulting cantilever displacement versus time. This result puts a hard limit on the time resolution of tr-EFM or FF-tr-EFM; if two different sample time constants produce identical cantilever position *versus* time data, no amount of post-processing can distinguish between them.

In contrast, Figure 2.6 shows a pk-EFM measurement of the charging time constant. We applied ($< 1\,\mathrm{\mu s}$) voltage pulses to the cantilever tip on $N = 100$ consecutive cantilever oscillation cycles (A). The demodulated cantilever amplitude, frequency and phase are plotted in Figure 2.6B–D. Figure 2.6E shows that the pulses shift the cantilever amplitude or phase, depending on the phase of the cantilever at the time of the voltage pulse. The magnitude of the amplitude or phase shift is related to the pulse time t_{p}. For instantaneous sample charging, we would expect $\Delta A_{\max} \propto t_{\mathrm{p}}$. Figure 2.6F shows that the magnitude of $\Delta A_{\max}/t_{\mathrm{p}}$ diminishes for short pulse times, consistent with charge being unable to get in and out of the sample on the timescale of the fastest pulses. From $t_{\mathrm{p}} = 50\,\mathrm{ns}$ to $t_{\mathrm{p}} = 800\,\mathrm{ns}$, the magnitude of the sample's response changes by a factor of 2. For a pulse time of $400\,\mathrm{ns}$, the measured amplitude response has reached its DC value. For tr-EFM, however, the measured amplitude only reaches its DC value on the timescale of the lock-in amplifier filter, 10s of $\mathrm{\mu s}$ (Figure 2.5D). Even measured directly in the time-domain, the cantilever takes an order of magnitude longer ($\sim$$5\,\mathrm{\mu s}$) to reach its new equilibrium value

(Figure 2.5K). The key difference is that in pk-EFM, a tip voltage pulse of length t_{p} effectively probes the average value of the sample response G_{samp} response over the interval $t = 0$ to t_{p}. This is dramatically different from the tr-EFM measurement of Figure 2.5D–F, where the measured amplitude, frequency, or phase at a given point in time is always averaged over the width of the lock-in amplifier filter.

To quantitatively describe the experiment of Figure 2.6A–F, we account for the finite charging and discharging time of the sample in response to a square pulse by writing $V_{\mathrm{t}}(t) = V(1 - e^{-t/\tau_{\mathrm{c}}})$ for $t \in (0, t_{\mathrm{p}})$ and $V_{\mathrm{t}}(t) = V(1 - e^{-t_{\mathrm{p}}/\tau_{\mathrm{c}}})e^{-(t-t_{\mathrm{p}})/\tau_{\mathrm{c}}}$ subsequently, where V is the amplitude of the square pulse, τ_{c} the effective sample charging time and t_{p} the duration of the square pulse. Reworking the derivation of the amplitude jump from this starting point gives $\Delta A/t_{\mathrm{p}} = \delta x_{\mathrm{c}} \sin\phi_{\mathrm{p}} \left(1 - \tau_{\mathrm{c}} t_{\mathrm{p}}^{-1} - \tau_{\mathrm{c}} t_{\mathrm{p}}^{-1} e^{-t_{\mathrm{p}}/\tau_{\mathrm{c}}}\right)$ with the phase shift $\phi_{\mathrm{p}} = 2\pi f_0 t_{\mathrm{d}}$ controlled by the pulse time delay t_{d} and $\delta x_{\mathrm{c}} = V^2 C_{\mathrm{t}}'/(2k_0)$ a DC deflection due to electrostatic forces. The measured cantilever amplitude change in Fig. 2.6B shows the expected sinusoidal dependence on delay time. Figure 2.6C shows that the $\Delta A/t_{\mathrm{p}}$ *vs.* t_{p} data is well described by the above equation with $\tau_{\mathrm{c}} = 34 \pm 5\,\mathrm{ns}$.

To provide evidence that pk-EFM can likewise measure nanosecond photocapacitance dynamics, we simulated cantilever dynamics using a model similar to Equations 2.4–2.7. The simulations included independently measured effects from (a) near-surface cantilever frequency fluctuations [59, 60, 61], (b) thermal fluctuations in cantilever position [62], (c) detector noise [60], and (d) transient force and force gradients arising from the gated photocapacitance signal. Representative numerical simulations assuming 30 minutes of signal averaging per curve — including realistic ms-duration photocapacitance "reset" delays — are shown in Fig. 2.6D. A photocapacitance rise time of $10 \pm 2\,\mathrm{ns}$ is clearly resolved.

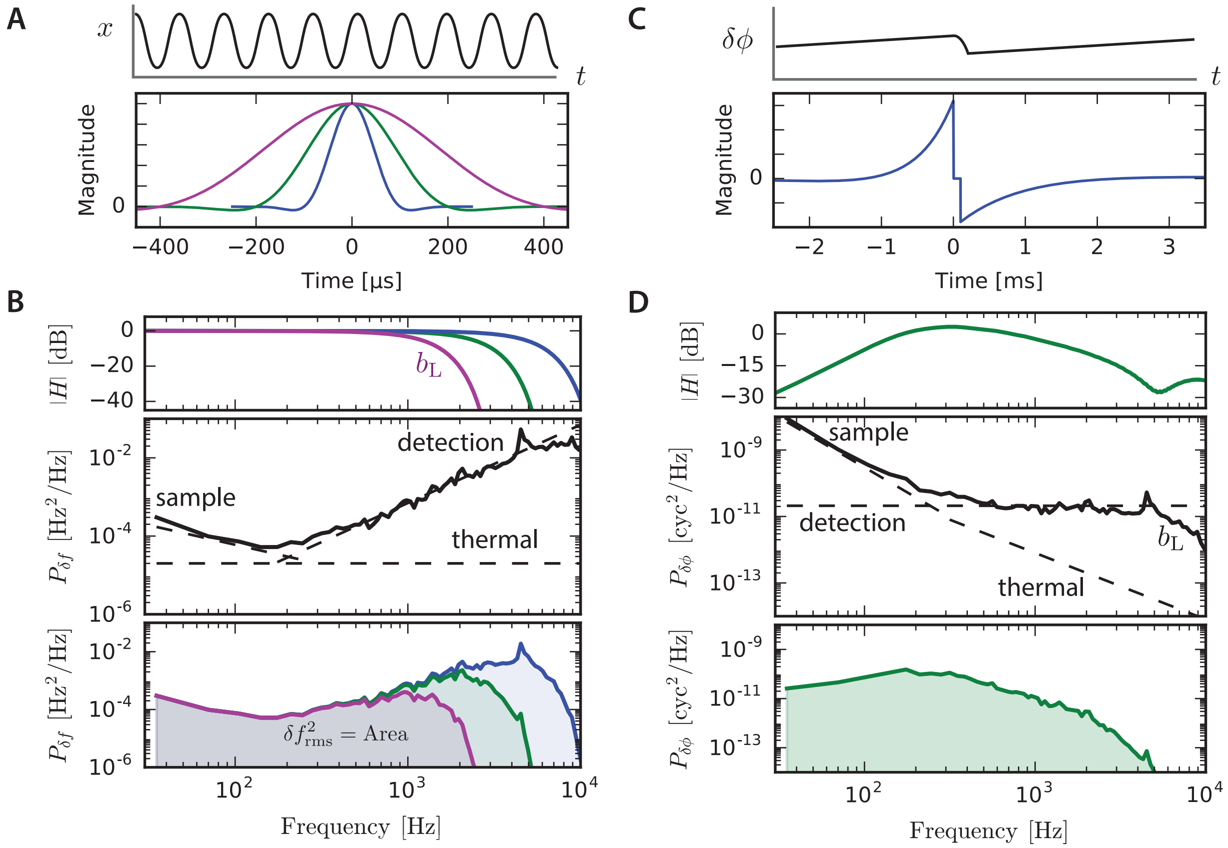

Figure 2.7: **Frequency noise and phase noise in tr-EFM and pk-EFM**. (**A**) Cantilever position-*versus*-time data is demodulated using a filter with varying bandwidths (Fig. 2.9). (**B**) top: Fourier transform of the filters in (A); middle: experimental power spectral density of frequency fluctuations (PFB:F8BT on ITO, $V_\mathrm{t} = 0\,\mathrm{V}$, $h = 250\,\mathrm{nm}$); bottom: product of top and middle traces, shaded to indicate that the mean-square frequency noise is the integral under this curve. (**C**) The cantilever phase (calculated by demodulation) is filtered to estimate the phase difference $\Delta\phi$ acquired during the pulse. The before and after filters are weighted least squares filters, with exponential weight time constants before $\tau_\mathrm{b} = 0.67\,\mathrm{ms}$ and after $\tau_\mathrm{a} = 1.2\,\mathrm{ms}$, see section A.1. (**D**) top: Fourier transform of the filter function in (C); middle: experimental power spectral density of phase fluctuations (PFB:F8BT on ITO, $V_\mathrm{t} = 0\,\mathrm{V}$, $h = 250\,\mathrm{nm}$); bottom: product of top and middle traces, shaded to indicate that the mean-square phase noise is the integral under this curve. Adapted from Ref. 34, licensed under https://creativecommons.org/licenses/by-nc/4.0/.

2.3 Discussion

In this work, we demonstrate a new indirect photocapacitance measurement, pk-EFM. The pk-EFM measurement uses the cantilever as a mechanical integrator and measures cantilever phase shift, a new observable. By measuring phase shift, the average frequency shift during the pulse is inferred without relying on slow modulation and lock-in techniques.

A comparison with the tr-EFM experiment is instructive. In FF-tr-EFM the cantilever oscillation is detected, demodulated, and filtered; the measured parameter is the time t_{FP} at which the resulting cantilever frequency transient reaches a maximum. This observed quantity depends not just on the photocapacitance rise time but on a number of ancillary parameters including the filter parameters and the sample's steady-state photocapacitance. For this reason, an empirical calibration step is required to relate the measured t_{FP} to the sample's underlying photocapacitance rise time. It is unclear how this calibration procedure works if the sample's photocapacitance evolves on multiple time scales, as does the sample studied here.

In pk-EFM the cantilever charge is pulsed and the cantilever oscillation is detected, modulated, and filtered; the measured parameter is the cantilever phase shift. No calibration step is required and the full photocapacitance transient is recovered by measuring the phase shift as a function of the pulse time. In contrast to previous indirect KPFM measurements, pk-EFM makes one phase shift measurement per pulse time, providing crucially important flexibility to include arbitrary wait times and voltage pulses before or after each measurement. This experimental flexibility allows pk-EFM to obtain reproducible photocapacitance measurements in organic semiconductor samples despite lengthy charge equilibration times.

The method's indirect measurement approach allows pk-EFM to measure the full photocapacitance transient, not just its risetime. This capability was demonstrated by uncovering a second, fast photocapacitance risetime not observed before in a nominally well-studied material. The pk-EFM measurement employs well-defined cantilever physics, which enables simulation (including relevant noise sources) of the experiment across a range of timescales. The experiment admits a rigorous signal-to-noise analysis which details how sample fluctuations, thermal noise, and detection noise affect the measurement's phase resolution. The experiments show that pk-EFM is capable of measuring a photocapacitance transient whose rise time is much shorter than the inverse demodulation bandwidth and the cantilever period. Numerical simulations indicate that pk-EFM is capable of resolving a photocapacitance transient whose dynamics are six orders of magnitude faster than the inverse detection bandwidth (Fig. 2.6G).

The pk-EFM measurement, with a faster pulsed light source and modest improvements in the time response of the cantilever-circuit charging time, is poised to achieve nanosecond resolution, comparable to what time-resolved microwave conductivity can achieve. Nanosecond-resolution time-resolved microwave conductivity (TRMC) measurements have generated the first evidence that Marcus theory governs charge carrier generation in dilute donor-acceptor films prepared on non-conductive substrates [17]. TRMC measures the charge-mobility product. Despite Ginger *et al.*'s empirical connection between the tr-EFM risetime and device efficiency, it is not clear what microscopic material property the time-resolved EFM photocapacitance experiment is measuring. Ginger and coworkers observe that light affects primarily the risetime, not the magnitude, of the photocapacitance signal in the EFM experiment. This finding suggests to us that the tr-EFM experiment is mainly probing the sample's photoconductivity. More work is required to test this hypothesis. Tirmzi *et al.* recently reformulated a theory for the EFM experiment in terms of a complex sample impedance [33]. Unifying the Ref. 33 treatment of the EFM experiment with the pk-EFM theory presented here is the next logical step towards connecting the pk-EFM transient signal to materials properties and, ultimately, to microscopic theory.

Given its high temporal and spatial resolution, the phase-kick electric force microscope method introduced here clearly opens up many exciting possibilities for studying charge carrier generation and recombination in a wide range of device-relevant semiconductor films.

2.4 Materials and Methods

2.4.1 Sample preparation

ITO substrates (Nanocs, $10\,\Omega/\mathrm{sq.}$) for depositing organic semiconductors were scrubbed with an Aquet liquid detergent/DI water solution, rinsed with DI water, and sonicated in a fresh Aquet solution for five minutes. The chips were rinsed, sonicated in pure DI water for five minutes and dried with high pressure nitrogen gas. Prior to depositing the solar cell blend, the chips were plasma cleaned for 10 minutes.

To prepare organic bulk heterojunction samples, $75\,\mathrm{mg}$ of PFB (poly(9,9′-dioctylfluorene-*co*-bis-*N*,*N*′-(4-butylphenyl)-bis-*N*,*N*′-phenyl-1,4-phenylenediamine)) and F8BT (poly(9,9′-dioctylfluorene-*co*-benzothiadiazole)) were separately dissolved in $5\,\mathrm{mL}$ p-xylenes. The solutions were filtered using PTFE syringe filters, then mixed together and used immediately. Approximately $200\,\mu\mathrm{L}$ was deposited on an indium tin oxide (ITO) substrate and was spin coated at 2000 rpm for $60\,\mathrm{s}$. All sample preparation was done in a dark room under orange light, and samples were immediately transferred to a nitrogen glovebox. The samples were transferred from the glovebox to the microscope at night, under red light illumination, and exposed to air for less than 15 minutes.

2.4.2 Scanned probe microscopy

All experiments were performed under vacuum ($8 \times 10^{-7}\,\mathrm{mbar}$) in a custom-built scanning Kelvin probe microscope [63]. The cantilever (MikroMasch HQ:NSC18/Pt conductive probe) had resonance frequency $f = 62.000\,\mathrm{kHz}$, spring constant $k = 6.9\,\mathrm{N\,m^{-1}}$ and quality factor $Q = 28000$ (Section A.5 and Fig. A.4). Cantilever motion was detected using a fiber interferometer operating at 1490 nm (Corning SMF-28 fiber). The laser diode's (QPhotonics laser diode QFLD1490-1490-5S) DC current was set using a precision current source (ILX Lightwave LDX-3620) and the current was modulated at radiofrequencies using the input on the laser diode mount (ILX Lightwave LDM-4984, temperature controlled with ILX Lightwave LDT-5910B) [64]. The interferometer light was detected with a $200\,\mathrm{kHz}$ bandwidth photodetector (New Focus model 2011, built-in high-pass filter set to $300\,\mathrm{Hz}$) and digitized at $1\,\mathrm{MHz}$ (National Instruments, PCI-6259). The cantilever was driven using a commercial phase locked loop (PLL) cantilever controller (RHK Technology, PLLPro2 Universal AFM controller), with PLL loop bandwidth $1.2\,\mathrm{kHz}$ (PLL feedback loop integral gain $I = 2.5\,\mathrm{Hz}^{-1}$, proportional gain $P = -12\,\mathrm{degrees/Hz}$).

For pk-EFM and tr-EFM photocapacitance measurements, the sample was illuminated from above with a fiber-coupled $405\,\mathrm{nm}$ laser (Thorlabs, LP405-SF10, held at $25\,^{\circ}\mathrm{C}$ with a Thorlabs TED200C). The laser was turned on and off using the external modulation input of the laser's current controller (Thorlabs, LDC202, $200\,\mathrm{kHz}$ bandwidth), and the laser power was measured using a fiber coupled power meter for each external voltage input. The light was coupled to the sample using a $50\,\mathrm{\mu m}$ core, 0.22 numerical aperture fiber

(Thorlabs FG050LGA) [63]. The estimated spot size on the sample was $(330 \times 120)\,\mu\mathrm{m}^2$, and the illumination intensity was estimated from the measured power and estimated spot size. The measured switching delay was $3.4\,\mu\mathrm{s}$, with a $2.5\,\mu\mathrm{s}$ 0 to 100 percent rise time (Fig. A.5). The tip voltage was switched to $10\,\mathrm{V}$ beginning $50\,\mathrm{ms}$ before the start of the light pulse, in order to allow sample charges to equilibrate (Fig. 2.2D). The cantilever drive was switched off $10\,\mathrm{ms}$ before the start of the light pulse to avoid complicating the cantilever motion with artifacts from the PLL response [30]. A commercial pulse and delay generator (Berkeley Nucleonics, BNC565) was used to generate tip voltage and light modulation pulses, as well as to turn off the cantilever drive voltage. The BNC565 was triggered synchronous with the cantilever oscillation (Section A.6). Between individual pulses, the sample was allowed to recover for $87\,\mathrm{ms}$ to $4\,\mathrm{s}$ with the tip voltage $V_{\mathrm{t}} = 0\,\mathrm{V}$.

Swept-voltage KPFM curves were taken before and after each pk-EFM or tr-EFM measurement to determine the tip-sample capacitance and surface potential [65]. The sample's voltage (controlled with Keithley Model 2400) was adjusted to the sample's surface potential (typically 0.2 to $0.4\,\mathrm{V}$), so that $V_{\mathrm{t}} - \Phi$ was held constant. Measurements were performed $250 \pm 10\,\mathrm{nm}$ above the surface, determined by measuring the 50 percent amplitude reduction point before and after each measurement. Datasets with significant tip-sample drift ($> 10\,\mathrm{nm}$) over the course of the 1 to 20 minute measurement were discarded. The initial cantilever zero-to-peak amplitude was $A = 50\,\mathrm{nm}$. At $t = 0$ the cantilever zero-to-peak amplitude was $42\,\mathrm{nm}$.

The raw cantilever oscillation data (digitized at $1\,\mathrm{MHz}$) was saved along with counter timings (PCI-6259, 80 MHz counter) indicating the precise starting time of the light pulse (synchronized to the cantilever oscillation), allowing the start of the the light pulse to be determined to within $12.5\,\mathrm{ns}$. Along with each pk-EFM phase shift data point, a control data point, identical except without turning on the light, was collected.

2.4.3 Data workup

The data was processed in Python using a virtual lock-in amplifier technique. First, the data was processed through a fixed-frequency lock-in amplifier, with the reference frequency f_{ref} equal to the frequency where the data's Fourier transform was a maximum. The lock-in filter was a modified Blackman finite impulse response filter, as described in Section 2.6, designed to pass frequencies below $f_{\mathrm{LP1}} = 2\,\mathrm{kHz}$ and to eliminate frequencies above $f_{\mathrm{LP2}} = 8\,\mathrm{kHz}$ (3 dB bandwidth $3.84\,\mathrm{kHz}$). To precisely determine the additional light-induced phase shift in the vicinity of large changes to the cantilever frequency caused by stepping the cantilever tip voltage, the data was also processed with a *frequency-variable* virtual lock-in amplifier, with

$$f_{\mathrm{ref}} = \begin{cases} f_1 & t \leq t_{\mathrm{p}} \\ f_2 & t > t_{\mathrm{p}}. \end{cases} \tag{2.31}$$

The complex output z of the lock-in amplifier was demodulated into amplitude $A = |z|$ and phase $\phi = \arg z$. The frequency was calculated from the phase using a central-difference numerical derivative.

pk-EFM phase difference filter — The filtering of the frequency and phase was performed analogously. The frequency f_1 was chosen to be the best estimate of the cantilever frequency before the start of the light pulse, determined by averaging $f(t)$ out of the lock-in with an exponential weighting with a time constant of $0.67\,\mathrm{ms}$. The frequency f_2 was chosen to be the best estimate of the cantilever frequency after the end of the voltage pulse, using a $1.2\,\mathrm{ms}$ exponential time constant. These same time constants were used to determine the phase estimate of the cantilever phase before and after the pulse. The time constants were chosen to minimize the noise, which is determined by the competition between low-frequency surface-induced noise, which needs to be allowed through the filter to better estimate the *actual* frequency and phase, and high-frequency detection noise, which needs to be rejected to estimate frequency and phase as precisely as possible. The time constants are different because after the pulse the tip voltage was set to $V_{\mathrm{t}} = 0\,\mathrm{V}$, reducing the surface noise and allowing the phase and frequency to be determined more precisely by averaging for a longer time (Fig. 2.10). The phase before and after the pulse was determined using a weighted linear fit with the same exponential weighting used to determine the frequency (Section A.1). The phase difference filter is shown in Fig. 2.7D.

As illustrated in Fig. 2.7D and Fig. 2.11, a weighted linear fit, with the same exponential time constants used to determine f_1, f_2, was use to analyze the control data before and after the end of the pulse. To determine the precise cantilever phase at the end of the pulse, the 20 displacement data points nearest to $t = t_{\mathrm{p}}$ were used to create a Krogh interpolator in Scipy [66, 67]. The Krogh interpolator and its first derivative evaluated at t_{p} give the cantilever position x and velocity v. The cantilever phase was calculated from x and v using,

$$\phi|_{t=t_{\mathrm{p}}} = \arg(x - \frac{v}{2\pi f[k]} i) \tag{2.32}$$

$$t_{\mathrm{d}} = 2\pi \phi f[k], \tag{2.33}$$

where $f[k]$ is the cantilever frequency determined by the digital lock-in amplifier at the data point nearest in time to t_{p}.

The resulting amplitude change ΔA *vs*. delay time t_{d} and phase shift $\Delta\phi$ *versus* t_{d} plots were fit to sinusoids, and the best-fit phase shift was used to correct the raw phase shift data acquired in the light-on pk-EFM dataset (Fig. 2.4A). The corrected phase shifts are plotted in Fig. 2.4(A and C).

The tr-EFM data was processed with a filter bandwidth dependent on the fastest time constant in the sample ($f_{\mathrm{LP1}} = 4\,\mathrm{kHz}$, $f_{\mathrm{LP2}} = 15\,\mathrm{kHz}$ for the $20, 100\,\mathrm{kW\,m^{-2}}$ intensity data sets). The resulting frequency-*versus*-time data was aligned relative to the start of the light pulse and averaged ($N = 32$ to 384). The $100\,\mathrm{kW\,m^{-2}}$ tr-EFM data is shown in Fig. 2.7B. See Section 2.6 for more information.

2.4.4 Statistical analysis

Signal-averaged tr-EFM frequency shift *versus* time data and processed phase shift *versus* pulse time data was fit to bi-exponentials using PyStan [68], a programming environment for Bayesian modeling. In both cases, the data was modeled assuming that the frequency shift *versus* time data was constant before the light pulse, and was characterized by a bi-exponential decay afterwards. The tr-EFM average frequency $\bar{f}$ and standard error σ_f at each time t were used to model the experimental data. The mean frequency shift $\bar{f}$ was modeled as normally distributed with standard deviation equal to the standard error. Using the notation $y \sim \mathcal{N}(\mu, \sigma)$ to indicate y is distributed normally ($\mathcal{N}$) with mean μ and standard deviation σ, the tr-EFM model was

$$\begin{cases} \bar{f}[t] \sim \mathcal{N}(f_0, \sigma_f[t]) & t \leq 0 \\ \bar{f}[t] \sim \mathcal{N}(f_0 + \Delta f_\infty \left[r(1 - e^{-t/\tau_1}) + \right. & \\ \qquad\qquad \left. (1-r)(1 - e^{-t/\tau_2}) \right], \sigma_f[t]) & t > 0, \end{cases} \tag{2.34}$$

where $\bar{f}[t], \sigma_f[t]$ were the experimental mean frequency shift and standard error calculated from signal-averaging N tr-EFM measurements. The model's parameters were f_0, the cantilever frequency before the pulse; Δf_∞, the steady state frequency shift caused by the photocapacitance; r, the fraction of the steady state frequency shift attributed to the faster time constant; and τ_1 and τ_2, the exponential time constants, with $\tau_1 < \tau_2$.

The pk-EFM model was more complicated, because more low-frequency phase noise enters the measurement at longer pulse times. We captured this time-dependent phase noise by modeling the phase noise standard deviation $\sigma_\phi[t_\mathrm{p}]$ as

$$\sigma_\phi[t_\mathrm{p}] = \sigma_0 + \sigma_1 t_\mathrm{p} + \sigma_2 t_\mathrm{p}^2, \tag{2.35}$$

with σ_0, σ_1, and σ_2 parameters. We modeled the observed $\Delta\phi[t_\mathrm{p}]$ using

$$\begin{aligned} \mu_\phi[t_\mathrm{p}] = \quad & \Delta f_\infty \left[r \left\{ t_\mathrm{p} - \tau_1 + \tau_1 e^{-t_\mathrm{p}/\tau_1} \right\} \right. && (2.36) \\ & \left. + (1-r) \left\{ t_\mathrm{p} - \tau_2 + \tau_2 e^{-t_\mathrm{p}/\tau_2} \right\} \right] \\ \phi[t_\mathrm{p}] \sim \mathcal{N}(\mu_\phi[t_\mathrm{p}], \sigma_\phi[t_\mathrm{p}]), & && (2.37) \end{aligned}$$

where $\mu_\phi[t_\mathrm{p}]$ is the integral of the frequency shift induced by the light pulse (Eqs. 2.3 and 2.19).

For both models, weakly informative priors were chosen for $\Delta f_\infty, \tau_1$, and τ_2. A uniform prior between 0 and 1 was used for the ratio r. Noise parameters σ_0, σ_1, and σ_2 used implicit flat priors. The parameter means, standard deviations, and 15, 50, 85 percentile best fit curves in Fig. 2.4 were calculated using at least $N = 6000$ samples drawn from the posterior. See Section A.7 for more information.

Experimental data and code to reproduce the analysis performed above are available freely online [69]. A standalone Python package for cantilever frequency demodulation is also available freely online [70].

2.5 Tip voltage photocapacitance clearing

Figure 2.1D shows that with the light off and the tip voltage V_t far from the the surface potential ϕ, the photocapacitance decays very slowly. By turning off the light and pulsing the tip voltage from $10\,\mathrm{V}$ back to $0\,\mathrm{V}$, we show that remnant photocapacitance can be cleared in 10s to 100s of microseconds (Fig. 2.8). For comparison, the data in Figure 2.4 of the manuscript was acquired with a delay time $\geq 87\,\mathrm{ms}$.

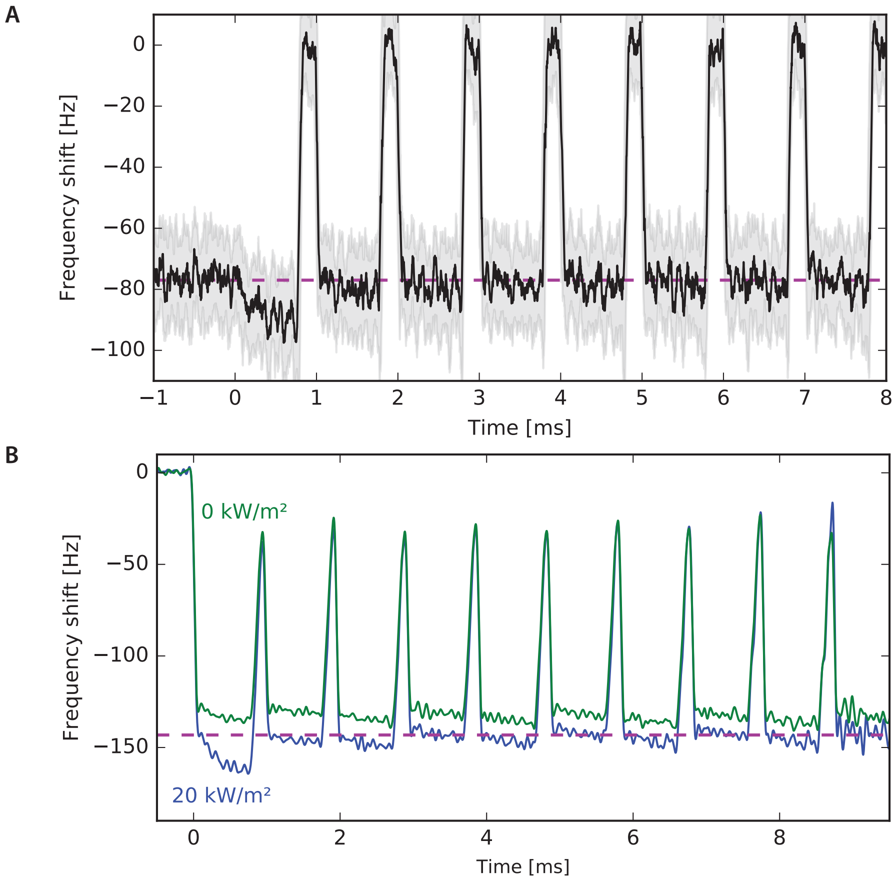

Figure 2.8: **Fast clearing of remnant photocapacitance**. (**A**) At time $t = 0$ with the tip-sample voltage set to $V_{\mathrm{t}} = 7\,\mathrm{V}$, a light pulse was sent to the sample (PFB:F8BT on ITO, see Methods; pulse duration = $900\,\mu\mathrm{s}$; pulse intensity $I_{h\nu} = 20\,\mathrm{kW\,m^{-2}}$). Thereafter, the tip voltage was cycled to $0\,\mathrm{V}$ for $100\,\mu\mathrm{s}$ and to $7\,\mathrm{V}$ for $900\,\mu\mathrm{s}$. The dark line is the mean frequency shift for $N = 64$ averages, worked up using $f_{\mathrm{LP1}} = 4\,\mathrm{kHz}$, $f_{\mathrm{LP2}} = 15\,\mathrm{kHz}$ (see Fig. 2.9). The gray shaded region shows the 25th to 75th percentiles. The purple line shows the mean frequency shift before the pulse, and indicates that the photocapacitance has recovered after 1 or 2 pulses of $100\,\mu\mathrm{s}$ duration with $V_{\mathrm{t}} = 0$. (**B**) The same experiment is repeated with shorter duration waits at $0\,\mathrm{V}$. After the light pulse, the tip voltage is repeatedly cycled to $0\,\mathrm{V}$ for $8.5\,\mu\mathrm{s}$ and $7\,\mathrm{V}$ for $900\,\mu\mathrm{s}$. Adapted from Ref. 34, licensed under https://creativecommons.org/licenses/by-nc/4.0/.

2.6 Data workup discussion

The data workup procedure is outlined in Fig. 2.9. The variable-frequency lock-in amplifier used a reference frequency reflecting the expected changes to the cantilever frequency caused by the changing tip voltage, $f_{\mathrm{L}} = f_0 - f_0 C_{\mathrm{t}}''(0) V_{\mathrm{t}}(t)^2/(4k_0)$. The resulting frequency difference is shown in Fig. 2.9A (bottom).

The low-pass lock-in filter H_{L} was constructed in the frequency domain, using a passband frequency f_{LP1}, below which the filter response should be 1, and a stopband frequency f_{LP2}, above which the frequency response should be 0. The frequency domain response was a Tukey window, which tapers from 1 to 0 between the passband frequency f_{LP1} and the stopband frequency f_{LP2}. The resulting time domain filter of $N = 16 f_{\mathrm{s}}/f_{\mathrm{LP1}}$ coefficients (where f_{s} is the sampling rate) was multiplied by a Blackman window to produce the final filter coefficients. The filter's 3-dB bandwidth was approximately $1.92 f_{\mathrm{LP1}}$. The filter magnitude response and time domain coefficients are shown in Fig. 2.9B.

The resulting complex lock-in signal z generated by the digital lock-in amplifier is

$$z[k] = H_{\mathrm{L}} * (x[k] \exp(-2\pi i f_{\mathrm{L}}[k])), \tag{2.38}$$

where x is the cantilever displacement and the square brackets indicate that we work with an array of discrete data points. The points have index $k = 1, 2, 3, \ldots, N$ corresponding to times $t = k\Delta t + t_0$, where $\Delta t = 1\,\mu\mathrm{s}$ is the sampling time (inverse of the National Instruments PCI-6259's sampling rate) and the initial time t_0 is an offset used to align the start of the light pulse to $t = 0$. The asterisk ($*$) denotes a discrete convolution. From the signal z, we computed amplitude $A[k] = |z[k]|$, phase $\phi[k] = \arg z[k]$, and frequency shift $\delta f[k] = (\phi[k+1] - \phi[k-1])/(4\pi \Delta t)$, where the frequency shift is a central difference estimate of the derivative of $\phi[k]$.

The signal-to-noise ratio of the pk-EFM measurement was sensitive to the chosen

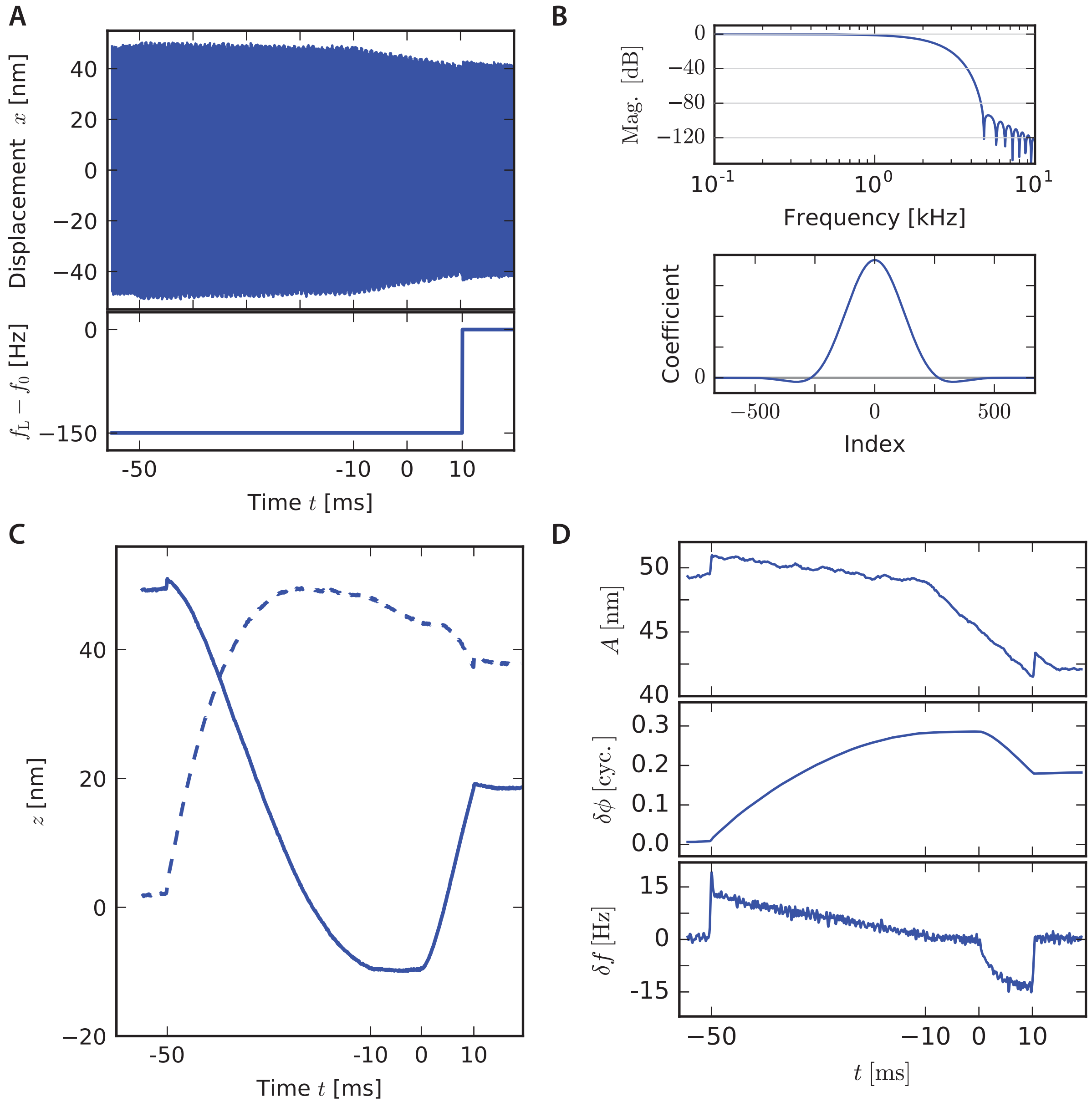

Figure 2.9: **Cantilever oscillation data workup protocol**. (**A**) Cantilever displacement *versus* time data. (**B**) Lock-in filter magnitude response and coefficients. (**C**) Real (solid) and imaginary (dashed) components of the lock-in output. (**D**) Lock-in output processed into amplitude, phase, and frequency *vs*. time. At $t = -10\,\mathrm{ms}$, the cantilever drive voltage was turned off. Adapted from Ref. 34, licensed under https://creativecommons.org/licenses/by-nc/4.0/.

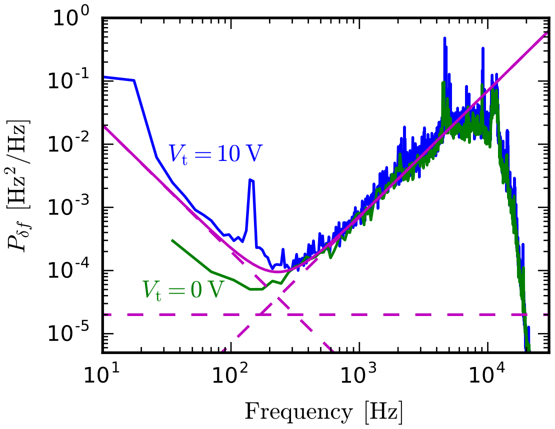

Figure 2.10: **Power spectral density of cantilever frequency fluctuations**. Adapted from Ref. 34, licensed under https://creativecommons.org/licenses/by-nc/4.0/.

phase-difference-filter time constant τ (Fig. 2.7D). If τ was too long, the estimated phase incorporated too much low frequency sample-induced phase noise. If τ was too short, the estimated phase was unduly influenced by high-frequency detection noise. The large low-frequency phase noise, $P_{\delta\phi} \propto f^{-3}$ (Fig. 2.7E), made it important to choose a relatively short τ. The time constant was chosen to be the inverse of the frequency f where

$$P_{\delta\phi}^{\text{det}}(f) = P_{\delta\phi}^{\text{samp}}(f) + P_{\delta\phi}^{\text{therm}}(f). \tag{2.39}$$

2.7 Reference amplitude and phase shift

To correctly estimate the cantilever phase shift during the pulse, we had to account for the phase shift caused by the abrupt change in tip-sample voltage at the end of the pulse. The measured phase shift $\Delta\phi$ includes both the light-induced phase shift $\Delta\phi_{h\nu}$ and the phase shift $\Delta\phi_{\text{ref}}$ resulting from the abrupt change in the cantilever voltage at the end of the cantilever pulse: $\Delta\phi = \Delta\phi_{h\nu} + \Delta\phi_{\text{ref}}$. First, the step change in V_t creates a frequency shift according to the standard KPFM equation (Eq. 2.1). Equation 2.1 gives the cantilever frequency ignoring any additional effects caused by abruptly changing the cantilever charge.

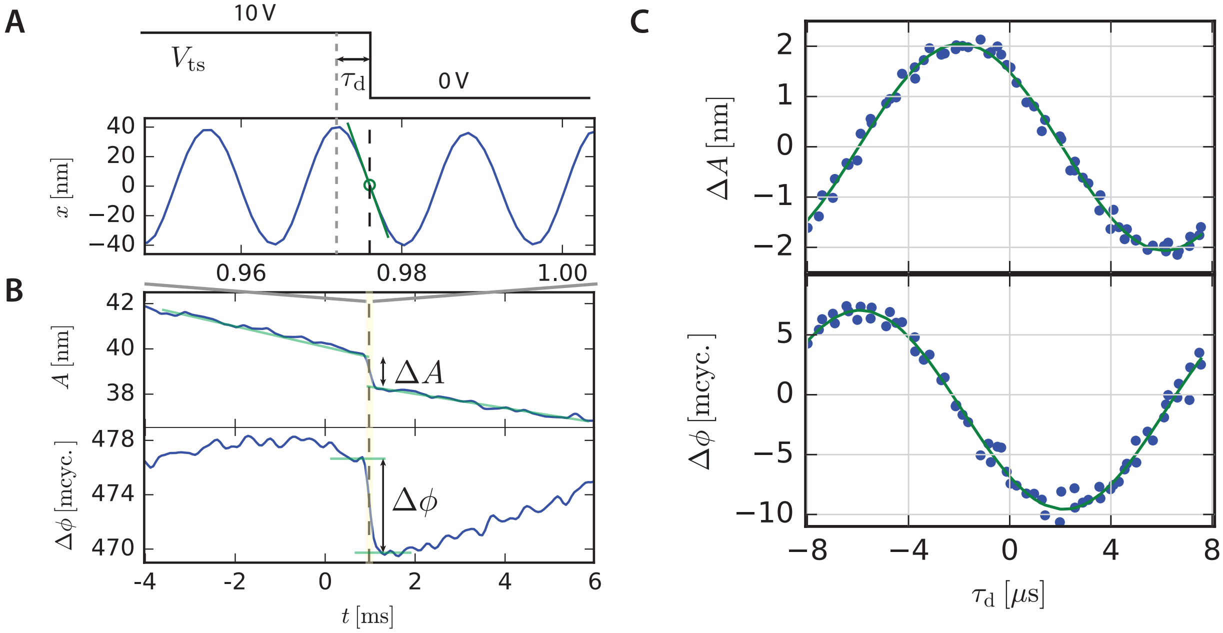

Figure 2.11: **Analysis of the amplitude and phase shifts imparted by the abrupt voltage step in the pk-EFM experiment**; data from a control dataset acquired at zero light intensity at a height $h = 250\,\mathrm{nm}$ above a film of PFB:F8BT on ITO. (**A**) The end of the tip voltage pulse occurs at time τ_{d} relative to the cantilever oscillation cycle, with $\tau_{\mathrm{d}} = 0$ defined as the time at which the cantilever reaches its maximum extension. (**B**) The resulting amplitude and phase shifts caused by abruptly turning off the tip voltage. (**C**) The amplitude and phase shifts for each pulse are plotted *versus* the delay time t_{d}. The amplitude and phase shifts imparted by the abrupt change at the end of the voltage pulse depend on τ_{d}, as described by Eqs. 2.21 and 2.22. Amplitude best-fit parameters: $A_{\max} = 2.06 \pm 0.02\,\mathrm{nm}$, $\theta = -136.6 \pm 0.7$ deg., and $\Delta A_0 = 0.01 \pm 0.02\,\mathrm{nm}$. Phase best-fit parameters: $\phi_{\max} = 8.3 \pm 0.1\,\mathrm{mcyc}$, $\theta = -137.9 \pm 0.9$ deg., and $\Delta\phi_0 = -1.3 \pm 0.1\,\mathrm{mcyc}$. Adapted from Ref. 34, licensed under https://creativecommons.org/licenses/by-nc/4.0/.

We account for the KPFM frequency and phase shift using a variable frequency lock-in amplifier (see text 2.6).

To account for the phase and amplitude shifts caused by the step change to the tip-sample voltage, we use Eqs. 2.21 and 2.22 to model the additional impulsive phase shift and amplitude shift delivered by the end of the pulse. As shown in Fig. 2.11, we fit the

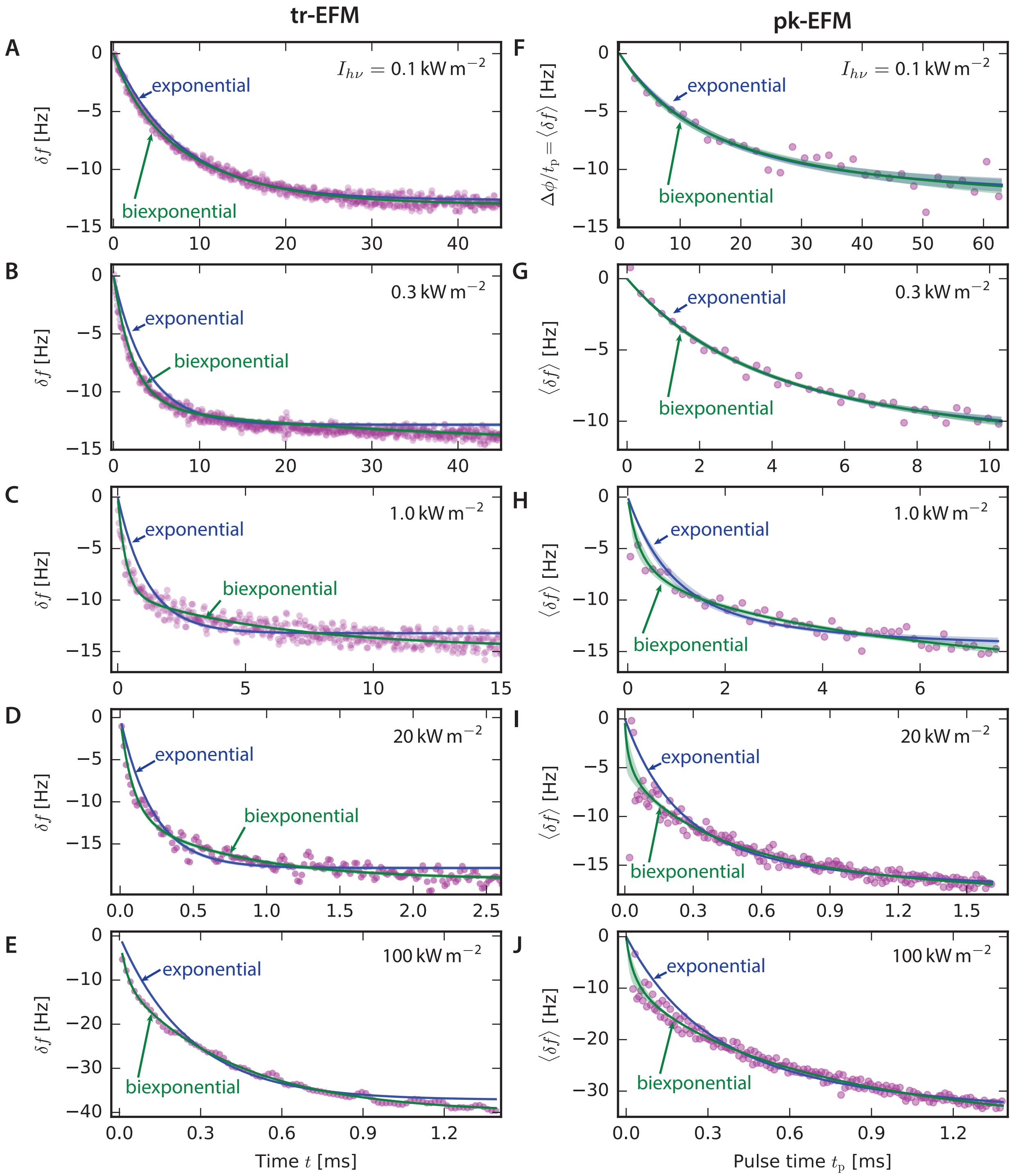

Figure 2.12: **Comparison of single and biexponential fits to tr-EFM and pk-EFM data.** (**A**–**E**) tr-EFM data (purple points) fitted to single exponential (blue curve) and biexponential (green curve) frequency shift models. (**F**–**J**) pk-EFM data (purple points) fitted to single exponential (blue curve) and biexponential (green curve) frequency shift models. The purple data points are the average of two (**F** – **H**) or four (**I**–**J**) adjacent pulse times. The blue and green regions show the 5th to 95th percentile of the single and biexponential curve fits respectively, determined from $N = 6000$ MCMC samples. Experimental parameters: PFB:F8BT on ITO, $h = 250\,\mathrm{nm}$, and $V_t = 10\,\mathrm{V}$. Adapted from Ref. 34, licensed under https://creativecommons.org/licenses/by-nc/4.0/.

control data to the equation

$$\Delta A_{\mathrm{mod}}(t_{\mathrm{d}}) = -A_{\mathrm{max}} \cos(2\pi f_{\mathrm{c}} t_{\mathrm{d}} + \theta) + \Delta A_0 \tag{2.40a}$$

$$\Delta \phi_{\mathrm{mod}}(t_{\mathrm{d}}) = \phi_{\mathrm{max}} \sin(2\pi f_{\mathrm{c}} t_{\mathrm{d}} + \theta) + \Delta \phi_0, \tag{2.40b}$$

with fitting parameters A_{max}, the maximum amplitude; ϕ_{max}, the maximum phase shift; θ, a phase offset accounting for the detector delay; ΔA_0, an amplitude offset; and ϕ_0, a phase-shift offset. The magnitudes of the amplitude and phase corrections are self-consistent. From Eqs. 2.21 and 2.22, we have

$$\Delta \phi_{\mathrm{max}} = \Delta A_{\mathrm{max}} / A_0 = 2.06\,\mathrm{nm}/40\,\mathrm{nm} = 8.2\,\mathrm{mcyc}, \tag{2.41}$$

which is within the error bar of the measured value of $\Delta \phi_{\mathrm{max}} = 8.3 \pm 0.1\,\mathrm{mcyc}$. The phase offsets θ from the amplitude and phase fits are also self-consistent. As the equations are defined, the two phases ϕ should be strictly equal. The calculated best fit values for ϕ differ by $1.3 \pm 1.1\,\mathrm{deg}$.

2.8 Biexponential curve fits

Figure 2.12 compares single and biexponential curve fits to the data of Figure 2.4. Both models adequately fit the $0.1\,\mathrm{kW\,m^{-2}}$ tr-EFM data (A). At all higher light intensities (B–E), the single exponential model does not fit the tr-EFM data as well. In each case, the single exponential model does not have enough degrees of freedom to capture both the initial rapid change in cantilever frequency shift and the slow, extended movement towards equilibrium.

For the pk-EFM data, we plot the average cantilever frequency shift during the pulse $\langle \delta f \rangle = \Delta \phi(t_{\mathrm{p}})/t_{\mathrm{p}}$ to highlight the difference between the two models at short pulse times t_{p}. Both models adequately fit the $0.1\,\mathrm{kW\,m^{-2}}$ pk-EFM data (Fig. 2.12F). The $0.3\,\mathrm{kW\,m^{-2}}$

pk-EFM data (G) is collected over a much shorter range of pulse times (0 to $10\,\mathrm{ms}$) than the $0.3\,\mathrm{kW\,m^{-2}}$ tr-EFM data (B, $45\,\mathrm{ms}$), so both models are still able to adequately capture the dynamics over this shorter period of time. For the higher intensity pk-EFM data (H–J), the single exponential model misses the short time dynamics as it did for the tr-EFM data. Overall, the pk-EFM data is consistent with the tr-EFM data, and in both cases a single exponential model fits the data poorly.

2.9 Alternative explanations of photocapacitance dynamics

At the highest light intensities ($I_{h\nu} = 20\,\mathrm{kW\,m^{-2}}$ and $100\,\mathrm{kW\,m^{-2}}$), the timescale of the fast component of the sample dynamics starts to approach the cantilever's characteristic timescale $\omega_{\mathrm{c}}^{-1} = 2.6\,\mathrm{\mu s}$ (Fig. 2.4D). In this case, the effect of the forcing term $\mathbf{b}(t) \propto C_{\mathrm{t}}'(t)$ must be considered. The situation is similar to the one considered in Equation 2.23, but the pulse time t_{p} used in the tr-EFM and pk-EFM experiments of Figure 2.4 is usually longer than a cantilever period. In this case, the approximate additional cantilever position shift induced by the light pulse is

$$\Delta x_{h\nu}^{F}(t>0) = \underbrace{\delta x_{h\nu}\Big(1 - \frac{\omega_{\mathrm{c}}^2\tau_{\mathrm{x}}^2}{1+\omega_{\mathrm{c}}^2\tau_{\mathrm{x}}^2} e^{-t/\tau_{\mathrm{x}}}\Big)}_{\text{shift in cantilever DC displacement}} \\ \qquad - \underbrace{\frac{\delta x_{h\nu}}{1+\omega_{\mathrm{c}}^2\tau_{\mathrm{x}}^2}(\cos\omega_{\mathrm{c}} t + \omega_{\mathrm{c}}\tau_{\mathrm{x}}\sin\omega_{\mathrm{c}} t)}_{\text{oscillation at the cantilever frequency}}. \tag{2.42}$$

The first term is just the expected DC cantilever deflection resulting from a change in tip-sample force F. This term is filtered out by the lock-in amplifier filter when we measure cantilever amplitude or phase. The second term shows that the force induces an oscillation at the cantilever frequency with amplitude $A_{\mathrm{x}} = \delta x_{h\nu}/\sqrt{1+\omega_{\mathrm{c}}^2\tau_{\mathrm{x}}^2}$. For the cantilever frequency, we use $\omega_{\mathrm{c}} = \omega_0 + \delta\omega(t=0)$. We use τ_{x} to allow for the possibility that the

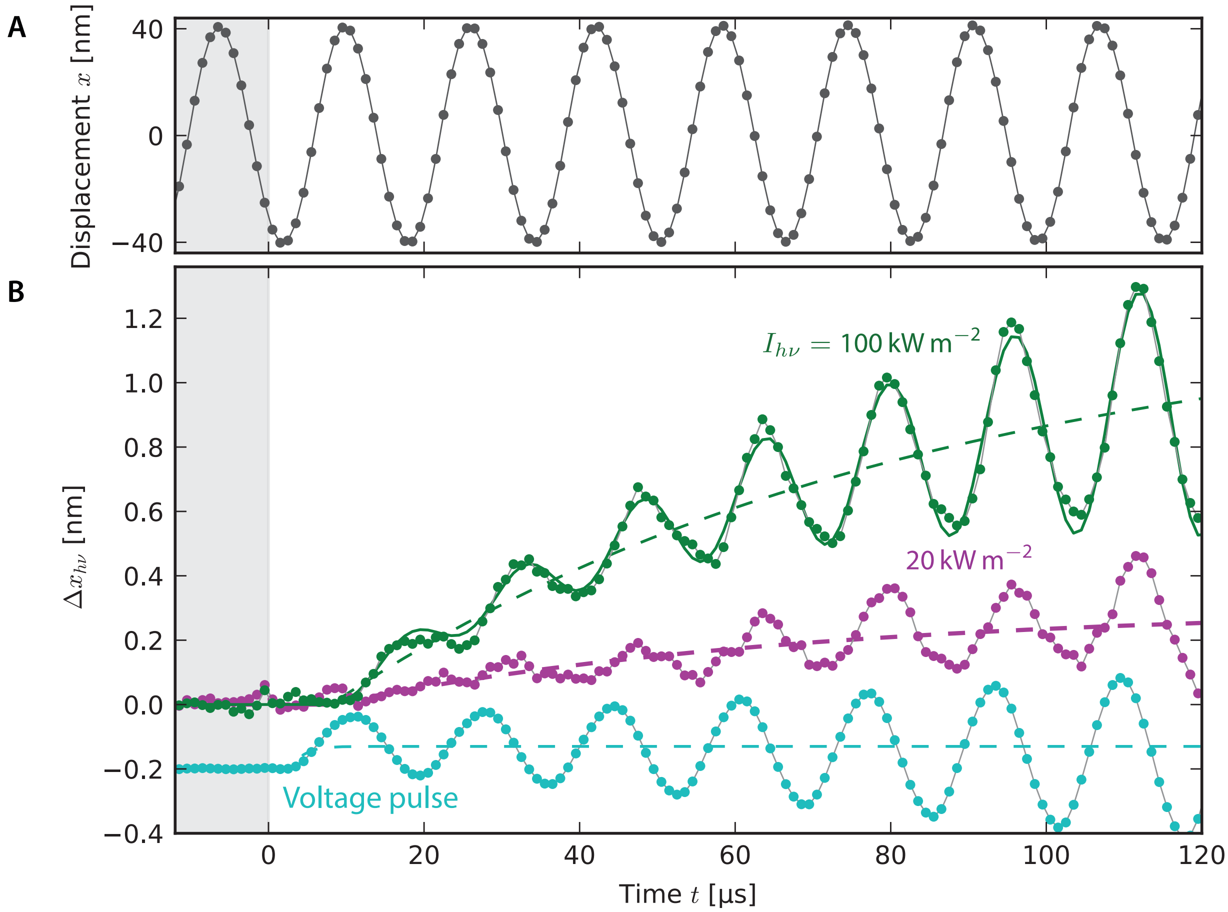

Figure 2.13: **Light-induced changes in cantilever displacement**. (**A**) Signal-averaged displacement *versus* time data from the $I_{h\nu} = 100\,\mathrm{kW\,m^{-2}}$ dataset. Best-fit parameters for the model of Equation 2.43: $X_0 = -22.551(3)\,\mathrm{nm}$, $Y_0 = 34.687(3)\,\mathrm{nm}$, $f_1 = 61\,840.51(1)\,\mathrm{Hz}$, and $Q = 22\,000(200)$. **(B)** Light-induced changes in displacement for the $I_{h\nu} = 100\,\mathrm{kW\,m^{-2}}$ and $20\,\mathrm{kW\,m^{-2}}$ intensity tr-EFM experiments. The voltage-induced position shift from Figure 2.5K is plotted for comparison (scaled and offset: we plot $0.05\Delta x_V(t) - 0.2\,\mathrm{nm}$). The dashed lines show the evolution of the DC cantilever displacement (first term of Eq. 2.42). The green curve shows the best-fit parameters for the model of Equation 2.45: $\tau_{\mathrm{x}} = 69(2)\,\mathrm{\mu s}$, $t_0 = 6.6(4)\,\mathrm{\mu s}$, $\delta x_{h\nu} = 1.16(1)\,\mathrm{nm}$, $X_1 = -4.3(1)\,\mathrm{nm}$, $Y_1 = 0.3(7)\,\mathrm{nm}$, and $\tau_{\delta f} = 18(4)\,\mathrm{\mu s}$.

time constant associated with the forcing term may be different than the time constant(s) associated with the force gradient term ($\Delta\phi(t)$ and $\delta f(t) \propto C_{\mathrm{t}}''$).

To assess the size of this short-time effect, we examine the $100\,\mathrm{kW\,m^{-2}}$ signal-averaged tr-EFM data set in the time domain (Figure 2.13A). To see the effect of the light pulse on the cantilever motion at very short times, we fit the cantilever data *before* the light was turned on, when the cantilever was oscillating at a fixed frequency with a slowly decaying amplitude to a damped sinusoid (x_{DHO}). The residuals have a standard deviation of $21\,\mathrm{pm}$. If the light had no effect on the tip-sample force, we would expect the cantilever to continue oscillating at its resonance frequency with a slowly decaying amplitude as described by the fit from $t < 0$. To isolate the effect of the light, Figure 2.13B plots the difference between the measured cantilever displacement $x(t)$ and the expected cantilever motion $x_{\mathrm{DHO}}(t)$. This light-induced displacement $\Delta x_{h\nu}(t) = x(t) - x_{\mathrm{DHO}}(t)$ reflects changes to both the force $\mathbf{b}(t)$ on the cantilever and the cantilever's resonance frequency (Equation 2.1). The effect of the forcing term $\mathbf{b}(t)$ is purely additive (Equation 2.12), so we can estimate the risetime of the C' term and the change in displacement $\delta x_{h\nu}$ directly from Figure 2.13B. For the $100\,\mathrm{kW\,m^{-2}}$ dataset, we find a $\delta x_{h\nu} = 1.16(2)\,\mathrm{nm}$ position shift induced by the light with a time constant $\tau_{\mathrm{x}} = 69(4)\,\mu\mathrm{s}$ (2σ uncertainties). The corresponding induced oscillation amplitude is $A_{\mathrm{x}} = 43\,\mathrm{pm}$. The induced oscillation is almost exactly 90 degrees out of phase with the cantilever motion, so the total phase shift caused by the neglected $\mathbf{b}(t)$ dynamics is $\Delta\phi_{\mathrm{x}} = A_{\mathrm{x}}/A_0 = 0.17(1)\,\mathrm{mcyc}$, where $A_0 = 41.4\,\mathrm{nm}$ is the amplitude of the cantilever oscillation at $t = 0$ (Figure 2.13A, see Equation 2.22). This phase shift is insignificant compared to the phase shift induced by the cantilever frequency shift (Fig. 2.4A).

In summary, the model derived from the pk-EFM theory fits the cantilever's short time dynamics well (data analysis described below in section 2.10). At $100\,\mathrm{kW\,m^{-2}}$, the surface potential measured at long times shifted by $\Delta\Phi_{h\nu} = +440\,\mathrm{mV}$. On its own, this would correspond to a cantilever frequency shift of $\Delta f = 15\,\mathrm{Hz}$; in contrast, the total measured frequency shift, including contributions from both shifts in tip-sample capacitance and surface potential was $-41\,\mathrm{Hz}$. The experiments here do not preclude a shift in surface potential contributing to the measured position and frequency shift. However, the data of Figure 2.13B does make it unlikely that the fast dynamics are wholly explained by surface potential shifts. Since there is no evidence of a positive frequency shift Δf in Figure 2.12 or a negative position shift $\Delta x_{h\nu}(t)$ in 2.13, the transient surface potential shift would either have to be *negative* (compared to positive at long times), or always masked by a larger negative frequency shift induced by the change in photocapacitance.

2.10 Time domain cantilever oscillation fits

See section 2.9 for the motivation of this model. We fit the signal-averaged position data from $t = -1.5\,\mathrm{ms}$ to $t = 0$ to a damped, variable frequency sinusoid:

$$x_{\mathrm{DHO}}(t; X_0, Y_0, f_1, Q) = e^{-\pi f_1 t/Q} \left(X_0 \cos(2\pi f_1 t) + Y_0 \sin(2\pi f_2 t) \right) \tag{2.43}$$

The fit parameters are the cantilever phase factors X_0, Y_0, frequency f_1, and quality factor Q. While this is a good model of the cantilever motion, it neglects the non-linearity of our interferometer position detector. To account for this non-linearity (see section A.2, Fig. A.1), we performed a linear, least-squares fit of the residuals $r_{\mathrm{DHO}}(t) = x(t) - x_{\mathrm{DHO}}(t)$ to the equation

$$f_{\mathrm{harm.}}(t, f_1; X_n, Y_n) = \sum_{n=2}^{5} (X_n \cos(2\pi n f_1 t) + Y_n \sin(2\pi n f_1 t)). \tag{2.44}$$

The fit parameters were the weights $X_2, Y_2 \ldots X_5, Y_5$. This fit removes the components of the residuals at the second through fifth harmonics of the cantilever frequency which are phase-locked to the cantilever oscillation (see Fig. A.1). The frequency f_1 was fixed equal to the value determined from the fit of Equation 2.43. The resulting light-induced displacement $\Delta x_{h\nu}(t) = x(t) - x_{\mathrm{DHO}}(t) - f_{\mathrm{harm.}}(t)$ are plotted in Figure 2.13B.

The light-induced displacement was fit to the equation

$$f(t' = t - t_0, \omega_{\mathrm{c}}; \tau_{\mathrm{x}}, \delta x_{h\nu}, t_0, X_1, Y_1, \tau_{\delta f}) = \\ \Delta x_{h\nu}^{F}(t') + \left[X_1 \cos(\omega_{\mathrm{c}} t) + Y_1 \sin(\omega_{\mathrm{c}} t)\right] \Delta\phi(t', \tau_{\delta f}) \quad (2.45)$$

where the fit parameters were the risetime τ_{x} of the light-induced change in C', the light-induced change in DC displacement $\delta x_{h\nu}$, the time at which the light pulse began t_0, phase factors X_1, Y_1, and the timescale of changes to the cantilever frequency $\tau_{\delta f}$ (the usual τ found from the data of Figure 2.4). The phase shift $\Delta\phi$ was the single exponential risetime phase shift from Equation 2.19, with $t_{\mathrm{p}} = t - t_0$. The magnitude of the phase shift is determined by the size of X_1, Y_1 compared to X_0, Y_0 from the fit of Equation 2.43. The cantilever frequency ω_{c} was fixed equal to $2\pi f_1$, with f_1 determined from Equation 2.43.

The time-domain fits in Figure 2.5J–L are carried out in the same way. In this case, however, the contribution of the photodetector high pass filter response time $\tau_{\mathrm{HP}} = \omega_{\mathrm{HP}}^{-1} = 530\,\mu\mathrm{s}$ is significant. The high pass filter's step response to an input of magnitude $\delta x_{h\nu}$ is approximated by $\delta x_{h\nu} \exp(-t'/\tau_{\mathrm{HP}})$, so the slow decay of the DC component of Δx^F is approximated by subtracting $\delta x_{h\nu} t'/530\,\mu\mathrm{s}$. This is a good approximation when $\tau_{\mathrm{c}} \ll \tau_{\mathrm{HP}}$ and $t' > 3\tau$.

CHAPTER 3

PHOTOCAPACITANCE MEASUREMENT THEORY

In this chapter, we develop a Magnus expansion for the cantilever position and momentum during a photocapacitance measurement. We extend our previous results from Ref. [34] so that the approximation we develop is relevant to both phasekick electric force microscopy (pk-EFM) [34] and feedback-free time-resolved electric force microscopy (FF-trEFM) [30, 31, 32].

We consider the reduced state space system for the cantilever position x and momentum p:

$$\dot{x} = p/m \tag{3.1}$$

$$\dot{p} = -(k_0 + \delta k(t))\, x - 2\gamma p + F(t) \tag{3.2}$$

with damping frequency $\gamma = \omega_0/(2Q)$, cantilever frequency $\omega_0 = \sqrt{k_0/m}$, the time-dependent spring constant shift

$$\delta k(t) = -\frac{1}{2} C_{\mathrm{t}}''(t) V_{\mathrm{t}}(t)^2, \tag{3.3}$$

and the force equal to the sum of the tip-sample capacitive force F_{ts} and a drive force F_{drive}:

$$F(t) = F_{\mathrm{ts}}(t) + F_{\mathrm{drive}}(t). \tag{3.4}$$

The time-dependent capacitive tip-sample force is

$$F_{\mathrm{ts}}(t) = \frac{1}{2} C_{\mathrm{t}}'(t) V_{\mathrm{t}}(t)^2. \tag{3.5}$$

We include the drive force F_{drive} because it is relevant for the FF-trEFM experiment discussed later. In Eq. 3.3, C_{t}' and C_{t}'' are the first and second derivatives of the tip-sample capacitance with respect to height. The tip voltage V_{t} includes the effect of any broadening due to parasitic capacitance or inductance. Equations 3.1 and 3.2 are two coupled linear equations with time-dependent coefficients.

While there is no general analytic solution to Eqs. 3.1 and 3.2, we can use the Magnus expansion to obtain a highly accurate approximate solution [57, 58]. The cantilever's evolution can be written in terms of the state vector $\boldsymbol{x} = (x\ p)^T$,

$$\dot{\boldsymbol{x}} = \boldsymbol{A}(t)\boldsymbol{x} + \boldsymbol{b}(t), \tag{3.6}$$

with a state matrix

$$\boldsymbol{A}(t) = \begin{pmatrix} 0 & 1/m \\ -m\omega_0^2\left(1+\kappa(t)\right) & -2\gamma \end{pmatrix} \tag{3.7}$$

where ω_0 is the cantilever resonance frequency $\omega_0 = \sqrt{k_0/m}$ and κ is the normalized spring-constant shift

$$\kappa(t) \equiv \delta k(t)/k_0. \tag{3.8}$$

The generalized force $\boldsymbol{b}$ is

$$\boldsymbol{b}(t) = \begin{pmatrix} 0 \\ F(t) \end{pmatrix}. \tag{3.9}$$

The exact solution for the time evolution of the state vector in Eq. 3.6 can be written in terms of the system's propagator $\boldsymbol{U}$,

$$\boldsymbol{x}(t) = \boldsymbol{U}(t,t_0)\,\boldsymbol{x}(t_0) + \int_{t_0}^{t} \boldsymbol{U}(t,t')\,\boldsymbol{b}(t')\,dt'. \tag{3.10}$$

The Magnus expansion writes the propagator as the exponential of a certain matrix $\boldsymbol{\Omega}$, $\boldsymbol{U}(t,t_0) \equiv \exp\boldsymbol{\Omega}(t,t_0)$. The first-order Magnus approximation for $\boldsymbol{\Omega}$ is

$$\boldsymbol{\Omega}(t,t_0) \approx \int_{t_0}^{t} \boldsymbol{A}(t')dt'. \tag{3.11}$$

For high-quality-factor cantilevers ($Q \gg 1$), the resulting approximate propagator is

$$\boldsymbol{U}(t, t_0) \approx e^{-\gamma(t-t_0)} \begin{pmatrix} c + \frac{1}{2} Q^{-1}\, s & (m\,\bar{\omega})^{-1}\, s \\ -m\,\bar{\omega}\, s & c - \frac{1}{2} Q^{-1}\, s \end{pmatrix} \tag{3.12}$$

where c and s abbreviate cosine and sine respectively:

$$c = \cos\left(\,\bar{\omega}\,(t - t_0)\right) \qquad\qquad s = \sin\left(\,\bar{\omega}\,(t - t_0)\right), \tag{3.13}$$

where $\bar{\omega}(t, t_0)$ is a *time-dependent frequency* representing the average cantilever frequency between the time t_0 and t,

$$\bar{\omega}(t, t_0) = \omega_0 \left(1 + \frac{1}{t - t_0} \int_{t_0}^{t} \kappa(t')\, dt'\right)^{1/2}. \tag{3.14}$$

Likewise, $\theta(t, t_0) = \bar{\omega}\,(t - t_0)$ is the cantilever phase accumulated between t_0 and t. Typically $\kappa \ll 1$ so the phase is well-approximated by

$$\theta(t, t_0) \approx \omega_0\,(t - t_0) + \frac{\omega_0}{2} \int_{t_0}^{t} \kappa(t')\, dt'. \tag{3.15}$$

The usual KPFM expression for the cantilever frequency is the instantaneous frequency $f(t) = \frac{1}{2\pi} d\theta/dt = -f_0 C''(V_{\mathrm{t}} - \phi)^2/(4k_0)$. Eq. 3.15 is a good first-order approximation for arbitrarily fast changes to the cantilever capacitance or tip voltage. Any additional first order effects must come from changes in the tip-sample force $F_{\mathrm{ts}}(t)$.

3.1 Definition of amplitude and phase

We use Eq. 3.10 to calculate the effect of changes in F_{ts} on the cantilever position and momentum. Photocapacitance experiments use measurements of the cantilever amplitude, phase, or frequency to determine the light-induced changes in capacitance $C'(t)$ or $C''(t)$. We introduce a definition of the cantilever amplitude and phase in terms of the cantilever position and momentum so we can relate F_{ts} to the measured photocapacitance observables.

We derive our expressions for amplitude and phase from a consideration of the cantilever's usual dynamics in the absence of abrupt changes in the tip-sample force or force gradient. We break the cantilever state evolution into two terms

$$\boldsymbol{x}(t) = \boldsymbol{x}_{\text{fg}}(t) + \boldsymbol{x}_{\text{f}}(t) \tag{3.16}$$

where $\boldsymbol{x}_{\text{fg}}$ describes the cantilever oscillation under the effect of the drive force and changes in the tip-sample force-gradient δk:

$$\boldsymbol{x}_{\text{fg}}(t) = \boldsymbol{U}(t, t_0) \begin{pmatrix} x_0 - x_{\text{eq}} \\ p_0 \end{pmatrix} + \int_{t_0}^{t} U(t, t') \begin{pmatrix} 0 \\ F_{\text{drive}}(t') \end{pmatrix} dt' \tag{3.17}$$

where the initial state vector is $\boldsymbol{x}(t_0) = (x_0 \; p_0)^T$. The second term $\boldsymbol{x}_{\text{f}}$ describes the cantilever evolution under the effect of the tip-sample force and the equilibrium cantilever displacement x_{eq}:

$$\boldsymbol{x}_{\text{f}}(t) = U(t, t_0) \begin{pmatrix} x_{\text{eq}} \\ 0 \end{pmatrix} + \int_{t_0}^{t} U(t, t') \begin{pmatrix} 0 \\ F_{\text{ts}}(t') \end{pmatrix} dt'. \tag{3.18}$$

If the Fourier transform of $F_{\text{ts}}(t)$ has little content at the cantilever resonance frequency, the force-gradient state $\boldsymbol{x}_{\text{fg}}$ and the force state $\boldsymbol{x}_{\text{f}}$ evolve separately. The force-gradient state $\boldsymbol{x}_{\text{fg}}(t)$ describes the cantilever oscillation's amplitude and phase. The force state $\boldsymbol{x}_{\text{f}}(t)$ describes the cantilever's equilibrium or DC displacement. Typical frequency-modulated Kelvin probe force microscopy (FM-KPFM) vary δk and F_{ts} vary sinusoidally at a frequency far below the cantilever resonance frequency by modulating the tip voltage [22]. For these measurements, the approximation that $\boldsymbol{x}_{\text{fg}}$ controls the cantilever's amplitude and phase and $\boldsymbol{x}_{\text{f}}$ controls the cantilever's DC deflection is justified. The observable is the cantilever frequency shift and therefore the small change in the cantilever's DC displacement caused by $\boldsymbol{x}_{\text{f}}$ is ignored. However, photocapacitance measurements involve transient changes to δk and F_{ts} which have spectrally broad Fourier or Laplace transforms. For photocapacitance measurements, it is important to include the effect of the tip-sample force F_{ts} [32, 34].

Consider the case where the tip-sample force and force-gradient are constant, with $F_{\text{ts}} = F_{\text{dc}}$. We drive the cantilever using a cosinusoidal force with a fixed amplitude F_{d} and frequency ω_{d}: $F_{\text{drive}}(t) = F_{\text{d}} \cos(\omega_{\text{d}} t)$. The contribution to the cantilever oscillation from the force-gradient term and the drive is

$$\boldsymbol{x}_{\text{fg}}(t) = \begin{pmatrix} A\cos(\omega_{\text{d}} t + \phi) \\ -Am\omega_{\text{d}} \sin(\omega_{\text{d}} t + \phi) \end{pmatrix} \tag{3.19}$$

and the contribution from the force term is

$$\boldsymbol{x}_{\text{f}}(t) = \begin{pmatrix} x_{\text{eq}} \\ 0 \end{pmatrix}. \tag{3.20}$$

The cantilever oscillates at the drive frequency ω_{d} with a fixed phase relative to the drive force. The constant tip-sample force contributes a DC offset to the cantilever position, with $x_{\text{eq}} = F_{\text{dc}}/k$

Based on our analysis of the cantilever dynamics, we associate a phase with each cantilever state $\boldsymbol{x} = (x \ p)^T$ as follows. We write the cantilever amplitude and phase using a complex number z:

$$z = (x - x_{\text{eq}}) - \frac{p}{m\omega_{\text{d}}} i \tag{3.21}$$

where x_{eq} is the cantilever's *time-dependent* equilibrium displacement $x_{\text{eq}}(t) = F_{\text{ts}}(t)/k_0$. With this definition, the ordinary evolution of the cantilever is

$$z(t) = z(t_0) e^{i\omega_{\text{d}}(t - t_0)} \tag{3.22}$$

and the corresponding cantilever position and momentum are

$$x(t) = \operatorname{Re}\big(z(t)\big) + x_{\text{eq}}(t) \tag{3.23}$$

$$p(t) = -m\omega_{\text{d}} \operatorname{Im}\big(z(t)\big). \tag{3.24}$$

In terms of the complex number z, the cantilever amplitude is

$$A = |z| \tag{3.25}$$

and the absolute cantilever phase is

$$\phi_{\mathrm{abs}} = \arg z. \tag{3.26}$$

To remove the effect of the ordinary evolution of the cantilever, we define the phase difference between the drive and the cantilever. If we take the drive force $F_{\mathrm{drive}}(t)$ equal to

$$F_{\mathrm{drive}}(t) = F_{\mathrm{d}} \cos(\omega_{\mathrm{d}} t + \phi_{\mathrm{d}}), \tag{3.27}$$

the phase difference ϕ is

$$\phi = \phi_{xp} = \arg \Big(z \exp(-i\omega_{\mathrm{d}} t) \exp(-i\phi_{\mathrm{d}}) \Big). \tag{3.28}$$

We use the subscript ϕ_{xp} to note that this is the phase calculated from the cantilever position x and momentum p. With equations 3.21 and 3.28, we can approximate the cantilever's phase using simulations or analytic approximations of the cantilever position and momentum. We show the relationship between the cantilever position, momentum, amplitude and phase in Fig. 3.1.

3.2 Amplitude and phase shifts caused by abrupt forces

The position and momentum oscillation $\boldsymbol{x}_{\mathrm{f}}$ caused by an abrupt change in F_{ts} is added to the oscillation described by x_{fg} (Eq. 3.16). For small changes in the cantilever position δx and momentum δp, the resulting change in the cantilever amplitude and phase is

$$\begin{pmatrix} \delta A \\ \delta \phi \end{pmatrix} = \begin{pmatrix} \cos\phi & -(m\omega_{\mathrm{d}})^{-1} \sin\phi \\ -A^{-1} \sin\phi & -(Am\omega_{\mathrm{d}})^{-1} \cos\phi \end{pmatrix} \begin{pmatrix} \delta x \\ \delta p \end{pmatrix} \tag{3.29}$$

where the magnitude of the position and momentum change are much smaller than the cantilever's initial amplitude A: $|\delta x| \ll A$ $|\delta p/(m\omega_{\mathrm{d}})| \ll A$.

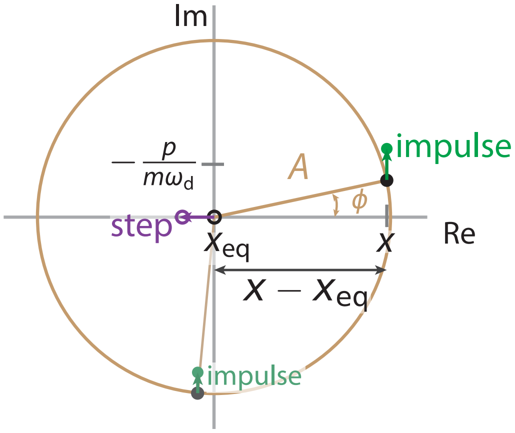

Figure 3.1: An illustration of the amplitude and phase representation of the cantilever state.

We consider two limits for the abrupt change in tip-sample force: an impulsive force and a step-like force. For an impulsive force, the entire change in tip-sample force occurs over a very short time $t_{\text{impulse}} \ll \omega_c^{-1}$. The effect of the impulsive force is to deliver a small impulse of momentum to the cantilever $\delta p = \int_0^{t_{\text{impulse}}} F(t) dt$. The impulse abruptly shifts the cantilever amplitude and phase by

$$\delta A = -(m\omega_d)^{-1} \sin\phi \, \delta p \tag{3.30}$$

$$\delta\phi = -(Am\omega_d)^{-1} \cos\phi \, \delta p \tag{3.31}$$

respectively (second column of Eq. 3.29). In Fig. 3.1, the impulsive force causes a small shift in the cantilever state along the momentum or imaginary axis.

A step-like force

$$F(t) = \begin{cases} 0 & t \leq 0 \\ \Delta F & t > 0 \end{cases} \tag{3.32}$$

causes an abrupt change in the cantilever's equilibrium displacement $\delta x_{\text{eq}} = \Delta F / k_0$. By Eq. 3.21, the change in equilibrium displacement corresponds to an abrupt shift $\delta x = -\delta x_{\text{eq}}$ along the position or real axis of Fig. 3.1. The step abruptly shifts the amplitude and phase by

$$\delta A = \cos\phi\,\delta x = -\cos\phi\,\delta x_{\mathrm{eq}} \tag{3.33}$$

$$\delta\phi = -A^{-1}\sin\phi\,\delta x = A^{-1}\sin\phi\,\delta x_{\mathrm{eq}} \tag{3.34}$$

respectively (first column of Eq. 3.29).

In each case, the same change in position or momentum can cause an amplitude shift or a phase shift depending on the cantilever's initial phase when the abrupt force occurs. The change in position or momentum affects the cantilever phase more when the cantilever's initial amplitude A is smaller.

We can extend this reasoning about the effect of abrupt and step-like changes in the tip-sample force to intermediate timescales by approximating the integral for $\boldsymbol{x}_{\mathrm{f}}$ (Eq. 3.18). The integral can be done in closed-form if the cantilever's force gradient is constant. We consider an exponential risetime change to the tip-sample force

$$F_{\mathrm{ts}} = \begin{cases} 0 & t < 0 \\ F_{h\nu}(1-\exp(t/\tau_{\mathrm{s}})) & t \geq 0 \end{cases} \tag{3.35}$$

where $F_{h\nu}$ is the steady-state light-induced change in force and τ_{s} is the photocapacitance risetime. For convenience, we take $\delta k(t) = 0$ so the cantilever frequency is equal to ω_0. We are interested in times $t \ll \gamma^{-1}$ so we also neglect cantilever dissipation by setting $\gamma = 0$. In this case, the extra force-induced position is

$$x_{\mathrm{f}}(t) = \frac{F_{h\nu}}{k_0}\left(1 - \frac{\omega_0^2\tau_{\mathrm{s}}^2}{1+\omega_0^2\tau_{\mathrm{s}}^2}e^{-t/\tau_{\mathrm{s}}}\right) \underbrace{-\frac{F_{h\nu}/k_0}{1+\omega_0^2\tau_{\mathrm{s}}^2}\Big(\cos(\omega_0 t) + \omega_0\tau_{\mathrm{s}}\sin(\omega_0 t)\Big)}_{x_{\mathrm{osc}}} \tag{3.36}$$

The underbraced term x_{osc} is the induced oscillation at the cantilever frequency. The component of x_{osc} in phase with the cantilever's existing oscillation appears as an amplitude shift. The component of x_{osc} out of phase with the cantilever's existing oscillation appears as a phase shift. If the time constant τ_{s} is much greater than ω_0^{-1}, the change in force is adiabatic, rather than abrupt, and there is no oscillation induced at the cantilever frequency. If the time constant τ_{s} is much smaller than ω_0^{-1}, the change in force results in the abrupt step limit discussed above, with $\delta x_{\text{eq}} = F_{h\nu}/k_0$.

3.3 FF-trEFM time resolution

Feedback-free time-resolved electric force microscopy (FF-trEFM) [30, 31, 32] is a variant of tr-EFM designed to resolve photocapacitance dynamics with better time resolution. Ordinary tr-EFM measurements directly fit the cantilever frequency shift versus time data to extract the sample's photocapacitance risetime τ_{s}. In FF-trEFM, the cantilever is driven at a fixed frequency ω_{d} with a fixed tip voltage V_{t}. The light is turned on at a specific point in the cantilever cycle and the cantilever oscillation data is signal-averaged and demodulated to obtain the cantilever's instantaneous frequency shift δf versus time. The time-to-first-frequency-shift peak t_{FP} is calculated from $\delta f(t)$. To calibrate the measurement, voltage pulses with different rise times τ_{v} are applied to the sample and t_{FP} is measured versus τ_{v}. The sample photocapacitance risetime τ_{s} is estimated using the t_{FP} versus τ_{v} calibration curve. Ginger and co-workers have shown that sub-cycle time resolution can be obtained with this technique. Through numerical simulations, they demonstrated that the effect of the cantilever tip-sample force $F_{\text{ts}} \propto C'$ gives rise to the sub-cycle time resolution.

In this section, we apply our Magnus expansion approximation for cantilever dynamics to the FF-trEFM experiment. We show that the FF-trEFM experiment is only sensitive to the total magnitude of the force-induced phase shift at short times. To extract a spe-

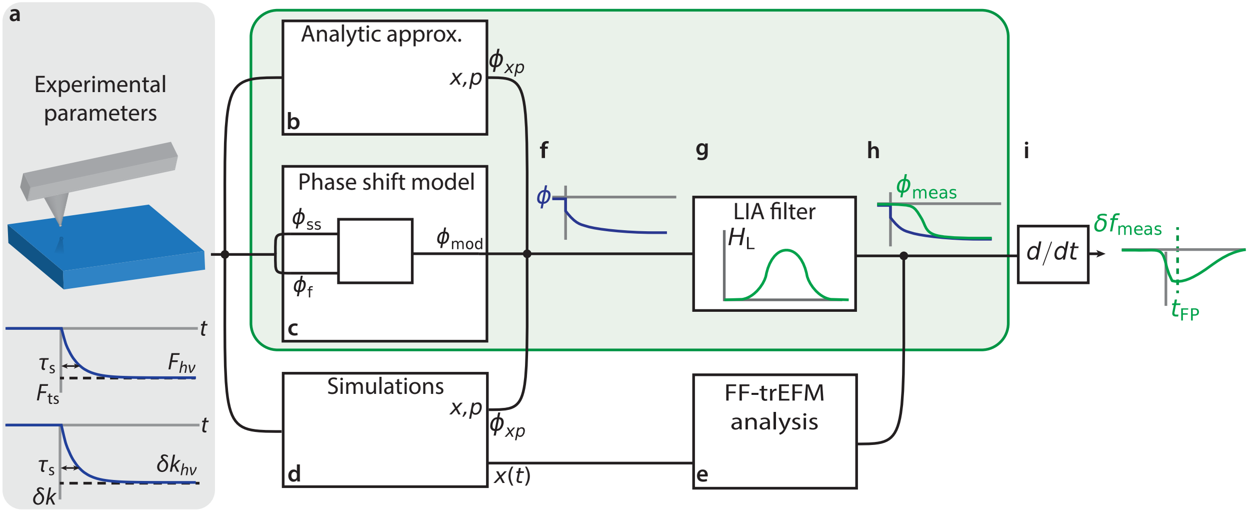

Figure 3.2: Analysis of the FF-trEFM experiment.

cific time constant in the limit that $\tau_{\mathrm{s}} \ll \omega_0^{-1}$, an assumption must be made about the magnitude of the abrupt change in the tip-sample force.

Figure 3.2 illustrates our analysis of the FF-trEFM experiment. The phase and frequency versus time (Fig. 3.2(h,i)) depend on both sample parameters and the particular choice of demodulation filter. To isolate the effect of the sample parameters on the phase and frequency, we model the *measured* cantilever phase as the convolution of the cantilever's actual phase and a demodulation or lock-in amplifier low-pass filter (Fig. 3.2f–h). The measured cantilever phase shift is

$$\phi_{\text{meas}}(t) = (H_{\mathrm{L}} * \phi)(t) \tag{3.37}$$

where H_{L} is the lock-in amplifier or demodulation filter impulse response function, $*$ denotes convolution in the time domain, and ϕ is the sample's *actual* phase relative to the phase of the cantilever drive force. The measured cantilever frequency shift is the derivative of the measured phase

$$\delta f_{\text{meas}}(t) = \frac{1}{2\pi} \frac{d\phi_{\text{meas}}}{dt}. \tag{3.38}$$

At $t = t_{\mathrm{FP}}$, the derivative of the measured frequency shift is equal to zero (Fig. 3.2i).

The specific time t_{FP} is sensitive to the choice of lock-in amplifier filter H_{L}. For a particular choice of H_{L}, differences in t_{FP} are related to differences in the cantilever's actual phase $\phi(t)$. We connect $\phi(t)$ to experimental parameters using our Lagrangian model of the cantilever dynamics magnitude and risetime of changes to the tip-sample force $F_{\mathrm{ts}}(t)$ and force gradient $\delta k(t)$ (Fig. 3.2a–c). By relating $F_{\mathrm{ts}}(t)$ and $\delta k(t)$ to $\phi(t)$, we can then determine how these experimental parameters affect the measured t_{FP}. We verify the relationship between experimental parameters and ϕ by estimating the phase in multiple ways. In particular, we estimate the phase from simulations of the cantilever position and momentum (Fig. 3.2d). We separately analyze the simulation cantilever position data using the Ginger group's analysis code[71]. We calculate the same t_{FP} with both approaches, which connects our new analysis (shaded green region of Fig. 3.2) to that used by Ginger and co-workers.

3.3.1 Cantilever force and force gradient in FF-trEFM

We describe the experiment using the description of the cantilever amplitude and phase developed in the previous section. We consider a cantilever force

$$F(t) = F_{\mathrm{ts}}(t) + F_{\mathrm{drive}}(t) \tag{3.39}$$

with the tip-sample capacitance force equal to

$$F_{\mathrm{ts}} = \begin{cases} 0 & t < 0 \\ F_{h\nu}(1 - \exp(t/\tau_{\mathrm{s}})) & t \geq 0 \end{cases} \tag{3.40}$$

and the drive force

$$F_{\mathrm{drive}}(t) = F_{\mathrm{d}} \cos(\omega_{\mathrm{d}} t + \phi_{\mathrm{d}}) \tag{3.41}$$

with F_d the drive magnitude, ω_d the drive frequency, and ϕ_d the drive phase. The change in tip-sample force gradient is

$$\delta k(t) = \begin{cases} 0 & t < 0 \\ \delta k_{h\nu}(1 - \exp(t/\tau_\mathrm{s})) & t \geq 0 \end{cases} \tag{3.42}$$

with $\delta k_{h\nu}$ the steady-state change in the force gradient. To a good approximation, the resulting cantilever instantaneous frequency is

$$\omega(t) = \omega_0(1 + \delta k(t)/(2k_0)) \tag{3.43}$$

where we differentiate Eq. 3.15 to obtain Eq. 3.43.

The two forces on the cantilever, the drive force and the tip-sample capacitance force, affect the cantilever's phase very differently. The drive force determines the cantilever's oscillation frequency. Together, the properties of the drive force and the propagator determine the cantilever's amplitude and phase difference relative to the drive force. In contrast, F_ts only determines the equilibrium displacement about which the cantilever oscillates unless it contains significant energy at ω_0.

3.3.2 Approximate phase shift model

To gain insight into the dynamics of the cantilever phase, we develop an approximate model to describe small cantilever phase shifts (Fig. 3.2c). The separation of the cantilever dynamics into $\boldsymbol{x}_\mathrm{fg}$ and $\boldsymbol{x}_\mathrm{f}$ also motivates our approximate model of the cantilever phase shift. When the light is turned on, changes in capacitance affect the phase difference between the drive force and the cantilever through (1) changes in the tip-sample force gradient and (2) abrupt changes in the tip-sample force.

The change in the cantilever's natural resonance frequency $\omega(t)$ causes a resulting phase shift. At steady state, the phase difference between the cantilever and the drive changes according to the cantilever transfer function

$$\phi_{\mathrm{ss}}(t) = \arg\left(\left[1 - \frac{\omega_{\mathrm{d}}^2}{\omega(t)^2} + \frac{i\omega_{\mathrm{d}}}{Q\omega(t)}\right]^{-1}\right). \tag{3.44}$$

where $\omega(t)$ is given by Eq. 3.43. For small phase shifts, the cantilever response to the changes in $\Delta\phi_{\mathrm{ss}}$ is first-order with a characteristic frequency $\gamma = \omega_0/(2Q)$:

$$\dot{\phi}_{\mathrm{fg}} = -\gamma\phi_{\mathrm{fg}} + \gamma\phi_{\mathrm{ss}}(t). \tag{3.45}$$

where we use the subscript "fg" for force gradient. The drive force and force gradient cause the slow evolution of ϕ_{fg} and the corresponding sinusoidal evolution of the force-gradient state vector $\boldsymbol{x}_{\mathrm{fg}}$.

The change in tip-sample force affects the cantilever phase differently. Abrupt changes in the tip-sample force F_{ts} induce an additional oscillation at the cantilever resonance frequency. For the FF-trEFM experiment, the existing oscillation near $t = 0$ is $x(t) = -A\sin(\omega_{\mathrm{d}}t)$, so the cosine term from Eq. 3.36 causes an abrupt phase shift

$$\Delta\phi_{\mathrm{f}} = \frac{F_{h\nu}/k_0}{A}\frac{1}{1+\omega_0^2\tau_{\mathrm{s}}^2} \tag{3.46}$$

where A is the cantilever zero-to-peak amplitude near $t = 0$, and $\Delta\phi_{\mathrm{f}}$ is in units of radians. For times $t \leq \tau_{\mathrm{s}}$, the phase shift oscillates and approaches $\Delta\phi_{\mathrm{f}}$. For the sake of our model, we assume

$$\phi_{\mathrm{f}}(t \geq 0) = \Delta\phi_{\mathrm{f}}(1 - e^{-t/\tau_{\mathrm{s}}}). \tag{3.47}$$

With the force contribution to the cantilever phase accounted for, we need to correct Eq. 3.45 to take into account ϕ_{f}. The total cantilever phase is the sum of the force-gradient phase ϕ_{fg} and ϕ_{f}

$$\phi = \phi_{\mathrm{fg}} + \phi_{\mathrm{f}} \tag{3.48}$$

We describe the combined effects of the force and force-gradient terms with the differential equation

$$\dot{\phi}_{\mathrm{fg}} = -\gamma\big(\phi_{\mathrm{fg}} + \phi_{\mathrm{f}}(t)\big) + \gamma\phi_{\mathrm{ss}}(t). \tag{3.49}$$

If the phase $\phi = \phi_{\mathrm{fg}} + \phi_{\mathrm{f}}$ is equal to the steady state phase ϕ_{ss}, the derivative $\dot{\phi}_{\mathrm{fg}} = 0$ and the normal oscillator dynamics do not change the cantilever phase. Together Equations 3.48 and 3.49 describe a state space model with two inputs $\phi_{\mathrm{ss}}(t)$ and $\phi_{\mathrm{f}}(t)$, one state variable ϕ_{fg}, and one output ϕ:

$$\begin{pmatrix} \dot{\phi}_{\mathrm{fg}} \end{pmatrix} = \begin{pmatrix} -\gamma \end{pmatrix} \begin{pmatrix} \phi_{\mathrm{fg}} \end{pmatrix} + \begin{pmatrix} \gamma & -\gamma \end{pmatrix} \begin{pmatrix} \phi_{\mathrm{ss}}(t) \\ \phi_{\mathrm{f}}(t) \end{pmatrix} \tag{3.50}$$

$$\begin{pmatrix} \phi \end{pmatrix} = \begin{pmatrix} 1 \end{pmatrix} \begin{pmatrix} \phi_{\mathrm{fg}} \end{pmatrix} + \begin{pmatrix} 0 & 1 \end{pmatrix} \begin{pmatrix} \phi_{\mathrm{ss}}(t) \\ \phi_{\mathrm{f}}(t) \end{pmatrix} \tag{3.51}$$

With this model, we can write closed-form expressions for the cantilever phase when exponential risetime inputs are applied to ϕ_{ss} and ϕ_{f}.

With either simulations of the cantilever position and momentum, or the approximate phase shift model, we can write the cantilever's *actual* phase ϕ.

3.3.3 Simulations

To verify the phase model developed above, we simulate cantilever dynamics for a cantilever and analysis similar to that performed by Karatay and co-workers in their demonstration of $10\,\mathrm{ns}$ time resolution [32]. We used a cantilever frequency at $t = 0$ equal to $\omega_0 = 2\pi \times 10\,\mathrm{MHz}/19 = 2\pi \times 526\,315\,\mathrm{Hz}$ so that the cantilever frequency is evenly divisible by the $10\,\mathrm{MHz}$ sampling rate. The cantilever spring constant and quality factor were $k_0 = 72.7\,\mathrm{N\,m^{-1}}$ and $Q = 499$ respectively. We set the drive frequency $\omega_{\mathrm{d}} = \omega_0$. We

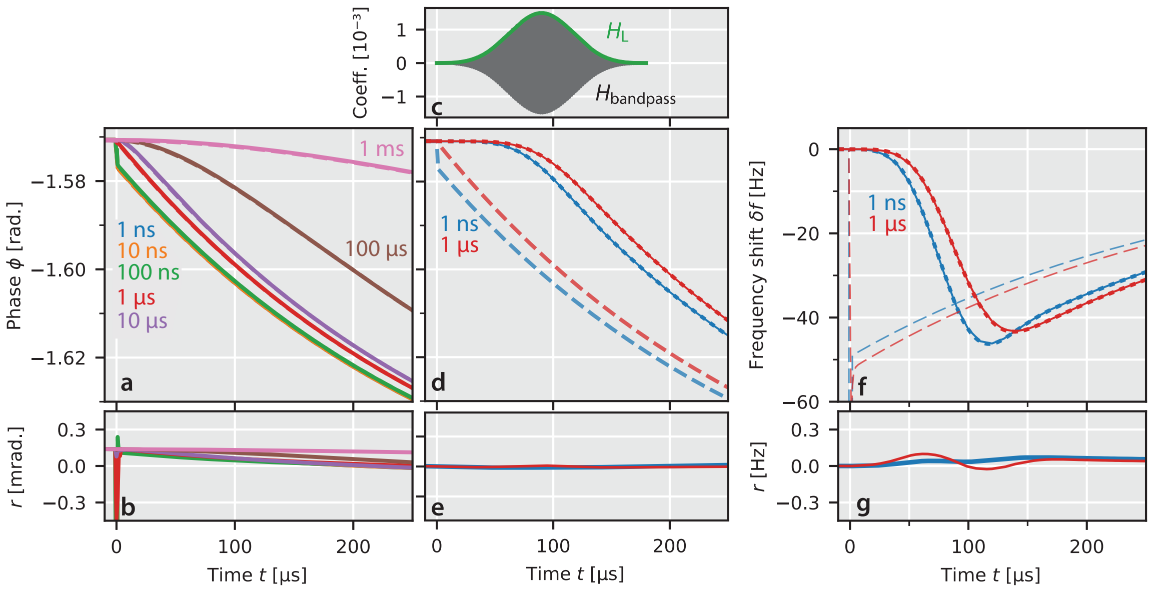

Figure 3.3: Actual and measured cantilever phase and frequency calculated using models and simulations. (a) Relative phase ϕ between the cantilever position and the drive force for sample photocapacitance risetime constants τ_s from $1\,\mathrm{ns}$ to $1\,\mathrm{ms}$. The phase was calculated from simulations of cantilever position and momentum (ϕ_{xp}, solid lines) and the approximate small phase shift model (ϕ_mod, dashed lines). (b) Phase difference between the two models $r = \phi_{xp} - \phi_\mathrm{mod}$. (c) The lock-in amplifier filter (green line) used to determine ϕ_meas from ϕ and the bandpass filter used to determine ϕ_meas from simulated cantilever position data. (d) Measured phase shift calculated from ϕ_mod (solid lines) and from simulated position versus time data using the Ginger group analysis package FFTA with bandpass filter H_bandpass (dot-dashed lines). (e) Phase difference between the two calculated, measured phases $r = \phi_\mathrm{meas}^\mathrm{mod} - \phi_\mathrm{meas}^\mathrm{FFTA}$. (f) Corresponding measured frequency shift calculated from $\phi_\mathrm{meas}^\mathrm{mod}$ (solid lines) and $\phi_\mathrm{meas}^\mathrm{FFTA}$ (dot-dashed lines). Dashed lines show the frequency shift calculated from ϕ_mod. (g) Frequency shift difference $r = \delta f_\mathrm{meas}^\mathrm{mod} - \delta f_\mathrm{meas}^\mathrm{FFTA}$.

used a drive amplitude $F_\mathrm{d} = k \times 10\,\mathrm{nm}/Q$ and a drive phase $\phi_\mathrm{d} = \pi$ for maximum time resolution. The cantilever's simulated zero-to-peak amplitude at $t = 0$ was $A = 10\,\mathrm{nm}$. The light-induced change in spring constant was $\delta k_{h\nu} = -2k_0 \times 10^{-4}$, corresponding to a cantilever frequency shift of $\Delta\omega_{h\nu} = 2\pi \times 52.6\,\mathrm{Hz}$. The light-induced change in the tip-sample force was $F_{h\nu} = -k_0 \times 0.06\,\mathrm{nm}$, inducing a $0.06\,\mathrm{nm}$ shift in the cantilever's equilibrium displacement x_eq.

3.3.4 Results

Figure 3.3 demonstrates the close agreement between the different models for the cantilever phase shift illustrated in Figure 3.2. In Figure 3.3a, we show the results of simulations for a series of sample photocapacitance risetimes τ_{s} from $1\,\mathrm{ns}$ to $1\,\mathrm{ms}$. From the simulated cantilever position and momentum, we calculated the cantilever phase ϕ_{xp} using Eq. 3.28. In Fig. 3.3a, we plot ϕ_{xp} convolved with a rectangular filter with width $T = 2\pi/\omega_0$ to remove phase oscillations at multiples of the cantilever frequency (solid lines). We also plot the modeled phase ϕ_{mod} (dashed lines), which was calculated using Eqs. 3.44,3.47, 3.50, and 3.51. The simulated phase ϕ_{xp} agrees closely with the phase predicted by the analytic model ϕ_{mod}. Fig. 3.3b shows that the phase difference $r = \phi_{xp} - \phi_{\mathrm{mod}}$ is small and approaches zero at long times. Fig. 3.3(a,b) demonstrates good agreement between our different models of the cantilever's actual phase (Fig. 3.2b–d).

Next we determine the *measured* phase shift ϕ_{meas}. First we calculate ϕ_{meas} using ϕ from Fig. 3.3a and the convolution model illustrated in Fig. 3.2f–h (Eq. 3.37). To demonstrate the agreement between this description of the phase and the phase calculated from the FF-trEFM workup, we use the same simulation data used to calculate ϕ_{xp} to perform the FF-trEFM analysis of Ginger and co-workers using their publicly available package [71, 32]. The bandpass filter applied to the $x(t)$ data in the FF-trEFM analysis serves the same role as the low-pass filter H_{L} in our analysis. We use a Parzen window bandpass filter that passes frequencies $f_0 - b < f < f_0 + b$. The corresponding Parzen window low-pass filter has cutoff frequency b. Fig. 3.3c shows the filters used in our analysis, with $b = 5.1\,\mathrm{kHz}$. Fig. 3.3d shows that the measured phase calculated using the model (solid lines) and the FFTA analysis (dot-dashed lines) agrees closely. For comparison, the input to the low-pass filter ϕ_{mod} (dashed lines) is also shown. The low-pass filter blurs and delays the phase. Fig. 3.3e shows the maximum difference between $\phi_{\mathrm{meas}}^{\mathrm{mod}}$ and $\phi_{\mathrm{meas}}^{\mathrm{FFTA}}$

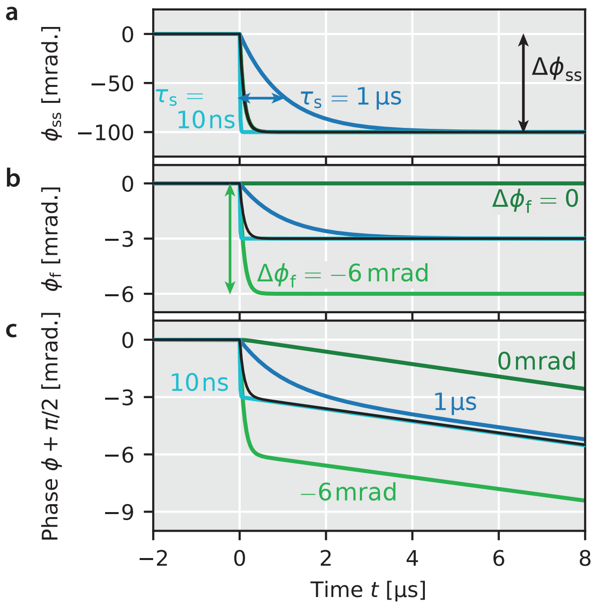

Figure 3.4: Dependence of ϕ on photocapacitance risetime and force-induced phase shift. (a) The steady-state photocapacitance ϕ_{ss} for different photocapacitance risetimes. (b) The force-induced phase shift for different photocapacitance risetimes (blue) and different magnitudes of $\Delta\phi_f$. (c) The phase determined from the inputs in (a) and (b), offset by the initial phase shift $\pi/2$.

is $8\,\mu\mathrm{rad}$. Fig. 3.3(f,g) shows that the corresponding measured frequency shifts and time to first frequency shift peaks agree closely as well. The maximum frequency difference is $0.1\,\mathrm{Hz}$.

The data of Fig. 3.3 demonstrate that the new models we introduced to describe the measured phase in the FF-trEFM experiment agree closely with the measured phase as calculated by Ginger and co-workers. We examine the dependence of ϕ on experimental parameters to better understand how the experimental parameters affect the measured phase and time-to-first frequency-shift peak.

We can describe cantilever phase during a FF-trEFM experiment in closed form with the state-state model of Equations 3.50 and 3.51. In the analytic model, the cantilever's actual phase is

$$\phi(t \geq 0) = \phi_0 + \Delta\phi_{\text{ss}} - \Delta\phi_{\text{f}} e^{-t/\tau_{\text{s}}} + \frac{\Delta\phi_{\text{ss}} - \Delta\phi_{\text{f}}}{1 - \gamma\tau_{\text{s}}}\left(\gamma\tau_{\text{s}} e^{-t/\tau_{\text{s}}} - e^{-\gamma t}\right) \quad (3.52)$$

where $\Delta\phi_{\text{ss}}$ is the steady-state phase shift: $\Delta\phi_{\text{ss}} = \phi_{\text{ss}}(\infty) - \phi_{\text{ss}}(0)$ from Eq. 3.44; and $\Delta\phi_{\text{f}}$ is the total phase shift induced by the abrupt change in the tip-sample force (Eq. 3.46).

Fig. 3.4 illustrates how the cantilever phase ϕ_{mod} depends on $\Delta\phi_{\text{f}}$ and the photocapacitance risetime τ_{s}. We plot the inputs to the model in Fig. 3.4(a,b) and the cantilever phase calculated using Eq. 3.52 in Fig. 3.4c. The black curve shows the case where the steady-state phase shift is $\Delta\phi_{\text{ss}} = 100\,\text{mrad}$, the force-induced phase shift is $\Delta\phi_{\text{f}} = -3\,\text{mrad}$, and the photocapacitance risetime is $\tau_{\text{s}} = 100\,\text{ns}$. The two blue curves show the effect of varying the photocapacitance risetime: $\tau_{\text{s}} = 10\,\text{ns}$ (light blue) and $\tau_{\text{s}} = 1\,\mu\text{s}$ (dark blue). The two green curves show the effect of varying the magnitude of the force-induced phase shift: $\Delta\phi_{\text{f}} = -6\,\text{mrad}$ (light green) and $0\,\text{mrad}$ (dark green). Changing the magnitude of $\Delta\phi_{\text{f}}$ causes large, persistent differences in the resulting ϕ_{mod} versus time data (Fig. 3.4c). In contrast, changing τ_{s} by an order of magnitude causes almost no difference in the resulting ϕ_{mod} versus time data (Fig. 3.4c) after the first few microseconds. The small, transient differences in ϕ_{mod} caused by changes in τ_{s} would be even more difficult to detect after convolving with the $64\,\mu\text{s}$ FWHM low-pass measurement filter. The persistent differences in ϕ_{mod} related to $\Delta\phi_{\text{f}}$ indicate that the measured ϕ_{meas} versus time and calculated time-to-first-frequency-shift peak should be very sensitive to changes in $\Delta\phi_{\text{f}}$.

Figure 3.5 illustrates how differences in $\phi_{\text{mod}}(t)$ relate to differences in the measured frequency shift δf_{meas} and time to first frequency shift peak t_{FP} in the region where the sample response is faster than the inverse of the filter bandwidth. Figure 3.5a shows δf_{meas} for a series of photocapacitance risetimes from $1\,\text{ns}$ to $1\,\mu\text{s}$ with the magnitude of the change in cantilever tip-sample force $F_{hv} = -k_0 \times 0.06\,\text{nm}$. The time to first frequency

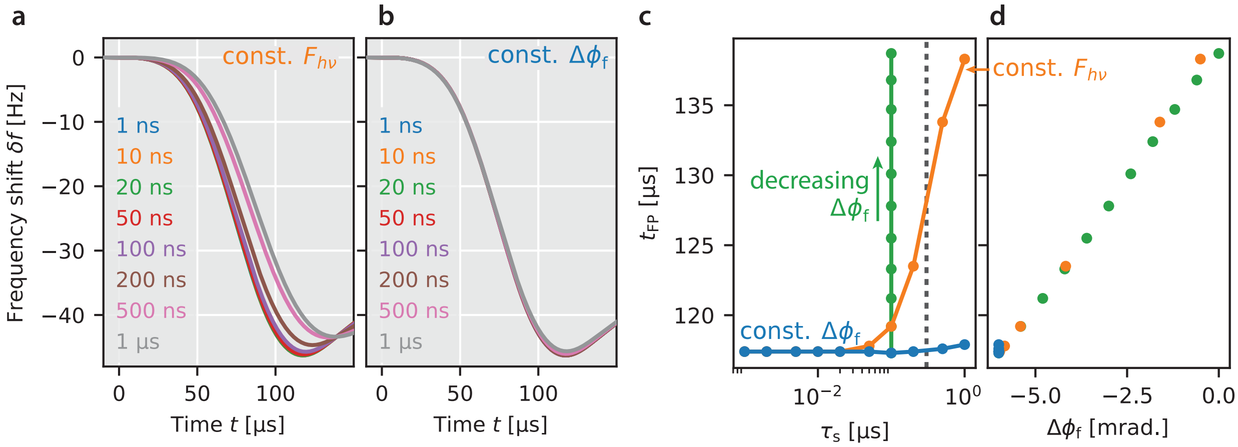

Figure 3.5: Time to first frequency shift peak for different abrupt changes in cantilever phase. (a) Demodulated frequency shift versus pulse time for simulated photocapacitance dynamics with risetime $\tau_s = 1\,\mathrm{ns}$ to $\tau_s = 1\,\mathrm{\mu s}$, keeping the light-induced tip-sample force $F_{h\nu} = -k_0 \times 0.06\,\mathrm{nm}$. (b) Demodulated frequency shift versus pulse time for simulated photocapacitance dynamics with risetime $\tau_s = 1\,\mathrm{ns}$ to $\tau_s = 1\,\mathrm{\mu s}$ keeping the total phase shift induced by the change in tip-sample force constant: $\Delta\phi_f = -6.0\,\mathrm{mrad}$. The steady-state phase shift $\Delta\phi_{ss} = -99.5\,\mathrm{mrad}$ for both (a,b). (c) The time-to-first frequency shift t_{FP} calculated from the data in (a,b) as well as a series of data points with $\tau_s = 100\,\mathrm{ns}$ and $\Delta\phi_f = 00\,\mathrm{mrad}$ to $-6\,\mathrm{mrad}$. (d) The time-to-first frequency shift t_{FP} plotted versus the force-induced phase shift $\Delta\phi_f$.

shift peak t_{FP} becomes shorter at faster photocapacitance risetimes. From Equation 3.46, we know that the magnitude of the force-induced phase shift increases dramatically as τ_s becomes faster than the cantilever inverse angular frequency. For comparison, we show δf_{meas} for a series of photocapacitance risetimes from $1\,\mathrm{ns}$ to $1\,\mathrm{\mu s}$ with the magnitude of force-induced frequency shift held constant as $\Delta\phi_f = -6\,\mathrm{mrad}$, equivalent to $\Delta\phi_f$ for the fastest photocapacitance risetimes in FIg. 3.5a. With $\Delta\phi_f$ held constant, there is very little change in t_{FP} over the range of photocapacitance risetimes. These differences are summarized in Fig. 3.5c which plots the time to first frequency shift peak calculated from the data in Fig. 3.5a–b. We also plot in green the time to first frequency shift peak calculated by fixing the photocapacitance risetime $\tau_s = 100\,\mathrm{ns}$ and varying the magnitude of the force-induced phase shift $\Delta\phi_f$ from $0\,\mathrm{mrad}$ to $-6\,\mathrm{mrad}$. Depending on the differences in $\Delta\phi_f$, any t_{FP} could be obtained with a photocapacitance risetime $\tau_s = 0$ to $1\,\mathrm{\mu s}$.

Figure 3.5d plots the same t_{FP} data versus the force-induced phase shift $\Delta\phi_{\mathrm{f}}$. The three different curves from Fig. 3.5 collapse to a single line, with t_{FP} linearly related to $\Delta\phi_{\mathrm{f}}$ over this range of time constants and force-induced phase shifts. The theory and simulations indicate that for photocapacitance risetimes τ_{s} much smaller than the inverse filter bandwidth $1/(2\pi b)$, FF-trEFM is mainly sensitive to the total magnitude of the force-induced phase shift $\Delta\phi_{\mathrm{f}}$. The force-induced phase shift depends on both the magnitude of the change in force and the photocapacitance risetime. To relate t_{FP} to a specific timescale, additional informational must be known or assumed about the magnitude of the abrupt change in tip-sample force.

CHAPTER 4

POSITION-MODULATED KELVIN PROBE FORCE MICROSCOPY

In this chapter we describe a modification to frequency-modulated Kelvin force microscopy[22] (FM-KPFM) that enables the direct spatial imaging of electric fields near a surface along multiple directions simultaneously. The lateral electric field in a FM-KPFM measurement has to date been obtained by numerically differentiating the measured surface potential versus position to obtain a plot of electric field versus position [72, 73, 74, 75, 76]. This microscopically measured electric field can be helpful for understanding both device physics and materials properties. Bürgi et al. showed experimentally that the potential measured by FM-KPFM above a transistor reflected the electrostatic potential of the accumulation layer at the transistor's buried semiconductor-insulator interface [72]. This finding was subsequently justified theoretically by Silveira, Dunlap, and coworkers [23]. Building on this observation, Bürgi and coworkers introduced the idea of using the locally-inferred electric field, the locally-inferred electrostatic potential, and the measured bulk current to infer the mobility at each location in the channel of a polymer field-effect transistor [72]. The thus-measured mobility was analyzed as a function of temperature and local electric field and conclusions were obtained concerning charge-transport mechanisms in the polymeric semiconducting material. If an abrupt voltage drop is apparent at a transistor's contact, then the contact resistance can be computed by dividing the observed voltage drop by the measured current and likewise studied versus temperature and injecting-contact composition [77]. In samples where no such voltage drop is apparent, Silveira et al. showed that charge injection could nevertheless be studied microscopically by measuring the lateral electric field at the injecting contact and current simultaneously as a function of applied voltage and temperature; plots of the current versus the electric field can be more directly compared to charge-injection theory [73, 74]. This procedure has been used to assign an "ohmicity" to the metal-organic

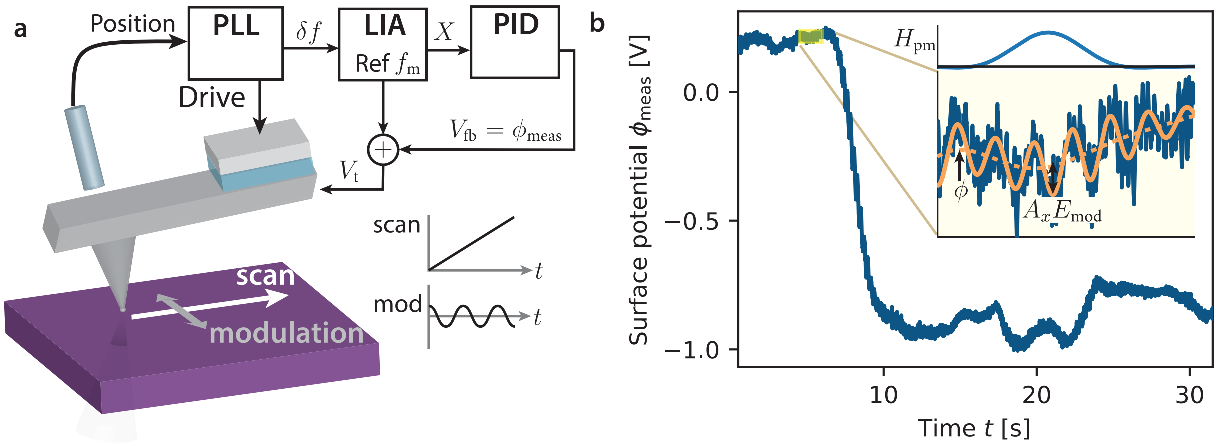

Figure 4.1: Experimental setup and data processing. (a) The cantilever position signal was filtered and phase-shifted by the phase-locked loop (PLL). The PLL drove the cantilever at its resonance frequency and measured the cantilever frequency shift δf. A lock-in amplifier (LIA) measured the component of δf at the voltage-modulation frequency f_m. A proportional-integral-derivative (PID) controller nulled the LIA X-channel by controlling the feedback voltage V_fb. Below, the sample was simultaneously scanned using a linear ramp pattern and modulated using a sinusoidal waveform at the position-modulation frequency. (b) The surface potential-versus-time data measures the surface potential and electric field in the *scan* direction at low frequencies and the electric field in the *modulation* direction at the modulation frequency. Inset: Using the filter H_pm (top), the raw data (bottom, dark curve) was processed using a software lock-in amplifier to determine the scan-direction surface potential (light dashed curve), and modulation-direction electric field (light sinusoid). Experimental parameters: position-modulation amplitude $A_\mathrm{pm} = 45\,\mathrm{nm}$, frequency $f_\mathrm{pm} = 4.5\,\mathrm{Hz}$, tip velocity $v = 414\,\mathrm{nm\,s^{-1}}$, tip-sample separation $h = 200\,\mathrm{nm}$, cantilever zero-to-peak amplitude $A = 50\,\mathrm{nm}$.

contact in a two-terminal device exhibiting no potential drop at the injecting contact[78].

Below we report measurements over an organic field-effect transistor made from the hole-transporting small molecule DPh-BTBT [79]. We used DPh-BTBT because it is an air-stable small molecule that can be easily evaporated to produce high-mobility field-effect transistors ($\mu = 2\,\mathrm{cm^2\,V^{-1}\,s^{-1}}$). To fabricate the transistor, we evaporated 100 nanometers of DPh-BTBT onto a room-temperature transistor substrate at $\sim 1\,\mathrm{nm\,s^{-1}}$. The transistor substrates were cleaned before use by sonicating in 1:1 acetone:isopropyl alcohol for 15 min, scrubbing and sonicating 10 min with distilled water and detergent (Aquet), sonicating in distilled water 10 min, and ozone cleaning for 5 min. The transistor substrate was a highly n-doped silicon gate, a $300\,\mathrm{nm}$ thermally grown silicon oxide insulator layer, and $40\,\mathrm{nm}$-thick gold source and drain electrodes with a $5\,\mathrm{nm}$ chromium adhesion layer. The electrodes were deposited using thermal evaporation in an interdigitated array. The channel length was $5\,\mathrm{\mu m}$ and the channel width was $19.8\,\mathrm{cm}$.

In FM-KPFM (Fig. 4.1a), the sample's surface potential is determined by oscillating the cantilever at its resonance frequency using a phase-locked loop controller and nulling the cantilever frequency shift δf induced by tip-sample electrostatic forces

$$\delta f = -\frac{f_{\mathrm{c}}}{4k_{\mathrm{c}}} C''(V_{\mathrm{t}} - \phi)^2, \tag{4.1}$$

where f_{c} is the cantilever resonance frequency, k_{c} the cantilever spring constant, C'' the second derivative of the tip-sample capacitance with respect to the vertical direction, V_{t} the cantilever tip voltage, and ϕ the sample's surface potential. The tip voltage is the sum of a fixed-frequency modulation voltage and a feedback voltage V_{fb}: $V_{\mathrm{t}} = V_{\mathrm{m}} \sin(2\pi f_{\mathrm{m}} t) + V_{\mathrm{fb}}$, where V_{m} is the voltage-modulation amplitude and f_{m} is the voltage-modulation frequency. A lock-in amplifier measures the oscillating frequency shift at the modulation frequency

$$\delta f(f_{\mathrm{m}}) = -\frac{f_{\mathrm{c}}}{2k_{\mathrm{c}}} C'' V_{\mathrm{m}} (V_{\mathrm{fb}} - \phi). \tag{4.2}$$

A proportional-integral-derivative controller feedback loop adjusts V_{fb} to maintain $\delta f(f_{\mathrm{m}})$ at zero. With large enough feedback gain, $\delta f(f_{\mathrm{m}}) \approx 0$, and the feedback voltage tracks the surface potential closely: $V_{\mathrm{fb}} \approx \phi$. The feedback voltage is the *measured* surface potential. The assumption that $V_{\mathrm{fb}} = \phi$ is only valid at low frequencies or long times. The feedback voltage V_{fb} also varies due to the effects of detector noise, low-frequency position noise, and surface potential fluctuations.

Many KPFM measurements derive information mainly from contrast in surface potential images or the average difference in surface potential over different regions of the sample. These properties are relatively insensitive to feedback loop dynamics, noise and surface potential fluctuations. In contrast, these sources of error affect the calculated electric field dramatically. To highlight the effect of these error sources, we write the *measured* surface potential as

$$\phi_{\mathrm{meas}} = V_{\mathrm{fb}} = H * (\phi + \phi_{\mathrm{n}}) \tag{4.3}$$

where H is the feedback loop's impulse response function, $*$ denotes convolution in the time domain, ϕ is the sample's actual surface potential and ϕ_{n} is an equivalent surface potential noise that accounts for noise in ϕ_{meas}.

Noise in the measured surface potential typically arises from two sources: detector noise and low-frequency surface potential noise. The effect of detector noise can be minimized by operating at a sufficiently large modulation voltage or cantilever amplitude. Low-frequency surface potential noise could arise from position hysteresis and noise or real surface potential fluctuations caused by trapped charge or dielectric fluctuations [61, 80, 81]. In either case, the effect of surface potential noise can be mitigated by increasing the scan speed.

Increasing the scan speed, however, comes at a cost. The feedback loop response function H has a bandwidth b. This temporal bandwidth limits the *spatial* resolution of the measured surface potential and electric field when the tip is scanned [82]. For a tip velocity v, the measurement response function distorts the surface potential and electric field when they change on a length scale smaller than $x_{\mathrm{res}} = v/(2\pi b)$. We find significant distortion near the contact of a DPh-BTBT transistor when $x_{\mathrm{res}} > 10\,\mathrm{nm}$ (Fig. C.2).

If the scan speed is carefully optimized, low-frequency surface potential noise along the scan axis can be avoided without distorting the measured electric field significantly. In a 2D raster scan, however, the electric field measured along the slow scan axis will still be subject to large low-frequency surface potential noise caused by position hysteresis and slow surface potential fluctuations.

To avoid this low-frequency noise, we modify the KPFM measurement by adding a small position modulation $\vec{\delta r}$. The position modulation allows us to measure the electric-field component along the position-modulation direction E_{pm}, since to first order in $\vec{\delta r}$

$$\phi(\vec{r} + \vec{\delta r}(t)) \approx \phi(\vec{r}) + \nabla\phi \cdot \vec{\delta r} = \phi(r) - \vec{E} \cdot \vec{\delta r}(t). \tag{4.4}$$

We use a modulation having a direction $\hat{\delta r} = \hat{x}$ or $\hat{y}$ and a magnitude

$$\delta r(t) = A_{\mathrm{pm}} \sin(2\pi f_{\mathrm{pm}} t), \tag{4.5}$$

with A_{pm} the modulation amplitude and f_{pm} the modulation frequency. We detect the electric field as an oscillating potential at the modulation frequency with amplitude $\delta\phi(f_{\mathrm{pm}}) = A_{\mathrm{pm}} E_{\mathrm{pm}}$. To measure E_{pm} accurately, the modulation amplitude A_{pm} must be small enough that the potential can be approximated to first order in δr as in Eq. 4.4. Because we detect $\delta\phi(f_{\mathrm{pm}})$ using the KPFM feedback loop, the modulation frequency f_{pm} must be significantly smaller than the feedback loop bandwidth b. In our measurements, we used $A_{\mathrm{pm}} = 30\,\mathrm{nm}$ and $f_{\mathrm{pm}} = 4.5\,\mathrm{Hz}$, with $b = 20\,\mathrm{Hz}$ over the gate and $b = 40\,\mathrm{Hz}$ over the source/drain electrodes ($b \propto C''$).

To perform the position-modulated KPFM measurement, we used the experimental setup from Figure 4.1a and saved the measured surface potential ϕ_{meas}-versus-time data (digitized at $8.192\,\mathrm{kHz}$). The surface potential-versus-time data measures the surface potential and electric field in the *scan* direction at low frequencies and the electric field in the *modulation* direction at the modulation frequency. We low-pass filtered ϕ_{meas} using the filter H_{pm} to estimate the sample surface potential along the scan direction. We processed ϕ_{meas} again using a software lock-in amplifier with lock-in filter H_{pm} to extract $\delta f(f_{\mathrm{pm}}) = A_{\mathrm{pm}} E_{\mathrm{pm}}$ (section C.3). The Fig. 4.1b inset shows this analysis in a representative region near the contact where ϕ along the scan direction is relatively constant and the

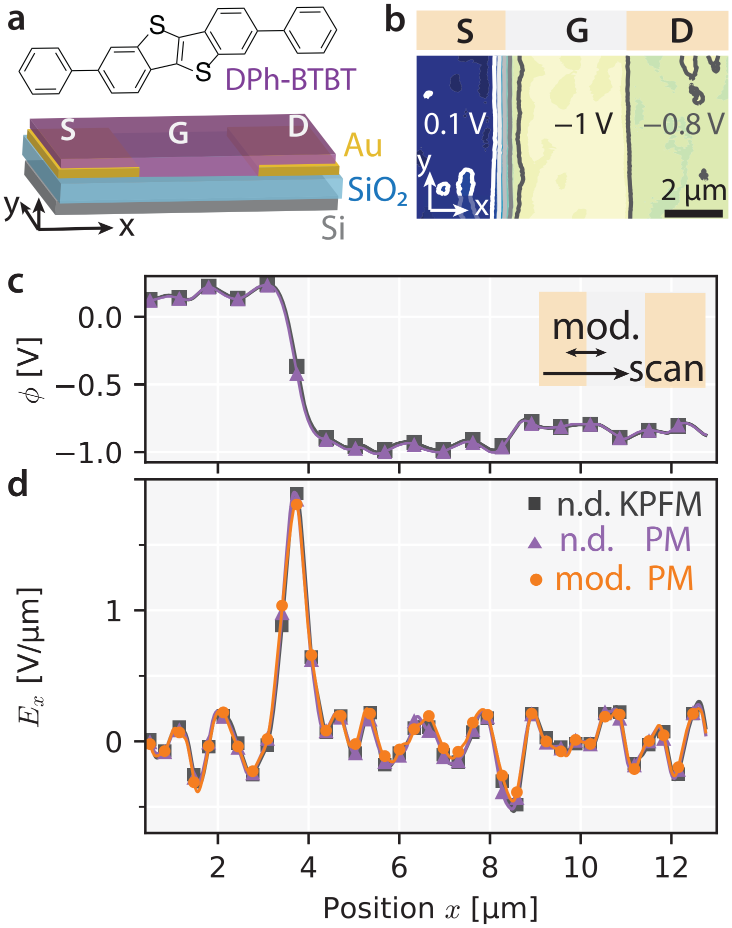

Figure 4.2: Demonstration of position-modulated KPFM on a transistor. (a) Cartoon of the transistor. (b) FM-KPFM image of the transistor channel, acquired with tip-sample separation $h = 150\,\mathrm{nm}$, zero-to-peak oscillation amplitude $A = 50\,\mathrm{nm}$, transistor source, gate, and drain voltages $V_{\mathrm{S}} = 0\,\mathrm{V}$, $V_{\mathrm{G}} = -10\,\mathrm{V}$, and $V_{\mathrm{D}} = -1\,\mathrm{V}$ respectively. Lines show contours at -0.9, -0.7, -0.4, -0.1, and $0.1\,\mathrm{V}$. (c) Surface potential measured using KPFM (squares) and *position-modulated* KPFM (triangles). The scan and modulation are both along the x-axis (inset). (d) Comparison of the electric fields measured using KPFM and *position-modulated* KPFM. Numerical derivative of the KPFM surface potential (squares), numerical derivative of the *position-modulated* KPFM surface potential (triangles), and the modulation component of *position-modulated* surface potential (circles). Experimental parameters: $A_{\mathrm{pm}} = 30\,\mathrm{nm}$, $f_{\mathrm{pm}} = 4.5\,\mathrm{Hz}$, $v = 0.41\,\mathrm{\mu m\,s^{-1}}$, voltage-modulation amplitude $V_{\mathrm{m}} = 2\,\mathrm{V}$ and frequency $f_{\mathrm{m}} = 160\,\mathrm{Hz}$.

electric field along the modulation direction is significant.

Figure 4.2 shows our new position-modulated KPFM technique performed on a DPh-BTBT thin-film transistor. Figure 4.2b shows a FM-KPFM image of the transistor with the source, gate, and drain electrodes labeled.

To verify the accuracy of the electric field calculated from our new position-modulated KPFM technique, we performed position-modulated KPFM and FM-KPFM line scans across the transistor channel. So that both techniques measure E_{pm}, we applied the position modulation along the scan axis (Fig. 4.2c inset). The data in Fig. 4.2c confirms that the two techniques measure the same surface potential ϕ. We low-pass filtered the surface potential at $0.8\,\mathrm{Hz}$, which corresponds to a spatial frequency low-pass filter at $\nu = 2.2\,\mu\mathrm{m}^{-1}$.

From the two line scans, we calculated the electric field E_{pm} three ways (Fig. 4.2d). We numerically differentiated the FM-KPFM surface potential (squares) and the position-modulated KPFM surface potential (triangles). To calculate the electric field from the position-modulation signal, we processed the raw surface potential data using a software lock-in amplifier whose reference frequency was set equal to the position-modulation frequency $f_{\mathrm{pm}} = 4.5\,\mathrm{Hz}$. To make a fair comparison to standard FM-KPFM, we used a $0.8\,\mathrm{Hz}$ bandwidth lock-in amplifier filter, identical to the filter used for the surface potential. We plot the electric field $E_{\mathrm{pm}} = X_{\mathrm{LI}}/A_{\mathrm{pm}}$, where X_{LI} is the in-phase channel of the phased lock-in amplifier output (circles). The electric field and surface potential calculated from our new position-modulated technique agree closely with the standard FM-KPFM electric field and surface potential. At equivalent bandwidth, all three electric field measurements have similar noise.

In Figure 4.3 we use PM-KPFM to measure the electric field along the slow scan axis more precisely. We collected AFM and KPFM images over the DPh-BTBT transistor with

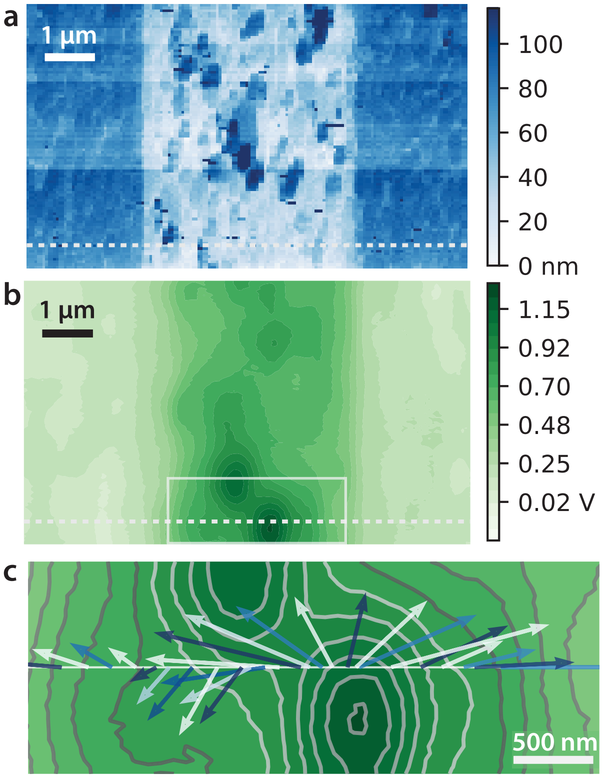

Figure 4.3: PM-KPFM vector electrometer demonstration. (a) AFM image of the transistor channel. Full scale is $120\,\mathrm{nm}$. The image was clipped at the data's 99th percentile for clarity. (b) FM-KPFM image of the transistor channel with $V_{\mathrm{S}} = V_{\mathrm{D}} = V_{\mathrm{G}} = 0$. Contours are shown every $75\,\mathrm{mV}$. (c) An expanded view of the FM-KPFM surface contours in the boxed region of (b), with the vector electric field calculated from a PM-KPFM linescan. KPFM experimental parameters: tip-sample separation $h = 200\,\mathrm{nm}$, zero-to-peak amplitude $A = 50\,\mathrm{nm}$, tip velocity $v = 1.55\,\mathrm{\mu m\,s^{-1}}$, scan spacing along the slow scan axis $\Delta y = 50\,\mathrm{nm}$, scan spacing along the fast scan axis $\Delta x = 90\,\mathrm{nm}$. PM-KPFM experimental parameters: $A_{\mathrm{pm}} = 30\,\mathrm{nm}$, $f_{\mathrm{pm}} = 4.5\,\mathrm{Hz}$, $v = 0.37\,\mathrm{\mu m\,s^{-1}}$.

source, gate, and drain voltages set to zero (Fig. 4.3(a,b)). The KPFM image revealed pockets of trapped charge in the transistor channel (dark spots in box in Fig. 4.3b).

To probe the electric field near these trapped charges, we took a PM-KPFM linescan (Fig. 4.3c; Fig. 4.4). We applied the position modulation *perpendicular* to the scan direction so that we measured E_{x} and E_{y} simultaneously; E_x was determined by numerically differentiating the measured ϕ with respect to the fast scan direction while E_y was obtained from X_{LI} as discussed above. Figure 4.3c shows the KPFM image contours along with

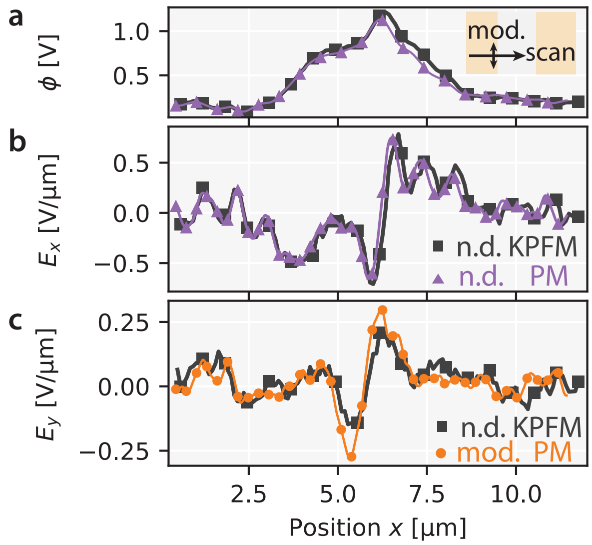

Figure 4.4: (a) Surface potential measured using KPFM (squares) and *position-modulated* KPFM (triangles). The scan was along the x-axis and the modulation was along the y-axis (inset). (b) Electric fields measured along the scan axis. Numerical derivatives of the KPFM surface potential (squares) and the PM-KPFM surface potential (triangles). (c) Electric fields measured along the slow scan or modulation axis. Numerical derivative of the KPFM surface potential (squares) and the modulation component of the PM-KPFM surface potential. The KPFM surface potential was filtered along the y-axis before taking the numerical derivative (see section C.4). Experimental parameters given in Fig. 4.3.

the *in-plane* electric field *vector* (E_x, E_y) measured by PM-KPFM. One consequence of the electric field being the negative gradient of the electrostatic potential is that the electric field vector at location $\vec{r}$ must be perpendicular to a line tangent to the constant-$\phi(x, y)$ surface passing through $\vec{r}$. This perpendicular relationship is clearly evident in Fig. 4.3c, demonstrating PM-KPFM's ability to serve as a *vector electrometer*.

In Figure 4.4, we quantitatively compare the surface potential and the electric field measured by FM-KPFM and PM-KPFM. Both measurements computed the electric field along the fast scan axis (E_x) by numerical differentiation, using surface potential data averaged for $200\,\mathrm{ms}$ in each case. The two measurements of E_x are in close agreement (Fig. 4.4b). Along the slow scan axis, the PM-KPFM electric field E_y (light circles, Fig. 4.4c) shows lower noise than the FM-KPFM electric field (dark squares, Fig. 4.4c). The FM-

KPFM E_y was computed by subtracting surface potential points acquired $8\,\mathrm{s}$ apart. Slow drift in the surface potential on this timescale thus shows up as noise in the FM-KPFM E_y [52]. In contrast, PM-KPFM allows E_y to be measured simultaneously with E_x.

Looking at the measurements in the frequency domain, the FM-KPFM measurement of E_y incorporates surface potential noise at temporal frequencies near $(8\,\mathrm{s}/\text{line})^{-1} \sim 0.1\,\mathrm{Hz}$. The PM-KPFM measurement of E_y incorporates surface potential noise at frequencies near $f_{\mathrm{pm}} = 4.5\,\mathrm{Hz}$, where overall surface potential noise is near a minimum (Fig. C.6).

We anticipate that the simple modification of FM-KPFM introduced here will be useful for electric field measurements in a variety of systems. Although we demonstrate its use for measuring lateral electric fields, it should also be possible to measure vertical electric fields with an additional vertical position modulation. The 2D electric field images demonstrated here are already an advance from lateral electric field line scans, and we envision applying the PM-KPFM technique to measure local electric fields in bulk heterojunction solar cell blends. The 2D electric field scans could show the current flow direction at domain boundaries in illuminated samples during operation near the open-circuit voltage V_{OC}.

CHAPTER 5

PM-KPFM THEORY

5.1 Introduction

Local electric field measurements help researchers understand charge injection, charge transport, and charge trapping in semiconducting materials and devices. Optical microscopy techniques have measured the local electric field in organic transistors [83, 84] and solar cells [85] with micrometer resolution. Kelvin probe force microscopy (KPFM) has imaged local electric fields in field-effect transistors [72, 77, 73, 78, 74, 86, 87, 88], light-emitting electrochemical cells [75, 76], light-emitting diodes [89], and solar cells [90, 91, 92, 93, 94].

KPFM electric field measurements have obtained the electric field by numerically differentiating the surface potential along a linescan, only measuring the electric field component along the linescan direction. We have modified frequency-modulated Kelvin probe force microscopy [22] (FM-KPFM) by adding an additional position modulation which allows measuring the electric field along multiple axes simultaneously [95].

Figure 5.1 summarizes the *position-modulated* KPFM experiment (PM-KPFM) introduced in Ref. 95. We measure the sample surface potential ϕ using FM-KPFM. The position modulation $\vec{\delta r}$ produces an oscillating potential proportional to the electric-field component along the position-modulation direction E_{pm}, since to first order in $\vec{\delta r}$

$$\phi(\vec{r} + \vec{\delta r}(t)) \approx \phi(\vec{r}) + \nabla\phi \cdot \vec{\delta r} = \phi(r) - \vec{E} \cdot \vec{\delta r}(t). \tag{5.1}$$

We use a sinusoidal modulation

$$\delta r(t) = A_{\mathrm{pm}} \sin(2\pi f_{\mathrm{pm}} t), \tag{5.2}$$

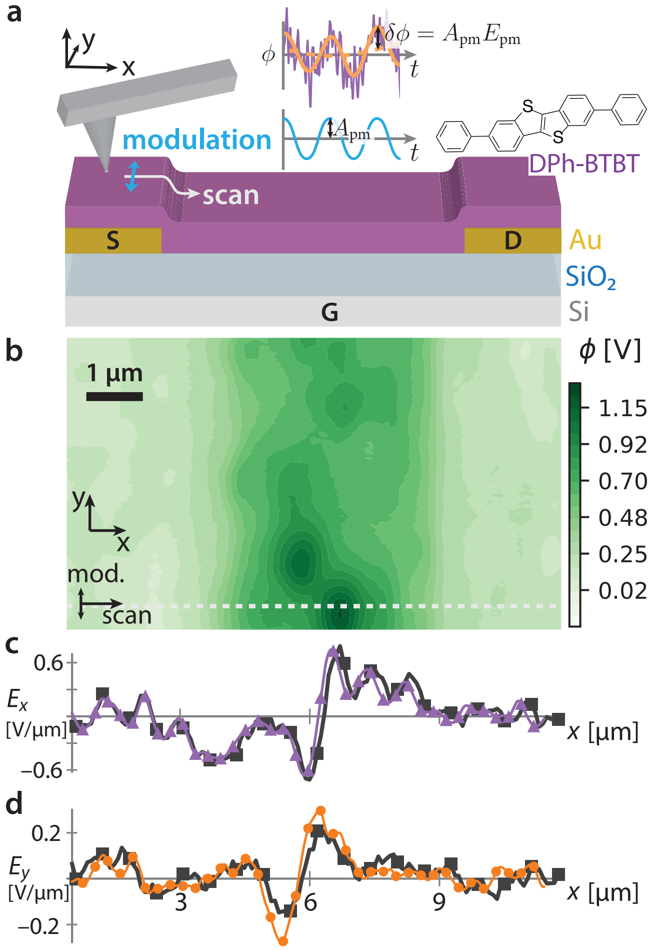

Figure 5.1: An overview of the position-modulated KPFM experiment. (a) Cartoon of the scanned probe cantilever over the DPh-BTBT transistor. The *position modulation* induces an oscillating surface potential $\delta\phi$ proportional to the electric field along the modulation direction. (b) A FM-KPFM image of the transistor channel collected with source, drain, and gate voltages set to zero: $V_{\mathrm{S}} = V_{\mathrm{D}} = V_{\mathrm{G}} = 0$. Contours are shown every $75\,\mathrm{mV}$. A PM-KPFM linescan was collected along the dashed line. (c) Electric field E_x (along the linescan direction) measured by numerically differentiating the FM-KPFM surface potential ϕ (black squares) and numerically differentiating the *position-modulated* KPFM linescan (purple triangles). (d) Electric field E_y (perpendicular to the linescan direction) measured by numerically differentiating the FM-KPFM surface potential ϕ (black squares) and measured by tracking the surface potential signal at the *position-modulation* frequency (orange circles). KPFM experimental parameters: tip-sample separation $h = 200\,\mathrm{nm}$, zero-to-peak amplitude $A = 50\,\mathrm{nm}$, tip velocity $v = 1.55\,\mathrm{\mu m\,s^{-1}}$, scan spacing along the slow scan axis $\Delta y = 50\,\mathrm{nm}$, scan spacing along the fast scan axis $\Delta x = 90\,\mathrm{nm}$. PM-KPFM Experimental parameters: $A_{\mathrm{pm}} = 30\,\mathrm{nm}$, $f_{\mathrm{pm}} = 4.5\,\mathrm{Hz}$, $v = 0.37\,\mathrm{\mu m\,s^{-1}}$.

with A_{pm} the modulation amplitude and f_{pm} the modulation frequency. We detect the electric field as an oscillating potential at the modulation frequency

$$\widehat{\delta\phi}(f_{\mathrm{pm}}) = A_{\mathrm{pm}} E_{\mathrm{pm}} \tag{5.3}$$

as illustrated in Fig. 5.1a. To measure E_{pm} accurately, the modulation amplitude A_{pm} must be small enough that the potential can be approximated to first order in δr as in Eq. 5.1.

To illustrate the experiment, we performed KPFM measurements over a DPh-BTBT bottom-gate bottom-contact field-effect transistor [79] (Fig. 5.1a; see Ref. 95 for sample preparation details). We set the transistor source, drain, and gate voltages equal to zero and collected a FM-KPFM (KPFM for brevity) image of the surface potential $\phi(x, y)$ over the transistor (Fig. 5.1b). To collect the KPFM image, we acquired a series of 128 linescans along the x-axis. Each linescan was acquired in $T_{\mathrm{linescan}} = 8\,\mathrm{s}$.

We collected a PM-KPFM linescan along the dotted line (Fig. 5.1b) by scanning along the x-axis and applying a small $30\,\mathrm{nm}$ position modulation along the y-axis. Figure 5.1c plots the electric field component along the linescan direction E_x. The black squares show E_x calculated by numerical differentiation of the KPFM image and the purple triangles show E_x calculated by numerical differentiation of the PM-KPFM linescan. The measured electric fields agree closely and have comparable noise.

Figure 5.1d plots the electric field component E_y. In the KPFM image, the y-axis is called the slow scan axis because adjacent pixels in the y-direction were separated in time by $T_{\mathrm{linescan}} = 8\,\mathrm{s}$. In the PM-KPFM linescan, the y-axis was the modulation direction. In Fig. 5.1, the black squares show E_y calculated by numerical differentiation of the KPFM surface potential map $\phi(x, y)$ and the orange circles show the PM-KPFM E_y calculated from the oscillating surface potential at the position-modulation frequency. The PM-KPFM E_y has less noise and better spatial resolution than KPFM E_y. Furthermore, PM-KPFM allows E_y to be measured *simultaneously* with E_x.

The improved measurement of the vector electric field via PM-KPFM was the main finding of our previous work [95]. This chapter extends our previous work by explaining the principle underlying the measurement, deriving how experimental parameters and noise sources affect the measured electric fields, and discussing the experimental settings necessary to achieve good performance with the PM-KPFM measurement.

5.2 Signal and Noise in FM-KPFM

We begin by describing the measured surface potential and noise sources in FM-KPFM (Fig. 5.2a).

5.2.1 The FM-KPFM surface potential measurement

In FM-KPFM, the sample's surface potential is determined by oscillating the cantilever at its resonance frequency using a phase-locked loop controller and nulling the cantilever frequency shift δf induced by tip-sample electrostatic forces

$$\delta f = -\frac{f_{\mathrm{c}}}{4k_{\mathrm{c}}} C''(d)(V_{\mathrm{t}} - \phi)^2 \tag{5.4}$$

where f_{c} is the cantilever resonance frequency, k_{c} the cantilever spring constant, C'' the second derivative of the tip-sample capacitance with respect to the vertical direction, d the tip-sample separation, V_{t} the cantilever tip voltage, and ϕ the sample's surface potential. The tip voltage is the sum of a fixed-frequency modulation voltage and a feedback voltage V_{fb}: $V_{\mathrm{t}} = V_{\mathrm{m}} \sin(2\pi f_{\mathrm{m}} t) + V_{\mathrm{fb}}$, where V_{m} is the voltage-modulation amplitude and f_{m} is the voltage-modulation frequency. A lock-in amplifier (LIA) measures the oscillating

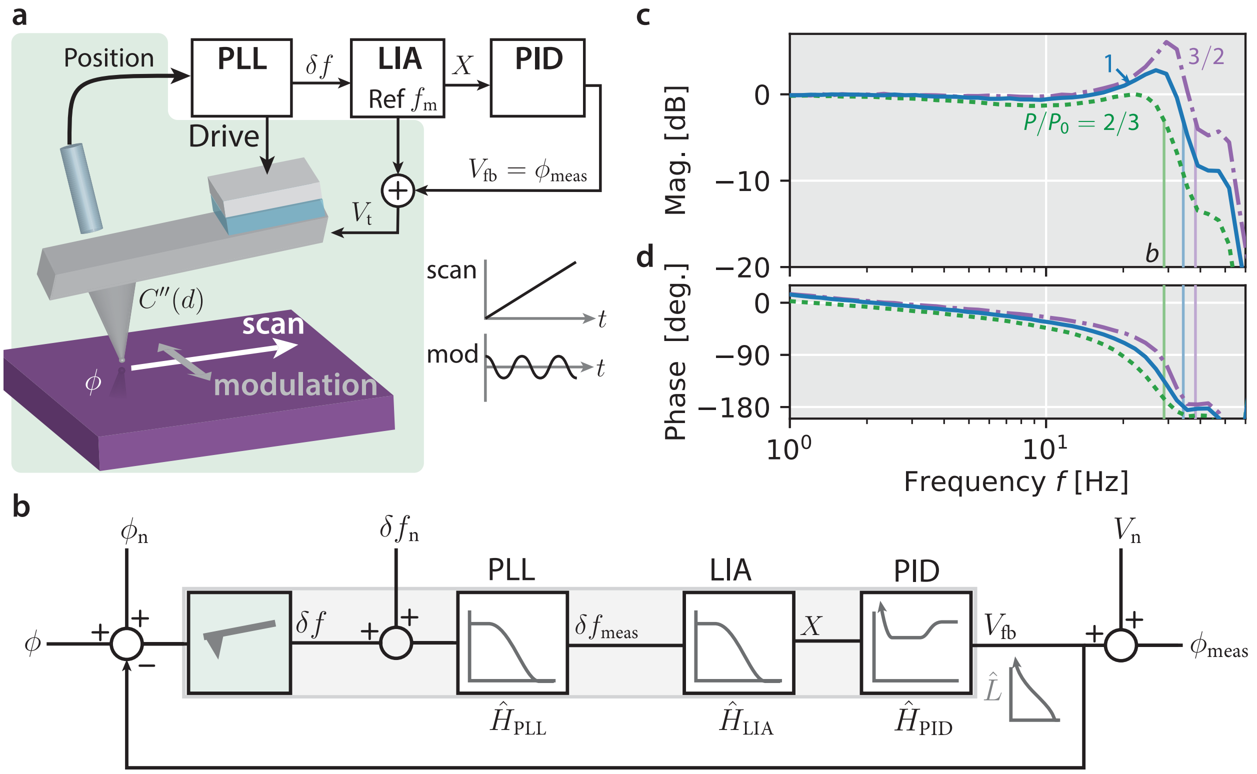

Figure 5.2: The voltage-modulation feedback loop in FM-KPFM. (a) Cartoon illustrating the voltage modulation used in FM-KPFM. (b) Block diagram showing the steps in measuring the surface potential ϕ using FM-KPFM. The measured closed-loop transfer function $\hat{H}$ (Eq. 5.6) for three different proportional gains, $P = (2/3, 1, 3/2)P_0$, where P_0 was chosen to be the proportional gain that ensures a gain margin of 3. (c) The magnitude $|\hat{H}(f)|$; and (d) the phase $\arg(\hat{H}(f))$. The vertical lines mark the feedback loop 3-dB-bandwidths $b = 29, 34$, and $38\,\mathrm{Hz}$ respectively.

frequency shift at the modulation frequency

$$\widehat{\delta f}(f_\mathrm{m}) = -\frac{f_\mathrm{c}}{2k_\mathrm{c}} C''(d) V_\mathrm{m} (V_\mathrm{fb} - \phi) \tag{5.5}$$

A proportional-integral-derivative (PID) controller feedback loop uses V_fb to maintain $\widehat{\delta f}(f_\mathrm{m})$ at zero. With large enough feedback gain, $\delta f(f_\mathrm{m}) \approx 0$, and the feedback voltage tracks the surface potential closely: $V_\mathrm{fb} \approx \phi$. The feedback voltage is the *measured* surface potential. The assumption that $V_\mathrm{fb} = \phi$ is only valid at low frequencies or long times.

We quantify the relationship between the feedback voltage V_fb and the sample's surface potential ϕ by analyzing the KPFM feedback loop. In Fig. 5.2a, the relationship between the sample's actual and measured surface potential is not immediately clear. We re-write the block diagram in Fig. 5.2b to highlight the relationship between the output ϕ_{meas} and the input ϕ. We represent the tip-sample interaction (shaded region of Fig. 5.2a) as a single block on the diagram with a transfer function given by Eq. 5.5.

In the frequency domain, the transfer function $\hat{H}$ between the feedback voltage and the surface potential is

$$\hat{H}(f) = \frac{\hat{V_{\mathrm{fb}}}}{\hat{\phi}} = \frac{\hat{L}(f)}{1 + \hat{L}(f)} \tag{5.6}$$

with $\hat{L}$ the open-loop transfer function between V_{fb} and ϕ. In the frequency domain, $\hat{L}(f)$ is the product of the transfer functions of the individual loop components:

$$\hat{L}(f) = \hat{H}_{\mathrm{PID}}(f)\hat{H}_{\mathrm{LIA}}(f)\hat{H}_{\mathrm{PLL}}(f)\frac{f_{\mathrm{c}}}{2k_{\mathrm{c}}}C''(d)V_{\mathrm{m}}. \tag{5.7}$$

Fig. 5.2b shows qualitative plots of the component transfer functions. The transfer functions $\hat{H}_{\mathrm{PLL}}$ and $\hat{H}_{\mathrm{LIA}}$ are low-pass filters. Because of the PID controller's integral gain, the PID controller's transfer function $\hat{H}_{\mathrm{PID}}(f) \propto 1/f$ at low frequencies. The PID-controller parameters are adjusted so the loop transfer function $\hat{L}(f) \gg 1$ at low frequencies.

To reliably operate the feedback loop at a consistent bandwidth, we set the PID proportional gain P using a gain margin criteria. We set up the KPFM experiment and increased the PID proportional gain until the loop becomes unstable ($P = P_{\mathrm{unstable}}$). Then we reduced the gain to $P_0 = P_{\mathrm{unstable}}/3$, corresponding to a gain margin of 3. Figure 5.2(c,d) show the magnitude and phase response of the *closed*-loop transfer function $\hat{H}$ for three different settings of the PID-controller proportional gain $P = (2/3, 1, 3/2)\, P_0$. The closed-loop transfer function $\hat{H}$ was a low-pass filter with respective 3-dB bandwidths $b = 29, 34$, and $38\,\mathrm{Hz}$.

The properties of the closed-loop transfer function $\hat{H}$ are determined by the properties of the open-loop transfer function $\hat{L}$. In particular, $\hat{L}$ is proportional to the tip-

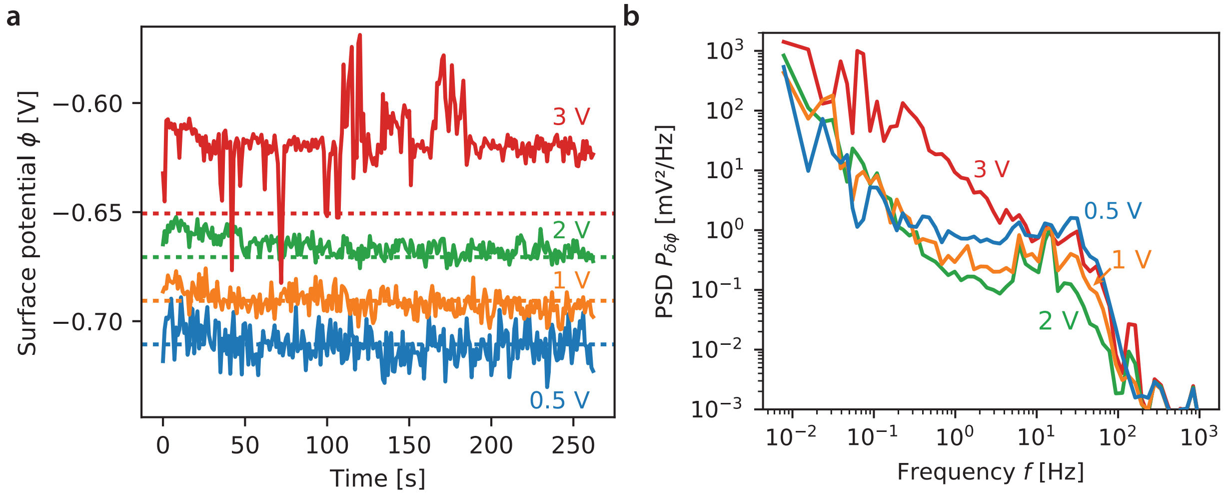

Figure 5.3: FM-KPFM surface potential noise collected over the drain electrode (Fig. 5.1a) with $V_{\mathrm{D}} = -1\,\mathrm{V}$. (a) Surface potential versus time measured through the FM-KPFM feedback loop for different modulation voltages $V_{\mathrm{m}}/\sqrt{2} = V_{\mathrm{rms}} = 0.5$, 1.0, 2.0 and $3\,\mathrm{V}$. The curves are offset for clarity. The dashed lines show $\phi = -0.71\,\mathrm{V}$ for the surface potential data of the same color. (b) Power spectral density of surface potential fluctuations $P_{\delta\phi}$ calculated from the data in (a). Experimental parameters: Cantilever zero-to-peak amplitude $A = 50\,\mathrm{nm}$, tip-sample separation $h = 200\,\mathrm{nm}$, voltage-modulation frequency $f_{\mathrm{m}} = 160\,\mathrm{Hz}$.

sample capacitance $C''(d)$. During the measurement, $C''(d)$ may change because the tip is scanned over materials with different capacitances or because of tip-sample drift. These changes affect the closed-loop bandwidth b in the same way as changes in PID-proportional gain P. Therefore, the traces in Fig. 5.2(c,d) equivalently show $\hat{H}$ for $P = P_0$ and $C'' = (2/3, 1, 3/2)\,C_0''$, where C_0'' was the capacitance derivative when the feedback loop proportional gain was set. For the gain margin criteria we used, the magnitude of the closed-loop response $|\hat{H}| \approx 1$ for frequencies $f < 10\,\mathrm{Hz}$.

w

5.2.2 FM-KPFM noise sources

The transfer function $\hat{H}$ describes how the measured surface potential ϕ_{meas} responds to changes in the sample's actual surface potential ϕ. To analyze how noise sources affect the measured surface potential, we left the cantilever tip stationary and collected ϕ_{meas} versus time data at different modulation-voltage amplitudes V_{m} over the drain electrode (Fig. 5.3a). From the data in Fig. 5.3a, we calculated the power spectral density of surface potential fluctuations (Fig. 5.3b). Surface potential noise ϕ_{n} and frequency noise δf_{n} both enter the measured surface potential through the feedback loop, so both are filtered by the transfer function $\hat{H}$. Above the feedback loop bandwidth b, we see only the voltage noise V_{n}, which is *much* smaller. Therefore, we consider only noise sources which enter through the KPFM feedback loop. Because we measure surface potential, it is useful to relate cantilever frequency noise to an equivalent surface potential noise source. Using Eqs. 5.4 and 5.5, the equivalent potential noise is

$$\hat{\phi}_{\mathrm{n}}^{\mathrm{eq}}(f) = \frac{-k_{\mathrm{c}}}{f_{\mathrm{c}} C''(d) V_{\mathrm{m}}} \Big(\widehat{\delta f}_{\mathrm{n}}(f_{\mathrm{m}} + f) + \widehat{\delta f}_{\mathrm{n}}(f_{\mathrm{m}} - f) \Big). \tag{5.8}$$

For frequencies $f \ll f_{\mathrm{m}}$,

$$\hat{\phi}_{\mathrm{n}}^{\mathrm{eq}}(f) = \frac{-2k_{\mathrm{c}}}{f_{\mathrm{c}} C''(d) V_{\mathrm{m}}} \widehat{\delta f}(f_{\mathrm{m}}) \tag{5.9}$$

In our measurements, the dominant frequency noise source at $f_{\mathrm{m}} = 160\,\mathrm{Hz}$ is position detector noise. Position detector noise $\hat{x}_{\mathrm{n}}$ near the cantilever frequency f_{c} creates an equivalent frequency noise $\widehat{\delta f}(f_{\mathrm{m}}) = \hat{x}_{\mathrm{n}}(f_{\mathrm{c}}) f_{\mathrm{m}}/A$, with A the cantilever zero-to-peak amplitude. The position-noise-induced surface potential noise and any low-frequency surface potential noise should be independent. The total noise power is the sum of the power spectral densities

$$P_{\delta\phi}^{\mathrm{tot}}(f) = P_{\delta\phi}(f) + \frac{4 k_{\mathrm{c}}^2 f_{\mathrm{m}}^2}{f_{\mathrm{c}}^2 C''(d)^2 V_{\mathrm{m}}^2} \frac{P_{\delta x}(f_{\mathrm{c}})}{A^2} \tag{5.10}$$

Eq. 5.10 helps us understand the observed dependence of $P_{\delta\phi}$ on the modulation voltage V_{m} (Fig. 5.3b). For low modulation voltages $V_{\mathrm{rms}} = V_{\mathrm{m}}/\sqrt{2} < 3\,\mathrm{V}$, the total measured power spectral density $P_{\delta\phi}^{\mathrm{tot}}$ is approximately independent of V_{m}. In this region, the dominant noise source is potential fluctuations $P_{\delta\phi}$. At higher frequencies, $P_{\delta\phi}$ decreases with increasing modulation voltage, indicating the dominant noise source is $P_{\delta f}$, or more precisely $P_{\delta x}$. All of the noise sources considered so far depend only on temporal frequency f. In the next section, we consider our signal, the surface potential $\phi(x(t))$, which will depend only on the spatial frequency ν_x.

5.2.3 Effect of feedback dynamics and noise on the measured surface potential and electric field

We analyze how the feedback loop dynamics and surface potential noise sources affect the measured surface potential during a FM-KPFM linescan. To highlight the effect of these error sources, we write the *measured* surface potential as

$$\phi_{\mathrm{meas}}(t) = V_{\mathrm{fb}}(t) = \big[H * (\phi(x(t)) + \phi_{\mathrm{n}})\big](t) \tag{5.11}$$

where the feedback loop impulse response function H is the inverse Fourier transform of $\hat{H}$ (Eq. 5.6), $*$ denotes convolution in the time domain, ϕ is the sample's actual surface potential, and ϕ_{n} is the total equivalent surface noise from Eq. 5.10. For a typical FM-KPFM linescan, we scan along the x-axis at a constant tip velocity v_{t}: $x(t) = v_{\mathrm{t}} t$. We associate the surface potential $\phi_{\mathrm{meas}}(t)$ with the position $v_{\mathrm{t}} t$, so that the position axis x is just a rescaled version of the time axis. Ignoring noise, the relationship between the temporal Fourier transforms of the *measured* and *actual* surface potential is given by

$$\hat{\phi}_{\mathrm{meas}}(f) = \hat{H}(f)\hat{\phi}(f). \tag{5.12}$$

The time axis t and the position axis x are just scaled versions of each other, so using the scaling property of the Fourier transform, we can re-write Eq. 5.12 in terms of spatial

Fourier transforms:

$$\hat{\phi}_{\mathrm{meas}}(\nu_x) = \hat{H}(v_{\mathrm{t}}\nu_x)\hat{\phi}(\nu_x) \tag{5.13}$$

The spatial Fourier transform of the measured surface potential $\phi_{\mathrm{meas}}(x)$ is the spatial Fourier transform of the actual surface potential times the temporal Fourier transform of the feedback-loop transfer function $\hat{H}$. The effect of the feedback loop is to filter out surface potential components at spatial frequencies $\nu_x > \nu_{\mathrm{LP}} = b/v_{\mathrm{t}}$. We found significant distortion near the contact of a DPh-BTBT transistor when $\nu_{\mathrm{LP}} < 15\,\mathrm{\mu m}^{-1}$ [95].

The measured electric field is

$$E_x^{\mathrm{meas}}(x) = \frac{1}{v}\frac{d\phi_{\mathrm{meas}}}{dt}. \tag{5.14}$$

In the temporal frequency domain,

$$\hat{E}_x^{\mathrm{meas}}(f) = \frac{2\pi i f}{v}\hat{H}(f)\hat{\phi}(f) \tag{5.15}$$

where we use the derivative property of the Fourier transform. Converting to spatial frequency,

$$\hat{E}_x^{\mathrm{meas}}(\nu_x) = 2\pi i \nu_x \hat{H}(v_{\mathrm{t}}\nu_x)\hat{\phi}(\nu_x) \tag{5.16}$$

The signal-to-noise ratio is exactly the same as for surface potential measurements; however, the results can *look* different, because the electric field signal is concentrated at higher spatial frequencies, so it is important not to attenuate these frequencies through insufficient feedback loop bandwidth. To measure the electrical field accurately, we must measure the sample's surface potential accurately. Both the surface potential and electric field become dominated by noise at high spatial/temporal frequencies.

Fig. 5.4 shows the power spectral density (PSD) of potential fluctuations during a trace/retrace linescan. The measured power spectral density should be

$$P_{\phi}^{\mathrm{meas}}(\nu_x) = |\hat{H}(v_{\mathrm{t}}\nu_x)|^2 \Big(P_{\phi}(\nu_x) + P_{\delta\phi}^{\mathrm{tot}}(v_{\mathrm{t}}\nu_x) \Big) \tag{5.17}$$

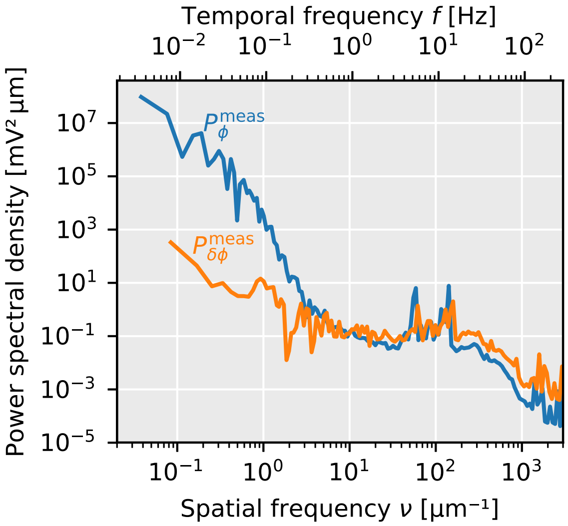

Figure 5.4: Power spectral density of the measured surface potential collected during a trace-retrace linescan across the transistor channel (Fig. 5.1a). Experimental parameters: Cantilever zero-to-peak amplitude $A = 50\,\mathrm{nm}$, tip-sample separation $h = 200\,\mathrm{nm}$, voltage-modulation frequency $f_{\mathrm{m}} = 160\,\mathrm{Hz}$, tip velocity $v_{\mathrm{t}} = 0.21\,\mu\mathrm{m\,s^{-1}}$, transistor source, drain and gate voltages $V_{\mathrm{S}} = 0$, $V_{\mathrm{D}} = -5$, and $V_{\mathrm{G}} = -10\,\mathrm{V}$ respectively.

We write $P_{\phi}(\nu_x)$ because we expect the power spectrum of the potential to depend almost entirely on the spatial frequency $\nu_x = f/v_{\mathrm{t}}$. The noise sources and feedback-loop filter, on the other hand, depend on the temporal frequency $f = v_{\mathrm{t}}\nu_x$. We plot P_{ϕ}^{meas} with both a spatial and temporal frequency axis. For comparison, we plot the measured PSD of surface potential *fluctuations* $P_{\delta\phi}^{\mathrm{meas}}(f)$ for $V_{\mathrm{rms}} = V_{\mathrm{m}}/\sqrt{2} = 2\,\mathrm{V}$ from Fig. 5.3b. For spatial (temporal) frequencies greater than $3\,\mu\mathrm{m}^{-1}$ $(0.3\,\mathrm{Hz})$, the measured surface potential PSD and the measured PSD of surface potential fluctuations agree closely: $P_{\phi}^{\mathrm{meas}} \approx P_{\delta\phi}^{\mathrm{meas}}$. The close agreement between P_{ϕ}^{meas} and $P_{\delta\phi}^{\mathrm{meas}}$ indicates that we measure mostly noise at spatial frequencies greater than $3\,\mu\mathrm{m}^{-1}$. The close agreement also provides some support for our assumption that the noise sources depend almost exclusively on temporal frequency.

Along the line-scan direction, electric field components at a spatial frequency ν_{x} are detected at a temporal frequency $f = v_{\mathrm{t}}\nu_x$. The noise is lower at higher temporal frequency, so increasing the scan speed can improve the signal-to-noise ratio by moving the signal power away from low-frequency $1/f$ noise.

For a 2D image, however, taking the derivative along the slow scan axis (y) requires subtracting data points collected many seconds apart. For an image acquired with a linescan time T_{line} and a distance Δy between adjacent lines, the electric field E_y could be approximated by

$$E_y^{\text{meas}}(x, y; t) = -\frac{\phi(t + T_{\text{line}}) - \phi(t - T_{\text{line}})}{2\Delta y}. \tag{5.18}$$

Consider a square 128×128 image, collected with a tip-velocity along the fast scan axis $v_x = v_{\text{t}}$. We could consider performing the scan by using a constant slow scan-axis velocity $v_y = v_{\text{t}}/128$. Then the surface potential components used to calculate the electric field along the slow scan axis E_y are located at a temporal frequency a factor of 128 lower. For the surface potential power spectral density shown in Fig 5.4, even the highest frequency component of the electric field, located at a temporal frequency $f = 1\,\text{Hz}$, would incorporate temporal frequency noise at $8\,\text{mHz}$, well into the high-noise region dominated by $1/f$ surface potential fluctuations.

5.3 Results

We developed position-modulated KPFM to avoid poor electric field measurements along the slow scan axis. To measure the electric field components along the fast scan and slow scan axes simultaneously, we apply a small position modulation perpendicular to the fast scan direction. The resulting surface potential is

$$\phi(t) = \phi(x(t), y(t)) \tag{5.19}$$

where x is the fast scan direction and y is the slow scan direction. The position as a function of time is

$$x(t) = vt \qquad \text{and} \qquad y(t) = A_{\text{pm}} \cos(2\pi f_{\text{pm}} t). \tag{5.20}$$

where v is the tip velocity, A_{pm} is the position-modulation amplitude, and f_{pm} is the position-modulation frequency.

5.3.1 PM-KPFM surface potential in the position domain

The displacement along the y-axis is small, so we consider approximating $\phi(x, y)$ as a low-degree polynomial in y. Due to the cosinusoidal modulation, $y(t)$ is usually near the extreme points $\pm A_{\text{pm}}$. In this case, very good approximations to $\phi(x, y)$ can be obtained by truncating the Chebyshev expansion of $\phi(x, y)$:

$$\phi(x, y) = \frac{1}{2} c_0(x) + \sum_{k=1}^{\infty} c_k(x) T_k(y/A_{\text{pm}}) \tag{5.21}$$

where T_k is the Chebyshev polynomial of degree k and c_k are Chebyshev coefficients given by

$$c_k(x) = \frac{1}{\pi} \int_{-\pi}^{\pi} d\theta \, \phi(x, A_{\text{pm}} \cos\theta) \cos(k\theta). \tag{5.22}$$

We approximate ϕ by truncating the infinite sum, including only terms up to degree N:

$$\phi(x, y) \approx \phi^{(N)}(x, y) = \frac{1}{2} c_0(x) + \sum_{k=1}^{N} c_k(x) T_k(y/A_{\text{pm}}). \tag{5.23}$$

To analyze how the PM-KPFM experiment filters components of the electric field at different spatial frequencies, we write the coefficients c_k in terms of the Fourier transform of ϕ with respect to y

$$c_k(x) = \frac{1}{\pi} \int_{-\pi}^{\pi} d\theta \left(\int_{-\infty}^{\infty} d\nu_y \hat{\phi}(x, \nu_y) e^{2\pi i \nu_y A_{\text{pm}} \cos\theta} \right) \cos(k\theta). \tag{5.24}$$

Using the Bessel function identity $e^{iz\cos\theta} = \sum\limits_{n=-\infty}^{\infty} i^n J_n(z) e^{in\theta}$ and switching the order of integration, we obtain

$$c_k(x) = \int_{-\infty}^{\infty} d\nu_y \hat{\phi}(x, \nu_y) \sum_{n=-\infty}^{\infty} J_n(2\pi\nu_y A_{\text{pm}}) \frac{i^n}{\pi} \underbrace{\int_{-\pi}^{\pi} d\theta \, e^{in\theta} \cos(k\theta)} \, . \tag{5.25}$$

The underbraced integral in Eq. 5.25 is only non-zero for $n = \pm k$. For c_0, collapsing the sum over n gives

$$c_0(x) = \; 2 \int_{-\infty}^{\infty} d\nu_y \hat{\phi}(x, \nu_y) J_0(2\pi\nu_y A_{\text{pm}}). \tag{5.26}$$

In the position domain, $c_0(x)/2$ is the average value of the surface potential for $y = -A_{\text{pm}}$ to A_{pm}, weighted by the amount of time the cantilever spends at a given y. In the limit $A_{\text{pm}} \to 0$, the coefficient $c_0(x)/2$ is equal to the surface potential $\phi(x, 0)$. In the frequency domain, the position modulation attenuates components of the surface potential at high spatial frequencies ν_y.

Just as $c_0(x)$ is a filtered version of the potential $\phi(x, 0)$, the coefficient $c_1(x)$ is a filtered version of the electric field $E_y(x, 0)$:

$$c_1(x) = 2i \int_{-\infty}^{\infty} d\nu_y \, \hat{\phi}(x, \nu_y) J_1(2\pi\nu_y A_{\text{pm}}). \tag{5.27}$$

Using the derivative property of the Fourier transform and $E_y = -\partial\phi/\partial y$, the Fourier transform of the electric field with respect to y is $\hat{E}_y(x, \nu_y) = -2\pi i \nu_y \hat{\phi}(x, \nu_y)$. Substituting this expression into Eq. 5.27, we obtain

$$c_1(x) = -A_{\text{pm}} \int_{-\infty}^{\infty} d\nu_y \, \hat{E}_y(x, \nu_y) \frac{J_1(2\pi\nu_y A_{\text{pm}})}{\pi\nu_y A_{\text{pm}}}. \tag{5.28}$$

Figure 5.5 illustrates the relationship between the sample surface potential and electric field and the Chebyshev coefficients in the spatial and spatial frequency domains. We constructed a cubic spline interpolating function $\phi(x, y)$ from an experimental KPFM

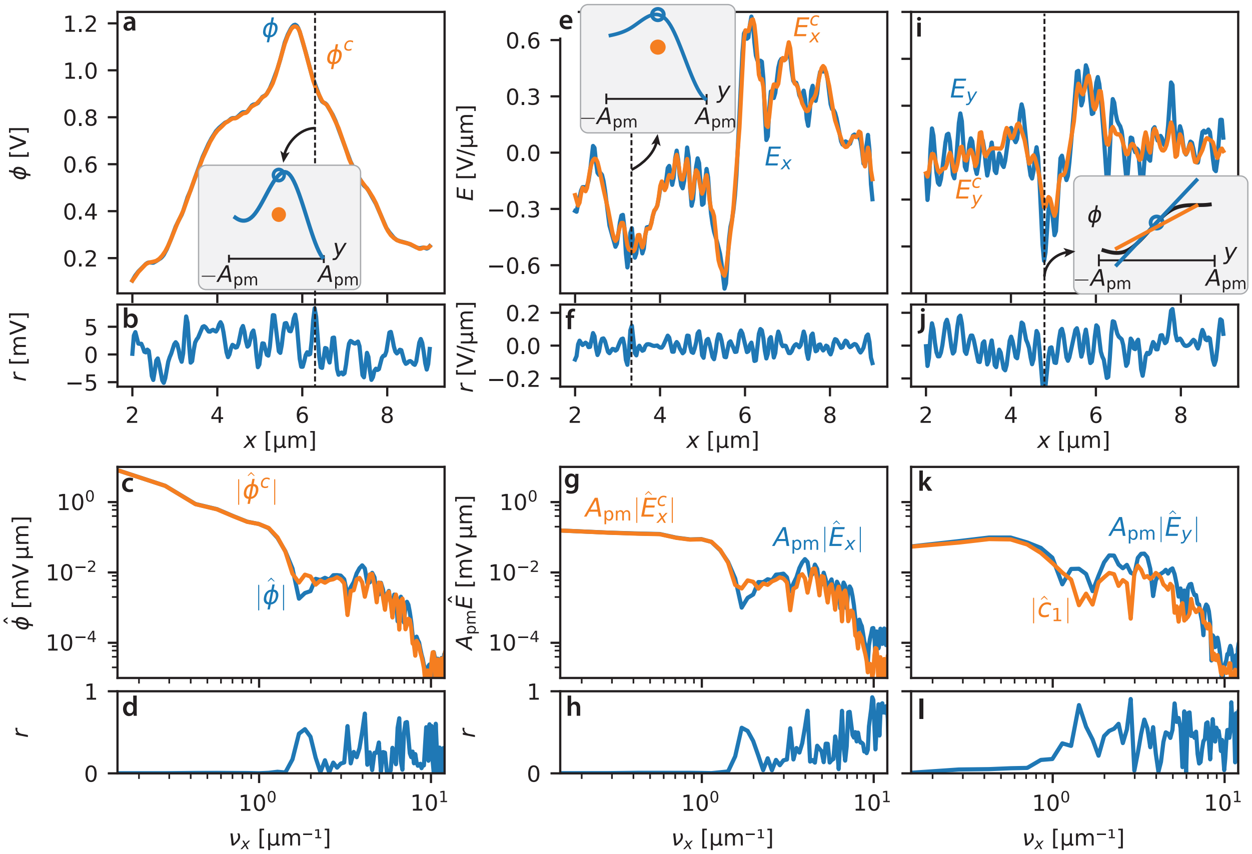

Figure 5.5: (a) Surface potential ϕ and Chebyshev approximation $\phi^c = \frac{1}{2}c_0$. Inset: The approximation (orange point) is inaccurate when ϕ (blue line) is quadratic in y. (b) Residual $r = \phi - \phi^c$. (c) Magnitude of the spatial Fourier transform of ϕ and ϕ^c from (a). (d) Relative difference between $|\hat{\phi}|$ and $|\hat{\phi}^c|$. (e) Electric field E_x and Chebyshev approximation $E_x^c = -\frac{1}{2}dc_0/dx$; and (f) residual. Inset: The approximation (orange point) is inaccurate when E_x (blue line) is quadratic in y. (g) Scaled magnitude of the spatial Fourier transforms $\hat{E}_x$ and $\hat{E}_x^c$; and (h) relative difference. (i) Electric field E_y and Chebyshev approximation $E_y^c = -c_1/A_{\mathrm{pm}}$; and (j) residual. Inset: The approximation (slope of orange line) for E_y (slope of blue line) is inaccurate when ϕ (black curve) is cubic in y. (k) Scaled magnitude of the spatial Fourier transform of E_y and spatial Fourier transform of c_1; and (l) relative difference.

image of a DPh-BTBT transistor. The experimental KPFM image was acquired with transistor source, drain and gate voltages $V_{\mathrm{S}} = V_{\mathrm{D}} = V_{\mathrm{G}} = 0$. We used the interpolating function to calculate the electric fields for a x-axis linescan: $E_x(x, y = 0)$ and $E_y(x, y = 0)$. We used Eq. 5.22 to calculate $c_0(x)$ and $c_1(x)$ for a modulation $A_{\mathrm{pm}} = 60\,\mathrm{nm}$.

Fig. 5.5a shows that $\phi^c = c_0(x)/2$ is a good approximation to the surface potential $\phi(x)$. The maximum residual $r = \phi - \phi^c$ is $5\,\mathrm{mV}$. The inset shows that the maximum residual occurs at positions x_0 where $\phi(x_0, y)$ is parabolic in y with an extrema at $y = 0$. Fig. 5.5c shows that the magnitude of the Fourier transforms of ϕ and c_0 begin to differ at high spatial frequencies. Fig. 5.5d plots the relative difference between $\hat{\phi}$ and $\hat{c}_0/2$, which is concentrated at high spatial frequencies ν_x. Equation 5.26 indicates that components of the surface potential at high spatial frequency along the modulation direction ν_y are filtered out, while saying nothing about components of the surface potential at high spatial frequency along the scan direction ν_x. Presumably, the filtering along both directions occurs because of a correlation between high-spatial-frequency components in x and y: both components arise from the same source.

Fig. 5.5e plots the electric field along the scan direction $E_x = -\partial\phi/\partial x$ along with the electric field as measured from c_0: $E_x^c = -\frac{1}{2} dc_0/dx$. Just as for the surface potential, the measured and actual electric field agree closely. The measured electric field smooths some of the high-frequency oscillations in the electric field. The inset shows that the electric field . The difference in the electric field $r = E_x - E_x^{\mathrm{est}}$ is concentrated at high spatial frequencies, as shown in Figure 5.5f–g. Overall, the electric field signal is concentrated at higher spatial frequencies, so the smoothing effects of the measurement are more noticeable.

Fig. 5.5i plots the electric field along the modulation direction $E_y = -\partial\phi/\partial y$ along with the electric field as measured from c_1: $E_y^c = -c_1/A_{\mathrm{pm}}$. The modulation filters out components of the electric field at high spatial frequency. The inset shows that the points x_0 where the residual $r = E_y - E_y^c$ is large have a surface potential $\phi(x_0, y)$ with a significant y^3 term.

5.3.2 PM-KPFM surface potential in the time domain

So far, our analysis has shown how the position modulation affects the measured surface potential and electric field at a fixed position x. In the experiment, we scan the position x at a fixed velocity and measure the sample's surface potential as a function of time. Just as in normal FM-KPFM, we associate the surface potential data point collected at time t with the position $x = v_{\mathrm{t}} t$. The component of the surface potential near DC should contain information about $\phi(x)$ and $E_x(x)$. We expect the component of the surface potential near the position-modulation frequency f_{pm} to contain information about the electric field along the modulation direction $E_y(x)$.

By writing $\phi(x, y)$ in terms of Chebyshev polynomials, we can determine the properties of $\mathcal{F}_t[\phi(t)]$, the Fourier transform of ϕ with respect to time. In the time domain, the surface potential is

$$\phi(t) = \frac{1}{2} c_0(v_{\mathrm{t}} t) + c_1(v_{\mathrm{t}} t) \cos(2\pi f_{\mathrm{pm}} t) + \sum_{k=2}^{\infty} c_k(v_{\mathrm{t}} t) \cos(2\pi k f_{\mathrm{pm}} t) \tag{5.29}$$

where we use the identity $T_n(\cos\theta) = \cos(n\theta)$. In the frequency domain, the functions are concentrated near DC (Fig. 5.4). In the frequency domain, the surface potential is

$$\hat{\phi}(f) = \frac{1}{2v_{\mathrm{t}}} \sum_{k=-\infty}^{\infty} c_k \left(\frac{f - k f_{\mathrm{pm}}}{v_{\mathrm{t}}} \right). \tag{5.30}$$

The coefficients c_k depend on the spatial frequency ν_x (Fig. 5.5). For temporal frequencies near DC, we evaluate Eq. 5.30 at frequencies $f = v_{\mathrm{t}} \delta\nu$:

$$\hat{\phi}(v_{\mathrm{t}} \delta\nu) = \frac{1}{2v_{\mathrm{t}}} \Big(c_0(\delta\nu) + c_1(\delta\nu - \nu_{\mathrm{pm}}) + c_1(\delta\nu + \nu_{\mathrm{pm}}) + \dots \Big) \tag{5.31}$$

where the spatial frequency $\nu_{\mathrm{pm}} = f_{\mathrm{pm}}/v_{\mathrm{t}}$ determines which spatial frequency components of $\hat{c}_0, \hat{c}_1$ overlap in the temporal frequency domain. In our experiments, we use a position-modulation frequency $f_{\mathrm{pm}} = 4.5\,\mathrm{Hz}$ and a tip velocity $v_{\mathrm{t}} = 0.4\,\mathrm{\mu m\,s^{-1}}$, which corresponds to $\nu_{\mathrm{pm}} = 11.2\,\mathrm{\mu m^{-1}}$. Figure 5.5(c and k) show that $\hat{c}_1(\nu_{\mathrm{pm}} + \delta\nu) \ll \hat{c}_0(\delta\nu)$. As long as we choose the position-modulation frequency and tip-velocity correctly, we can measure ϕ and E_{x} accurately from the low-frequency component of $\phi(t)$:

$$\hat{\phi}(v_{\mathrm{t}}\delta\nu) \approx \frac{1}{2v_{\mathrm{t}}} c_0(\delta\nu) = \frac{1}{v_{\mathrm{t}}}\hat{\phi}^c(\delta\nu). \tag{5.32}$$

We need to modulate quickly enough and scan slowly enough that the surface potential spectrum $\hat{c}_0$ and the electric field along the modulation direction spectrum $\hat{c}_1$ do not overlap significantly.

To measure the electric field along the modulation direction E_y, we evaluate $\hat{\phi}$ at a frequency $f = f_{\mathrm{pm}} + v_{\mathrm{t}}\delta\nu$:

$$\hat{\phi}(f_{\mathrm{pm}} + v_{\mathrm{t}}\delta\nu) = \frac{1}{2v_{\mathrm{t}}}\Big(c_1(\delta\nu) + c_0(\nu_{\mathrm{pm}} + \delta\nu_{\mathrm{pm}}) + c_1(\nu_{\mathrm{pm}} + 2\nu_{\mathrm{pm}}) + \dots\Big) \tag{5.33}$$

The $\hat{c}_0(\nu_{\mathrm{pm}})$ and $\hat{c}_1(2\nu_{\mathrm{pm}})$ terms are much smaller than $\hat{c}_1(\delta\nu)$ (Fig. 5.5(c,k)). Therefore, a good approximation for the surface potential evaluated near the modulation frequency is

$$\hat{\phi}(f_{\mathrm{pm}} + v_{\mathrm{t}}\delta\nu) \approx c_1(\delta\nu) = A_{\mathrm{pm}}\hat{E}_y^c(\delta\nu) \tag{5.34}$$

Therefore, we measure the electric field along the modulation direction by isolating the surface potential component at a frequency f_{pm} using a lock-in amplifier with a bandwidth b_{pm}. For a phased lock-in amplifier, $E_y^{\mathrm{meas}} = X_{\mathrm{LI}}/A_{\mathrm{pm}}$. The error in the measured electric field is related to the *spatial* filtering imposed by the modulation (Fig. 5.5i) and the temporal filtering imposed by the lock-in-amplifier filter, which filters components of the electric field E_y at high x-axis spatial frequencies $\nu_x > b_{\mathrm{pm}}/v_{\mathrm{t}}$.

In the last two sections of the paper, we have derived expressions for the surface potential and electric field measured using PM-KPFM. By expanding the surface potential in terms of its Chebyshev coefficients c_k, we identified how the measured surface potential and electric field depend on the spatial spectrum of the sample's surface potential and experimental parameters. Our results are consistent with the simple description of PM-KPFM presented in Eqs. 4.4–5.3, but also indicates when the description of Eqs. 4.4–5.3 breaks down. In the next section, we use our more complete description of the PM-KPFM measurement to correctly choose experimental parameters.

5.3.3 Experimental settings

In performing the position-modulated KPFM experiment, we can choose the scan speed v_{t}, the position-modulation frequency f_{pm}, and the position-modulation amplitude A_{pm}. To determine how to set these parameters, we use the feedback loop bandwidth b and the maximum spatial frequencies in the x and y directions $\nu_x^{\max}$ and $\nu_y^{\max}$. In a spatially "symmetric" system, it is natural for $\nu_x^{\max} = \nu_y^{\max}$. In a transistor, however, the surface potential spectrum $\hat{\phi}(\nu_x, \nu_y)$ may be very different parallel and perpendicular to the transistor channel.

Figure 5.6 shows the spatial filtering along the modulation direction imposed by the position modulation. To minimize attenuation of E_y, we choose $A_{\mathrm{pm}} < 0.1/\nu_y^{\max}$.

The position-modulation frequency needs to be large enough that the low-frequency signal used to determine ϕ and E_x does not overlap significantly with the modulation-frequency signal used to determine E_y. For this purpose, $f_{\mathrm{pm}} > 2 v_{\mathrm{t}} \nu_x^{\max}$. The modulation-frequency must be small enough that no component of the modulation signal is significantly attenuated by the feedback-loop filter $\hat{H}$. For the representative feedback loop shown in Fig. 5.2c, $f_{\mathrm{pm}} < 11\,\mathrm{Hz}$ ensures less than 5 percent error. Within that range, f_{pm} can be chosen to avoid vibration or noise peaks (Fig. 5.3b). We chose $f_{\mathrm{pm}} = 4.5\,\mathrm{Hz}$ for

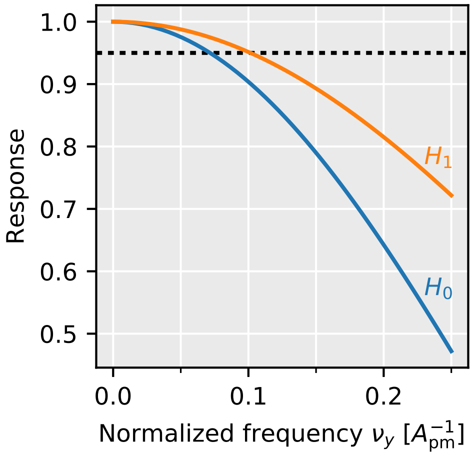

Figure 5.6: Bessel function spatial frequency transfer functions for the surface potential $H_0(\nu) = J_0(2\pi\nu A_{\mathrm{pm}})$ and for the electric field component along the modulation frequency $H_1 = J_1(2\pi\nu A_{\mathrm{pm}})/(\pi\nu A_{\mathrm{pm}})$. The dashed line shows $|H| = 0.95$.

these experiments, near the surface potential noise minimum (Fig. 5.3b).

Once the position-modulation frequency is chosen, the tip velocity must be less than $\nu_x^{\max}/(2f_{\mathrm{pm}})$. To limit the effect of low-frequency surface potential noise (Fig. 5.3b), v_{t} should be near this limit. In our experiment, we chose $v_{\mathrm{t}} = 0.4\,\mathrm{\mu m\,s^{-1}}$

5.4 Discussion

We have presented an explicit derivation of the measured electric field and the relevant noise sources for FM-KPFM. In doing so, we have focused on the often-neglected impact of the FM-KPFM feedback loop and how different noise sources affect the measured surface potential. The spatial filtering of the surface potential imposed by the scanned probe tip has been treated extensively [96, 97]. While we have ignored this spatial filtering for the sake of clarity, the spatial filtering does not affect the position-modulated PM-KPFM technique differently than ordinary numerical differentiation of the FM-KPFM surface

surface potential.

There are a variety of possible extensions to the PM-KPFM measurement presented here. The measurement bandwidth could be increased by combining the position-modulation technique with a high-bandwidth variant of FM-KPFM such as heterodyne-KPFM [98, 82] or dissipation-KPFM [99, 100]. This modification could be especially useful for extending PM-KPFM to measure the complete 3D-electric-field vector by modulating in the z-direction.

We have derived expressions describing how PM-KPFM filters the surface potential and electric field along the modulation direction. The Bessel function filtering limits the size of the position-modulation amplitude A_{pm}. We have also described how the PM-KPFM experimental parameters should be chosen. We anticipate that PM-KPFM will be useful for electric field measurements in a variety of semiconductor materials and devices. The 2D electric field images demonstrated here are already an advance from KPFM measurements of the lateral electric field and optical microscopy measurements of the electric field magnitude.

CHAPTER 6

METHODS AND CONCLUSIONS

This chapter gives an overview of the scanned probe microscopy experiments performed in the Marohn group. We highlight the modifications made to the microscope to perform the experiments described in this thesis, with an eye towards potential new experiments. We analyze the experiments using the impedance description of electric force microscopy developed in Ref. 33. The impedance description of electric force microscopy captures the dependence of cantilever frequency and amplitude on the complex sample impedance. This more complete description of the tip-sample interaction allows us to describe the cantilever tip-sample force on the seconds to nanoseconds time scale, even though the sample's response—and correspondingly the charge and electrostatic force—may change dramatically over these time scales.

Section 6.1 was adapted with permission from Ref. 33 (Copyright 2017 American Chemical Society).

6.1 Impedance spectroscopy EFM theory

For the purposes of this chapter, the tip-sample electrostatic interaction is described by a potential energy

$$U = \frac{1}{2}\frac{q^2}{C(x)} \tag{6.1}$$

with x the cantilever displacement in the vertical direction, q the cantilever charge, and C the tip-sample capacitance. The electrostatic force F on the scanned probe tip depends on sample properties through the tip-sample charge q:

$$F(x, q) = -\frac{dU}{dx} = \frac{C'(x)}{2C(x)^2} q(x, V_{\mathrm{ts}})^2, \tag{6.2}$$

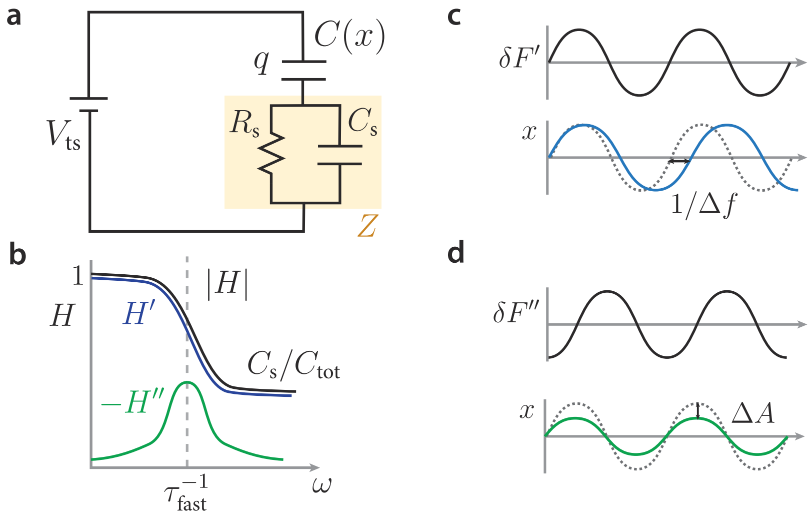

Figure 6.1: (a) The equivalent circuit for the cantilever and sample. (b) The associated response function H (upper, blue: real part, H'; lower, green: imaginary part, H''). (c) The in-phase force causes a cantilever frequency shift. (d) The out-of-phase force causes a cantilever amplitude shift (dissipation). Adapted with permission from Ref. 33. Copyright 2017 American Chemical Society.

where x is the tip displacement, $C(x)$ the tip capacitance, $C'(x) = dC/dx$, and q depends on displacement x and the applied tip-sample voltage V_{ts}. The time-dependent charge can be well-approximated by

$$q(t) = \Big(C(x(t))\,(V_{\mathrm{ts}}(t) - \phi) \Big) * H(t), \tag{6.3}$$

where ϕ is the sample surface potential and $*$ denotes convolution in the time domain. In the frequency domain, the transfer function H between applied tip-sample voltage V_{ts} and the tip voltage drop $V_{\mathrm{t}} = q/C$ is

$$\hat{H}(\omega) = \frac{\hat{V}_{\mathrm{t}}(\omega)}{\hat{V}_{\mathrm{ts}}(\omega)} = \frac{1/(j\omega C_{\mathrm{t}})}{Z(\omega) + 1/(j\omega C_{\mathrm{t}})}, \tag{6.4}$$

where Z is the sample impedance and $C_{\mathrm{t}} = C(0)$.

To describe dynamics on the ms to µs timescale, we model the sample as a parallel resistor R_{s} and capacitor C_{s}. The sample impedance is given by $Z = (R_{\mathrm{s}}^{-1} + j\omega C_{\mathrm{s}})^{-1}$ (Fig. 6.1a). The resulting transfer function H (Fig. 6.1b) is a lag compensator with time constant τ_{fast} and gain parameter g given by, respectively,

$$\tau_{\text{fast}} = R_{\text{s}}(C_{\text{s}} + C_{\text{tip}}) = R_{\text{s}} C_{\text{tot}} \;\text{ and }\; g = C_{\text{tot}}/C_{\text{s}}. \tag{6.5}$$

All our experiments probe oscillating forces. We determine the relevant oscillating forces by controlling the displacement x and voltage $V(t) = V_{\text{ts}} - \phi$. In all cases, the displacement x is small, so we can linearize the force F to first order in x as follows. The displacement x affects the force through the capacitance $C(x)$ and its derivatives, so a small displacement means one where $C_{\text{t}}' x / C_{\text{t}} \ll 1$ and $C_{\text{t}}'' x / C_{\text{t}}' \ll 1$. We linearize the capacitances about the point $x = 0$, replacing $C(x)$ and its derivatives with $C_{\text{t}} = C_{\text{tip}} = C(0)$. For the force of Equation 6.2, the oscillating force obtained by treating x and q^2 as the dependent variables and expanding the force in a first-order Taylor series in these variables:

$$\delta F = \left(\frac{\partial F}{\partial x} \right)_q x + \left(\frac{\partial F}{\partial q^2} \right)_x \delta q^2(x, V). \tag{6.6}$$

The first term is the force gradient between the tip and sample at constant charge. The second term describes the oscillating charge at constant displacement. The first term only contributes to force-gradient experiments that measure $\partial F / \partial x$. The two derivatives are

$$\left(\frac{\partial F}{\partial x} \right)_q = \frac{1}{2} \underbrace{\left(C_{\text{t}}'' - \frac{2 C_{\text{t}}'^2}{C_{\text{t}}} \right)}_{C_q''} \frac{q^2}{C_{\text{t}}^2} = \frac{1}{2} C_q'' \frac{q^2}{C_{\text{t}}^2} \tag{6.7}$$

$$\left(\frac{\partial F}{\partial q^2} \right)_x = \frac{1}{2} \frac{C_{\text{t}}'}{C_{\text{t}}^2}. \tag{6.8}$$

We introduce the variables

$$\Delta C'' = 2 \frac{C_{\text{t}}'^2}{C_{\text{t}}} \quad \text{and} \quad C_q'' = C_{\text{t}}'' - \Delta C''. \tag{6.9}$$

Using Equations 6.7–6.9 to simplify Equation 6.6, the total force is

$$F = \frac{1}{2} C_q'' \frac{q^2}{C_{\text{t}}^2} x + \frac{1}{2} C_{\text{t}}' \frac{q^2}{C_{\text{t}}^2}. \tag{6.10}$$

The experiments described in the chapter impose different oscillating charges. which to first order in x are

$$q(x, V) = \Big(\left(C_{\mathrm{t}} + C_{\mathrm{t}}' x\right) V(t) \Big) * H(t), \tag{6.11}$$

where we abbreviate $V_{\mathrm{ts}} - \phi$ as $V(t)$. The motivation for this description of the oscillating charge is that *both* small tip displacements and small changes in applied tip-sample voltage change the electric field between the tip and sample, which causes charge to flow. To first order in x, the tip-sample force is

$$F(t) = \frac{1}{2} C_q'' V_{\mathrm{t}}^2(t) x(t) + \frac{1}{2} \Delta C'' V_{\mathrm{t}}(t) \left[H * (x V_{\mathrm{ts}})\right](t) + \frac{1}{2} C_{\mathrm{t}}' V_{\mathrm{t}}^2(t) \tag{6.12}$$

where the tip voltage is recognized as $V_{\mathrm{t}} = H * (V_{\mathrm{ts}} - \phi)$. We use Eq. 6.12 to analyze how scanned probe measurements probe the sample impedance at different frequencies.

Taking the Fourier transform and using the convolution theorem [101],

$$\hat{F}(f) = \frac{1}{2} C_q'' \left[\hat{V}_{\mathrm{t}} * \hat{V}_{\mathrm{t}} * \hat{x}\right](f) + \frac{1}{2} \Delta C'' \left[\hat{V}_{\mathrm{t}} * \left(\hat{H}\left[\hat{V}_{\mathrm{ts}} * \hat{x}\right]\right)\right](f) + \frac{1}{2} C' \left[\hat{V}_{\mathrm{t}} * \hat{V}_{\mathrm{t}}\right](f) \tag{6.13}$$

where the Fourier transform of a function $g(t)$ is $\mathcal{F}_t[g(t)](f) = \hat{g}(f)$ and $*$ denotes convolution in the frequency domain. The Fourier transform of the tip voltage is $\hat{V}_{\mathrm{t}}(f) = \hat{H}(f) \hat{V}_{\mathrm{ts}}(f)$.

The transfer function H evaluated at the cantilever resonance frequency determines the relative phase between F and x. Forces oscillating in phase and out of phase with the cantilever motion affect the cantilever differently. The oscillating force has the form

$$\delta \hat{F} = \underbrace{\delta F'}_{\substack{\text{in-phase,} \\ \text{conservative}}} + \underbrace{j \delta F''}_{\substack{\text{out-of-phase,} \\ \text{dissipative}}}. \tag{6.14}$$

As shown in Figure 6.1c–d, the in-phase force $\delta F'$ shifts the cantilever's frequency by Δf while the out-of-phase force $\delta F''$ shifts the cantilever's amplitude by ΔA through an additional sample dissipation Γ_{s}:

$$\Delta f = -\frac{f_{\mathrm{c}}}{2k} \frac{\delta F'}{A} \quad \text{and} \quad \Gamma_{\mathrm{s}} = -\frac{1}{\omega_{\mathrm{c}}} \frac{\delta F''}{A}. \tag{6.15}$$

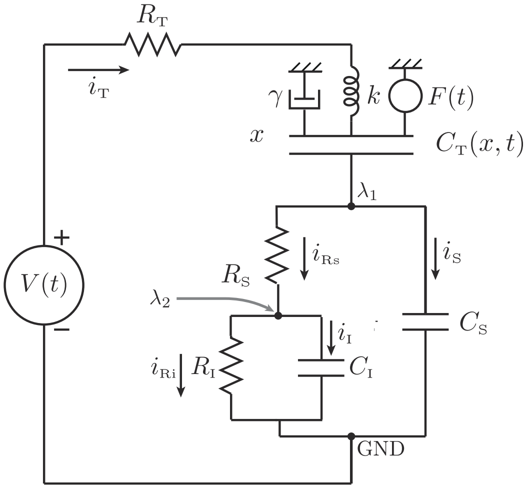

Figure 6.2: A circuit illustrating the types of dynamics observed in perovskite and organic semiconductor solar cells. Unless otherwise noted, we use the experimental parameters: $f_{\mathrm{c}} = 65\,000\,\mathrm{Hz}$, $k_0 = 3.5\,\mathrm{N\,m^{-1}}$, $Q = 26\,000$ (with $\gamma = 7.85\,\mathrm{s^{-1}}$), $F(t) = 0$, $R_{\mathrm{T}} = 0$, $R_{\mathrm{S}} = 200\,\mathrm{M\Omega}$, $C_{\mathrm{S}} = 1\times10^{-3}\,\mathrm{pF}$, $C_{\mathrm{I}} = 1\times10^{-3}\,\mathrm{pF}$. The position-dependent tip capacitance was $C_{\mathrm{T}}(x) = C + C'x + \frac{1}{2}C''x^2$ with $C = 1\times10^{-3}\,\mathrm{pF}$, $C' = -1.8\times10^{-4}\,\mathrm{pF\,\mu m^{-1}}$ and $C'' = 1.3\times10^{-4}\,\mathrm{pF\,\mu m^{-2}}$.

where A is the cantilever amplitude. The linear dependence of the force on the cantilever amplitude indicates that Δf and ΔA are force-gradient measurements.

6.2 Scanned probe microscopy methods

The experiments described below were performed in collaboration with Ali Tirmzi and are described in detail in Ref. 33.

6.2.1 Voltage parabolas

We start by considering the voltage-parabola experiment because it is the easiest to analyze. In this experiment, we set the tip-sample voltage equal to $V = V_{\mathrm{ts}} - \phi$ and drive

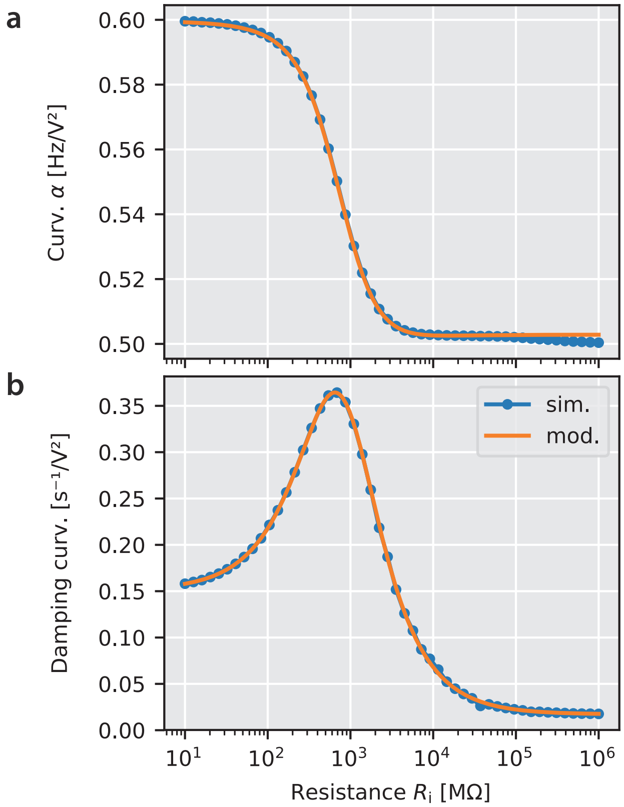

Figure 6.3: A circuit illustrating the types of dynamics observed in perovskite and organic semiconductor solar cells. Unless otherwise noted, we use the experimental parameters: $f_c = 65\,000\,\mathrm{Hz}$, $k_0 = 3.5\,\mathrm{N\,m^{-1}}$, $Q = 26\,000$ (with $\gamma = 7.85\,\mathrm{s^{-1}}$), $F(t) = 0$, $R_T = 0$, $C_T(x) = 1 \times 10^{-3}\,\mathrm{pF}$

the cantilever at its resonance frequency using a phase-locked loop controller. In the experiments of Ref. 33, we measured the cantilever frequency and amplitude after waiting a delay time $T_{\mathrm{delay}} \geq 3\tau_r$, with the ringdown time $\tau_r = 4\pi f_c^{-1} Q$. The delay allowed the cantilever time to settle to a new amplitude that reflected any dissipation caused by the tip-voltage. The resulting force gradient at the cantilever resonance frequency is

$$F_z = \hat{F}(f_c)/A = \hat{F}(f_c)/\hat{x}(f_c) = \frac{1}{2}\left(C_q''\hat{H}^2(0) + \Delta C''\hat{H}(0)\hat{H}(f_c)\right)(V_{ts} - \phi)^2 \tag{6.16}$$

The frequency and amplitude shift caused by F_z can be calculated by plugging $\hat{F}(f_c)$ into Eq. 6.9. The real component F_z gives rise to a frequency shift and the imaginary component gives rise to a amplitude shift (dissipation).

We simulated the experiment in Python for the sample impedance shown in Fig. 6.2. In Fig. 6.3 we compare the frequency-parabola curvature calculated from the simulation to the curvature predicted by the impedance model (Eq. 6.16a). The curvature was calculated by simulating the cantilever dynamics for $1\,\mathrm{ms}$ at 25 equally spaced voltages between $V_{\mathrm{ts}} - \phi = -3\,\mathrm{V}$ and $3\,\mathrm{V}$. From the same simulated data, we calculate the sample-induced dissipation per volt squared (Fig. 6.3). As we move from left to right, the time constant associated with the interface/ionic charge $\tau_{\mathrm{i}} = R_{\mathrm{I}} C_{\mathrm{I}}$ increases. As τ_{i} becomes longer than the inverse cantilever frequency ω_{c}^{-1}, the frequency shift and dissipation reach a maximum and then begin decreasing. The impedance theory model matches the simulated data very well for low resistances R_{I}. When $C_{\mathrm{I}} R_{\mathrm{I}} \gg \omega_{\mathrm{c}}^{-1}$, there is a slight discrepancy between the simulated frequency parabola curvature α and the impedance model prediction for α.

Conceptually, the important takeaway lesson from Equation 6.16 is that the cantilever frequency shift δf and dissipation γ depend on both the sample impedance at DC ($\hat{H}(0)$ depends on $Z(0)$) and the sample impedance at the cantilever resonance frequency. The first term of Eq. 6.16, proportional to C_q'', reflects the change in tip-sample force at constant charge. This force depends on the DC cantilever charge, which depends on the response function evaluated at zero frequency. The second term is related to the force caused by the charge oscillation induced by the oscillating tip. The oscillating tip acts to modulate the DC charge q_{DC} by a small fraction: $\delta q \approx q_{\mathrm{DC}} \hat{H}_{\omega_{\mathrm{c}}} A C_{\mathrm{t}}' / C_{\mathrm{t}}$. The fraction of charge that oscillates on and off the cantilever tip each cycle is $A C_{\mathrm{t}}' / C_{\mathrm{t}}$, with A the cantilever amplitude, C_{t} the tip-capacitance at $x = 0$, and C_{t}' the first derivative of the tip-sample capacitance at $x = 0$. The oscillating charge is proportional to the product of the response function at zero frequency, which sets the DC charge q_{DC}, and the response function at ω_{c}, which determines how much of the sample charge is able to response at the cantilever frequency. This same basic picture holds for the more complicated measurements involving voltage modulation.

6.2.2 Kelvin probe force microscopy

Kelvin probe force microscopy (KPFM) measures the sample surface potential ϕ. In KPFM, a modulation voltage is applied to the cantilever tip at a frequency f_{m}. The surface potential can be measured by detecting the change in the cantilever's resonance frequency at the modulation frequency (frequency-modulation KPFM or FM-KPFM) or the change in the magnitude of the cantilever displacement at the modulation frequency (amplitude-mode) [97, 102]. In our group, we have typically performed frequency-modulation Kelvin probe force microscopy (FM-KPFM) [22]. FM-KPFM is a force-gradient measurement; that is, FM-KPFM measures the change in the tip-sample force as the cantilever's vertical displacement changes. The change in the tip-sample force is governed predominantly by the cantilever tip because it is close to the sample. In contrast, the alternative, amplitude-modulation Kelvin probe force microscopy (AM-KPFM) measures the tip-sample force, and therefore contains significant contributions from the cantilever cone and body, which is much further away from the cantilever but has much more area [21]. This motivates the usual argument, which is often supported by experimental results, that FM-KPFM should have higher spatial resolution than AM-KPFM. Note, however, that the highest-resolution Kelvin probe force microscopy images have been acquired by performing AM-KPFM using the cantilever's second resonance frequency while simultaneously performing FM-AFM using cantilever's first resonance frequency [39, 103]. In general, if performed sufficiently close to the sample, AM-KPFM and FM-KPFM can have similar spatial resolution [97, 102]. AM-KPFM can also be performed using a smaller modulation voltage, limiting the effect of band-bending on the measured surface potential [104, 96].

The standard analysis of FM-KPFM is given in the discussion of our position-modulated KPFM technique in Chapters 4 and 5. Here we discuss the component of the cantilever frequency shift at twice the modulation frequency $\delta f(2f_{\mathrm{m}})$. This frequency shift measures the magnitude of the tip-sample capacitance second derivative $\partial F/\partial x \propto C''$:

$$\delta f_{\mathrm{act}}(2f_{\mathrm{m}}) = -\frac{f_{\mathrm{c}}}{8k_{\mathrm{c}}}C''V_{\mathrm{m}}^{2}. \tag{6.17}$$

The ratio between the frequency shift at the two components $\delta f(f_{\mathrm{m}})/\delta f(2f_{\mathrm{m}})$ allows the surface potential to be determined without feedback [105]:

$$\delta f_{\mathrm{act}}(f_{\mathrm{m}}) = -\frac{f_{\mathrm{c}}}{2k_{\mathrm{c}}}C''V_{\mathrm{m}}(V_{\mathrm{fb}} - \phi) \tag{6.18}$$

and therefore

$$\frac{\delta f_{\mathrm{act}}(f_{\mathrm{m}})}{\delta f_{\mathrm{act}}(2f_{\mathrm{m}})} = \frac{-\frac{f_{\mathrm{c}}}{2k_{\mathrm{c}}}C''V_{\mathrm{m}}(V_{\mathrm{fb}} - \phi)}{-\frac{f_{\mathrm{c}}}{8k_{\mathrm{c}}}C''V_{\mathrm{m}}^{2}} = \frac{4(V_{\mathrm{fb}} - \phi)}{V_{\mathrm{m}}}. \tag{6.19}$$

6.2.3 Force measurements

All the experiments described above are force-gradient measurements; the observable is the cantilever frequency or amplitude shift. In each experiment, there is an analogous experiment where we turn the PLLPro2 drive off and observe the cantilever displacement x, which is a measurement of the tip-sample force because the oscillating cantilever displacement at a frequency f_{m} is

$$\hat{x}(f_{\mathrm{m}}) = \hat{\chi}(f_{\mathrm{m}})\hat{F}(f_{\mathrm{m}}) \tag{6.20}$$

where $\hat{\chi}$ is the Fourier transform of the cantilever impulse response function

$$\widehat{\chi}(f) = \frac{1}{k}\left(\frac{1}{1 - \frac{f^2}{f_{\mathrm{c}}^2} + \frac{if}{Qf_{\mathrm{c}}}}\right). \tag{6.21}$$

These experiments have a simpler dependence on the sample impedance because to first order, $x \approx 0$. We can simplify Eq. 6.13 and plug the result into Eq. 6.20 to obtain

$$\hat{x}(f_{\mathrm{m}}) = \frac{1}{2} C' \, \hat{\chi}(f_{\mathrm{m}}) \left[\hat{V}_{\mathrm{t}} * \hat{V}_{\mathrm{t}} \right] (f_{\mathrm{m}}). \tag{6.22}$$

The measured displacement at a frequency f_{m} depends only on the cantilever's impulse response function and the oscillating charge at the frequency f_{m}.

6.2.4 Photo-KPFM

Photo-KPFM probes the rise and fall time of the photo-potential, or any other non-linear sample property that changes with light and/or voltage [48, 49, 106, 107]. Consider the usual case: the sample's surface potential depends on a carrier density $n(t)$, which in turn depends on the sample's history of light exposure $I_{h\nu}(t)$.

We turn the light source on and off at the light-modulation frequency f_{m}. When the light is turned on, the surface potential ϕ rises abruptly. When the light is turned off, the surface potential decays slowly. Because of the asymmetry between the surface potential rise time and decay time, the average surface potential $\bar{\phi}$ is close to the light-on value of the surface potential. In the absence of a non-linearity, the average surface potential is set by the duty cycle D, the fraction of the time that the light source is turned on.

To better understand the measurement, we consider a simple example. When the light is on, the surface potential evolves towards its light-on value ϕ_{on} with a first-order time constant τ_{on}:

$$\dot{\phi} = \tau_{\mathrm{on}}^{-1} (\phi - \phi_{\mathrm{on}}). \tag{6.23}$$

When the light is off, the surface potential evolves towards its light-off value ϕ_{off} with a first-order time constant τ_{off}:

$$\dot{\phi} = \tau_{\text{off}}^{-1}(\phi - \phi_{\text{off}}) \tag{6.24}$$

We solve for the steady-state condition where the surface potential at the beginning of each modulation cycle is the same: $\phi(0) = \phi(T_{\text{m}})$. By integrating $\phi(t)$ over a single cycle, we obtain the average surface potential $\langle\phi\rangle$. For simplicity, we normalize the surface potential by choosing $\phi_{\text{off}} = 0$ and $\phi_{\text{on}} = 1$. The resulting equation for the average surface potential is

$$\langle\phi\rangle = D - 2f_{\text{m}}(\tau_{\text{on}} - \tau_{\text{off}}) \sinh\left(\frac{f_{\text{on}}}{f_{\text{m}}}\right) \sinh\left(\frac{f_{\text{off}}}{f_{\text{m}}}\right) \Big/ \sinh\left(\frac{f_{\text{on}} + f_{\text{off}}}{f_{\text{m}}}\right) \tag{6.25}$$

where D is the duty cycle and the frequencies f_{on} and f_{off} are calculated from the respective time constants and the fraction of the cycle that the light is on or off respectively:

$$f_{\text{on}} = \frac{D}{2\tau_{\text{on}}} \qquad \text{and} \qquad f_{\text{off}} = \frac{1-D}{2\tau_{\text{off}}}. \tag{6.26}$$

Figure 6.4 shows the results for illustrative cases. Starting with the 50-percent duty cycle data in (a), we observe that for angular frequencies $\omega_{\text{m}}/2$ much smaller than the inverse of the light-on and light-off time constants τ_{on}^{-1} and τ_{off}^{-1}, the average surface potential is equal to the duty cycle: $\langle\phi\rangle = D = 0.5$. The same would be true for a linear system, where $\tau_{\text{on}} = \tau_{\text{off}}$. Choosing the blue trace in (a) with $\tau_{\text{off}} = 1\,\text{ms}$, we see that the average surface potential increases sharply at a modulation frequency corresponding to τ_{off}^{-1}. At high frequencies, the average surface potential levels off. Using Eq. 6.25 and taking the limit $f_{\text{m}} \to +\infty$, we obtain

$$\langle\phi\rangle = \left(1 + \frac{1-D}{D}\frac{\tau_{\text{on}}}{\tau_{\text{off}}}\right)^{-1}. \tag{6.27}$$

If τ_{on} and τ_{off} are not significantly different, $\langle\phi\rangle$ does not go all the way to the light-on value, but reaches a constant value set by the ratio of the time constants and the duty cycle. For the usual case, where $\tau_{\text{on}} \ll \tau_{\text{off}}$, low duty cycles help resolve a large asymmetry

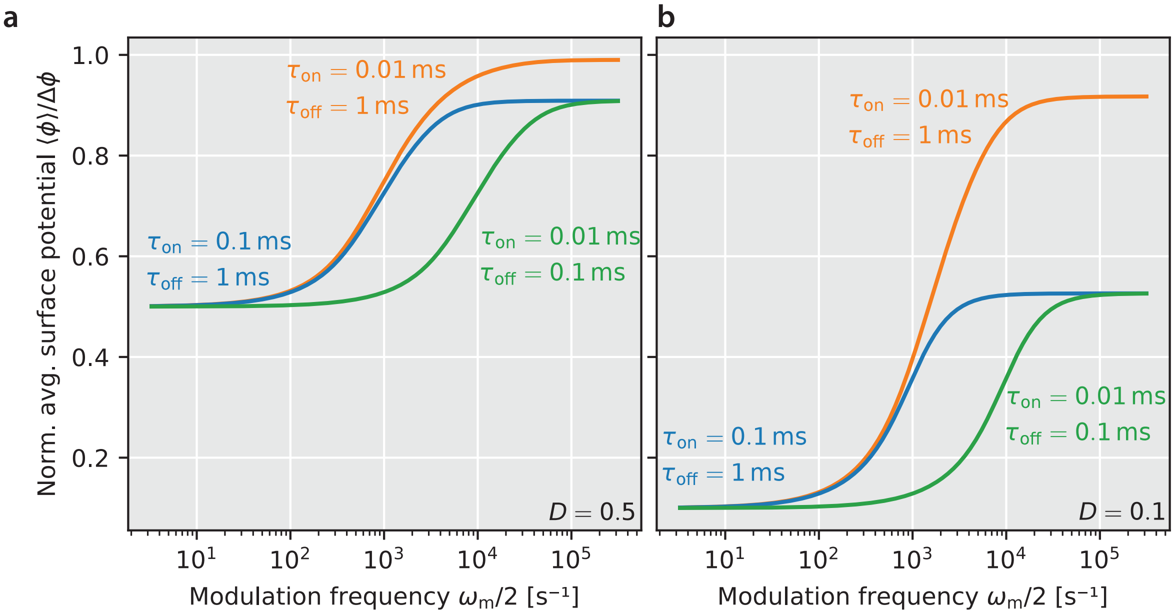

Figure 6.4: Simulated photo-KPFM data. The average surface potential measured for a frequency modulation with (a) 50-percent duty cycle ($D = 0.5$); and (b) 10-percent duty cycle ($D = 0.1$).

in time constants. In Fig. 6.4b, we see that even $\tau_{\text{on}}/\tau_{\text{off}} = 0.01$ is significantly different from 1 when the duty cycle is 0.1. The faster time constant can also be inferred by noting the frequency at which the average surface potential reaches its high frequency limit.

Overall, the simple model shows that the frequency at which the average surface potential changes most rapidly is roughly the inverse of the slower sample time constant (in this case, $\tau_{\text{off}} = 1\,\text{ms}$ or $0.1\,\text{ms}$). The average value of the surface potential at high frequencies reports provides information about the ratio $\tau_{\text{on}}/\tau_{\text{off}}$. By using lower duty cycles, some information about the ratio can be obtained even when $\tau_{\text{on}}/\tau_{\text{off}}$ is very small.

6.3 Microscope components

Many components of the PSB B19 electric force microscope have been added to the Baker 146 microscope in order to perform the experiments in this thesis.

6.3.1 PLLProII

The PLLPro commercial phase-locked loop controller was substituted for a new PLLProII controller. The PLLProII controller has two built-in lock-in amplifiers synchronized to the phase-locked loop. In the pk-EFM and tr-EFM experiments, we use one of these lock-in amplifiers to output a sine wave at a fixed phase shift from the cantilever oscillation (Fig. B.7). These lock-in amplifiers could be used to perform new, higher-speed KPFM measurements [82, 99, 100]. There are also built-in proportional-integrator (PI) feedback loops so that AFM or KPFM could be performed using only the PLLProII.

We connect the cantilever-position photodetector output to the PLLProII feedback input. The PLLProII feedback input is terminated in a $50\,\Omega$ resistor. To avoid drawing large currents from the battery-powered photodetector, we pass the cantilever signal through a buffer amplifier (located on a heavily modified version of Ryan's signal conditioning circuit). For $75\,\mathrm{kHz}$ cantilevers, it would be reasonable to remove the termination resistor from the feedback input, but for higher frequency cantilevers or measurements at the second resonance frequency of a $75\,\mathrm{kHz}$ cantilever, the termination resistor is useful for preventing reflections.

The PLLProII also gives the user control of the phase-locked-loop proportional and integral gain, which control the PLL bandwidth. In our experiment, with $66\,\mathrm{kHz}$ cantilevers, the closed-loop feedback bandwidth is approximately $b = 100\,\mathrm{Hz/deg.} \times [P\,\mathrm{deg.}]$.

6.3.2 Relay switch

To turn off the cantilever drive, we took the relay switch from the PSB B19 microscope. The switch is open when the relay voltage is $5\,\mathrm{V}$. The delay to close the switch is about $250\,\mathrm{\mu s}$. It is important to use a relay because an ordinary solid-state switch can have poor isolation at high frequencies; in the positive feedback circuit version 2 which I built, the ADG1402 switch ($40\,\mathrm{pF}$ capacitance) allowed 0.2 percent of the input signal through to the output at $60\,\mathrm{kHz}$. If you want to switch the drive signal faster than than the relay would allow, a low-capacitance switch, or another suggestion from Ref. 108 (see pages 175–181) could help.

6.3.3 Fiber-coupled visible light sources

To couple higher-intensity visible light to the sample, we bought blue and green fiber-coupled laser diodes (and, recently, red and IR). Driving the blue and green lasers requires a current source capable of supplying greater than 5 volts. From the PSB B19 microscope, we took the Thorlabs LDC202 current source (capable of supplying up to $200\,\mathrm{mA}$ of current at a voltage of up to $10\,\mathrm{V}$) and Thorlabs TED200C temperature controller. Using the modulation input of the LDC202, the laser can be turned on with a 1 to $5\,\mathrm{\mu s}$ risetime (see Fig. A.5).

To turn on the laser with a faster risetime, we use the RF modulation input of the Thorlabs LDM9LP laser diode mount. By applying the correct voltage profile to the RF modulation input, nanosecond risetime voltage pulses can be obtained. We use the newly acquired Keysight 33622A Waveform Generator ($120\,\mathrm{MHz}$, 2 channels) to apply the voltage profile. Currently, we only apply nanosecond duration voltage pulses to the laser with the RF modulation input, but it would be possible to output a longer duration pulse with a nanosecond risetime by simultaneously applying a voltage to the RF modulation input and the LDC202 external modulation input.

Photodetector

To measure the output power of the lasers with nanosecond time resolution, we purchased a high-speed photodetector (Thorlabs DET02AFC; $1\,\mathrm{GHz}$ bandwidth Si photodetector, wavelength range 400 to $1100\,\mathrm{nm}$). Currently, we measure the detector voltage drop through a $50\,\Omega$ terminating resistor on the $70\,\mathrm{MHz}$ bandwidth oscilloscope.

A $50\,\Omega$ terminating resistor makes it difficult to detect the laser power accurately below the laser threshold current. We consider an example to illustrate the point, using the notation from the DET200 manual. At a laser wavelength of $640\,\mathrm{nm}$, the photodetector responsivity is $\mathcal{R} = 0.36\,\mathrm{A/W}$. Below threshold, the laser output power may be $P = 10\,\mu\mathrm{W}$. The corresponding photodetector current is $I_{\mathrm{out}} = \mathcal{R}P = 3.6\,\mu\mathrm{A}$. Across an $R_{\mathrm{load}} = 50\,\Omega$ terminating resistor, the measured oscilloscope voltage $V_{\mathrm{out}} = I_{\mathrm{out}}R_{\mathrm{load}} = 180\,\mu\mathrm{V}$. This small voltage drop is very difficult to detect. To increase the measured voltage drop, there are two choices. We could increase the value of the load resistor R_{load}. Increasing R_{load} limits the photodetector bandwidth according to the equation

$$f_{\mathrm{BW}} = (2\pi R_{\mathrm{load}} C_{\mathrm{j}})^{-1} \tag{6.28}$$

with $C_{\mathrm{j}} = 1.73\,\mathrm{pF}$ the junction capacitance. If we increased R_{load} to $50\,\mathrm{kHz}$ so that the voltage $V_{\mathrm{out}} = 180\,\mathrm{mV}$, the bandwidth would be reduced to $f_{\mathrm{BW}} = 1.8\,\mathrm{MHz}$, corresponding to a risetime of $t_{\mathrm{r}} = 0.35/f_{\mathrm{BW}} = 190\,\mathrm{ns}$.

The alternative is to use an op-amp current-to-voltage converter (also called a transimpedance amplifier). In this case, the bandwidth is

$$f_{\mathrm{BW}} = \sqrt{\tfrac{1}{2}(\mathrm{GBP})(2\pi R_{\mathrm{f}} C_{\mathrm{D}})^{-1}} \tag{6.29}$$

where GBP is the operational amplifier's gain-bandwidth product, and C_{D} is the sum of the junction capacitance, op-amp input capacitance, and any other stray capacitances in the system. For the AD711, for example, $\mathrm{GBP} \approx 4\,\mathrm{MHz}$ at room temperature. The bandwidth of the current-to-voltage converter can be viewed as one-half the geometric mean of GBP and $(2\pi R_{\mathrm{f}} C_{\mathrm{D}})^{-1}$. It only makes sense to use an op-amp current-to-voltage converter if an amplifier with very high GBP can be designed. For most use cases in our group, it is probably better to just use a different terminating resistor. The current-to-voltage converter or transimpedance amplifier is called a photodiode amplifier or front-end amplifier, and is a very common design problem. See Ref. 109 (Chapter 18, "Front Ends", in the second edition, available online) or Ref. 108 Sec. 8.11 (pages 537–555).

6.4 Future Directions

On the perovskite samples studied by Tirmzi and coworkers in Ref. 33, scanning measurements of dissipation, local, and broadband dielectric spectroscopy could provide useful information about the spatial variation of electronic, ionic, or trapped charges.

For both the dielectric spectroscopy measurements and pk-EFM, it would be be very useful to modulate the tip charge at higher frequencies. On the Baker 146 microscope, it may be possible to do this by adding SMA connectors on an expanded microscope head, with a design similar to the Marohn group's MRFM probe [110]. On the organic semiconductor samples we have studied using pk-EFM, it would be useful to perform the array of dielectric spectroscopy and dissipation measurements we developed to probe the perovskite samples. In particular, both cantilever dissipation versus light intensity, and a more systematic analysis of the slow recovery of the photo-capacitance in the dark may be worthwhile.

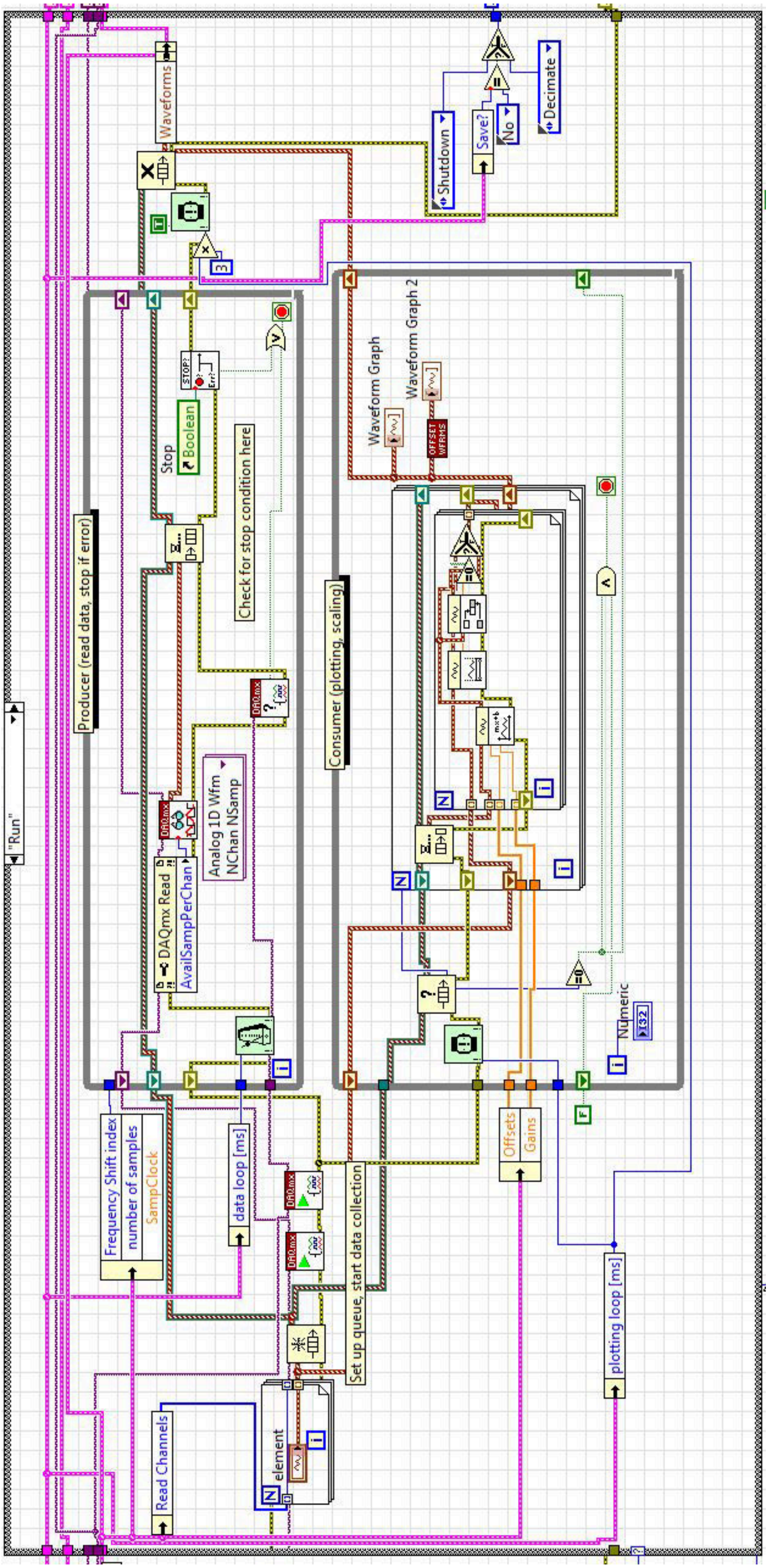

Figure 6.5: Producer-consumer design pattern.

Higher speed and resolution scanning would be another worthwhile goal, especially for studying perovskite samples, which have hundreds of nanometer domains that are ideal for spatially-resolved measurements. To these ends, it would be useful to buy a higher bandwidth photodetector that allowed the cantilever's first resonance frequency $f_{\mathrm{c}} \sim 75\,\mathrm{kHz}$ and second resonance frequency $f_1 \sim 500\,\mathrm{kHz}$ to be tracked simultaneously. The higher bandwidth photodetector would enhance the signal at the second resonance frequency by a factor of 16 and enable single pass FM-AFM and FM-KPFM measurements of sample topography, surface potential, and capacitance. Without upgrading the photodetector, it would be possible to perform simultaneous FM-AFM and FM-KPFM by using a slightly higher KPFM modulation frequency (perhaps $f_{\mathrm{m}} = 500\,\mathrm{Hz}$) and using the DC cantilever frequency shift for AFM. In either case, the DC frequency shift would be $\delta f = \delta f_{\mathrm{AFM}}(z) - f_{\mathrm{c}} C''(z) V_{\mathrm{m}}^2 / 8k_0$, where z is the tip's vertical displacement and the second term is the component of the electrical frequency shift mixed down to DC. Ideally the DC frequency shift would be $\delta f = \delta f_{\mathrm{AFM}}(z)$ only, so that a feedback loop with input δf and output z would sense only the tip-sample van der Waals force rather than the also being sensitive to the tip-sample capacitance. A better feedback signal could be obtained by adding the magnitude of the frequency shift component at $2f_{\mathrm{m}}$, which is equal to the magnitude of the component at DC. By adjusting the gain, we could correct for the frequency shift caused by the voltage modulation.

For every experiment, the detection noise limits our ability to perform high-speed, ultrafast measurements of surface potential, capacitance, and dissipation. Keeping the detection noise to a minimum is therefore paramount. The detection noise is related to the laser amplitude/phase noise, which could be minimized by designing a new cantilever holder with the fiber optic cable on a piezo so that the distance can be adjusted precisely to keep the interferometer "on-fringe" at a few micrometer displacement between the cantilever and fiber [111]. Alternatively, a more expensive laser could be purchased that would allow lower noise interferometric detection of the cantilever position at our current hundreds of micrometer operating distance.

To push pk-EFM to nanosecond time resolution, a laser capable of delivering significant energy in a nanosecond duration pulse would be useful, in addition to the higher bandwidth voltage modulation discussed above.

To enable a tighter feedback loop between data acquisition and analysis, it would be useful to integrate Python analysis more closely into the LabView workflow. In particular, a LabView interface to the `kpfm.lockin` module would be useful for KPFM, tr-EFM, and pk-EFM experiments [112]. For KPFM surface potential and capacitance measurements, the frequency shift components at f_{m} and $2f_{\mathrm{m}}$ could be obtained simultaneously. An integrated Python analysis would enable open-loop KPFM measurements along the lines proposed by Collins and co-workers [113]. The most significant advantage would be the ability to combine high modulation-frequency KPFM (perhaps at $f_{\mathrm{m}} = 5\,\mathrm{kHz}$) with time-domain signal averaging to obtain sample surface potential and capacitance with sub-millisecond resolution.

For pk-EFM and tr-EFM, the data of Fig. 2.4 show that tens of microsecond time resolution is possible with a few seconds of active data acquisition time ($10\,\mathrm{ms/pulse} \times 784\,\mathrm{pulses} = 7.84\,\mathrm{s}$). Even assuming that the other necessary delays and photocapacitance reset times would require ten times longer, the entire experiment could be performed in $90\,\mathrm{s}$, fast enough to repeat for a variety of tip voltages, light intensities, wavelengths, tip-sample separations, or even to perform a simple linescan. The problem is that it would quickly grow impractical to save and process all of the data; the raw, saved data from each experiment was 300 to 600 megabytes. The problem grows even worse when better time resolution is desired or the detector noise is worse. The experiments could be performed as quickly, and with similar small data storage requirements, as other scanned probe measurements if the data were signal-averaged and analyzed directly in LabView.

In both of these cases, the experiment, LabView and Python code would be designed to be a "scanned probe oscilloscope;" small effects could be precisely measured by aligning data in the time domain relative to the stimulus and triggering. In LabView, a producer-consumer loop would maximize efficiency, allowing data to be continuously collected and analyzed, so that useful plots could be shown in real-time in LabView, and the resulting measurements saved immediately to HDF5 for any further analysis, fitting or plotting in Python (Fig. 6.5).

As a step towards this goal, we have observed the cantilever oscillation with a lock-in amplifier (with fixed reference frequency $f_{\mathrm{ref}} \approx f_{\mathrm{c}}$) and digitized the down-converted signal. This approach, however, still detects the cantilever oscillation through the low-bandwidth ($b \leq 0.1 f_{\mathrm{c}} \sim 5\,\mathrm{kHz}$) lock-in amplifier, rather than retaining the full $1.25\,\mathrm{MHz}$ digitization bandwidth. The full bandwidth transient allows for simultaneous analysis of the change in DC displacement and any changes in the cantilever frequency and phase.

The group will also have to move to Python 3 eventually—support for Python 2 is scheduled to expire in 2020, and many packages are starting to move to Python-3-only development for future releases [114]. I think it would make sense for a new student in the group to start by using and learning Python 3. The `kpfm` package should be compatible with Python 3 and our existing analyses and code should work. The simplified matrix operations (matrix multiplication with `@`) and continuing updates and features in IPython and Jupyter probably make this worthwhile despite the initial pain.

APPENDIX A

PHASEKICK ELECTRIC FORCE MIROSCOPY

A.1 Weighted best fit intercept filter

We used a weighted least squares linear filter to estimate the phase of the cantilever at the start and end of the light pulse in the pk-EFM experiment. The idea is that the cantilever phase near the start or end of the pulse is well-described by the following equations:

$$\phi(t) = \begin{cases} \phi(0) + f(0)\,t & \text{for } t \leq 0 \qquad \text{(A.1a)} \\ \phi(t_{\mathrm{p}}) + f(t_{\mathrm{p}})\,t & \text{for } t \geq t_{\mathrm{p}} \qquad \text{(A.1b)} \end{cases}$$

with ϕ in units of cycles. Since fast dynamics may be occurring during the pulse time, we only use data from $t \leq 0$ to determine the starting phase $\phi(0)$ and only use data from $t \geq t_{\mathrm{p}}$ to determine the ending phase $\phi(t_{\mathrm{p}})$.

Both of these equations are of the form $y = \alpha + \beta x$. Values for the best-fit intercept α and best-fit slope β were obtained by implementing a weighted least-squares fit using a time-domain filter. For equally spaced x values, α and β can be obtained using a finite-impulse-response filter [115]. For N points, we take the x-coordinates equal to $0, 1, \ldots, N-1$. For weighted least squares, we can write the resulting coefficient vector $\boldsymbol{\beta} = (\alpha\,\beta)^T$ as

$$\boldsymbol{\beta} = (\boldsymbol{x}^T W \boldsymbol{x})^{-1}\, \boldsymbol{x}^T W \boldsymbol{y}, \tag{A.2}$$

where

$$\boldsymbol{x} = \begin{pmatrix} 1 & 0 \\ 1 & 1 \\ \vdots & \vdots \\ 1 & N-1 \end{pmatrix}, \quad W = \begin{pmatrix} w_0 & & & \\ & w_1 & & \\ & & \ddots & \\ & & & w_{N-1} \end{pmatrix} \tag{A.3}$$

and

$$\boldsymbol{y} = \begin{pmatrix} y_0 \\ y_1 \\ \vdots \\ y_{N-1} \end{pmatrix}. \tag{A.4}$$

Then we can write the matrix multiplication as sums,

$$\boldsymbol{\beta} = \begin{pmatrix} \sum_{k=0}^{N-1} w_k & \sum_{k=0}^{N-1} k\, w_k \\ \sum_{k=0}^{N-1} k\, w_k & \sum_{k=0}^{N-1} k^2\, w_k \end{pmatrix}^{-1} \begin{pmatrix} \sum_{k=0}^{N-1} w_k y_k \\ \sum_{k=0}^{N-1} k w_k y_k \end{pmatrix} \tag{A.5}$$

Call the sums in the left matrix $s_j = \sum_{k=0}^{N-1} k^j w_k$. Inverting the matrix, we have,

$$\boldsymbol{\beta} = \frac{1}{s_0 s_2 - s_1^2} \begin{pmatrix} s_2 & -s_1 \\ -s_1 & s_0 \end{pmatrix} \begin{pmatrix} \sum_{k=0}^{N-1} w_k y_k \\ \sum_{k=0}^{N-1} k\, w_k y_k \end{pmatrix} \tag{A.6}$$

$$\boldsymbol{\beta} = \frac{1}{s_0 s_2 - s_1^2} \left(\sum_{k=0}^{N-1} w_k (s_2 - s_1 k) y_k, \quad \sum_{k=0}^{N-1} w_k (s_0 k - s_1) y_k \right)^{\mathrm{T}}. \tag{A.7}$$

The slope's filter coefficients H_β and intercept's filter coefficients H_α are just the portion of the sum excluding y_k. The filter coefficients are thus

$$H_\alpha[k] = w_k \frac{(s_2 - s_1 k)}{s_0 s_2 - s_1^2} \text{ for } k = 0, \ldots N-1 \text{ and} \tag{A.8}$$

$$H_\beta[k] = w_k \frac{(s_0 k - s_1)}{s_0 s_2 - s_1^2} \text{ for } k = 0, \ldots N-1. \tag{A.9}$$

For our phase-difference filter we chose a time constant τ and used exponential weights $w_k = e^{-k/(f_\mathrm{s}\tau)}$ with $N = \mathrm{round}(5 f_\mathrm{s} \tau)$. Figure 2.7(D and E) show the phase-difference filter coefficients and response function. A different time constant was used to fit the $\phi(t \leq 0)$ and $\phi(t \leq t_\mathrm{p})$ data sets. Each time constant was chosen empirically, to maximize the signal-to-noise ratio.

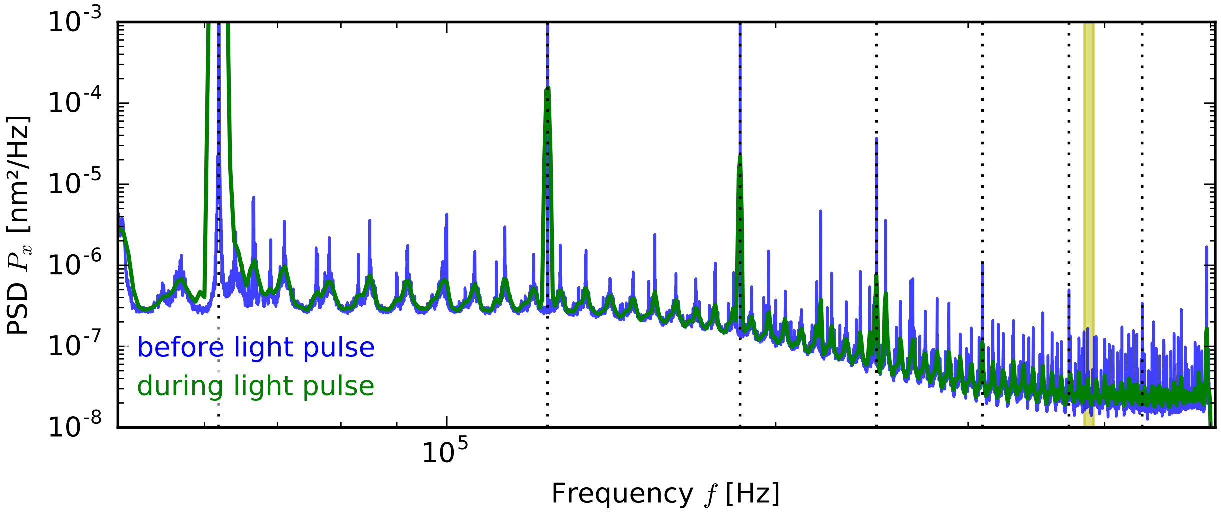

Figure A.1: **Cantilever position power spectral density during tr-EFM.** Power spectra calculated from signal-averaged $100\,\mathrm{kW\,m^{-2}}$ tr-EFM position *vs.* time data ($N = 784$, see data in Fig. 2.4 and 2.12E). The *before light pulse* curve (blue) uses data from $t = -50\,\mathrm{ms}$ to 0. The *during light pulse* curve (green) uses data from $t = 0$ to $1.75\,\mathrm{ms}$. The dotted lines show the harmonics of the cantilever's first resonance frequency ($f_0 = 62\,000\,\mathrm{Hz}$). The shaded yellow region shows where the cantilever's second resonance frequency would be ($f_{\mathrm{res.}}^{\mathrm{2nd}} = 6.27 f_0$, from Euler-Bernoulli beam theory). Both spectral densities were calculated using a Blackman window. Experimental parameters: PFB:F8BT on ITO, $h = 250\,\mathrm{nm}$, and $V_{\mathrm{t}} = 10\,\mathrm{V}$. Adapted from Ref. 34, licensed under https://creativecommons.org/licenses/by-nc/4.0/.

A.2 Higher cantilever eigenmodes

Figure A.1 shows that even at the highest light intensity, we do not excite higher cantilever resonances. The peaks at harmonics of the cantilever's first resonance frequency appear because we detect motion with an interferometer, so we detect $\delta x_{\mathrm{meas}}(t) \propto V_{\mathrm{photodetector}} \propto \sin\left(4\pi[x_0 + \delta x(t)]/\lambda\right)$, where x_0 is the distance between the fiber and cantilever with no drive or tip-sample voltage, δx is the cantilever's displacement, and $\lambda = 1488\,\mathrm{nm}$ is the interferometer wavelength. The sine term gives rise to odd harmonics of the cantilever frequency in the position spectrum ($\sin x = x - x^3/3! + x^5/5! + \ldots$). Since $4\pi x_0/\lambda$ is not exactly a multiple of π, there is also a small cosine term which gives rise to even harmonics of the cantilever frequency. The roll-off of the measured displacement noise is caused by

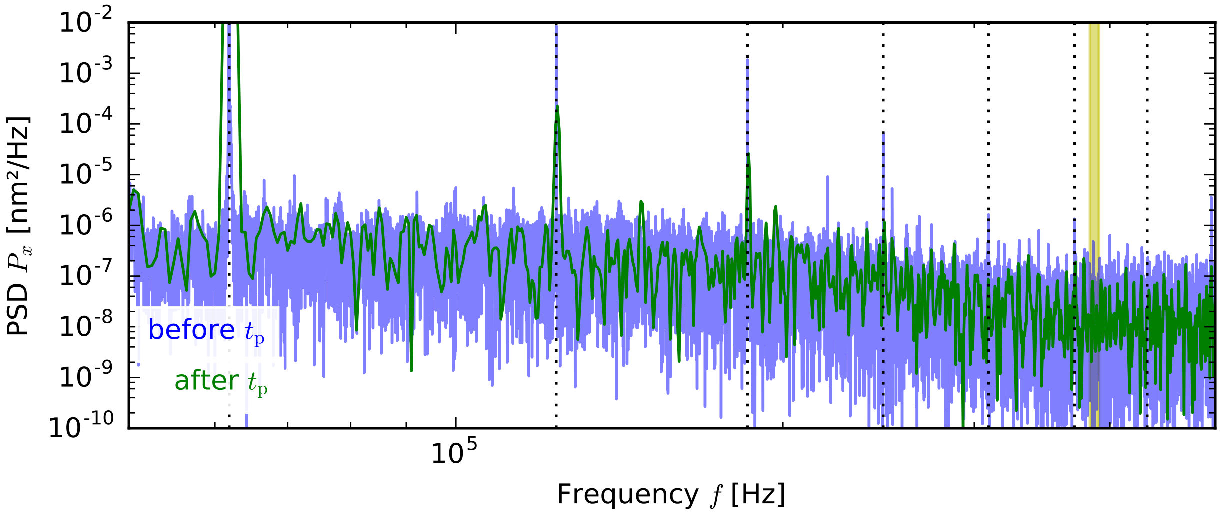

Figure A.2: **Cantilever position power spectral density during pk-EFM.** Power spectral density calculated from the $20\,\mathrm{kW\,m^{-2}}$ pk-EFM position *vs*. time data (see data in Fig. 2.4 and 2.12I). The power spectral density was calculated from the shortest pulse time dataset ($t_\mathrm{p} = 0.8\,\mathrm{\mu s}$). The *before* t_p curve (blue) uses data from $t = -50\,\mathrm{ms}$ to $t_\mathrm{p} = 0.8\,\mathrm{\mu s}$. The *after* t_p curve (green) uses data from $t = t_\mathrm{p} = 0.8\,\mathrm{\mu s}$ to $t_\mathrm{p} + 2\,\mathrm{ms} = 2.0008\,\mathrm{ms}$, when the cantilever could conceivably be excited at a higher resonance mode. The dotted lines show the harmonics of the cantilever's first resonance frequency $f_0 = 62\,000\,\mathrm{Hz}$. The shaded yellow region shows where the cantilever's second resonance frequency would be ($f_\mathrm{res.}^\mathrm{2nd} = 6.27 f_0$, from Euler-Bernoulli beam theory). Both spectral densities were calculated using a Blackman window. Experimental parameters: PFB:F8BT on ITO, $h = 250\,\mathrm{nm}$, and $V_\mathrm{t} = 10\,\mathrm{V}$. Adapted from Ref. 34, licensed under https://creativecommons.org/licenses/by-nc/4.0/.

our photodetector's $200\,\mathrm{kHz}$ bandwidth.

The voltage step at the end of the light pulse does not excite the cantilever's higher resonance modes either, as shown in Figure A.2. We also see no evidence that the cantilever's higher resonance modes are appreciably excited by the 50 to $800\,\mathrm{ns}$ voltage pulses applied during the experiments of Figure 2.6A–F. Even if higher resonance modes were excited a small amount, the digital lock-in amplifier filters used in the data workup strongly reject frequencies more than a few kilohertz from the cantilever's first resonance frequency. Figure 2.9 shows that $10\,\mathrm{kHz}$ away from the cantilever resonance frequency, the lock-in amplifier filter transfer function's magnitude response is $-120\,\mathrm{dB} = 10^{-6}$.

A.3 Photothermal effects

The sample is a thin PFB:F8BT layer ($\sim 100\,\mathrm{nm}$) on a thin indium tin oxide (ITO) layer ($\sim 700\,\mathrm{nm}$) on a thick glass substrate ($1.1\,\mathrm{mm}$). An upper limit for the temperature change ΔT is obtained by neglecting the relatively high thermal conductivity ITO layer and assuming that all of the incident light is absorbed in the PFB:F8BT layer. We assume the PFB:F8BT layer can be approximated as constant temperature, and solve for the steady-state temperature increase by considering the diffusion of heat into the glass substrate, which we treat as semi-infinite. Cahill gives the steady-state temperature increase in Equation 11 of Ref. 116:

$$\Delta T_0 = \frac{P_{h\nu}}{2\sqrt{\pi} w_0 \Lambda}. \tag{A.10}$$

At the highest light intensity ($I_{h\nu} = 100\,\mathrm{kW\,m^{-2}}$), the laser power $P_{h\nu} = 3\,\mathrm{mW}$. At the sample surface, the beam shape is elliptical with $330\,\mathrm{\mu m}$ and $120\,\mathrm{\mu m}$ major and minor axes (diameters). We approximate the beam radius w_0 by considering a circular beam of equivalent area: $w_0 = \sqrt{120\,\mathrm{\mu m} \times 330\,\mathrm{\mu m}/4} = 100\,\mathrm{\mu m}$. We take the thermal conductivity Λ of the glass substrate to be $1.0\,\mathrm{W\,m^{-1}\,K^{-1}}$. In this case, the DC temperature rise $\Delta T_0 = 8.5\,\mathrm{K}$. This analysis is broadly consistent with the calculation performed by Luria and coworkers in Supplementary Note 5 of Ref. 117.

Even this temperature change is small, given the large tip-sample separation ($h = 250\,\mathrm{nm}$). The temperature change for our $1.5\,\mathrm{ms}$ and shorter light pulses is even smaller. The frequency ω_{heat} at which the system reaches the steady-steady temperature calculated above is

$$\omega_{\mathrm{heat}} = \frac{\Lambda}{\pi w_0^2 \, C_{\mathrm{P}} \, \rho}, \tag{A.11}$$

where $C_{\mathrm{P}} = 840\,\mathrm{J\,kg^{-1}\,K}$ and $\rho = 840\,\mathrm{kg\,m^{-3}}$ are the specific heat capacity and density of the glass substrate respectively. The corresponding timescale is $\omega_{\mathrm{heat}}^{-1} = 20\,\mathrm{ms}$, significantly longer than the pulse time $t_{\mathrm{p}} \sim 1\,\mathrm{ms}$. The temperature change in this limit is given

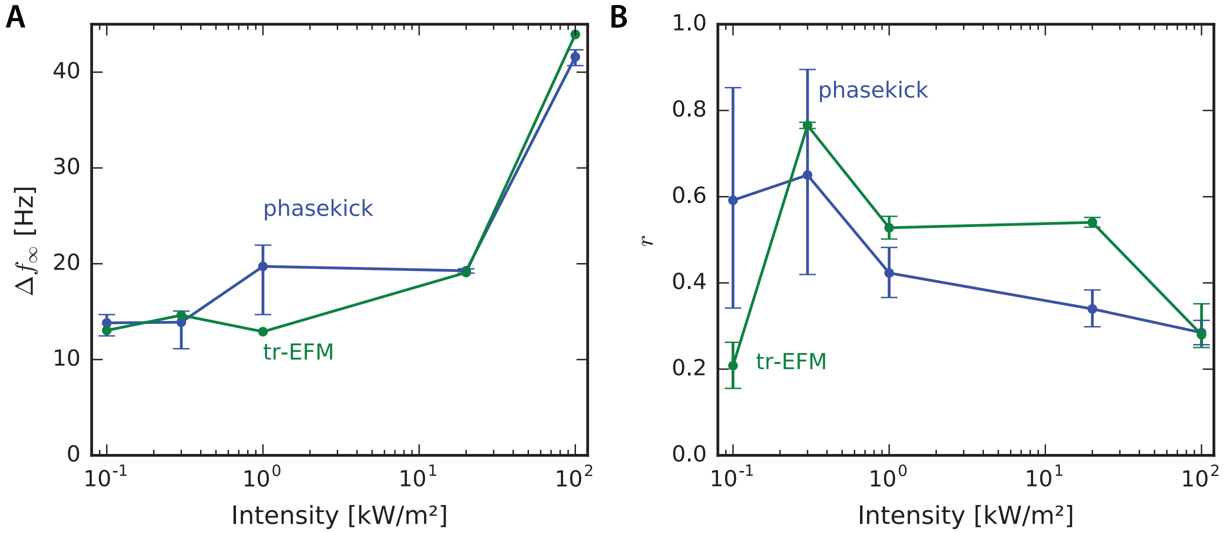

Figure A.3: **Additional comparison of pk-EFM and tr-EFM steady-state photocapacitance** (PFB:F8BT on ITO, $h = 250\,\mathrm{nm}$). (**A**) Steady state photocapacitance *versus* light intensity. (**B**) Fraction of the total steady state capacitance associated with the faster time constant. See time constants τ_1 and τ_2 in Fig. 2.4D. Adapted from Ref. 34, licensed under https://creativecommons.org/licenses/by-nc/4.0/.

by Cahill's Eq. 13:

$$\Delta T = \frac{P_{h\nu}}{\pi w_0^2 \sqrt{\omega \Lambda\, C_{\mathrm{P}}\, \rho}}. \tag{A.12}$$

Evaluating this equation at $\omega = (1.5\,\mathrm{ms})^{-1}$, we find a temperature change of only $2.1\,\mathrm{K}$.

A.4 Numerical simulations

The numerical simulations shown in Fig. 2.6D were performed for the following system of ordinary differential equations:

$$\dot{x} = v \tag{A.13}$$

$$\dot{v} = -\omega_0^2 x - \frac{\omega_0}{Q} v + \frac{C_\mathrm{t}'}{2mC_\mathrm{t}^2}(1+\alpha_{h\nu})q_\mathrm{t}^2 + \frac{C_\mathrm{t}''}{2mC_\mathrm{t}^2}(1+\alpha_{h\nu})x q_\mathrm{t}^2 + \frac{F_\mathrm{n}(t)}{m} \tag{A.14}$$

$$\dot{q}_\mathrm{t} = \frac{-q_\mathrm{t}}{R_\mathrm{t}} C^{-1}(x) + \frac{1}{R_\mathrm{t} C_1} q_1 \tag{A.15}$$

$$\dot{q}_1 = \frac{q_\mathrm{t}}{R_\mathrm{t}} C^{-1}(x) - \left(\frac{1}{C_1 R_1} + \frac{1}{R_\mathrm{t} C_1}\right) q_1 - \frac{\phi}{R_1} + \frac{V_\mathrm{t}(t)}{R_1} \tag{A.16}$$

$$\dot{\alpha}_{h\nu} = -\frac{1}{\tau_\mathrm{s}} \alpha_{h\nu} + \frac{I_{h\nu}(t)}{\tau_\mathrm{s}} \tag{A.17}$$

$$\dot{\phi} = \phi_\mathrm{n}(t). \tag{A.18}$$

The state vector variables were cantilever displacement x, cantilever velocity v, cantilever tip charge q_t, cabling charge q_1, fractional change in photocapacitance $\alpha_{h\nu}$, and surface potential ϕ. The cantilever parameters were mass $m = 46\,\mathrm{ng}$, spring constant $k_0 = 7\,\mathrm{N/m}$, resonance frequency $\omega_0 = \sqrt{k_0/m} = 2\pi \times 62\,\mathrm{kHz}$ and quality factor $Q = 2.7 \times 10^4$. In writing these equations the tip-sample capacitance $C(x)$ was linearized as follows:

$$C(x) = C_\mathrm{t} + C_\mathrm{t}'(1+\alpha_{h\nu})x + \frac{1}{2} C_\mathrm{t}''(1+\alpha_{h\nu})x^2 \tag{A.19}$$

$$C^{-1}(x) = C_\mathrm{t}^{-1} + \frac{C_\mathrm{t}'(1+\alpha_{h\nu})x}{C_\mathrm{t}^2} + \frac{C_\mathrm{t}''(1+\alpha_{h\nu})x^2}{2C_\mathrm{t}^2}. \tag{A.20}$$

The linearized tip-sample capacitance and its derivatives were $C_\mathrm{t} = 0.01\,\mathrm{pF}$, $C_\mathrm{t}' = 1.14 \times 10^{-4}$ pF µm^{-1}, and $C_\mathrm{t}'' = 6.72 \times 10^{-4}\,$pF µm^{-2}. The other circuit elements were the tip resistance $R_\mathrm{t} = 100\,\Omega$, cabling resistance $R_1 = 3\,\Omega$, cabling capacitance $C_1 = 10\,\mathrm{pF}$, and the input tip voltage $V_\mathrm{t}(t)$ ($10\,\mathrm{V}$ during the pulse, as in Fig. 2.2). The light "intensity" was $I_{h\nu} = 0.4$ for $t > 0$, corresponding to a total change in capacitance of 40 percent for $t \gg \tau_\mathrm{s}$. Simulations were performed for photocapacitance risetimes $\tau_\mathrm{s} = 2\,\mathrm{ns}$, $10\,\mathrm{ns}$ and $50\,\mathrm{ns}$.

The inputs $F_\mathrm{n}(t)$ and $\phi_\mathrm{n}(t)$ account for thermal and surface-potential noise. Both noise terms are approximated using a piecewise function with Gaussian, randomly distributed values. The force noise function $F_\mathrm{n}(t)$ takes a new random value every $\Delta t_\mathrm{F} = 16\,\mathrm{ps}$. The surface potential noise function $\phi_\mathrm{n}(t)$ takes a new random value every $\Delta t_\phi = 10\,\mathrm{\mu s}$. The variance of the Gaussian random numbers used to mimic the force noise was

$$\sigma_{F_\mathrm{n}}^2 = \frac{k_0 k_\mathrm{B} T}{\pi Q f_0 \Delta t_\mathrm{F}}$$

with $T = 293\,\mathrm{K}$ the temperature and $f_0 = 62\,\mathrm{kHz}$ the cantilever frequency. The standard deviation of the potential fluctuations was taken to be $\sigma_\phi = 10\,\mathrm{\mu V}\,\mathrm{\mu s}^{-1}$. The experimental power spectral density of cantilever frequency fluctuations had a $1/f$ character at low offset frequency f. Such $1/f$ noise is difficult to implement in a numerical simulation. The slowly varying potential produced low-frequency f_c noise having a $P_{\delta f_\mathrm{c}} \propto 1/f^2$ power spectrum and a variance approximately equal to that of the low-frequency f_c fluctuations seen experimentally (Fig. 2.10).

Simulations were performed with the Julia language package ODE, using a variable time step, stiff solver to handle the wide range of timescales present in the system.

A.5 Cantilever characterization

Figure A.4 shows the power spectral density of cantilever position fluctuations. The extracted parameters are the cantilever frequency $f_0 = 61999.54 \pm 0.03\,\mathrm{Hz}$, cantilever spring constant $k_0 = 6.9 \pm 0.2\,\mathrm{N\,m^{-1}}$, quality factor $Q = 28000 \pm 1000$, and detector noise floor $P_\mathrm{det} = 0.237 \pm 0.002\,\mathrm{pm^2\,Hz^{-1}}$.

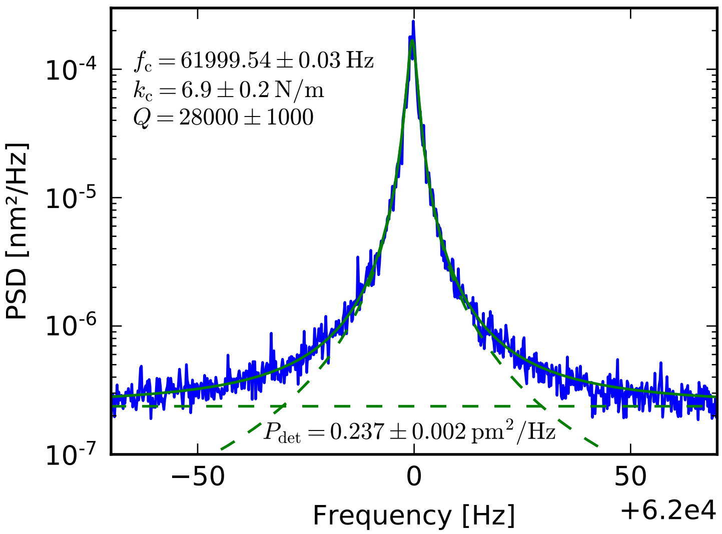

Figure A.4: **Power spectral density of cantilever thermomechanical position fluctuations**. The displayed data was calculated by signal-averaging 32 power spectra each calculated from $5\,\mathrm{s}$ of interferometer displacement data (sampling rate $1\,\mathrm{MHz}$). Adapted from Ref. 34, licensed under https://creativecommons.org/licenses/by-nc/4.0/.

A.6 Experimental timing

The start of the light pulse was triggered at a consistent point in the cantilever oscillation, and step changes to the cantilever tip voltage and drive signal were also precisely timed [30]. The circuit and instruments used to control this timing are shown in Fig. A.6. The photodetector output (upper left) was the cantilever displacement signal. The PLLPro2 generated the cantilever drive voltage and also output a $1\,\mathrm{V}$, phase-shifted sine wave copy of the cantilever oscillation, generated by an internal lock-in amplifier coupled to the phase-locked loop (Arb. ϕ out on diagram). A homebuilt gated cantilever clock circuit converted this $1\,\mathrm{V}$ phase-shifted sine wave to a square wave, which was used as a clock for timing tip voltage and light pulses. A $5\,\mathrm{V}$ digital signal output by the National Instruments PCI-6259 gates the clock, controlling the start of the experiment.

The BNC565 was used to trigger all signals relative to the cantilever clock. The $50\,\mathrm{ms}$

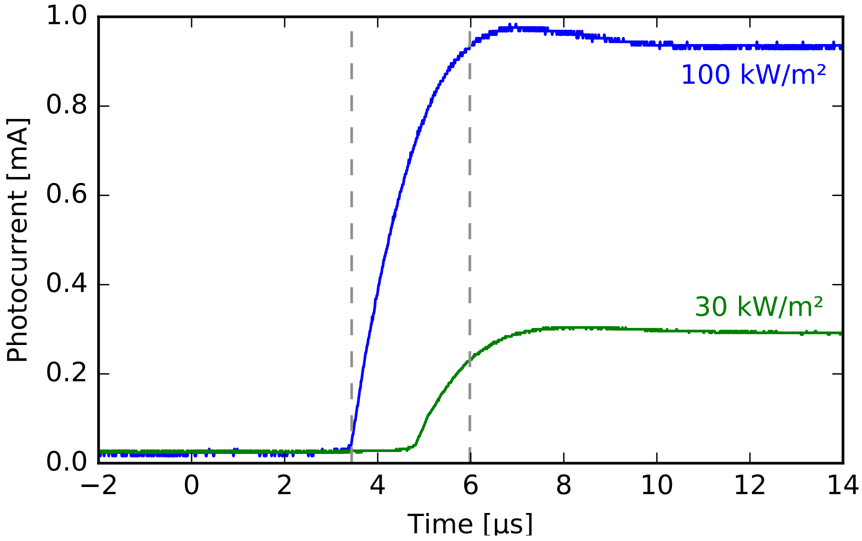

Figure A.5: **Photocurrent delay and risetime**. At $t = 0$, the voltage pulse which controls the light intensity is sent from the BNC565 digital delay generator to the LDC202 external modulation input that controls the laser current (see Figure A.6). The curves show the delay and risetime of the $405\,\mathrm{nm}$ laser, which is mainly limited by the $200\,\mathrm{kHz}$ bandwidth of the LDC202. The gray lines indicate the 0 to 100 percent risetime at $100\,\mathrm{kW\,m^{-2}}$ intensity. At these light intensities, the delay is less than $5\,\mathrm{\mu s}$ and the risetime less than $3\,\mathrm{\mu s}$. Adapted from Ref. 34, licensed under https://creativecommons.org/licenses/by-nc/4.0/.

delay between the setting of the cantilever tip voltage to $10\,\mathrm{V}$ and the start of the light pulse was coded as an $N = 3100\,\mathrm{cyc}$ delay in the BNC565. The pulse lengths, times, and adjustable voltage output levels (for the tip-sample voltage, visible light laser external modulation input) for the BNC565 were programmed using GPIB in LabView.

The gated cantilever clock circuit used an AD790 comparator, with $55\,\mathrm{mV}$ of hysteresis added to prevent unwanted oscillations, to convert the sine wave to a square wave clock signal. The square wave was input to the latch enable pin ($\overline{\mathrm{LE}}$) of a transparent D-type latch (CD74HC563E) and a NOR gate (CD4001BE). The output ($\overline{\mathrm{Q}}$) is transparent to the input when the latch enable is high. The digital PCI-6259 signal was sent to a data pin of the latch. The latch prevented a partial pulse (not phase locked to the cantilever oscillation) from being triggered when the PCI-6259 output went high while the cantilever clock

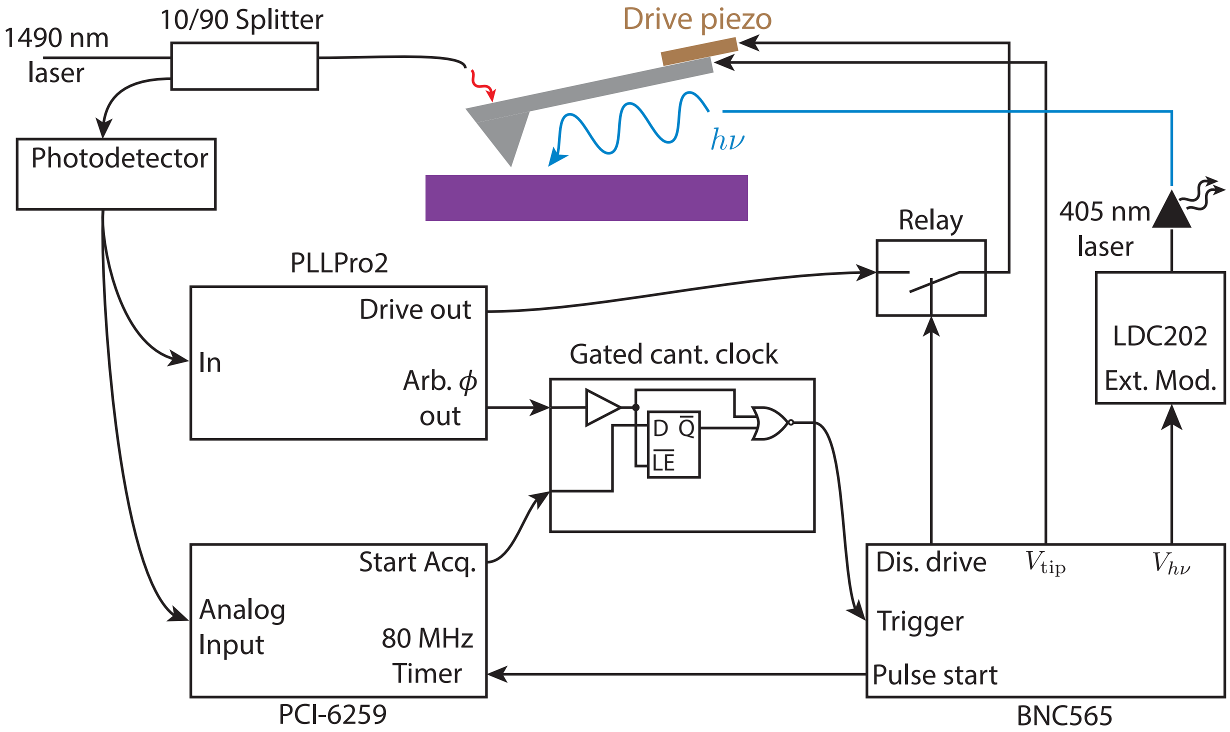

Figure A.6: **Block diagram showing the experimental setup and timing circuitry**. Adapted from Ref. 34, licensed under https://creativecommons.org/licenses/by-nc/4.0/.

was also high.

To verify that the measured photocapacitance risetimes were caused by the sample, and were not an artifact, we measured or estimated the risetimes of the laser and the cabling carrying voltage to the cantilever tip. The laser risetime, with the same settings used in the experiment, was verified using a high-speed photodetector (Thorlabs DET02AFC) and measuring the detector voltage drop through a $50\,\Omega$ terminating resistor on a $70\,\mathrm{MHz}$ bandwidth oscilloscope. The results for 30 and $100\,\mathrm{kW\,m^{-2}}$ estimated intensity are shown in Fig. A.5. The risetime was $< 3\,\mathrm{\mu s}$, consistent with the current source's stated $200\,\mathrm{kHz}$ bandwidth, and much faster than the $40\,\mathrm{\mu s}$ (and slower) risetimes observed in the sample.

The tip charge risetime was more difficult to measure independently. The applied voltage traveled through $3.5\,\mathrm{m}$ of 19-wire cable and $2\,\mathrm{m}$ of 36 AWG wire before reaching the cantilever tip. The total tip voltage cabling capacitance was $\sim 1.3\,\mathrm{nF}$. The BNC565 pulse generator had a current drive ability of $120\,\mathrm{mA}$ and a $50\,\Omega$ output impedance. The output impedance and the cabling capacitor form a low-pass filter with an estimated cutoff frequency of $2.4\,\mathrm{MHz}$ and the BNC565 current drive capability limited slew rates to $90\,\mathrm{V}\,\mu\mathrm{s}^{-1}$. By applying short duration tip voltages to the cantilever (Fig. 2.6D), we determined a tip charge risetime of $35\,\mathrm{ns}$.

A.7 Curve fitting using PyStan

20,000 posterior samples were used for analysis. These samples were generated as 4 independent chains of 5000 samples each. The potential chain reduction statistic (< 1.01 for all parameters) and trace plots (Fig. A.7) were used to discern convergence [118]. Kernel density estimates were calculated using seaborn [119].

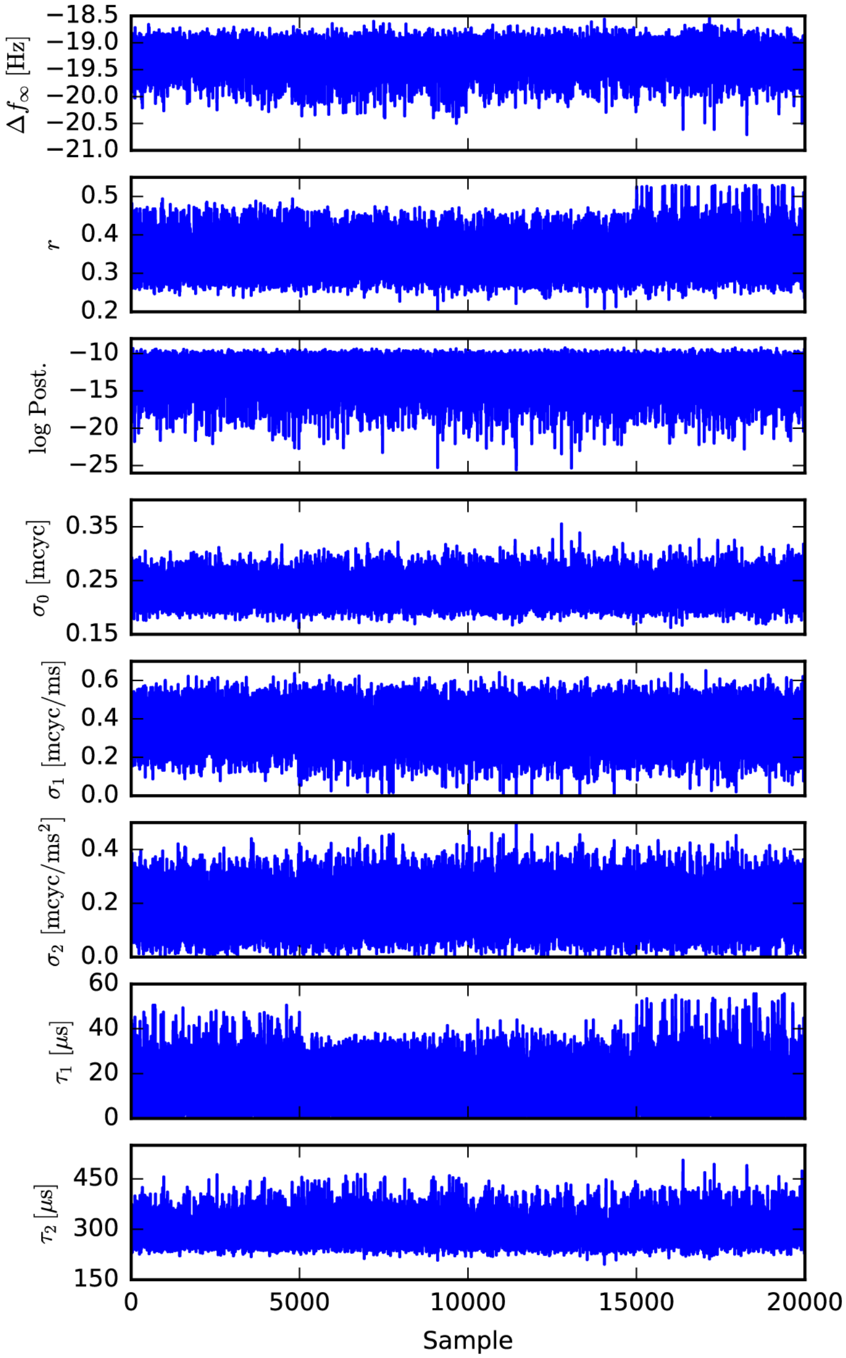

Figure A.7: **PySton sampling traces**. Traces showing parameter values for PyStan samples of posterior distributions from the $20\,\mathrm{kW\,m^{-2}}$ pk-EFM dataset. Samples from each chain (4 of 5000 samples each) are arranged sequentially. Adapted from Ref. 34, licensed under https://creativecommons.org/licenses/by-nc/4.0/.

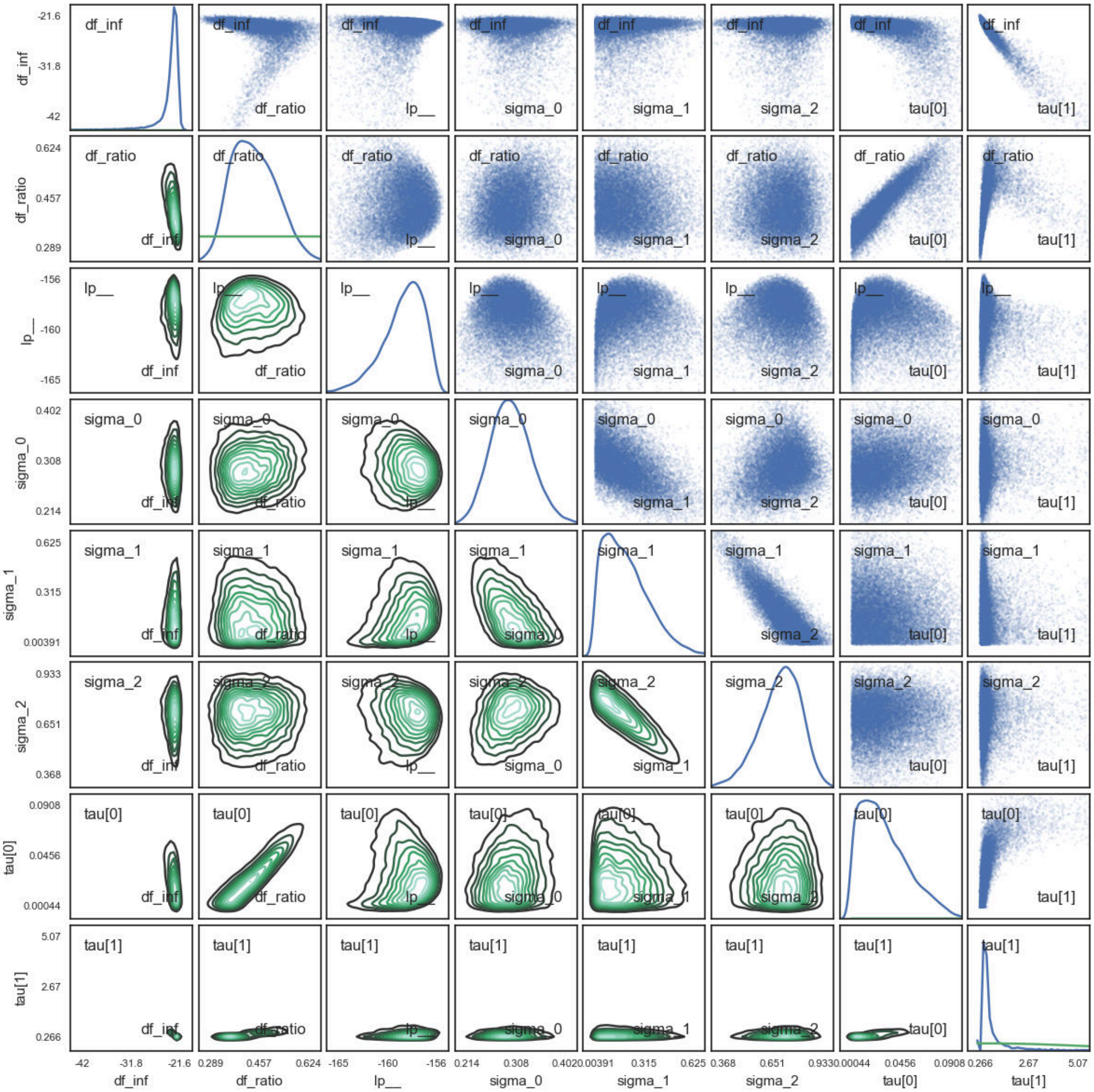

Figure A.8: **pk-EFM posterior distribution samples**. Pair plots illustrating the posterior distribution and correlations between parameters from the $20\,\mathrm{kW\,m^{-2}}$ pk-EFM dataset, estimated using $N = 20000$ samples. On the diagonal, a kernel density estimator (blue) shows the posterior distribution along with prior distribution (green). Parameter correlations are shown by plotting the samples (above diagonal) and using a 2D kernel-density estimator (below diagonal). The time constant τ is in units of milliseconds. Adapted from Ref. 34, licensed under https://creativecommons.org/licenses/by-nc/4.0/.

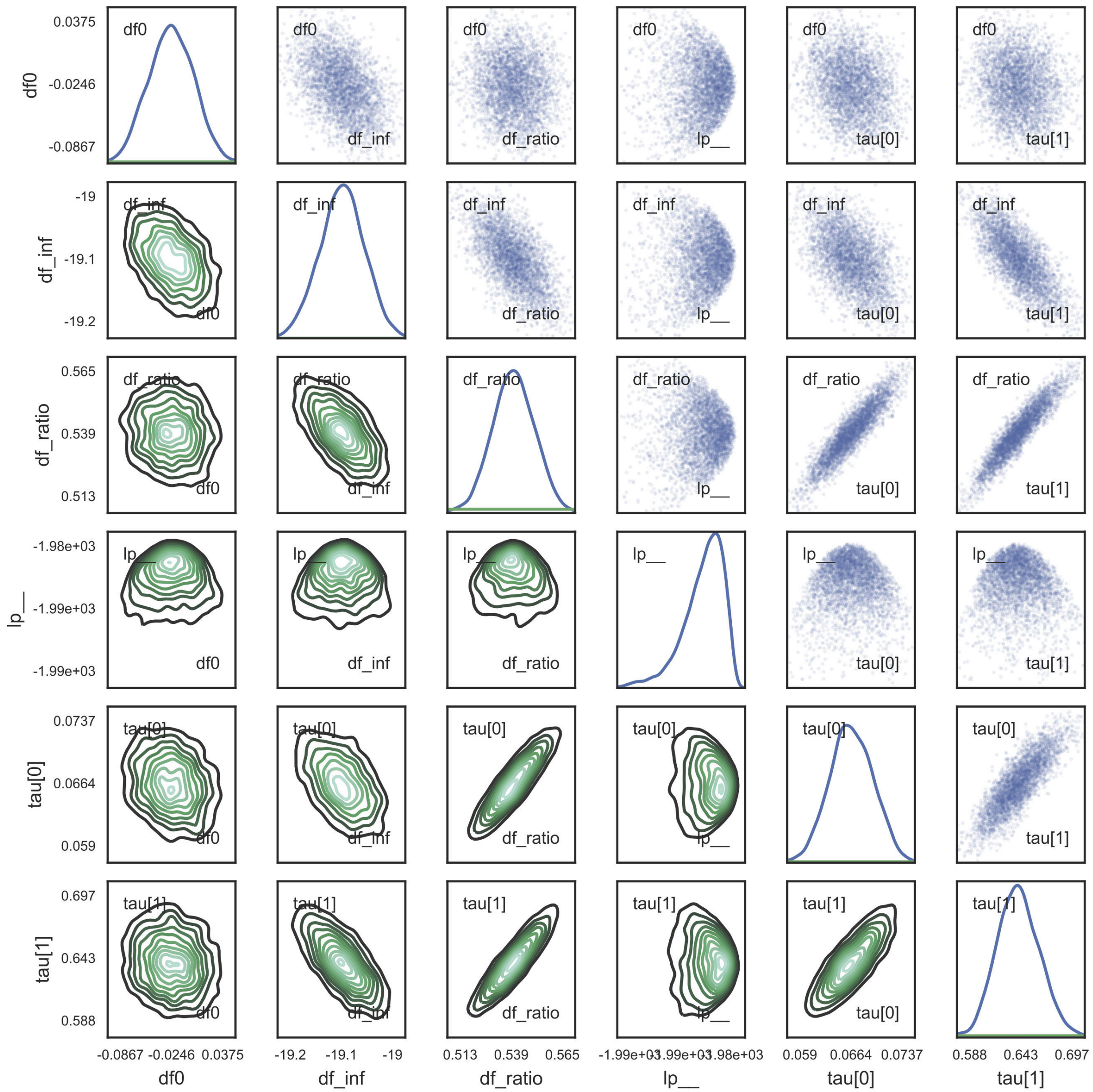

Figure A.9: **tr-EFM posterior distribution samples**. Pair plots illustrating the posterior distribution and correlations between parameters from the $20\,\mathrm{kW\,m^{-2}}$ tr-EFM dataset, estimated using $N = 6000$ samples. On the diagonal, a kernel density estimator (blue) shows the posterior distribution along with prior distribution (green). Parameter correlations are shown by plotting the samples (above diagonal) and using a 2D kernel-density estimator (below diagonal). The time constant τ is in units of milliseconds. Adapted from Ref. 34, licensed under https://creativecommons.org/licenses/by-nc/4.0/.

APPENDIX B

EXPERIMENTAL IMPLEMENTATION OF PHOTOCAPACITANCE MEASUREMENTS

This appendix explains the experimental circuits, code, and data analysis used to perform pk-EFM. Currently we have two related experimental setups for performing photocapacitance experiments. The two setups differ in how voltage pulses are sent to the cantilever tip and laser modulation input. The "DAQ" experimental setup uses the NI-6259 analog outputs and the "BNC" experimental setup uses the BNC565 (borrowed from the PSB B19 MRFM microscope).

B.1 Custom triggering circuit

Fig. B.1 shows the custom triggering circuit. The circuit takes two inputs, "clock" and "enable," and produces two outputs, "synchronized enable" and "BNC gate." The DAQ experimental setup uses the "synchronized enable" output and the BNC experimental setup uses the "BNC gate" output. On the diagram, the clock input signal (center wire) is labeled `CLK+`, and the clock input ground is labeled `CLK-`. The "clock" input should be a sine wave corresponding to the cantilever signal (or whatever other signal is being synchronized; a lock-in amplifier output, for example). The synchronized enable input goes high on the **negative to positive transition** of the clock sine wave. The BNC gate goes high on the **positive to negative transition** of the clock sine wave. Chapter 10 of Ref. 108 contains an introduction to digital logic that is useful background for the logic integrated circuits used here.

The comparator circuit converts the clock sine wave into a square wave (Fig. B.1a; integrated circuit U1). The bypass capacitors (C_{10} and C_{11}) and latch resistor ($R_{10} = 510\,\Omega$)

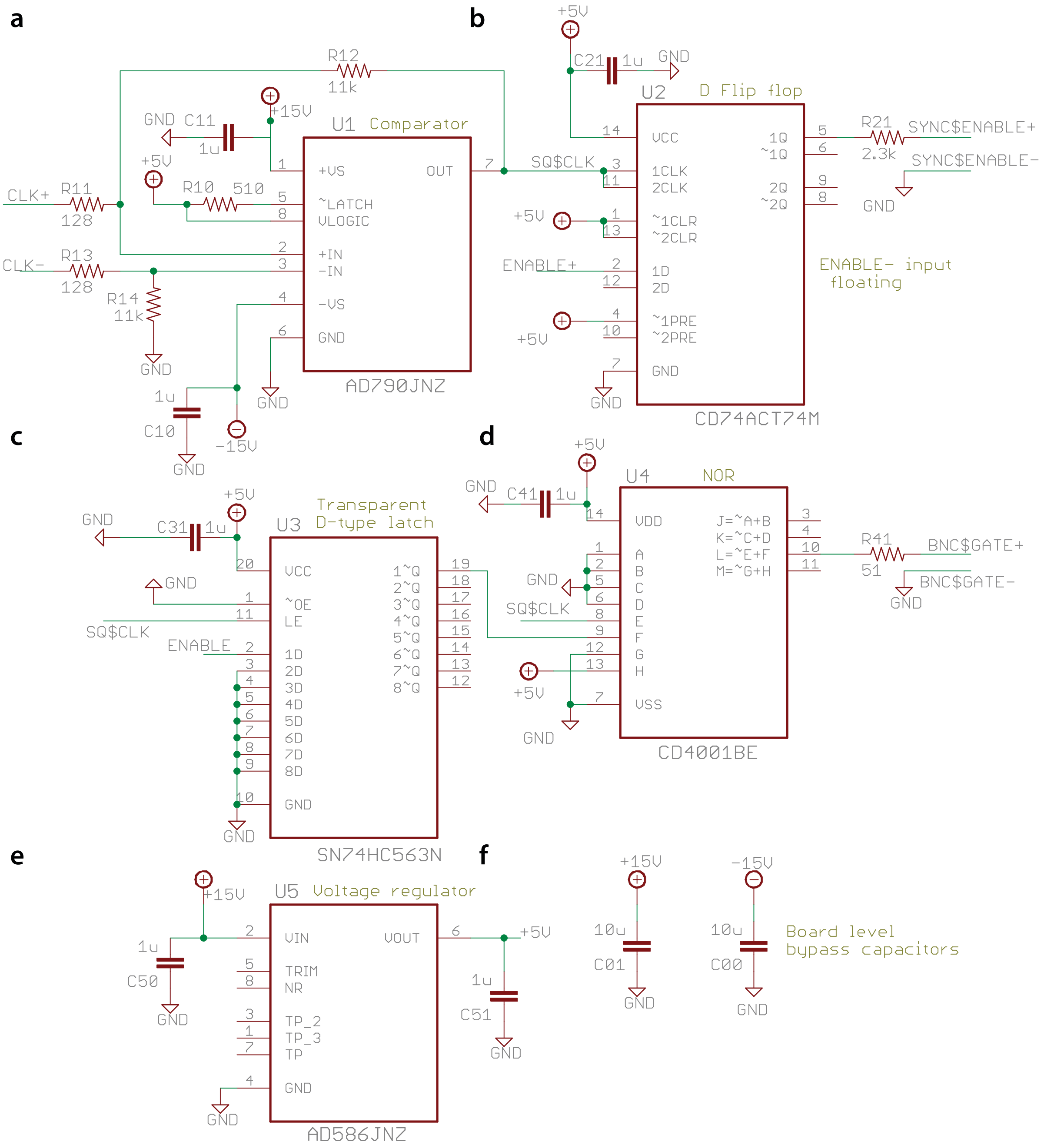

Figure B.1: Custom triggering circuit diagram.

are used as recommended on the AD790 datasheet. The clock input signal is compared to the clock input ground. The resistors R_{11} and R_{12} add $\Delta V = 55\,\mathrm{mV}$ of hysteresis was added as $\Delta V = R_{11} \times 5\,\mathrm{V}/R_{12}$. The added hysteresis prevents noise-induced switching of the comparator at high frequencies. The resistor R_{14} ensures that there is a DC path from the clock ground to the circuit ground. Upon further consideration, it may be better to remove R_{13} and replace R_{14} with a low-value resistor, perhaps 10 to $100\,\Omega$. For reference see Ref. 108 section 8.16.3.B (page 583). The square wave output of the comparator is labeled `SQ$CLK`.

We use a type-D flip flop to generate the synchronized enable signal (Fig. B.1b; U2). The flip flop is a one-bit memory. At the rising edge of the clock, the output `1Q` is set equal to the data `1D`. The output stays the same until the next clock rising edge. In this way, the flip flop synchronizes the enable signal from the DAQ to the cantilever clock.

In implementing the circuit, the output resistor R_{21} was added to prevent oscillations of the output. The enable signal from the DAQ was the data input (`ENABLE+`). The enable ground was left floating, although it would probably be better to tie `ENABLE-` to ground with a $10\,\Omega$ resistor at the circuit's ground point.

To produce the BNC gate signal, we use a transparent D-type latch and a NOR gate (Fig. B.1(c,d); U3 and U4). Before the beginning of the experiment, the latch enable input is low ($0\,\mathrm{V}$). The latch output $\overline{Q}_1$ or `1~Q` is high—note that bars (or tildes in the EAGLE diagram) indicate the not operation. The output of the NOR circuit is low because at least one input is high. When the enable signal goes high, the gated cantilever clock should go high on the next rising edge of the square wave clock. If the square wave clock is high when the enable input goes from low to high, the output $\overline{Q}_1$ immediately goes low. The output of the NOR gate remains low because the square wave clock—the other input to the NOR gate—is high. The output of the NOR gate goes high when the square wave

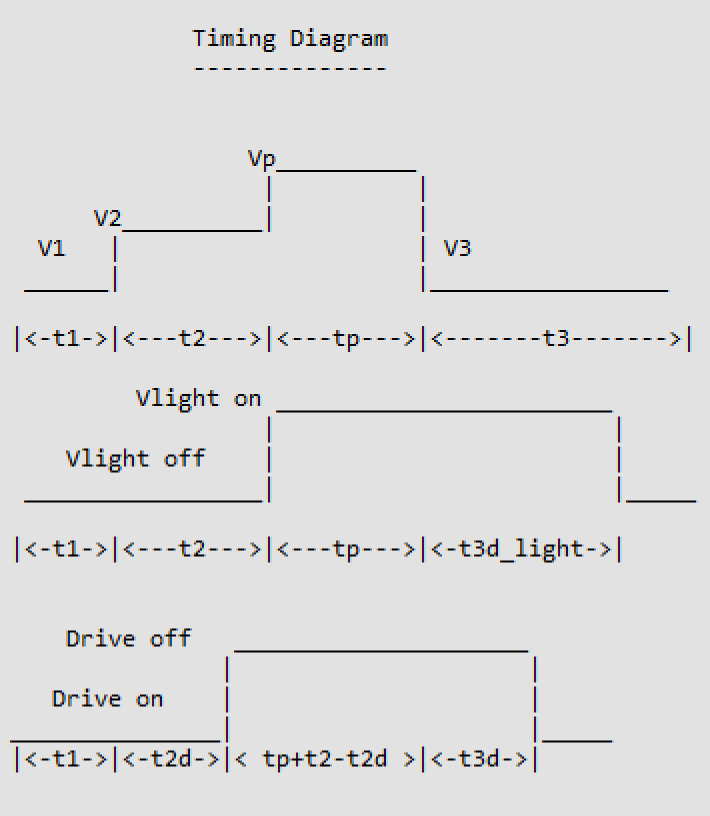

Figure B.2: Adiabatic timing diagram.

clock goes low. If the square wave clock is low when the enable input goes from low to high, the latch is disabled and the output $\overline{Q}_1$ stays high until the square wave clock goes high. The NOR gate will go high when the square wave clock goes from high to low. The resistor $R_{41} = 51\,\Omega$ was added to prevent oscillations of the output.

Figure B.1(e,f) show the voltage regulator and board-level bypass capacitors. The voltage regulator produces the $5\,\mathrm{V}$ supply voltage (labeled `+5V` on the diagram) used for the digital logic.

B.2 DAQ experimental setup

The custom triggering circuit phase-locks the beginning of the light and/or voltage pulses to a specific point in the cantilever cycle (or a specific point in some alternative modulation). The timing diagram of Fig. B.2 shows how the different LabView variables control the experiment. The start time of the analog input, analog output, digital output, and counter output are synchronized. We label this time, when the experiment starts, $t = 0$. Note that the actions on the diagram occur in parallel; we follow along with each of the groups in channels in turn. For reference, the top-level VIs for this experiment are located at `C:\LabView Restructured 2\adiabatic-phasekick\adiabatic-phase-kick-w-control-multiple-points.vi` and `C:\LabView Restructured 2\adiabatic-phasekick\df-A-x-signal-average.vi`.

Analog input — Starting at $t = 0$, we read $N = f_{\mathrm{s}}(t_1 + t_2 + t_{\mathrm{p}} + t_3)$ samples from each analog input channel, where f_{s} is the sampling rate. The beginning of the experiment is determined by a software trigger in LabView; it is not synchronized to the cantilever oscillation in any way.

Digital output — At $t = t_1 + t_{2\mathrm{d}}$, the cantilever drive signal (connected to the relay switch standalone circuit) is turned off. At $t = t_1 + t_2 + t_{\mathrm{p}} + t_{3\mathrm{d}}$, the cantilever drive signal is turned on.

Choice of timing values — The timings for both the analog input and the digital output are completely fixed. The voltage outputs and counters will introduce a synchronization delay time T_{sync} (`tp delay [ms]` variable in the LabView code), which serves to synchronize the start of the voltage/light pulse to the cantilever cycle. For a cantilever with a frequency f_{c}, we expect the synchronization delay to be less than or equal to the cantilever period: $T_{\mathrm{sync}} \leq f_{\mathrm{c}}^{-1}$, with the average synchronization delay time $T_{\mathrm{sync}} = \frac{1}{2} f_{\mathrm{c}}^{-1}$.

For example, a $62.5\,\mathrm{kHz}$ cantilever has a period of $16\,\mu\mathrm{s}$. It would be a bad idea to choose $t_{3\mathrm{d}} = 10\,\mu\mathrm{s}$, because the cantilever drive would turn on either slightly before or slightly after the end of the voltage pulse, depending on the specific value of the synchronization delay time. For similar reasons, t_3 should not be too small either, or the analog input will stop reading before the end of the light/voltage pulse.

Analog output — At $t = 0$, the tip voltage is set to V_1. At a time $t = t_1$, the tip voltage is switched to V_2 and the analog output, which controls the tip voltage and light voltage, ends. The analog output data for the time t_p and t_3 is loaded. At this point, the NI-6259 waits for the Synchronized Enable output (from the custom triggering circuit) to trigger the next analog output.

Counter output — At the time $t = t_1 + t_2$, a $5\,\mathrm{V}$ digital pulse is sent from the PCI-6259 (DIO0) to the the custom triggering circuit enable input. The time is set as $N = f_\mathrm{s}(t_1 + t_2)$ ticks of the analog output clock. The next time the cantilever or modulation input crosses from negative to positive (is this correct?), the synchronized enable output goes from $0\,\mathrm{V}$ to $5\,\mathrm{V}$. The synchronized enable is the digital trigger for the start of the analog output.

Counter input — When the counter output triggers the enable digital signal, the counter input begins counting ticks at $80\,\mathrm{MHz}$ until the synchronized enable is received from the custom synchronization circuit. The counter time is equal to T_sync, the delay between $t = t_2$ and the beginning of the light and voltage pulses.

Analog output — At the time $t = t_1 + t_2 + T_\mathrm{sync}$, the tip voltage is switched to V_p and the light voltage is switched to $V_\mathrm{light\_on}$. After a time t_p, the tip voltage is switched to V_3 (at the time $t = t_1 + t_2 + T_\mathrm{sync} + t_3$). After a time $t_\mathrm{p} + t_\mathrm{3d\_light}$, the light voltage is switched back to $V_\mathrm{light\_off}$.

B.2.1 LabView code

In this section, we outline how the LabView code controlling the synchronization works. All of the digital signals we use are "active high." The file which the block diagram sections are taken from is `C:\LabView Restructured 2\adiabatic-phasekick\02-analog-write-read-start-trigger-read-time.vi`. A potentially useful resource from National Instruments is "Timing and Synchronization Features of NI-DAQmx" (http://www.ni.com/product-documentation/4322/en/#toc6).

Analog input — The analog input is standard. The other inputs and outputs are triggered off the analog input start trigger (`ai/StartTrigger`).

Analog output — Fig. B.3a shows the initial analog output setup, triggered off of analog input start trigger. We write $N = f_{\mathrm{s}} t_1 + 1$ samples. For the first $N - 1$ samples, the tip voltage is V_1 and the light voltage is $V_{\mathrm{light\_off}}$. The last sample switches the tip voltage to V_2, while leaving the light voltage as $V_{\mathrm{light\_off}}$.

After starting the experiment, the code shown in Fig. B.3b executes. We wait for the output from Fig. B.3a to complete, then stop the output. At this point, the tip voltage and light voltages remain V_2 and $V_{\mathrm{light\_on}}$, respectively, until the next analog output begins. Then we set up the analog output for the samples during t_{p} and t_3. First, we reset the sample clock. Then we setup a start trigger for the counter input channel, write the array of samples, and start the new acquisition. By starting the acquisition, the analog output now waits for the start trigger from the counter input channel. In order for the experiment to work, the code in Fig. B.3b must execute in a time $T < t_2$. I have not carefully checked the minimum time required, but I would expect that t_2 must be at least a few milliseconds.

Counter output — The lower part of Fig. B.3c contains the counter output which sends the enable signal to the synchronization circuit. We use counter 0 for the task. We use a

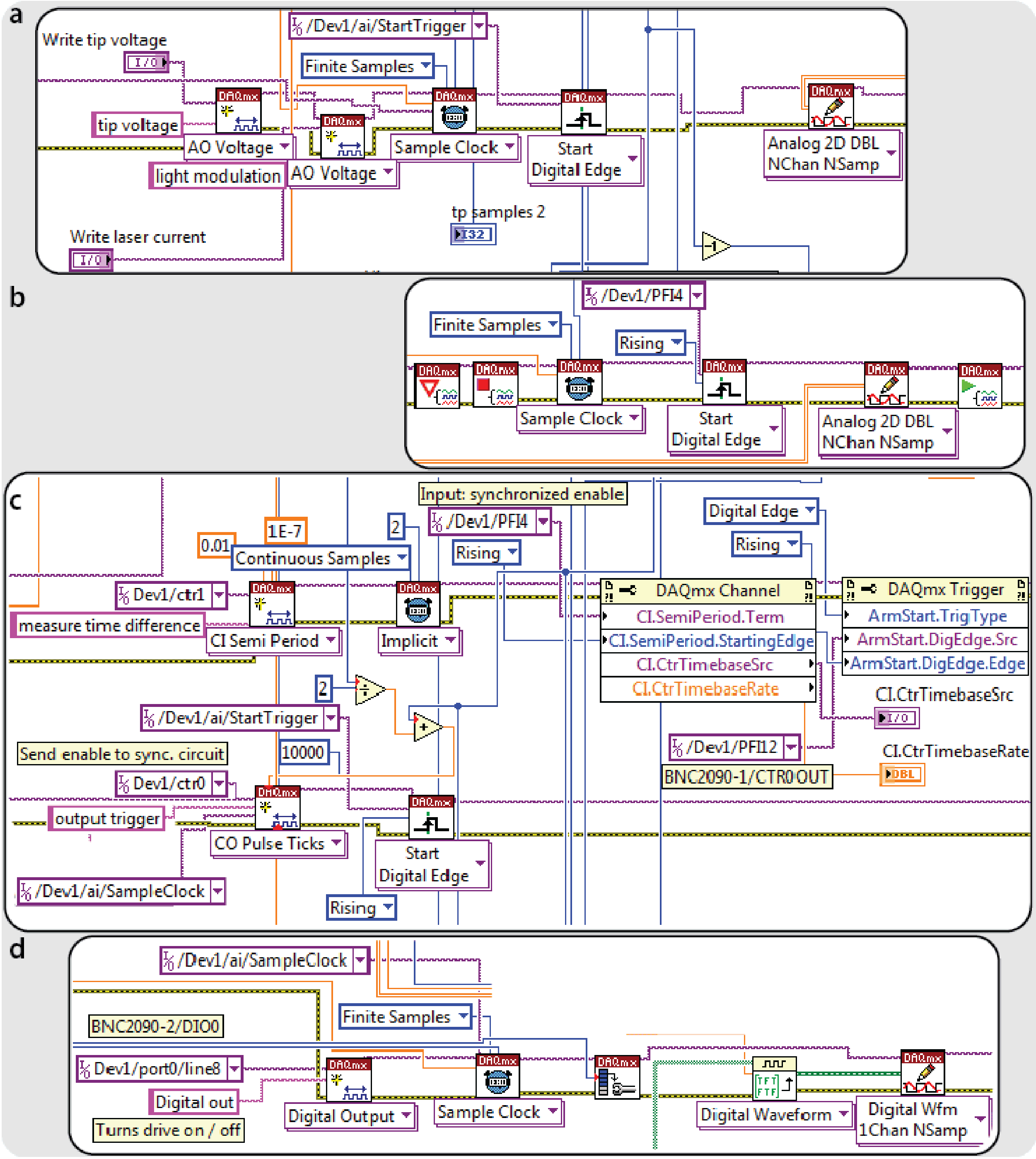

Figure B.3: LabView diagram for clock stuff.

small estimated minimum time of $1 \times 10^{-7}\,\mathrm{s}$ so that the counter operates at its maximum rate, $80\,\mathrm{MHz}$. We set the tick source to the analog input sample clock and trigger off the analog input start trigger. The output starts low ($V = 0\,\mathrm{V}$) for $N = f_\mathrm{s}(t_1 + t_2)$ ticks of the sample clock, then goes high ($V = 5\,\mathrm{V}$) for the remainder of the experiment. The counter 0 output is `PFI12` which is connected to the `CTR0OUT` pin on the upper BNC2090 panel. We connect the `CTR0OUT` pin to the `USER2` BNC connection on the upper BNC2090.

Counter input — We use counter 1 to measure the synchronization time delay T_sync. We want to measure the time between the enable signal output (channel switched from $0\,\mathrm{V}$ to $5\,\mathrm{V}$) from counter 0 and the synchronized enable signal received from the custom synchronization circuit (synchronized enable switched from $0\,\mathrm{V}$ to $5\,\mathrm{V}$). We set up the channel to measure a "Semi Period", which means that the counter returns the times for each transition (low to high, then high to low, then high to low...). For example, if the input were a constant period square wave equal to $5\,\mathrm{V}$ for $10\,\mathrm{\mu s}$, then $0\,\mathrm{V}$ for $5\,\mathrm{\mu s}$, the counter would measure $10, 5, 10, 5\ldots\,\mathrm{\mu s}$.

We choose `PFI4` as the input channel which the timer measures. We connect this terminal to `USER1` on the upper BNC2090. We start on a rising edge because we want to measure the first 0 to $5\,\mathrm{V}$ transition of the synchronized enable output.

The arm start determines when the counter begins ticking. We start at the 0 to $5\,\mathrm{V}$ transition of the enable output from counter 0; in the code, this transition is the rising edge of `PFI12`, which is the counter 0 output.

The setup for the counter input was not obvious to me; I sent example code to National Instruments and an application engineer chose the appropriate settings I needed. You must choose continuous samples for the implicit sampling clock, otherwise a second timer is used to set up the finite sampling clock. The example code from the application engineer is located at `C:\LabView Restructured 2\DAQ Triggered Output Change.vi`. This VI is much simpler than the pk-EFM or tr-EFM VIs, so may be useful for understanding the operation of the counters.

Digital output — The digital output is triggered off of the analog input sample clock. The channel `port0/line8` corresponds to `DOI0` on the lower BNC2090, which we connect to the `USER1` BNC connector.

B.2.2 Saved output file

The output is saved an an HDF5 file. In LabView, the time axis is shifted for analysis so that $t' = 0$ is the start of the light pulse. On the t' axis, the experiment starts at $t' = -(t_1 + t_2 + T_{\text{sync}})$. The HDF5 file has the structure

```
/0000
    /0000/cantilever-nm  (50000,)  <f8
    /0000/t0 [s]  ()  <f8
    /0000/dt [s]  ()  <f8
    /0000/tp delay [ms]  ()  <f8
    /0000/relative time [s]  ()  <f8
```

where the groups `0000`, `0001`... each contain the scalar datasets: `t0 [s]` the initial time on the t' axis; `dt [s]` the spacing between data points equal to the inverse sampling rate f_{s}^{-1}; `tp delay [ms]` the synchronization delay time T_{sync} *in milliseconds* (a poor design choice that all of the subsequent analysis code must account for—far better would have been to leave the units seconds for all time variables); and `relative time [s]` the total time from the beginning of the first experiment. The `relative time [s]` variable is useful for diagnosing any slow drift in sample properties.

In a pk-EFM experiment, there each group `0000`, `0001` is a subgroup within the `control` or `data` groups:

```
/control
    /0000
    /0001
/data
    /0000
    /0001
```

The top level also contains the datasets `ds`, which contains an array of group names corresponding to each pulse time. The corresponding pulse times, in milliseconds, are stored in the dataset `tp`.

At the top level, the HDF5 file contains the attributes

```
 Microscope Parameters.Cantilever:'160712',
 Microscope Parameters.Q         :31000.0,
 Microscope Parameters.Sample    :'Blank Transistor',
 Microscope Parameters.fc [Hz]   :66750.0,
 Microscope Parameters.kc [Hz]   :3.5,
 z [nm]                          :220.0,
 wait [ms]                       :25
```

where the unit on `kc` should be $\mathrm{N\,m^{-1}}$. After the end of an acquisition, the LabView code waits for `wait [ms]` before beginning the next experiment. In practice, it can take a significant length of time to save the data from an experiment, so the actual wait time may be significantly longer than `wait [ms]`.

Each subgroup contains the attributes

```
Adiabatic Sampling.Analog In Clock Source:'    ',
Adiabatic Sampling.Gains                 :[ 1332.5],
Adiabatic Sampling.Names                 :[28],
Adiabatic Sampling.Offsets               :[ 0.],
Adiabatic Sampling.Rate [Hz]             :1000000.0,
Adiabatic Sampling.Read Channels         :'        Dev1/ai8',
Adiabatic Sampling.Write laser current   :'    Dev1/ao2',
Adiabatic Sampling.Write tip voltage     :'    Dev1/ao3',
Adiabatic Parameters.Light source        :'405 nm laser',
Adiabatic Parameters.V1                  :0.0,
Adiabatic Parameters.V2                  :7.0,
Adiabatic Parameters.V3                  :0.0,
Adiabatic Parameters.Vlight off          :0.0,
Adiabatic Parameters.Vlight on           :2.0,
Adiabatic Parameters.Vp                  :7.0,
Adiabatic Parameters.t1 [ms]             :10.0,
Adiabatic Parameters.t2 [ms]             :20.0,
Adiabatic Parameters.t2d [ms]            :10.0,
Adiabatic Parameters.t3 [ms]             :10.0,
Adiabatic Parameters.t3d [ms]            :5.0,
Adiabatic Parameters.tp [ms]             :10.0,
Actual timing.Sample rate act [Hz]       :1000000.0,
Actual timing.t1 act [s]                 :10.0,
Actual timing.t2 act [s]                 :20.0,
Actual timing.t2d act [s]                :10.0,
Actual timing.t3d act [s]                :5.0,
Actual timing.tp act [s]                 :10.0
```

which correspond to the timings set in the LabView VI. The actual timings are outputs from the low-level subVI which sets up the data acquisition. The actual timings will differ from the parameters set in the VI if the actual sampling rate is different from the sampling rate specified on the front panel (`Adiabatic Sampling.Rate [Hz]`). For a single channel acquisition, the available sampling rates on the NI-6259 are $f_\mathrm{s} = 10\,\mathrm{MHz}/N$, where the

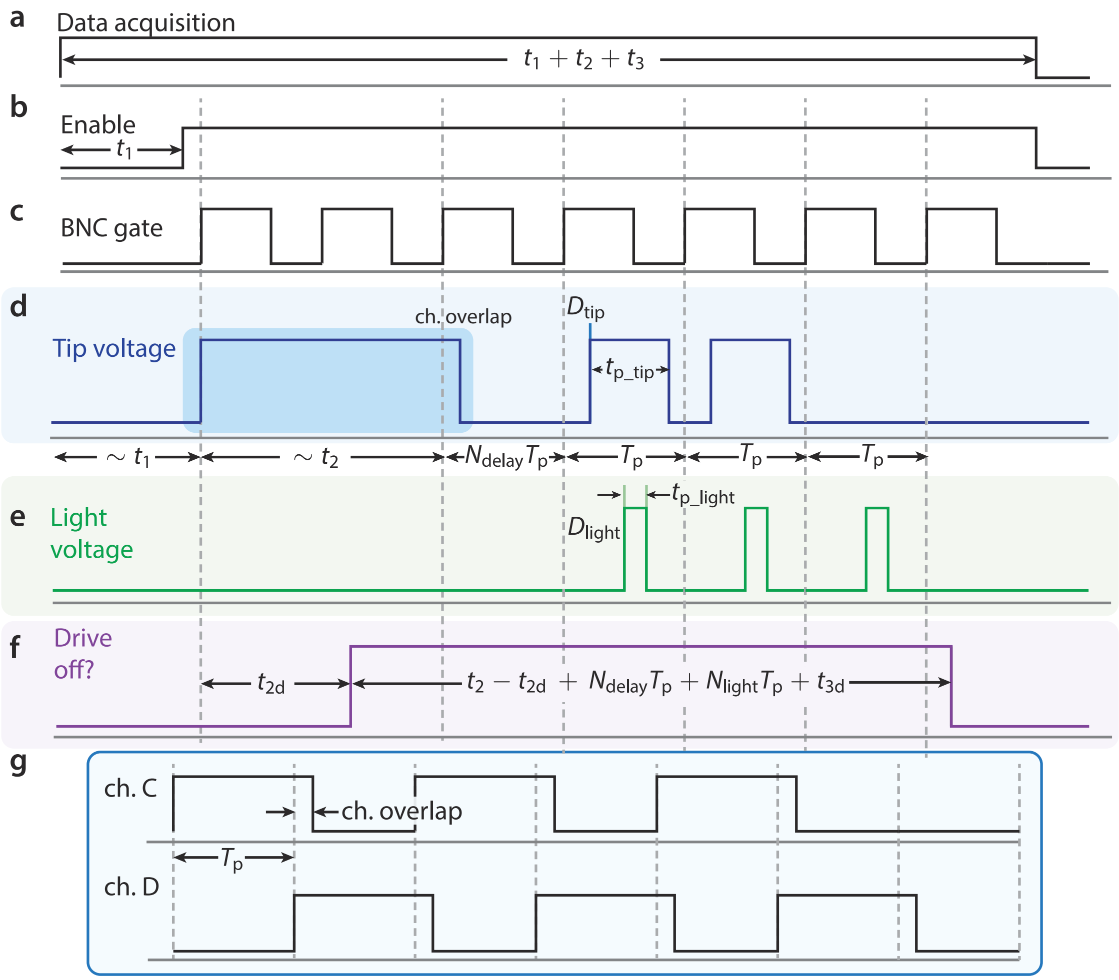

Figure B.4: Pulse timing diagram.

integer $N \geq 8$.

B.3 BNC experimental setup

In the BNC experimental setup, the BNC565 outputs all of the relevant experimental voltages. The code has the ability to perform the timing diagram of Fig. B.2 as well as a variety of other pulse sequences. Throughout the description of the timing and voltage pulses, we use bold font to highlight potential trouble spots. For reference, the top level VI is located at `C:\LabView Restructured`

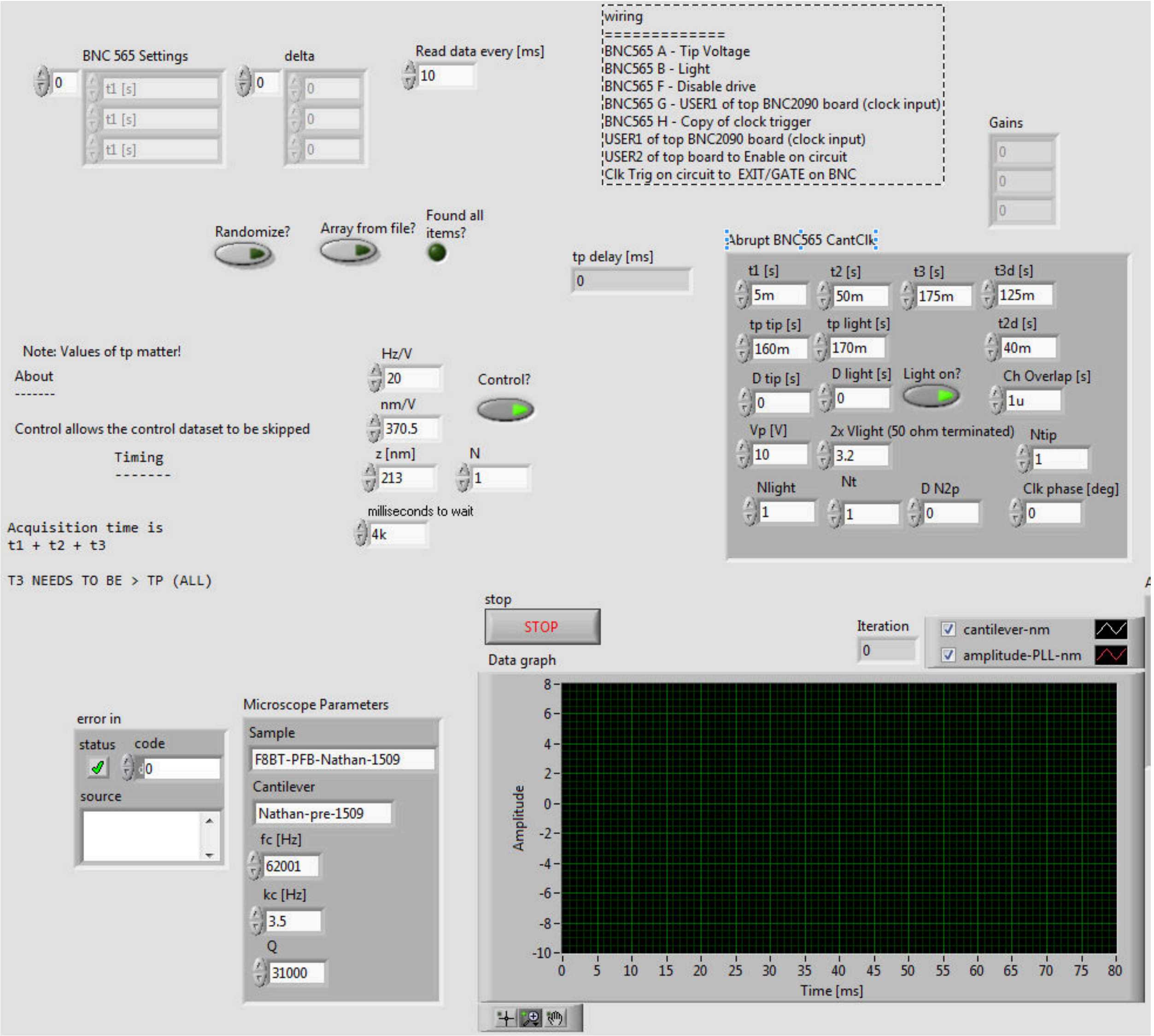

wiring
=============
BNC565 A - Tip Voltage
BNC565 B - Light
BNC565 F - Disable drive
BNC565 G - USER1 of top BNC2090 board (clock input)
BNC565 H - Copy of clock trigger
USER1 of top BNC2090 board (clock input)
USER2 of top board to Enable on circuit
Clk Trig on circuit to EXIT/GATE on BNC

BNC 565 Settings: 0; t1 [s]; t1 [s]; t1 [s]
delta: 0; 0; 0; 0
Read data every [ms]: 10
tp delay [ms]: 0
Gains: 0; 0; 0

Abrupt BNC565 CantClk
t1 [s]: 5m
t2 [s]: 50m
t3 [s]: 175m
t3d [s]: 125m
tp tip [s]: 160m
tp light [s]: 170m
t2d [s]: 40m
D tip [s]: 0
D light [s]: 0
Ch Overlap [s]: 1u
Vp [V]: 10
2x Vlight (50 ohm terminated): 3.2
Ntip: 1
Nlight: 1
Nt: 1
D N2p: 0
Clk phase [deg]: 0

Note: Values of tp matter!
About

Control allows the control dataset to be skipped
Timing

Acquisition time is
t1 + t2 + t3
T3 NEEDS TO BE > TP (ALL)

Hz/V: 20
nm/V: 370.5
z [nm]: 213
N: 1
milliseconds to wait: 4k
Iteration: 0

error in
status: ✓ code: 0
source:

Microscope Parameters
Sample: F8BT-PFB-Nathan-1509
Cantilever: Nathan-pre-1509
fc [Hz]: 62001
kc [Hz]: 3.5
Q: 31000

Figure B.5: BNC565 LabView code.

`2\abrupt-phasekick\abrupt-phase-kick-w-control-programmatic-delta.vi`. The version of the VI used in the experiments of Chapter 2 is located at `C:\LabView Restructured 2\abrupt-phasekick\abrupt-phase-kick-w-control.vi`.

The timing diagram of Fig. B.4 shows how the different LabView variables control the experiment. Note that the times on the diagram are not to scale. First, the data acquisition begins (Fig. B.4a). For a time t_1, the tip and sample output voltages are zero.

At $t = t_1$, the NI-6259 counter output controlling the "enable" channel transitions from low to high (Fig. B.4b). At the next negative to positive transition of the cantilever clock sine wave input, the BNC gate transitions from low to high (Fig. B.4c). For the duration of the experiment, the BNC gate is a square wave synchronized to the cantilever clock sine wave input.

At the first low to high transition of the BNC gate, the tip voltage is set to V_p (Fig. B.4d). After a time approximately equal to t_2, the voltage and light pulse sequence begins. The exact length of t_2 is determined by the period of the BNC gate and will be described in detail below.

The timing of the pulse sequence is determined by the period of the BNC gate signal T_p in the LabView code. The BNC gate period is the inverse of the cantilever frequency (`fc [Hz]` set in the "Microscope Settings" cluster) times the number of cantilever cycles per clock period N_t (`Nt` in the "Abrupt BNC565 CantClk" control): $T_\mathrm{p} = N_\mathrm{t}/f_\mathrm{c}$. All of the experimental timing is determined by T_p so **it is important to provide the correct value for f_c**.

Before starting the voltage and light pulses, the voltages remain at zero for N_delay cycles (set as `D N2p` in the "Abrupt BNC565 CantClk" cluster). In the Fig. B.4 diagram, $N_\mathrm{delay} = 1$. At the next rising edge of the clock, there is a delay of D_tip (set as `D tip [s]` in the "Abrupt BNC565 CantClk"), and then a voltage pulse of length $t_\mathrm{p\_tip}$. For the light pulse (Fig. B.4), there is a delay of D_tip (set as `D light [s]` in the "Abrupt BNC565 CantClk"), and then a voltage pulse of length $t_\mathrm{p\_light}$.

We repeat the tip and light pulse sequence, with the same delays and pulse widths, on the next N_tip and N_light clock cycles respectively. In the Fig. B.4 diagram, $N_\mathrm{tip} = 2$ and $N_\mathrm{light} = 3$. **If the time $D_\mathrm{tip} + t_\mathrm{p\_tip}$ (or $D_\mathrm{light} + t_\mathrm{p\_light}$) is longer than the period T_p, the**

subsequent pulses are triggered on the first rising edge of the clock after the end of the tip (or light) pulse.

The drive signal is not tied to the cantilever clock in the same way. After a fixed delay $t_{2\mathrm{d}}$, the drive is turned off for the rest of t_2, the total delay time before the start of the light and voltage pulses $N_{\mathrm{delay}} T_{\mathrm{p}}$, N_{light} additional clock periods, and the extra delay $t_{3\mathrm{d}}$. If it is important that the drive not be on during the measurement, **make sure that $t_{3\mathbf{d}}$ is long enough that the drive does not turn on during any of the light and/or voltage pulses**.

Choose t_3 long enough that the data acquisition does not end before the light and/or voltage pulses (Fig. B.4a).

The exact time at which the tip voltage is initially held at V_{p}, marked $\sim t_2$ on the diagram of Fig. B.4a, is determined by the cantilever clock. The voltage pulse is set as $N_2 = 2\,\mathrm{round}(t_2/[2T_{\mathrm{p}}])$ ticks of the cantilever clock, where we force N_2 to be an even number for programming reasons. To sent a continuous voltage pulse, we use channels C and D of the BNC565. We set each channel to go high for a pulse time of T_{p} plus the `ch overlap [s]` (Fig. B.4g). As a result, each channel fires on alternating clock cycles. We set channel A, the tip voltage channel, to "mux" channels A, C and D, so that whenever one of the channels is high, the tip voltage is high. The only caveat is that **if N_{delay} is zero, the tip voltage will be high for the first `ch overlap [s]` of the first tip voltage pulse period; this sets `ch overlap [s]` as the lower limit on the length of the tip voltage pulses which can be used in the pk-EFM experiments of Chapter 2.**

B.3.1 LabView code

For reference, the LabView code to set up the BNC565 is shown in Fig. B.6.

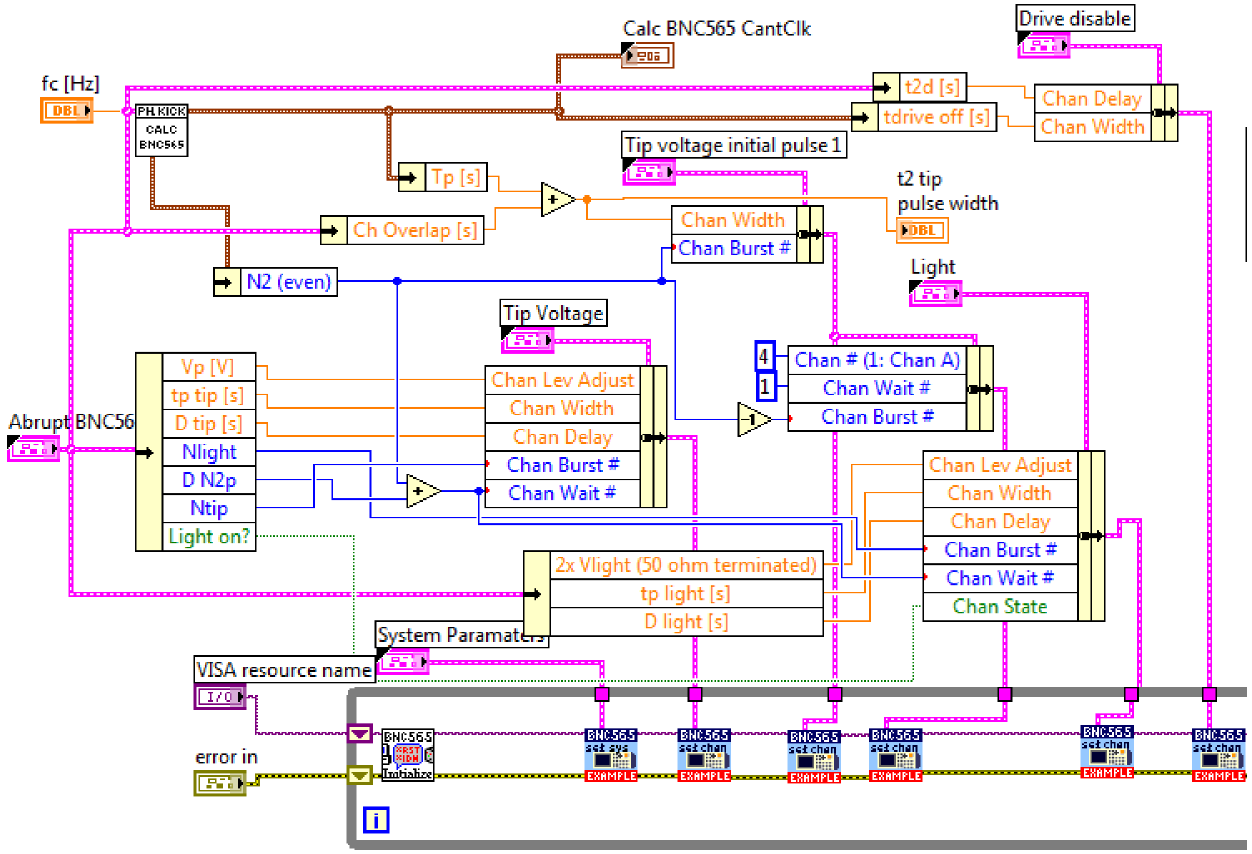

Figure B.6: Set BNC565 pulse and delay timing.

The data acquisition code is similar to the DAQ experimental setup LabView code (Sec. B.2). The code is simpler because the only channels set up are the analog input, the counter output to sent the enable signal to the custom triggering circuit, and the counter input to read back the BNC gate timings. For the BNC experimental setup, the counter input reads a BNC565 channel which multiplexes the cantilever tip voltage channels A and C. We determine when the voltage and light pulses start relative to the DAQ sampling clock by adding the semi-period timings from the counter input.

To make the period T_p longer while maintaining phase lock with the cantilever, we can divide the clock frequency down from f_c to $f_\mathrm{c}/N_\mathrm{t}$, where N_t is an integer. The corresponding pulse period $T_\mathrm{p} = N_\mathrm{t} T_\mathrm{c}$, where the cantilever period $T_\mathrm{c} = f_\mathrm{c}^{-1}$. To use a lower

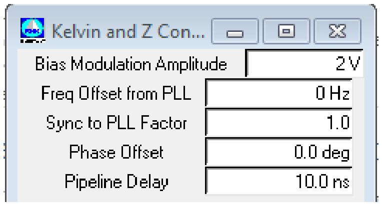

Bias Modulation Amplitude 2 V
Freq Offset from PLL 0 Hz
Sync to PLL Factor 1.0
Phase Offset 0.0 deg
Pipeline Delay 10.0 ns

Figure B.7: The PLLProII Kelvin controller settings, which control the Bias Drive output channel of the PLLProII. The Bias Drive output frequency is (Freq Offset from PLL) + (Sync to PLL Factor) × (PLL Freq).

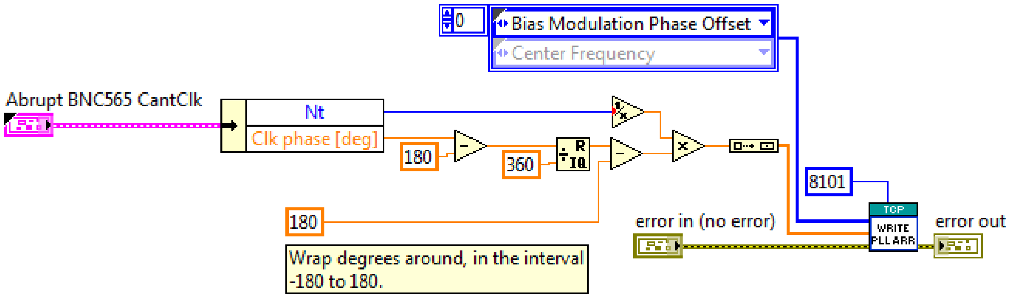

Figure B.8: LabView code to modify the PLLProII Bias modulation Phase Offset. The hard-coded “8101” constant is the PLLProII port number, which is set by the shell script that launches the PLLProII application.

frequency / longer period, set the “Sync to PLL Factor” on the PLLProII Kelvin controller to $1/N_{\mathrm{t}}$ (Fig. B.7). The LabView code adjusts the Bias Modulation Phase Offset so that the phase is relative to the cantilever period, not the longer pulse period (Fig. B.8).

B.3.2 Saved output file

The output is saved an an HDF5 file. The structure is the same as that for the DAQ experimental setup with a few minor differences.

```
/data
    /data/0000
        /data/0000/cantilever-nm  (65015,)  <f8
        /data/0000/t0 [s]  ()  <f8
        /data/0000/half periods [s]  (3102,)  <f8
        /data/0000/dt [s]  ()  <f8
        /data/0000/relative time [s]  ()  <f8
/ds  (768,)  |O
/tp tip [s]  (768,)  <f8
```

At the top level, the HDF5 file contains the attributes

```
Microscope Parameters.Cantilever  :'Nathan-pre-1509',
Microscope Parameters.Q           :31000.0,
Microscope Parameters.Sample      :'F8BT-PFB-Nathan-1509',
Microscope Parameters.fc [Hz]     :62001.0,
Microscope Parameters.kc [Hz]     :3.5,
z [nm]                            :290.0,
wait [ms]                         :87,
PLL Settings out.Amplitude Scaling:1.0,
PLL Settings out.Center Frequency :62000.2163,
PLL Settings out.Frequency I      :2.5,
PLL Settings out.Frequency P      :-12.0,
PLL Settings out.Frequency Scaling:20.0,
PLL Settings out.Phase Shift      :-119.13
```

where the unit on `kc` should be $\mathrm{N\,m^{-1}}$.

Each subgroup contains the attributes

```
Abrupt BNC Sampling.Analog In Clock Source         :'    ',
Abrupt BNC Sampling.Gains                          :[ 370.5],
Abrupt BNC Sampling.Names                          :[28],
Abrupt BNC Sampling.Offsets                        :[ 0.],
Abrupt BNC Sampling.Rate [Hz]                      :1000000.0,
Abrupt BNC Sampling.Read Channels                  :'        Dev1/ai8',
Abrupt BNC565 CantClk.2x Vlight (50 ohm terminated):4.9,
Abrupt BNC565 CantClk.Ch Overlap [s]               :8e-07,
Abrupt BNC565 CantClk.Clk phase [deg]              :0.0,
Abrupt BNC565 CantClk.D N2p                        :0,
Abrupt BNC565 CantClk.D light [s]                  :0.0,
Abrupt BNC565 CantClk.D tip [s]                    :0.0,
Abrupt BNC565 CantClk.Light on?                    :1,
Abrupt BNC565 CantClk.Nlight                       :1,
Abrupt BNC565 CantClk.Nt                           :1,
Abrupt BNC565 CantClk.Ntip                         :1,
Abrupt BNC565 CantClk.Vp [V]                       :10.0,
Abrupt BNC565 CantClk.t1 [s]                       :0.005,
Abrupt BNC565 CantClk.t2 [s]                       :0.05,
Abrupt BNC565 CantClk.t2d [s]                      :0.04,
Abrupt BNC565 CantClk.t3 [s]                       :0.01,
Abrupt BNC565 CantClk.t3d [s]                      :0.0075,
Abrupt BNC565 CantClk.tp light [s]                 :0.0011114,
Abrupt BNC565 CantClk.tp tip [s]                   :0.0011114,
Calc BNC565 CantClk.D t2p [s]                      :0.0,
Calc BNC565 CantClk.N2 (even)                      :3100,
Calc BNC565 CantClk.Tc [s]                         :1.61287721166e-05,
Calc BNC565 CantClk.Tp [s]                         :1.61287721166e-05,
Calc BNC565 CantClk.t2 act [s]                     :0.0499991935614,
Calc BNC565 CantClk.t2+t2dp+tptot [s]              :0.0500153223335,
Calc BNC565 CantClk.tdrive off [s]                 :0.0175153223335,
Calc BNC565 CantClk.total time [s]                 :0.0650153223335,
Calc BNC565 CantClk.tp total [s]                   :1.61287721166e-05
```

APPENDIX C

POSITION-MODULATED KELVIN PROBE FORCE MICROSCOPY

C.1 Scanned probe microscopy

All experiments were performed under vacuum ($1 \times 10^{-6}\,\mathrm{mbar}$) in a custom-built scanning Kelvin probe microscope [120, 121]. The cantilever (MikroMasch HQ:NSC18/Pt conductive probe) had resonance frequency $f_{\mathrm{c}} = 66\,401\,\mathrm{Hz}$, manufacturer-reported spring constant $k_{\mathrm{c}} = 3.5\,\mathrm{N\,m^{-1}}$ and quality factor $Q = 28900$. Cantilever motion was detected using a fiber interferometer operating at $1490\,\mathrm{nm}$ (Corning SMF-28 fiber). The laser diode's (QPhotonics laser diode QFLD1490-1490-5S) DC current was set using a precision current source (ILX Lightwave LDX-3620) and the current was modulated at radiofrequencies using the input on the laser diode mount (ILX Lightwave LDM-4984, temperature controlled with ILX Lightwave LDT-5910B) [64]. The interferometer light was detected with a $200\,\mathrm{kHz}$ bandwidth photodetector (New Focus model 2011).

Our FM-KPFM and position-modulated KPFM experiments used the experimental setup of Figure 4.1a. A detailed analysis of the experimental setup, feedback loop, and gains can be found in Chapter 5 of Ref. 121.

Figure C.1 shows the hardware used to perform the voltage modulation and position modulation in more detail. The cantilever was driven using a commercial phase locked loop (PLL) cantilever controller (RHK Technology, PLLPro2 Universal AFM controller), with PLL loop bandwidth $1\,\mathrm{kHz}$ (PLL feedback loop integral gain $I = 2.5\,\mathrm{Hz}^{-1}$, proportional gain $P = -10\,\mathrm{degrees/Hz}$). The PLL frequency shift δf was input to a Stanford Research Systems SR830 lock-in amplifier (LIA1, Fig. C.1) operating at the voltage-modulation frequency $f_{\mathrm{m}} = 160\,\mathrm{Hz}$. We set the LIA1 filter time constant to $10\,\mathrm{ms}$, the

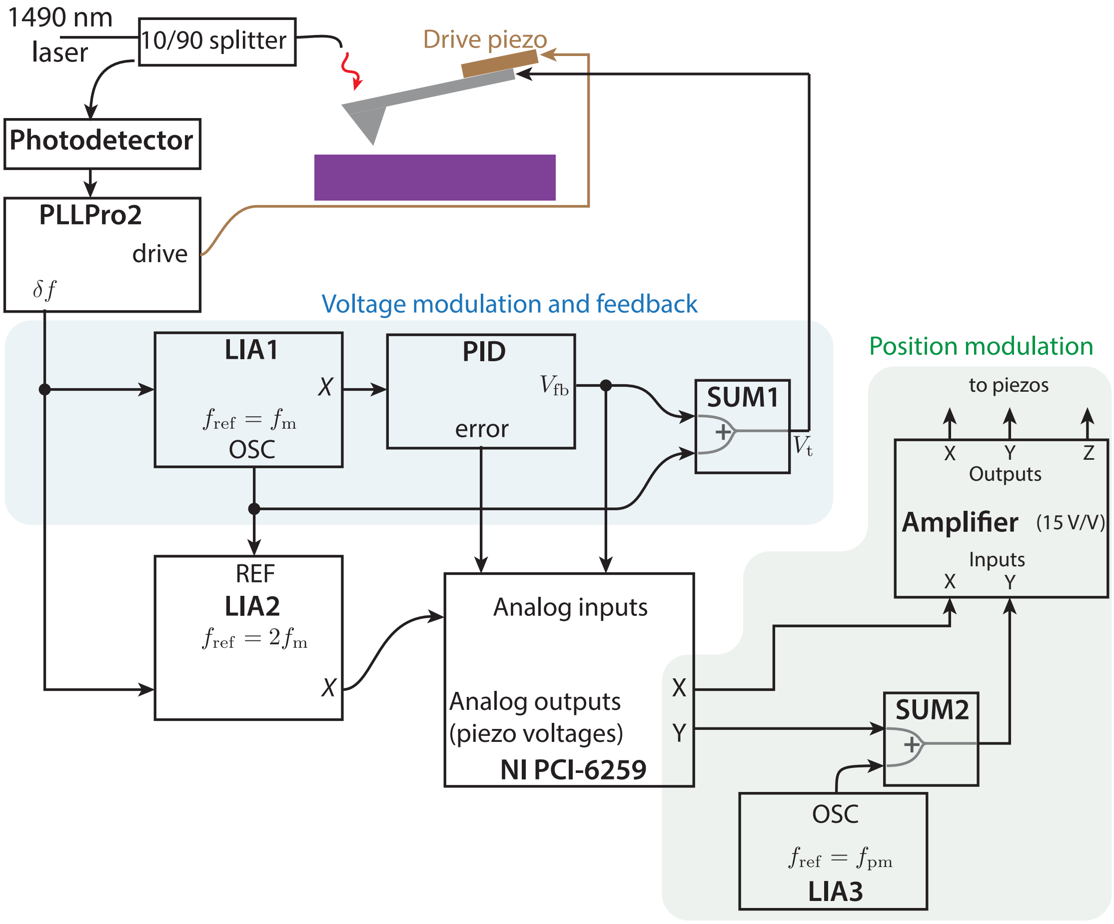

Figure C.1: A block diagram showing the hardware used to perform the voltage modulation and position modulation.

filter slope to $6\,\mathrm{dB\,octave^{-1}}$ and turned the synchronous filter setting on. To auto-phase LIA1, the time constant was increased to $\mathrm{TC} = 300\,\mathrm{ms}$ and a $1\,\mathrm{V}$ DC offset was applied to the tip ($V_{\mathrm{ts}} - \phi = 1\,\mathrm{V} + V_{\mathrm{m}} \sin(2\pi f_{\mathrm{m}} t)$). The X-channel LIA1 output, proportional to the cantilever frequency shift component at the modulation frequency $\delta f(f_{\mathrm{m}})$, was used as the measurement input to a proportional-integral-derivative (PID) controller (Stanford Research Systems SIM960).

We set the PID controller integral gain to $I = 50\,\mathrm{rad\,s^{-1}}$ and derivative gain to $D = 5 \times 10^{-5}\,\mathrm{s}$. Before each KPFM scan, we set the proportional gain by increasing the gain until the feedback loop became unstable ($P = P_{\mathrm{unstable}}$) and then reducing the gain to $P = P_{\mathrm{unstable}}/3$, corresponding to a gain margin of 3. Typically, the resulting proportional gain was $P = 0.1$ to 0.6. With this gain margin criteria, the overall feedback loop bandwidth was $b \sim 40\,\mathrm{Hz}$, measured using the network analyzer function on a Diligent Analog Discovery (see Figures 5.12 and 5.13 in Ref. 121). The proportional gain was set over the higher capacitance source and drain electrodes; the overall bandwidth was lower over the transistor channel ($b = 20$ to $30\,\mathrm{Hz}$).

The applied tip voltage was the sum of the f_{m}-LIA oscillator output voltage (OSC on LIA1, Fig. C.1) and the PID output voltage V_{fb}. We set the LIA1 oscillator rms-voltage to $V_{\mathrm{rms}} = V_{\mathrm{m}}/\sqrt{2} = 1.5\,\mathrm{V}$. A home-built summing circuit (Analog Devices AD711 operational amplifier; SUM1 in Fig. C.1) was used to add the two voltages.

A second lock-in amplifier (PerkinElmer Signal Recovery 7265; LIA2 in Fig. C.1) was used to track the component of the cantilever frequency shift at twice the voltage-modulation frequency $\delta f(2_{\mathrm{m}})$. This frequency shift component is proportional to the tip-sample capacitance derivative $C''(d)$. We set the LIA2 filter time constant $\mathrm{TC} = 50\,\mathrm{ms}$ and the filter slope to $6\,\mathrm{dB}\,\mathrm{octave}^{-1}$.

The sample position was modulated using the oscillator of a third lock-in amplifier (PerkinElmer Signal Recovery 7265, LIA3 in Fig. C.1) set to the position-modulation frequency f_{pm}. To apply the position modulation along the KPFM-scan axis (as in Figure 4.2), a home-built summing circuit (Analog Devices AD711 operational amplifier; SUM2 in Fig. C.1) was used to add the position-modulation sinusoid to the KPFM ramp signal (typically -5 to $5\,\mathrm{V}$). The summing circuit output was amplified by $15\,\mathrm{V/V}$ using a Piezomecanik 350 amplifier (Amplifier in Fig. C.1.

The tip-sample distance h was set by tapping the surface (60 percent amplitude set point, cantilever zero-to-peak amplitude $A = 50\,\mathrm{nm}$ away from the surface) over the source or drain electrode then retracting the z-piezo by $\Delta z = h - 0.6A$ so that the mean tip-sample distance was h.

For PM-KPFM and KPFM line scans, the PID feedback voltage $V_{\mathrm{fb}} = \phi_{\mathrm{meas}}$, PID error signal, and the X-channel of LIA2, proportional to the tip-sample capacitance, were digitized at a sampling rate $f_{\mathrm{s}} = 8.192\,\mathrm{kHz}$ using custom LabVIEW data acquisition code and a National Instruments PCI-6259. The full ϕ_{meas}, PID error signal, and tip-capacitance transients were saved for further analysis.

C.2 Scan speed

Figure C.2 shows that with increasing scan speed, the feedback loop could not track the abrupt changes in the sample's surface potential. We scanned across the transistor channel (Fig. 4.2) at a series of increasing scan speeds. We saw clear differences in the measured surface potential profile (Fig. C.2a) as the scan speed was increased from $v = 0.74\,\mathrm{\mu m\,s^{-1}}$ to $11.9\,\mathrm{\mu m\,s^{-1}}$. Fig. C.2b highlights these differences by plotting the difference between the higher speed linescans $\phi(x, v = 1.48\,\mathrm{\mu m\,s^{-1}} \ldots)$ and the slowest linescan $\phi(x, v = 0.74\,\mathrm{\mu m\,s^{-1}})$. The differences are consistent with increasing error $\phi_{\mathrm{error}} = \phi - \phi_{\mathrm{meas}}$ caused by the feedback loop responding too slowly to keep $V_{\mathrm{fb}} = \phi$ as the tip scans across the edge of the transistor channel.

This explanation is supported by the corresponding increase in the PID error e shown in Fig. C.2c. The error e is the X-channel of the phased lock-in amplifier operating at the modulation frequency f_{m}, which is related to the surface potential error ϕ_{error}: $X_{f_{\mathrm{m}}} \propto \delta f(f_{\mathrm{m}}) = -f_{\mathrm{c}} C'' V_{\mathrm{m}} \phi_{\mathrm{error}} / (2k_{\mathrm{c}})$. The capacitance data show the slow response of the lock-in amplifier operating at $2f_{\mathrm{m}}$ (Fig. C.2d).

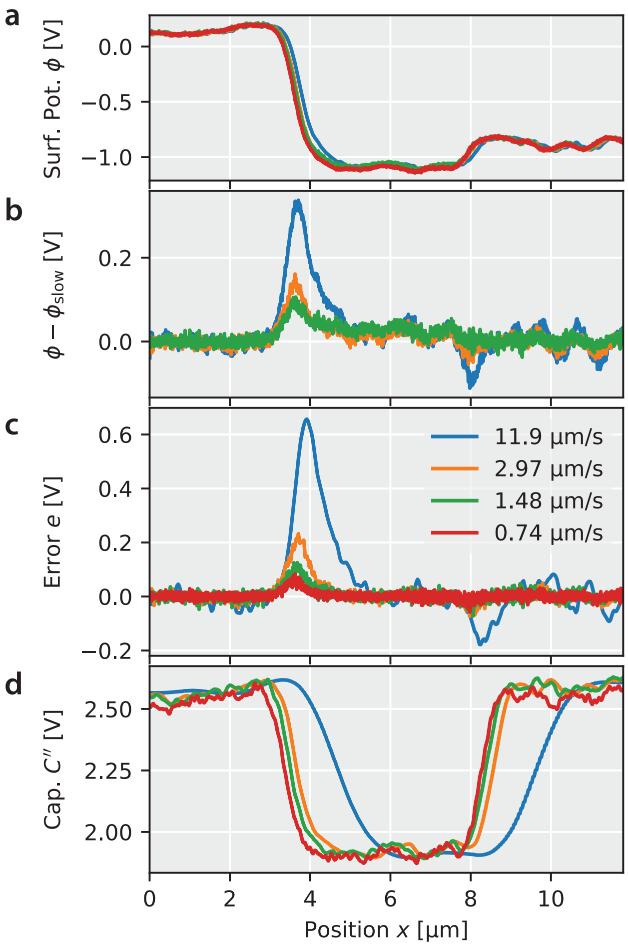

Figure C.2: Increasing scan speed causes surface potential errors. The scan velocity is given in the legend. (a) Measured surface potential $\phi_{\text{meas}} = V_{\text{fb}}$. (b) For the faster scan speeds v, the difference in surface potential compared to the slowest line scan: $\phi(v) - \phi(0.74\,\mu\text{m}\,\text{s}^{-1})$. (c) The X-channel of the LIA operating at f_{m}, which is the feedback loop error signal, $X_{f_{\text{m}}} \propto \delta f(f_{\text{m}})$. (d) The X-channel of the LIA operating at $2f_{\text{m}}$, which is proportional to the capacitance derivative C''. Experimental parameters: Tip-sample separation $h = 200\,\text{nm}$, $V_{\text{m}}/\sqrt{2} = 1.5\,\text{V}$, transistor voltages $V_{\text{S}} = 0$, $V_{\text{D}} = -1\,\text{V}$, and $V_{\text{G}} = -10\,\text{V}$.

Based on this data, in the manuscript we chose a tip velocity $v = 0.37\,\mu\mathrm{m\,s^{-1}}$ for PM-KPFM and FM-KPFM linescans. For FM-KPFM images, we chose a tip velocity $v = 1.5\,\mu\mathrm{m\,s^{-1}}$ ($8\,\mathrm{s}$/line) so that an entire 128 by 128 image could be collected in $17\,\mathrm{min}$.

C.3 Data analysis

Using the full surface potential transients, the Figure 4.1b data analysis was performed in Python. The raw surface potential $\phi_{\mathrm{meas}} = \Phi$ versus time transient was filtered using the finite-impulse-response filter H_{pm} to produce an estimate of the sample's surface potential ϕ:

$$\phi = H_{\mathrm{pm}} * \Phi, \tag{C.1}$$

where $*$ denotes discrete time convolution. We discarded the portion of ϕ where the filter H_{pm} did not overlap fully with the data Φ. We associated each data point ϕ_i with the position along the scan axis $x_i = vt_i$, where v is the tip velocity, $i = 0, 1 \ldots N-1$ is the index, $N = 262\,144$ the number of data points collected, the time $t_i = i/f_{\mathrm{s}}$, and the sampling rate $f_{\mathrm{s}} = 8.192\,\mathrm{kHz}$.

To calculate the electric field via numerical differentiation ($E = -\partial\phi/\partial x$), we used a 2nd order central difference approximation to compute the derivative of the potential

$$E_i = -\frac{(\phi_{i+1} - \phi_{i-1})}{2\Delta x} = -\frac{(\phi_{i+1} - \phi_{i-1})}{2v/f_{\mathrm{s}}}. \tag{C.2}$$

where Δx is difference in position between adjacent data points: $\Delta x = x_i - x_{i-1} = v/f_{\mathrm{s}}$.

To calculate the electric field using the modulation component, we processed the raw surface potential $\phi_{\mathrm{meas}} = \Phi$ with a software lock-in amplifier filter (Fig. C.3). First, the complex lock-in amplifier signal z was generated using

$$z = H_{\mathrm{pm}} * \Big(\exp(-2\pi j\, f_{\mathrm{pm}} t) \times \Phi \Big), \tag{C.3}$$

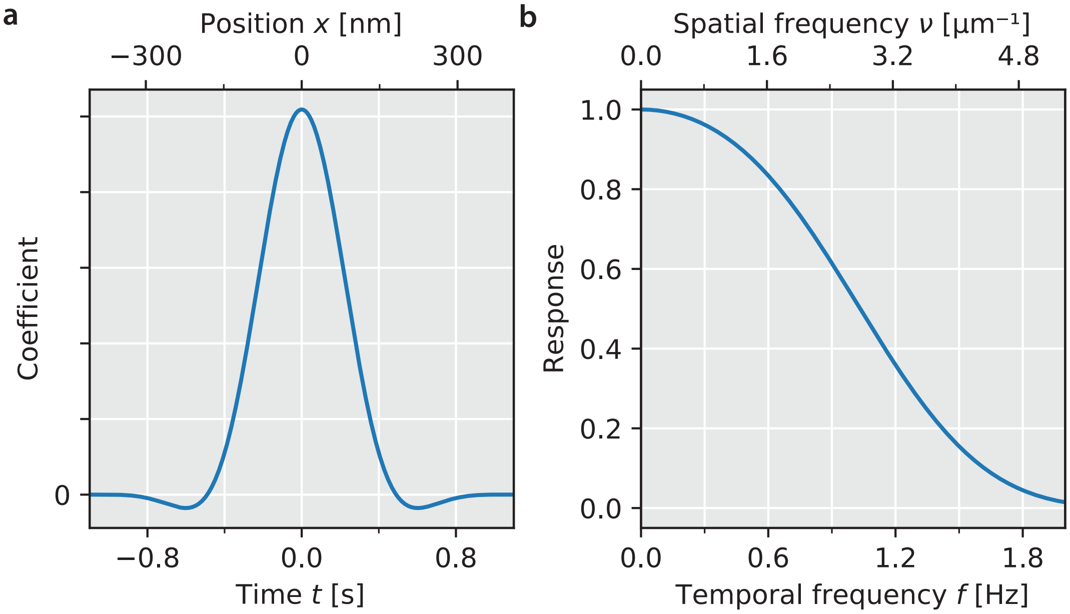

Figure C.3: The software lock-in amplifier filter. (a) The finite impulse response lock-in amplifier filter H_{pm} in the time domain. The upper position axis shows $x = vt$, with $v = 0.37\,\mathrm{\mu m\,s^{-1}}$ the cantilever tip velocity along the scan axis. (b) H_{pm} in the frequency domain. The upper spatial frequency axis shows $\nu = f/v$, with $v = 0.37\,\mathrm{\mu m\,s^{-1}}$ the cantilever tip velocity along the scan axis.

where H_{pm} is the finite-impulse-response filter, $j = \sqrt{-1}$, $f_{\mathrm{pm}} = 4.5\,\mathrm{Hz}$ is the position modulation frequency, and t is a vector of time data $t = (0, 1, \ldots N-1)/f_{\mathrm{s}}$. We discarded the portion of z where the filter H_{pm} did not overlap fully with the data (about $1.1\,\mathrm{s}$ at the beginning and end of the data set). From z, we calculated the signal's amplitude $A = |z|$ and phase $\theta = \arg z$. The real ($x = \mathrm{Re}\, z$) and imaginary ($y = \mathrm{Im}\, z$) components of z are shown in Figure C.4a.

The lock-in amplifier was phased by minimizing the signal in the out-of-phase channel. When phasing the lock-in amplifier, we also adjusted the lock-in amplifier reference frequency. This procedure corrects for any correct slow drift in the phase. We optimize using the cantilever amplitude and phase as follows:

$$\min_{\Delta f, \theta_0} \sum_{i}^{N} A_i^2 \left[\left| \underbrace{|\theta_i - 2\pi \Delta f t_i + \theta_0|}_{\Delta\theta} - \frac{\pi}{2} \right| - \frac{\pi}{2} \right]^2, \tag{C.4}$$

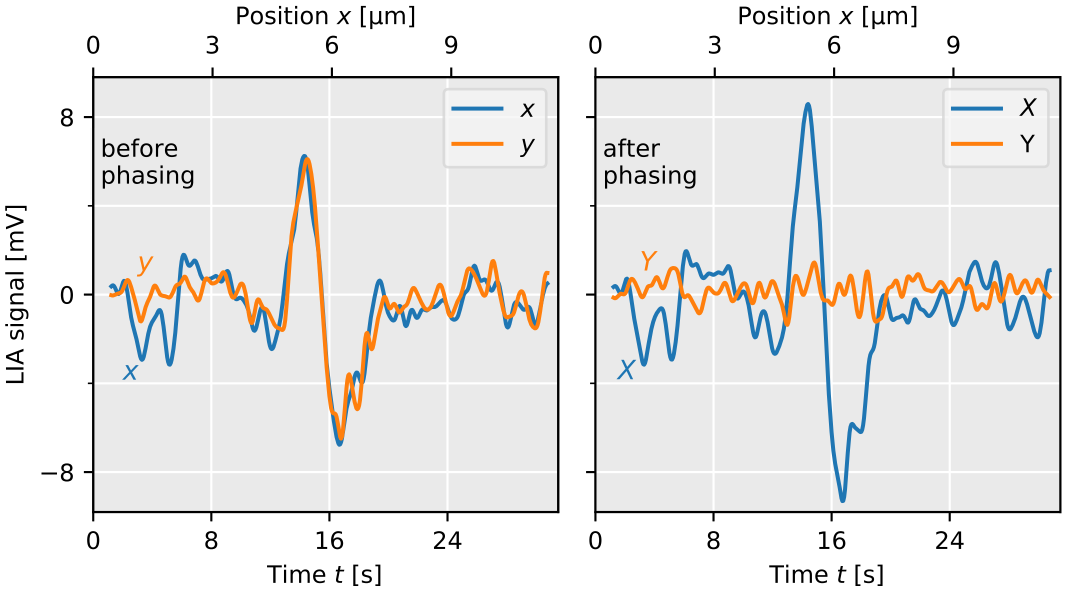

Figure C.4: The software lock-in amplifier output channels (a) before phasing and, (b) after phasing. The best-fit parameters (Eq. C.4) were $\Delta f = 4.8\,\mathrm{mHz}$ and $\theta_0 = 0.26\,\mathrm{rad}$.

where the frequency Δf is a correction to the reference frequency (typically 0 to $10\,\mathrm{mHz}$) and θ_0 is the lock-in amplifier phase. The under-braced term is the ordinary phase difference; the rest of the bracketed expression accounts for phase reversals caused by a change in sign of E_{mod}. With this correction, a phase difference $\Delta\theta = \pi$ contributes 0 to the sum, since $\Delta\theta = \pi$ corresponds to a signal of the opposite sign. After performing the minimization, the phased lock-in amplifier output is

$$Z = X + Yj = z\,\exp\big(-2\pi j \Delta f\,t - \theta_0\,j\big), \tag{C.5}$$

plotted in Figure C.4b. The electric field along the modulation direction was $E_{\mathrm{pm}} = X/A_{\mathrm{pm}}$, where A_{pm} was the zero-to-peak amplitude of the position modulation.

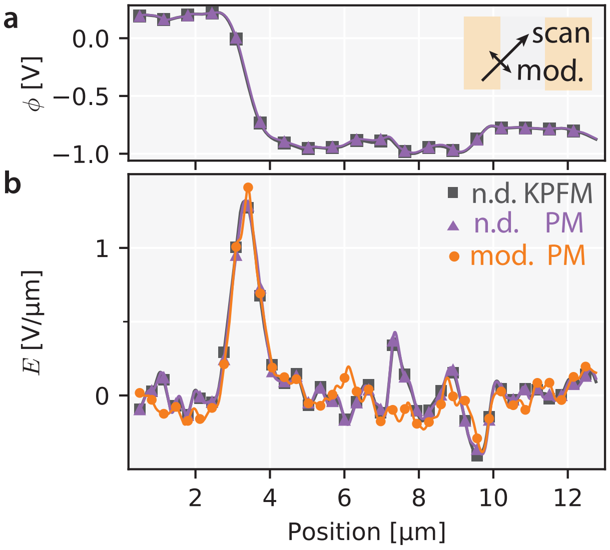

Figure C.5: Comparison of electric fields measured using PM-KPFM and KPFM. (a) Surface potential measured using KPFM and *position-modulated* KPFM. The scan and modulation are at $+45$ and -45 degrees relative to the x-axis respectively (inset). (b) Comparison of the electric fields measured using KPFM and *position-modulated* KPFM. Numerical derivative of the KPFM surface potential (squares), numerical derivative of the *position-modulated* KPFM surface potential (triangles), and the modulation component of *position-modulated* surface potential (circles). Experimental parameters: position-modulation amplitude $A_{\mathrm{pm}} = 30\,\mathrm{nm}$, frequency $f_{\mathrm{pm}} = 4.5\,\mathrm{Hz}$, tip velocity $v = 414\,\mathrm{nm\,s^{-1}}$.

C.4 Slow axis KPFM electric field measurement

The KPFM surface potential shown in Fig. 4.3 was not filtered. The electric field along the scan axis (Fig. 4.3d) was calculated using Equation C.2 with $\Delta x = 90\,\mathrm{nm}$. Before calculating the electric field along the slow-scan axis, the KPFM image was filtered along the y-axis using a filter designed using the same procedure as H_{pm}, with the same spatial bandwidth $\nu = 2.2\,\mathrm{\mu m^{-1}}$.

C.5 Modulating and scanning in perpendicular directions

Figure C.5 shows the new position-modulated KPFM measurement applied to measure perpendicular components of the electric field simultaneously. We scanned across the transistor channel (Fig. 4.2) at an angle of $+45$ degrees relative to the x-axis and applied a position modulation perpendicular to the scan axis (Fig. C.5a inset). In order to apply the modulation at an angle, an additional summing circuit SUM3 (AD711 op-amp) was used to add the modulation to the x-axis as well as the y-axis:

$$V_{\mathrm{x-piezo}} = G_{\mathrm{amp}} \underbrace{\left(V_{\mathrm{x,ramp}}(t) + V_{\mathrm{OSC}}(t)\right)}_{\text{SUM3}} \tag{C.6}$$

$$V_{\mathrm{y-piezo}} = G_{\mathrm{amp}} \underbrace{\left(V_{\mathrm{y,ramp}}(t) + V_{\mathrm{OSC}}(t)\right)}_{\text{SUM2}} \tag{C.7}$$

where the sums are labeled as in Fig. C.1 and $V_{\mathrm{x,ramp}}$ and $V_{\mathrm{y,ramp}}$ are the X and Y voltage outputs from the NI PCI-6259.

While the scan and modulation signals measure perpendicular components of the electric field in the Fig. C.5a experiment, both observe the same electric field drop at the transistor contacts because there the electric field was entirely along the x-axis (Fig. 4.2c). At the contacts, the electric field along the scan direction is $E_{\mathrm{scan}} = E_x \cos(45°) = E_x/\sqrt{2}$. Likewise, the electric field along the modulation direction is $E_{\mathrm{mod}} = E_x \cos(-45°) = E_x/\sqrt{2}$. Fig. C.5b shows that the position-modulated measurement tracks the electric field as measured by other KPFM measurements. At the source contact, the measured electric field agrees with the electric field measured in Fig. 4.2d.

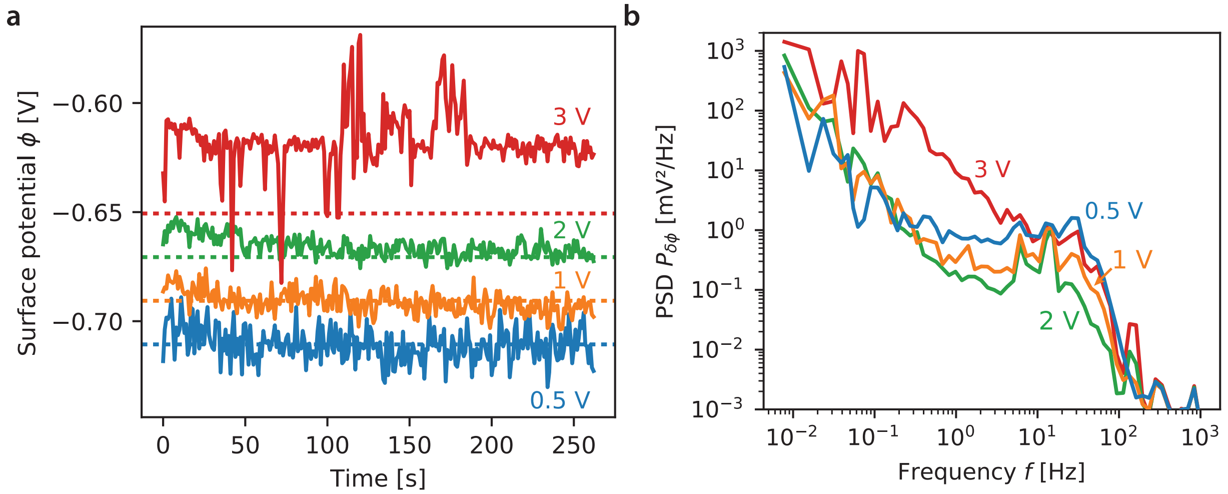

Figure C.6: FM-KPFM surface potential noise. (a) Surface potential *versus* time measured through the FM-KPFM feedback loop for different modulation voltages $V_{\mathrm{m}}/\sqrt{2} = V_{\mathrm{rms}} = 0.5$, 1.0, 2.0 and $3\,\mathrm{V}$. (b) Power spectral density of surface potential fluctuations $P_{\delta\phi}$ calculated from the data in (a).

C.6 Noise in FM-KPFM

We measured the surface potential noise under the optimized conditions used in this experiment. We collected surface-potential-versus-time data over the drain electrode ($V_{\mathrm{D}} = -1\,\mathrm{V}$) with the sample stationary (Fig. C.6a). The surface potential had some high-frequency noise plus slow drift on the seconds and longer time scale.

To better illustrate the surface potential noise *versus* frequency, Fig. C.6b plots the power spectral density of surface potential fluctuations calculated from the time domain data in Fig. C.6a. The slow drift caused increased spectral density below $1\,\mathrm{Hz}$. For rms-modulation voltages $2\,\mathrm{V}$ or less, the low-frequency noise was not cantilever frequency noise, because the contribution of cantilever frequency noise $P_{\delta f}$ to surface potential noise is inversely proportional to the modulation voltage V_{m}. There was a small region from approximately 1 to $10\,\mathrm{Hz}$ where the surface potential noise was minimized. For rms-modulation voltages $2\,\mathrm{V}$ or less, the surface potential noise in the majority of this region was inversely proportional to the modulation voltage V_{m}. This observation is consistent with voltage noise arising from position-detection noise [61]. The power spectral density of surface potential fluctuations exhibited a roll-off between 10 and $20\,\mathrm{Hz}$ due to the feedback-network filter, as expected.

The electric field calculated by numerically differentiating the FM-KPFM image along the slow-scan axis incorporates surface potential noise at temporal frequencies near the inverse line-scan time $(8\,\mathrm{s/line})^{-1} \sim 0.1\,\mathrm{Hz}$, where noise is increased by the slow drift. The PM-KPFM measurement incorporates surface potential noise at frequencies near $f_{\mathrm{pm}} = 4.5\,\mathrm{Hz}$, where overall surface potential noise is near a minimum.

APPENDIX D

VARYING THE WORKFUNCTION OF PEDOT:PSS ELECTROCHEMICALLY

This appendix includes experimental results and conclusions from a project performed in collaboration with undergraduate student Xueying Li [122].

Introduction — Kelvin probe force microscopy (KPFM) and electric force microscopy (EFM) measurements have shown striking differences in surface potential above organic bulk heterojunction solar cell films depending on the background charge carrier density (charge density before the solar cell has been exposed to light) [123, 38]. This background carrier density is determined by the workfunction of the underlying electrode. The goal of this project was to study the effect of background charges systematically, using the same material, but varying the workfunction.

In our group, undergraduate Joseph Singh and graduate student Louisa Smieska implemented a procedure to vary the workfunction of poly(3,4-ethylenedioxythiophene) (PEDOT) systematically. PEDOT films had been electro-polymerized [124] and electrochemically doped with ClO_4^- ions [125]. To be able to accurately measure the workfunction of the doped PEDOT, they also fabricated samples with alternating stripes of PEDOT and a platinum reference together within the $20\,\mu\mathrm{m}$ scan range of our microscope (as in Fig. D.1a). Preliminary measurements on these samples in the Marohn group's custom EFM showed that the workfunction of PEDOT could be varied by nearly a volt. We sought to extend on this work by depositing PEDOT on a transistor substrate.

In order to have a uniform PEDOT:ClO_4 thin film with controllable thickness, electrochemical polymerization was used in this study. The work of Damlin et al. have shown that the thickness and morphology of PEDOT:PSS films affect their electric properties

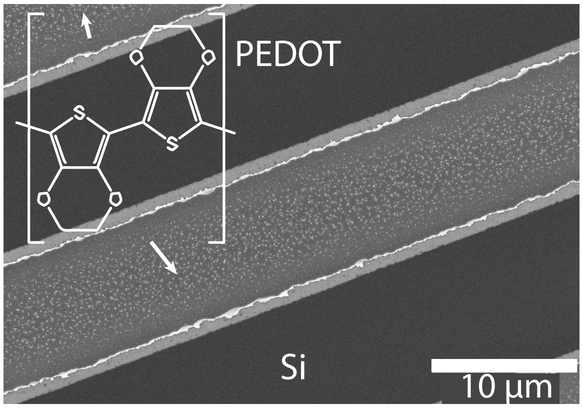

Figure D.1: Scanning electron micrograph of patterned PEDOT on silicon.

[126]. Thus, our desired PEDOT:ClO_4 film should be thicker than $40\,\mathrm{nm}$ and uniform.

Prior work — Several groups have demonstrated work on adjusting the workfunction of PEDOT:PSS or other polymers. Friend et al. modified the workfunction of PEDOT:PSS with addition of glycerol and achieved a drop of $0.12\,\mathrm{eV}$ in the workfunction [127]. Schwartz attached phosphonic acids to the PEDOT:PSS films to adjust the workfunction over a range of approximately $0.8\,\mathrm{eV}$ [128]. The Armstrong group reported a method to electrodeposit e-P3HT with an easily tuned workfunction [129].

In order to effectively adjust the workfunction of PEDOT, we need to find an effective range of doping level. The effect of polymerization current density and monomer concentration on the formation of the film structure was studied by Kvarnström et al. [130]. They electrochemically doped PEDOT:PSS in 0.1 M TBAPF6-acetonitrile. They showed that a wide range of doping levels from n-doping to p-doping can be achieved by electrochemical redox reactions. However, they also found that the workfunction of the doped

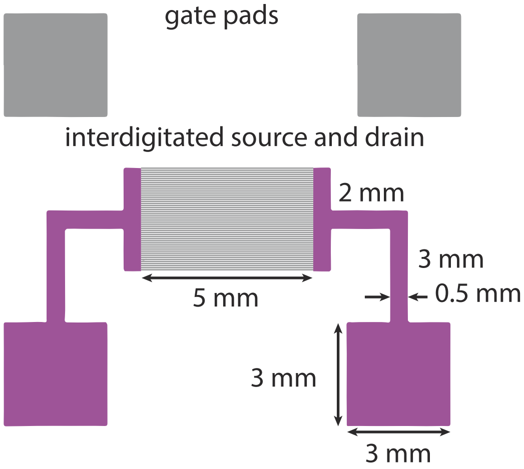

Figure D.2: The CAD file showing the geometry of the transistor substrate.

films can change over time, especially in the first few minutes after doping the film.

D.1 Experimental

Transistor substrates — The transistor substrates we used in this experiment are field-effect transistors with a highly n-doped silicon gate, $300\,\mathrm{nm}$ thermal SiO_2 insulator, and $100\,\mathrm{nm}$ thick evaporated gold source and drain electrodes.

We used relatively thick gold electrodes because of concerns over the resistance of the traces significantly impacting the thickness and uniformity of the PEDOT films. Our reasoning was as follows. We can write the resistance R of a thin metal film as

$$R = \rho\frac{\ell}{A} = \rho\frac{\ell}{wt} \tag{D.1}$$

where A is the area, ℓ is the length, w is the width, and t is the thickness. For an arbitrary collection of traces, the resistance is

$$R = \underbrace{\frac{\rho}{t}}_{R_{\mathrm{sh}}[\Omega/\mathrm{square}]} \sum \frac{\ell}{w} \tag{D.2}$$

where the underbraced term is the metal film's sheet resistance. To calculate the resistance, we need to know the length ℓ and width w of the trace carrying the voltage to the transistor. For the transistor substrates designed by Nikolas Hoepker, the dimensions are labeled in Fig. D.2. For the transistor with $5\,\mu\mathrm{m}$-gap,

$$R_5 = \frac{\rho}{t}\left(14\,\mathrm{sq.} + \frac{5000\,\mu\mathrm{m}}{5\,\mu\mathrm{m}}\right) \approx 1000\frac{\rho}{t}. \tag{D.3}$$

For the transistor with $15\,\mu\mathrm{m}$-gap,

$$R_{15} = \frac{\rho}{t}\left(14\,\mathrm{sq.} + \frac{5000\,\mu\mathrm{m}}{15\,\mu\mathrm{m}}\right) \approx 350\frac{\rho}{t}. \tag{D.4}$$

There is a significant resistance to get current to the farthest away portion of a $50\,\mathrm{nm}$-thick platinum electrode ($2.1\,\mathrm{k\Omega}$ for the $5\,\mu\mathrm{m}$-gap transistor, about $700\,\Omega$ for the $15\,\mu\mathrm{m}$-gap transistor; platinum resistivity $\rho = 1.06 \times 10^{-7}\,\Omega\,\mathrm{m}$). The corresponding voltage drop would be a substantial 0.14 to $0.42\,\mathrm{V}$ at the maximum current $I = 200\,\mu\mathrm{A}$. We minimize resistive losses by using $15\,\mu\mathrm{m}$-gap transistor and $100\,\mathrm{nm}$-thick gold electrodes, which limits the maximum resistance to $80\,\Omega$, corresponding to a maximum voltage drop of $16\,\mathrm{mV}$ at $I = 200\,\mu\mathrm{A}$.

Electrochemical polymerization — For the preparation of the polymer films, 20 mM commercial 3,4-ethylenedioxythiophene (EDOT; Sigma Aldrich, 97%) and 0.1 M tetrabutylammonium (Sigma Aldrich, $\geq$99.0%) were dissolved in acetonitrile to make the monomer solution for electrochemical polymerization. The EDOT was stored in a refrigerator. Prior to the polymerization, gold transistor substrates were cleaned thoroughly. Photoresist was removed by rinsing with acetone, isopropyl alcohol, and soaking in Microposit Remover 1165 (Rohm and Haas) at least 8 hours. Then the transistors were sonicated in acetone/isopropyl alcohol, rinsed and scrubbed using a cleanroom swab with soapy water, sonicated in distilled water, and electrochemically cycled in 0.1 M potassium

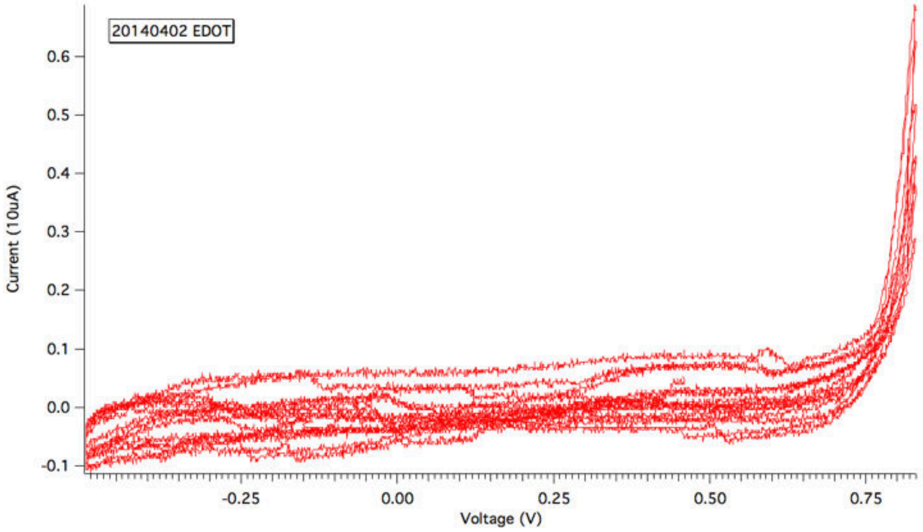

Figure D.3: Cyclic voltammetry of electrochemical polymerization of PEDTO:ClO_4 on gold in acetonitrile using EDOT monomer and TBAP electrolyte. The voltage is relative to a Ag/Ag^+ reference electrode. Adapted from Li, Ref. 122.

hydroxide. Considering roughness and uniformity, the films were grown through multiple (2 to 10) cycles of cyclic voltammetry from $-0.5\,\mathrm{V}$ to $0.83\,\mathrm{V}$ vs. Ag/Ag^+ (Fig. D.3). The cyclic voltammetry scan rate was $5\,\mathrm{mV\,s^{-1}}$. The electrochemical reaction cell was set up as shown in Fig. D.4. Gold on the transistor was used as the working electrode, platinum wire was used as the counter electrode, and Ag/Ag^+ was used as the reference electrode. The electrochemical polymerization was performed within 24 hours of the substrate cleaning.

Electrochemical doping — Later the films were doped by holding the voltage for 5 minutes in 0.1 M TBAP solution in acetonitrile. According to previous work by our group and Petr et al., the doping level was determined to be in the range of -0.5 V to 0 V [125]. This range ensures the films are p-doped. We confirmed that this doping range was appropriate with the cyclic voltammogram shown in Fig. D.5, with labeled regions corresponding to n- and p-doping.

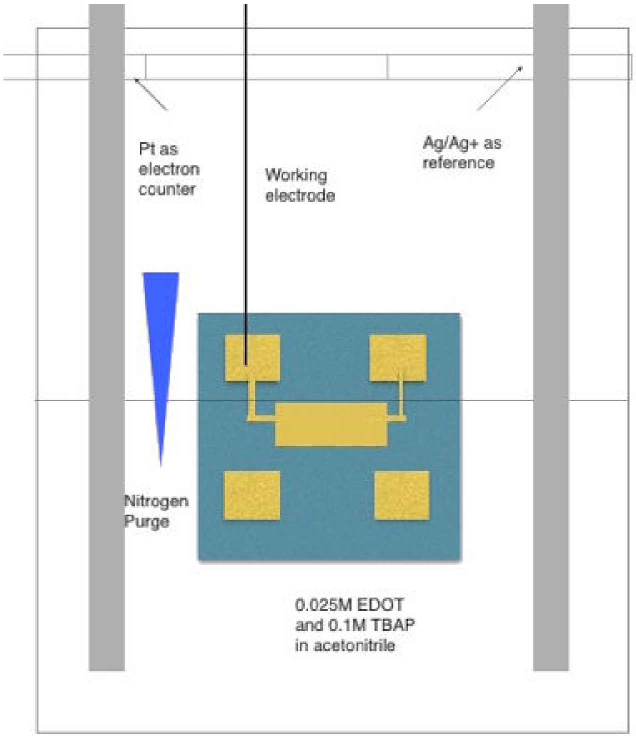

Figure D.4: Setup of electrochemical polymerization. Adapted from Li, Ref. 122.

The open circuit voltage was tracked in each trial from polymerization to doping. The PEDOT film was always doped to at least 200 mV different voltage to show the tunability of the workfunction. After rinsing with acetonitrile, the open circuit voltage of the electrode was measured again. This final measured open circuit voltage is plotted on the x-axis of Figure D.6. The doping and measurements were done within 2 hours to avoid significant surface potential drop.

D.2 Results

Figure D.6 summarizes the results of many KPFM measurements on electrochemically grown and doped PEDOT films. Reasonably smooth films of $\sim 100\,\mathrm{nm}$ thickness were produced. The surface potential measured via KPFM is the difference in surface potential

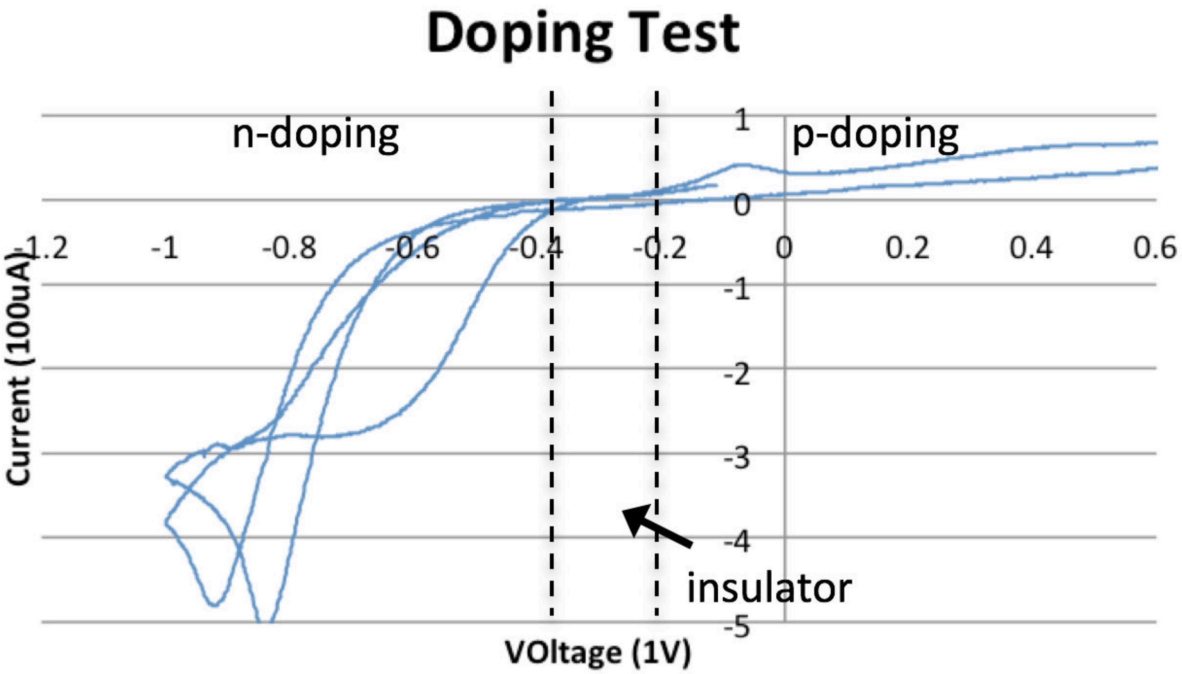

Figure D.5: Cyclic voltammogram showing the range of voltages required to achieve n-doping and p-doping of PEDOT:ClO$_4$. Experimental parameters: 0.02 M TBAP electrolyte in acetonitrile. The voltage is relative to a Ag/Ag$^+$ reference electrode. Adapted from Li, Ref. 122.

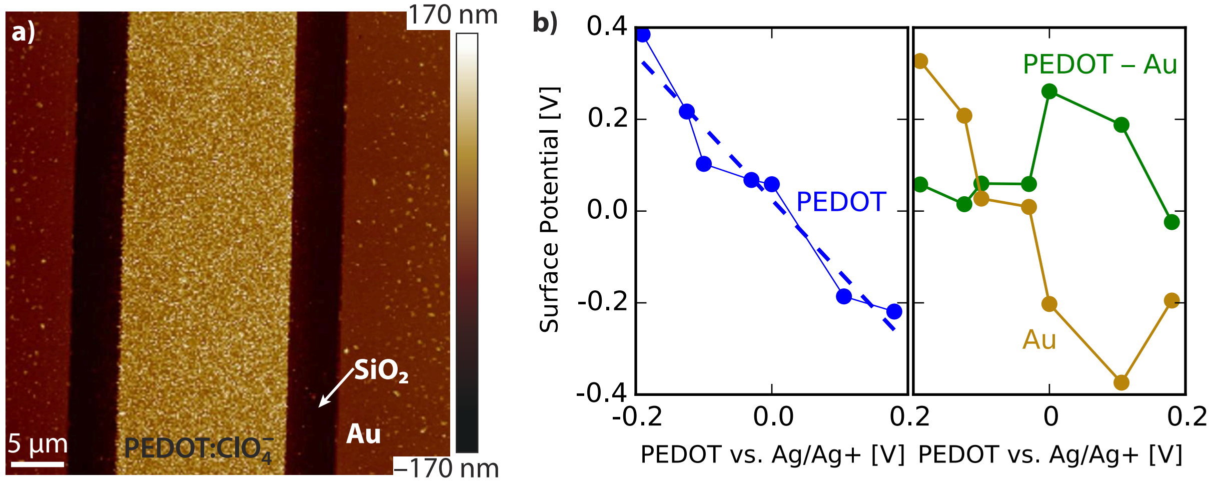

Figure D.6: Modifying charge-injection barriers. (a) PEDOT is electro-polymerized into one contact of a field effect transistor and ionically doped. (b) Left: The surface potential of the resulting PEDOT depends linearly on the electrochemical potential applied during the doping step. Right: Surface potential over the gold electrode. The potential plotted on the x-axis was the open circuit voltage read from the potentiostat after rinsing and drying the film. Li, Dwyer, and Marohn, unpublished.

between the sample material and the platinum-coated KPFM cantilever tip. The measured PEDOT workfunction showed a remarkably clear trend with the applied doping potential (Fig. D.6b). It is unclear why the nearby gold electrode, left uncoated as an internal reference, also varied systematically in the same way. (Fig. D.6(b)). The slope of the trend line of the PEDOT:ClO_4 surface potential versus equilibrium potential was -1.57, different from the expected value of -1.

In future work, therefore, we should shift the electrode workfunction by treating gold electrodes with a self-assembled monolayer [131, 132, 133, 134, 135, 136, 49, 137, 138]. In particular, the work of Liscio and co-workers creating asymmetric electrodes by selectively modifying one of the inter-digitated gold source-drain electrodes looks particularly promising [132].

APPENDIX E

DISSIPATION MEASUREMENTS ON ORGANIC SEMICONDUCTORS

Charge-charge interactions play an important role in the operation of organic electronic devices. Previous work has shown evidence that these interactions suppress noise in electric force microscopy measurement by many orders of magnitude relative to the free diffusion of charge carriers. In this appendix, we outline calculations that suggest the effect of charge carrier interactions on cantilever dissipation could be used to measure the local charge mobility in organic semiconductors. This work was a collaboration with Swapna Lekkala, Nicolas Hoepker, and Roger Loring. I have updated the discussion of this work by incorporating some of the insights from the impedance spectroscopy formulation of electric force microscopy presented in Chapter 6.

E.1 Introduction

Fluctuation microscopy is a scanned probe microscopy (SPM) technique that quantifies the fluctuating forces between an atomic force microscope (AFM) cantilever tip and sample [139]. These fluctuating forces provides information complementary to other SPM techniques that measure forces in phase with the cantilever oscillation.

Fluctuations can be measured both directly and indirectly. Jitter and the cantilever frequency power spectrum measure fluctuations in the tip-sample force in phase with cantilever oscillation. Jitter and the cantilever frequency power spectrum can probe surface potential, electric field, electric field gradient, and dielectric fluctuations at frequencies $f < 100\,\mathrm{Hz}$. At higher frequencies, jitter or sample-induced cantilever frequency noise is obscured by the detector noise. Sample-induced non-contact friction is a measure of the fluctuating out of phase tip-sample force at the cantilever resonance frequency (from tens to hundreds of kilohertz). This sample-induced friction or dissipation is linked to sample fluctuations by the fluctuation-dissipation theorem [140, 141, 142].

The fluctuating forces between a charged cantilever tip oscillating tens to hundreds of nanometers above a charged sample have the potential to reveal a wealth of information about the microscopic, time-varying electric fields and electric field gradients in semiconductor devices. Fluctuation microscopy could allow for spatially-resolved measurements of charge transport properties, such as charge mobility. For instance, Stowe and co-workers imaged dopant densities in silicon using fluctuation microscopy [143]. However, the usefulness of these techniques has been limited by poor theoretical understanding of the origins of the fluctuations.

Measuring charge mobility in organic semiconductor devices is challenging because the charge mobility can depend strongly on electric field [144, 145], charge density [146, 147], and frequency. Strong contact effects can also dramatically alter device performance, making it difficult to determine material properties from device measurements [148]. The standard measurement for inorganic semiconductors, using the Hall effect, does not work for low mobility semiconductors, which have carriers that are largely localized. For organic semiconductors, charge mobility is most commonly measured by collecting bulk current-voltage curves on the semiconductor in a field effect transistor (FET) geometry. Calculating this FET mobility ignores contact effects and requires the (incorrect!) assumption that charge mobility is independent of the electric field and charge density. Furthermore, this assumption prevents the technique from providing information about how the charge mobility does in fact depend on electric field and charge density.

Another common charge mobility measurement, time-of-flight (TOF) mobility, typically measures the mobility at a charge density many orders of magnitude smaller than the operating-device charge density because charge carriers must be optically excited by a short-duration light pulse. It difficult to extrapolate TOF mobility to the mobility in organic semiconductor devices because mobility can depend strongly on charge density [149]. Time-resolved microwave conductivity is another useful technique for measuring mobility, but since charges in low-mobility materials only move a few nanometers over the course of the measurement, mobilities can be greatly overestimated since charges do not have to cross grain boundaries—they may not even have to move to another molecule [150].

We believe fluctuation microscopy is well-poised to alleviate some of the problems with measuring charge mobility in organic semiconductors. Over organic small molecules and polymers, fluctuation microscopy measurements and close collaboration with theorists produced a linear response theory that explained the dependence of the experimental cantilever-frequency fluctuations on the electric field and electric field gradient fluctuations arising from thermal dielectric fluctuations [60, 151]. Extensions of this work showed that strong charge-charge interactions, which dramatically affect the performance of organic semiconductor devices [152, 153], suppress AFM cantilever frequency noise by 3–5 orders of magnitude relative to that predicted by free diffusion [61, 80].

Quantitative comparisons to experimental data, however, were limited by differences between the experimental transistor geometry and the simulated geometry, which was a semi-infinite slab of the organic material. Recently this theory has been extended to reflect the finite thickness of the sample and that charge transport only takes place in a narrow layer of the film near the semiconductor-insulator interface [81].

The new theory of Lekkala and co-workers explains a striking result from previous work measuring jitter over a molecularly doped polymer transistor. Contrary to the linear response theory, which predicted decreasing jitter J with increasing charge density ($J \propto \rho^{-1/2}$), the measured jitter was independent of charge density. However, when the theory was modified to confine charge carriers to a thin layer near the semiconductor-insulator interface, the rest of the organic film effectively screened low frequency charge carrier induced noise, resulting in a predicted jitter independent of charge density. At higher frequencies the rest of the film only minimally screens the noise. Therefore we predict that a positive signature of charge carrier interactions can be observed by measuring sample-induced noise at higher frequencies.

At higher frequencies, sample fluctuations cannot be measured directly because of photodetector noise [60]. These fluctuations can still be quantified by measuring their effect on the cantilever dissipation. We expect to see both increasing friction at low charge densities as the charge carriers diffuse freely and contribute to the fluctuations linked to cantilever dissipation. At higher charge densities, we should see the dramatic impact of charge carrier interactions, which suppresses fluctuations, resulting in reduced cantilever dissipation at high charge densities.

E.1.1 Sample preparation

Transistor substrates with a $5\,\mu\mathrm{m}$ channel width, $315\,\mathrm{nm}$ silicon oxide insulator layer, and gold source, drain and gate contacts were fabricated in the Cornell Nanofabrication Facility (CNF) on n-Si wafers [80].

Based on the results shown in Fig. E.3 and Fig. E.4, we would like a sample thinner than $100\,\mathrm{nm}$. Nikolas Hoepker's samples have typically been $70(7)\,\mathrm{nm}$. For thinner samples, we could use a different solvent, such as toluene or chloroform, or spin faster [154].

For cleaning and sample preparation, see Ref. 80. We also wash with soapy water and scrub with cleanroom swabs and Aquet detergent.

E.2 Practical Experimental Considerations

We use the organic semiconductor TPD (N,N'-Bis(3-methylphenyl)-N,N'-diphenylbenzidine) because it has a low-enough mobility that fluctuations can be observed at the cantilever's kHz resonance frequency. The maximum carrier density is determined by the degree of loading of the TPD in the polystyrene binder. A 10 percent loading corresponds to a density $\rho_{\mathrm{TPD}} = 1.4 \times 10^{26}\,\mathrm{m}^{-3}$ [155, pp. 393–402]. The accessible areal carrier densities in a transistor geometry, calculated from the capacitance, are

$$\rho_A = \frac{V_{\mathrm{g}} \epsilon_0 \epsilon_{\mathrm{i}}}{e h_{\mathrm{i}}}, \tag{E.1}$$

where V_{g} is the transistor gate voltage, ϵ_{i} the dielectric constant of the insulator, and h_{i} the thickness of the insulator. The three dimensional carrier density is

$$\rho = \frac{\rho_A}{h_{\mathrm{trans}}} = \frac{\epsilon_0 \epsilon_{\mathrm{i}} V_{\mathrm{g}}}{e h_{\mathrm{i}} h_{\mathrm{trans}}}, \tag{E.2}$$

where transport occurs in a layer of thickness h_{trans}, typically estimated to by about $1\,\mathrm{nm}$ [156, 157]. Knowing both the carrier density and the mobility, we can estimate the contribution to the dielectric constant from conductivity,

$$\epsilon''(f) = \frac{\sigma_0}{\epsilon_0 \omega} = \frac{\rho \mu e}{2\pi \epsilon_0 f}. \tag{E.3}$$

Using estimates of the charge density $\rho = 1 \times 10^{23}\,\mathrm{m}^{-3}$ and the mobility $\mu = 1 \times 10^{-7}\,\mathrm{cm}^2/\mathrm{V}/\mathrm{s}$, we calculate $\epsilon''(50\,\mathrm{kHz}) \approx 0.1$. This indicates that significant contributions to the dielectric constant should be visible in these low mobility materials. We can also look at higher frequencies or lower charge densities, with a lower bound set by an estimated intrinsic carrier density $\rho_i \approx 10^{-5}\,\rho_{\mathrm{TPD}}$ [74].

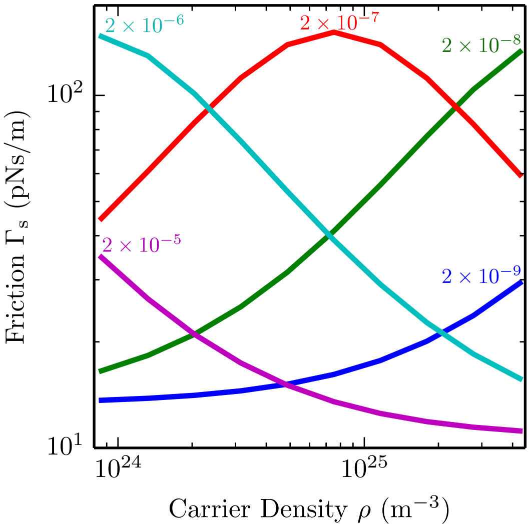

Figure E.1: Perpendicular geometry sample-induced friction vs. carrier density for a variety of mobility values, labeled in $\mathrm{cm}^2\mathrm{V}^{-1}\mathrm{s}^{-1}$. The charge density range corresponds to a transistor gate voltage range of 1 to $50\,\mathrm{V}$. The sample has thickness $70\,\mathrm{nm}$ and relative dielectric function $\epsilon_s = 3.4 - 0.05i$. The cantilever has resonance frequency $75\,\mathrm{kHz}$, quality factor 2000, and spring constant $2\,\mathrm{Nm}^{-1}$. The tip-sample voltage and distance were $5\,\mathrm{V}$ and $100\,\mathrm{nm}$.

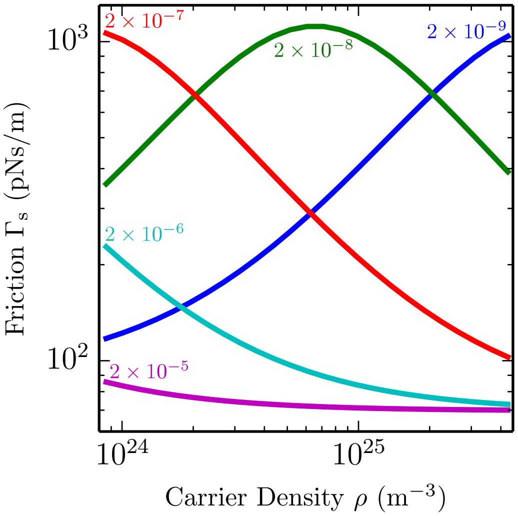

Figure E.2: Parallel geometry sample-induced friction vs. carrier density for a variety of mobility values, labeled in $\mathrm{cm}^2\mathrm{V}^{-1}\mathrm{s}^{-1}$. The charge density range corresponds to a transistor gate voltage range of 1 to $50\,\mathrm{V}$. The sample has thickness $70\,\mathrm{nm}$ and relative dielectric function $\epsilon_s = 3.4 - 0.05i$. The cantilever has resonance frequency $6.6\,\mathrm{kHz}$, quality factor 8.4×10^4, and spring constant $1\,\mathrm{mNm}^{-1}$. The tip-sample voltage and distance were $5\,\mathrm{V}$ and $100\,\mathrm{nm}$.

E.3 Theoretical Predictions

Using the theory from Ref. 81 for a dielectric spacer layer over a semi-infinite semiconductor, we can predict what mobilities correspond to experimentally observable charge densities. In Fig. E.1, we see the theoretical predictions for a typical commercial cantilever, which vibrates perpendicularly to the sample surface. Mobilities from 10^{-8} to $10^{-6}\ \mathrm{cm^2V^{-1}s^{-1}}$ are the region where carrier-induced friction is most easily visible. The mobility of TPD can be tuned by adjusting the weight percentage of TPD in the polystryrene binder. If we prepare samples of weight percentage between approximately 10 and 50 percent, we should be able to access this mobility range [158, 159]. Fig. E.3 shows the effect of sample thickness on the measured friction and includes the approximate minimum detectable friction for a good commercial cantilever. Similarly, Fig. E.4 shows the effect of tip-sample distance on the measured friction. Interestingly, for a thick sample layer, the characteristic peak of the friction becomes much less pronounced at small distances. This is not the case for thin samples (presumably the effect is related to the ratio $d/h_{\mathrm{dielectric}}$).

In conclusion, we should be able to measure the effects of sample-induced friction using commercial cantilevers if the cantilevers have a sufficiently high quality factor, the sample is thin, and the sample mobility is of the order $10 \times 10^{-8}\,\mathrm{cm^2V^{-1}s^{-1}}$. The estimated maximum friction from Ref. 81 gives an idea of the relevant factors for maximizing sample-induced friction,

$$\Gamma_{\perp}^{\mathrm{max}} \approx \frac{V_{\mathrm{ts}}^2 c(d)^2}{8\pi^2 \epsilon_0 f_c d^3}. \tag{E.4}$$

If we roughly approximate the tip-sample capacitance $c(d)$ as proportional to the tip-radius R_{tip}, we can write an approximate signal-to-noise ratio for the friction measure-

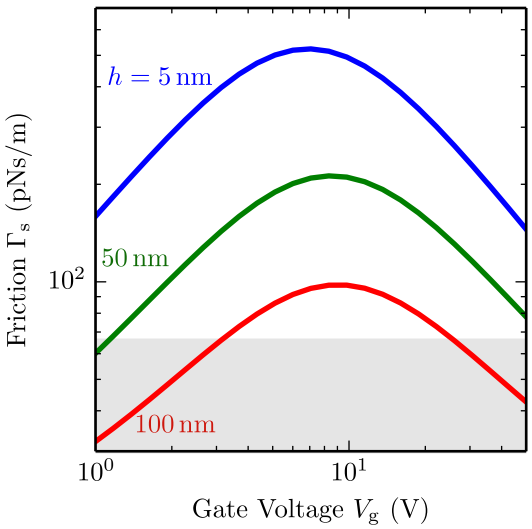

Figure E.3: Perpendicular geometry sample-induced friction vs. gate voltage for a variety of semiconductor thicknesses h. The gray region of the graph indicates an estimated detection limit for the simulated cantilever ($\Gamma_i = 2200\,\mathrm{pNms}^{-1}$). The semiconductor mobility is $2 \times 10^{-7}\,\mathrm{cm}^2\mathrm{V}^{-1}\mathrm{s}^{-1}$ and relative dielectric function $\epsilon_s = 3.4 - 0.05i$. The cantilever has resonance frequency $75\,\mathrm{kHz}$, quality factor 2000, and spring constant $2\,\mathrm{Nm}^{-1}$. The tip-sample voltage and distance were $5\,\mathrm{V}$ and $100\,\mathrm{nm}$.

ment

$$\mathrm{SNR} \propto \frac{\Gamma_s}{\Gamma_i} \propto \frac{R_{\mathrm{tip}} Q}{k_c} \frac{V_{ts}^2}{d^3}. \tag{E.5}$$

E.4 Modulating Tip Charge

Originally, we thought that we could measure fluctuations at different frequencies using friction (normally linked to sample fluctuations at the cantilever resonance frequency f_c) if we modulate the tip charge at some frequency f_{m}. We would expect the modulation to cause sample-induced dissipation related to sample fluctuations at $f_{\mathrm{m}} \pm f_{\mathrm{c}}$. However, the analysis we performed in Chapter 6 shows that the dissipation signal goes to zero for $f_{\mathrm{m}} \gg f_{\mathrm{c}}$. This matches our experimental observations of dissipation when modulating the cantilever tip charge at high frequency over cesium lead bromide perovskite and a

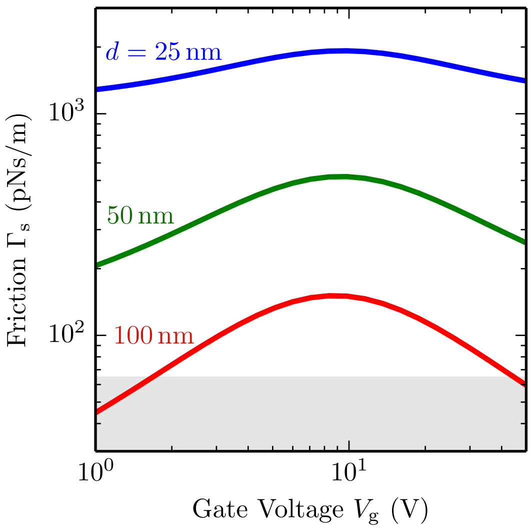

Figure E.4: Perpendicular geometry sample-induced friction vs. gate voltage for a variety of tip-sample distances d. The gray region of the graph indicates an estimated detection limit for the simulated cantilever ($\Gamma_i = 2200\,\mathrm{pNms^{-1}}$). The semiconductor has mobility $2 \times 10^{-7}\,\mathrm{cm^2V^{-1}s^{-1}}$, thickness $70\,\mathrm{nm}$ and relative dielectric function $\epsilon_s = 3.4 - 0.05i$. The cantilever has resonance frequency $75\,\mathrm{kHz}$, quality factor 2000, and spring constant $2\,\mathrm{Nm^{-1}}$. The tip-sample voltage and distance were $5\,\mathrm{V}$ and $100\,\mathrm{nm}$.

"kitchen-sink" perovskite blend (see Chapter 6).

E.5 Future Directions

In order to observe the predicted dissipation related to charge mobility, it would be important to deposit a very thin active layer with a relatively low mobility. It may help to switch to a higher frequency cantilever (potentially as high as practical in the microscope—perhaps $500\,\mathrm{kHz}$ with a higher-bandwidth photodetector). With a higher frequency cantilever, the dissipation peak is moved to higher charge density. It would also be highly beneficial to have a material with a low background charge density, so that some changes in dissipation could be observed even if the sample mobility were higher than anticipated.

The other insight from the perovskite work is that *ionic* conductors may be a very good fit for this kind of measurement. It is difficult to observe sample-induced dissipation in electronic materials because the sample's charge density needs to be very low for the sample's characteristic timescale $\epsilon/(\rho\mu e)$ to be equal to the cantilever's characteristic timescale ω_{c}^{-1}. The ionic mobility is typically much lower so it could be much easier to observe a dissipation peak near the cantilever resonance frequency. A thin layer ionic conductor or a mixed electronic-ionic conductor may be a good material for scanned probe microscopy studies [160, 161]. These materials are also potentially useful for a variety of energy applications.

APPENDIX F

FREQDEMOD ON 64-BIT LABVIEW

To use 64-bit LabView, I had to recompile all of the C extensions that we use. I was able to get it to work by doing the following.

- Install mingw64
- In the `mingw64` folder, use the `mingw64` command prompt. Running `gcc --version` should show the `mingw64` version of the gcc compiler.
- For `c` files with minimal dependencies, just compile with the `mingw64` compiler, and everything should work fine.
- If you are relying on other pre-compiled C libraries (such as `fftw3`), you need to acquire 64-bit compiled DLLs (or compile them yourself). For future reference, I was able to recompile `freq_demod` using the command,

```
gcc -c freq_demod.c -o freq_demod64.o -Ifftw-3.3.4-dll64
gcc -shared -static-libgcc freq_demod64.o -o freq_demod64.dll \
    -Lfftw-3.3.4-dll64 -Ifftw-3.3.4-dll64 -lfftw3 -lm
```

APPENDIX G

CUSTOM-BUILT CIRCUITS

G.1 Current source

G.2 Useful parts

This section contains a list of useful circuit parts for various applications, their datasheets, and key parameters.

G.2.1 15 Volt Supply Op-amps

On our typical ±15 V power supplies, we run a variety of circuits using op-amps to filter, add, and attenuate or amplify signals. The summing and tabling circuits are typically operated at low frequencies; perhaps a maximum signal frequency of 1 to 10 kHz. For these circuits, low-noise, low-offset most important operational parameter is probably the offset voltage. For circuits operating at the cantilever frequency (positive feedback circuit, cantilever signal conditioning circuit, for example), the slew rate and gain bandwidth product are also important.

AD711 Standard op-amp used in our designs. Reasonably fast (20 V/μs), reasonable offset voltage (0.5 mV), etc.

OP07D Capable of operating from both ±2.5 to ±18 V. Low offset voltage (40 μV typical). More precise version of standard OP07.

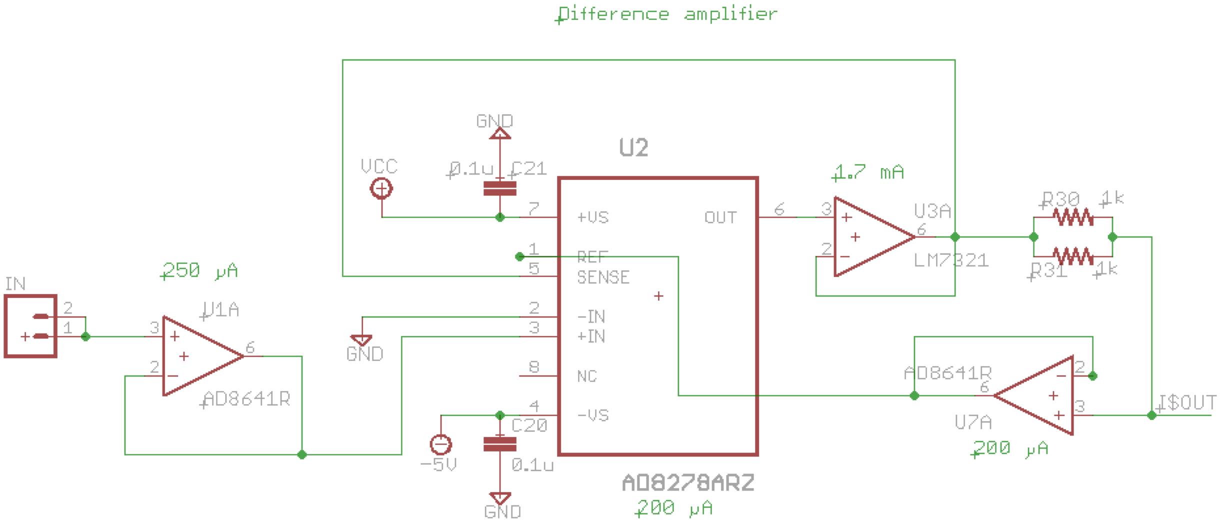

Figure G.1: The first part of the constant current source circuit. The green labels near each part show the estimated current drawn by the part.

OP184/284/484 Rail-to-rail input and outputs. Operates from ±1.5 to ±18 volts, or the corresponding single supply range.

OPA2132 Audio op-amp with 8 MHz bandwidth, 20 V/μs slew rate. Good for filter applications.

G.2.2 5 Volt supply op-amps

TLC2274 Rail-to-rail op-amp with great performance at both rails.

AD8622/8624 Quad op-amp.

LMP7708 A nice ±5 V supply op amp, with rail-to-rail in/out for active filter applications. Note: This is a decompensated op amp, so it is not unity gain stable.

G.2.3 Comparators

AD790 Comparator used in the positive feedback circuit.

LMV7219 7 ns, 2.7 to 5 V Comparator. Rail-to-rail output, allows ground sensing from 0 to 5 volt rails. I tested this comparator; it can handle a maximum input voltage of -200 mV, so is not a good choice for an AC circuit.

LMV761 A nice precision comparator; this could replace the AD790 in the positive feedback circuit.

G.2.4 Linear Regulators

To use newer parts, it may be necessary to create $\pm 5\,\mathrm{V}$ power on a PCB from our $\pm 15\,\mathrm{V}$ supplies. A nice matched pair of parts that are easy to configure on a board are ADP7118 and ADP7182, which can provide 200 mA of current is a small package with only external decoupling capacitors. Also consider the ADM7160.

TI also has a wide range of regulators; while not in nice 5-pin packages, the TPS7A30 and TPS7A49 are nice, low-noise supplies.

From Linear Technology, consider LT1761 for +5 V, and LT1964 for -5 V. These are a nicely matched, precision pair.

G.2.5 Resources

Analog Devices article showing best practices for op amp PCB layout (`http://www.analog.com/library/analogdialogue/archives/39-09/layout.html`).

Another similar presentation on PCB board layout from Analog Devices.

G.3 Circuit fabrication checklist

When building circuits in Eagle and ordering on OSHPark, here are a few things to keep in mind. My Eagle library is located on the group Dropbox in the folder `Circuits/ryan-eagle` (Eagle version 6.5).

Layout and design —

- Think carefully about what happens to the circuit and the output or microscope if the inputs are connected incorrectly or disconnected. Will the circuit be destroyed from the application of an incorrect voltage? Will the output voltage or current drift towards a rail?
  - An example: The tabling circuit outputs a voltage to the z-piezo

    $$Z = \frac{g_x}{10\,\mathrm{V}} x + \frac{g_y}{10\,\mathrm{V}} + z \tag{G.1}$$

    where the gains $\frac{g_x}{10\,\mathrm{V}}$, $\frac{g_y}{10\,\mathrm{V}}$ are the tabling coefficients for the x-axis and y-axis piezos. We added $100\,\mathrm{k\Omega}$ resistors to ground on the tabling circuit inputs because otherwise when the inputs were disconnected the z-piezo output voltage could increase and crash the cantilever tip into the surface.

Parts —

- For resistors and capacitors, 0805 or 0603 are good sizes(R-US0805. It is possible to solder either size resistor or capacitor to a pad designed for the other size, so it is not a big deal if you switch between them. At this point, 0805 parts are the largest size available at reasonable prices.

Style —

It is helpful to name parts rationally so that you can find them more easily. The system I use is as follows. See Fig. G.1 or Fig. B.1 to see what this scheme looks like on the schematic diagram. The layout for the current source circuit of Fig. G.1 is shown in Fig. G.2.

- Label integrated circuits (op-amps, multipliers, voltage references, etc) in order `U1`, `U2`, `U3`. . . . Eagle should automatically label most parts correctly.
- Label resistors `R(Integrated circuit number)0, 1, 2`. . . . This labeling helps locate the parts when laying out the board, and helps you know where to look for the part in the schematic after you have your board.
- Label capacitors the same way, but reserve `C(Integrated circuit number)0, 1` for the negative and positive supply bypass capacitors. In the same way, label board level bypass capacitors `C00` (negative supply) and `C01` (positive supply).
- Use the smash feature so that labels are all rotated the correct direction to read.

Board —

- Use a ground plane
- Avoid vias where possible
- Keep signal / feedback path as short as possible.

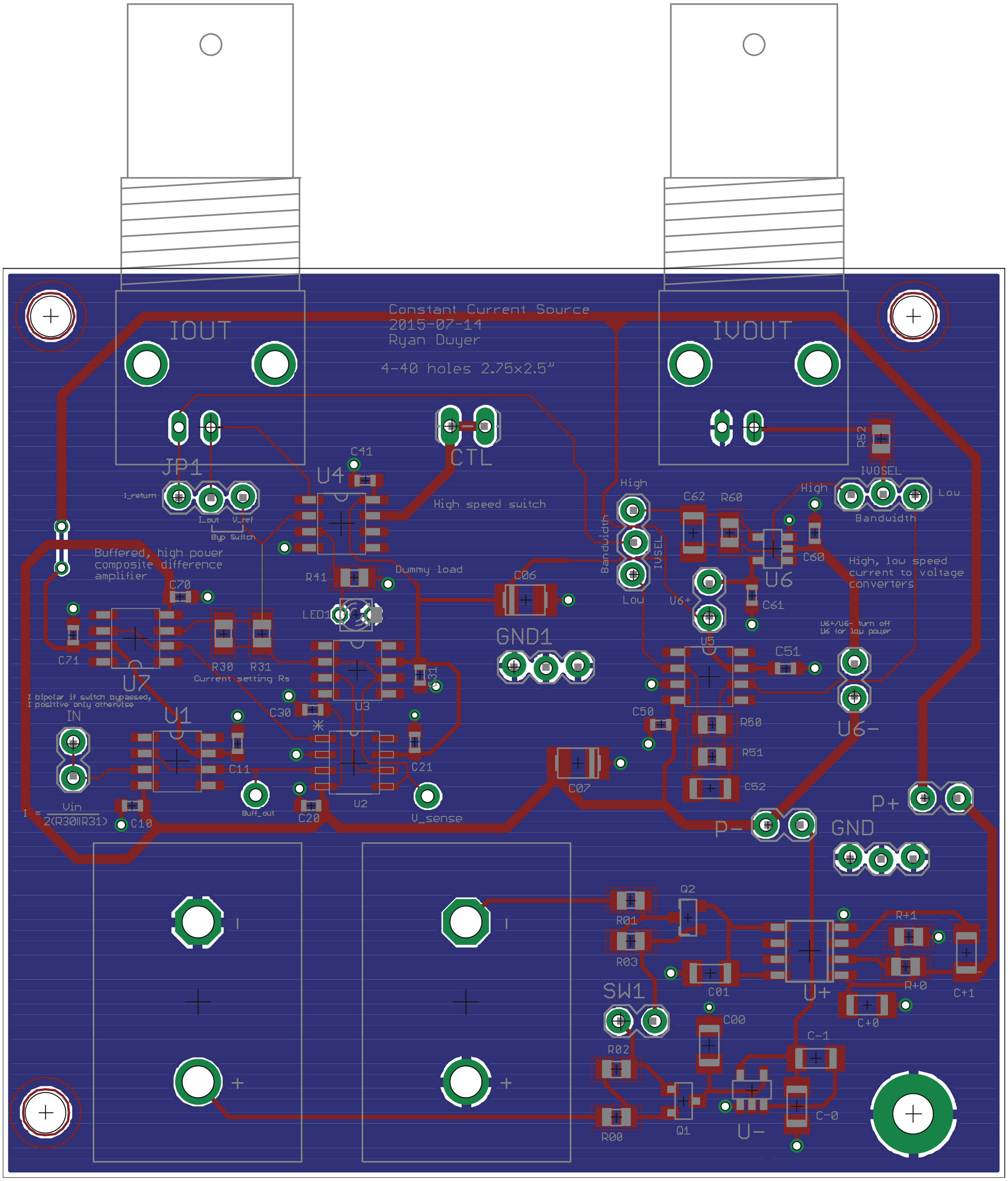

Figure G.2: Board layout for the constant current source circuit.

- Take out the ground plane under op-amp pins (except for power pins) by drawing polygons on the `bRestrict` layer.
- **After laying out the board, add top-side ground / power planes** – Might be a good idea to tie the two planes together with additional vias
- **Smash parts so labels are in nice positions** – Note: part values do not print on the board, only part names. In EAGLE, you can turn the values layer visibility (`tValues`) off if you want to see the board closer to how it will look after ordering.

APPENDIX H

ANNOTATED BIBLIOGRAPHY

Useful books and articles on a variety of topics.

Building Scientific Apparatus [162]. This would be a useful read before making any microscope modifications. Covers a very broad range of topics.

Building Electro-optical systems: Making it all work [109]. A great, opinionated guide to electro-optical systems. I found the discussions of signal-to-noise ratio in electro-optical measurements particularly useful.

"Feedback for physicists: A tutorial essay on control" [163]. A great introduction to feedback, which I found invaluable for choosing better feedback parameters for the PSB B19 RHK PLLPro2 phase-locked loop, and the Baker 146 microscope FM-KPFM feedback loop (Chapter 5).

The Art of Electronics [108]. Great for an introduction to electronics. In the new edition, the "Designs by the Masters" sections are interesting. They also have updated tables comparing op-amps and transistors for a variety of purposes. I found it useful to also read resources geared more towards beginners, such as "SparkFun" tutorials, because "Art of Electronics" can be very high-level for someone with very little electronics experience.

Op-amps for Everyone [164]. Just about every op-amp circuit we use in our group is in this book.

Grounding and shielding techniques [165]. Very nice physical insight into grounding and shielding. Nicely ties lumped element model (resistor, capacitor, inductor) approximations to a transmission line or Maxwell's equations picture.

Noise reduction techniques in electronic systems [166]. Another good reference on grounding, shielding, and noise reduction.

The Fourier Transform and Its Applications [101]. A really nice explanation of the Fourier transform, its uses, and other related transforms. Its explanation of Fourier transform properties and its graphical index of Fourier transforms are especially useful references.

Linear algebra and its applications [167]. Great insight into how to think about matrices.

Introduction to Dynamic Systems: Theory, Models, and Applications [168]. A gentle introduction to "dynamics systems"; mostly covers linear systems of differential or difference equations. Very nice examples covering a broad range of fields.

Understanding Digital Signal Processing [169]. A very practical introduction to digital signal processing.

The Scientist and Engineer's Guide to Digital Signal Processing [170]. Another practical DSP guide. Available free online.

Partial Differential Equations for Scientists and Engineers [171]. A gentle introduction to partial differential equations, written as a series of short, relatively self-contained chapters.

Optimal State Estimation: Kalman, H_∞, and Nonlinear Approaches [172]. This book was invaluable for learning more advanced Kalman filtering techniques, especially for how to deal with non-linearities, or the mixture of a continuous time system with sampled observations.

Numerical methods that work [173]. Many parts seem quite dated—for example, the book spends a lot of time working out faster polynomial approximations to exponential and trigonometric functions. If you get past that, however, there is a lot of insight about which numerical methods to select, how to recognize ill-conditioned problems, and other numerical computing "tips and tricks."

Introduction to Dynamic Systems: Theory, Models, and Applications [168]. I found this a very clear introduction to state-space analysis of both discrete and continuous time linear systems. It has nice examples from a wide variety of fields and is very concrete and applied.

Optimization by Vector Space Methods [174]. The math was a little higher-level than I am comfortable with, but if you can get past that, the geometrical insight is very helpful.

A First Look at Perturbation Theory [175]. Presents a collection of useful perturbation techniques for ordinary and partial differential equations at an easy-to-read, undergraduate level.

"Learn Python the Hard Way" [176]. Great resource for learning Python, especially useful if you are learning programming for the first time.

"Learn C the Hard Way" [177]. I found doing some C programming to be really useful for my LabVIEW programing. In comparison to Python, LabVIEW is very low-level and lacks many useful abstractions. LabVIEW is very similar to C, however, and makes adding a GUI, plotting, math, and signal processing much easier than it would be in C. To do the things that Python has high-level abstractions for, however, it is useful to know C: for example, LabView references offer functionality in a similar way to C pointers.

A Gentle Introduction to Effective Computing in Quantitative Research: What Every Research Assistant Should Know [178]. I didn't get a chance to read much of this book, but it seems like a nice survey of computation techniques.

Lectures in Quantitative Economics [179]. A nice introduction to Python or Julia with an emphasis on numerical computing.

“A Conceptual Introduction to Hamiltonian Monte Carlo” [180]. Written by one of the main developers of Stan [68]. Very useful for understanding why the Stan “NUTS” HMC sampler is efficient, as well as for understanding what you need to change to improve slow or inefficient sampling.

“Nineteen Dubious Ways to Compute the Exponential of a Matrix, Twenty-Five Years Later” [181]. Computing matrix exponentials is hard!

“DFT: A theory full of holes” [182]. As the abstract states: “This article is a rough, quirky overview of both the history and present state of the art of density functional theory.”

APPENDIX I

PSB B19 MICROSCOPE CAD

The CAD for the custom aluminum and teflon pieces for the one-quarter inch swagelok connectors was used without modification from the design of Longenecker [110].

We sought to address a number of problems by re-designing the microscope head in the PSB B19 microscope, outlined in the list below.

- Electrical problems
  - Eliminate shorts
  - Should source drain gate wiring be done intelligently? (4 wire, etc)
  - Should drive wire be attenuated on the middle plate?
  - Twisted-pair everything?
- Reduce vibrational problems
  - Tripod of critically damped springs which resonante at a frequency which is also blocked out by our air-table
  - Need to be careful about the spring constant and the range of extensions where Hook's law is valid for the spring
  - Use the screw through teflon piece trick to allow the table to be leveled precisely
  - Rounded / tapered ends?
- Reduce thermal drift
  - Screw together two rods with differing thermal expansion coefficients to reduce thermal drift from $200\,\mathrm{nm}\,\mathrm{K}^{-1}$ by at least a factor of 10.

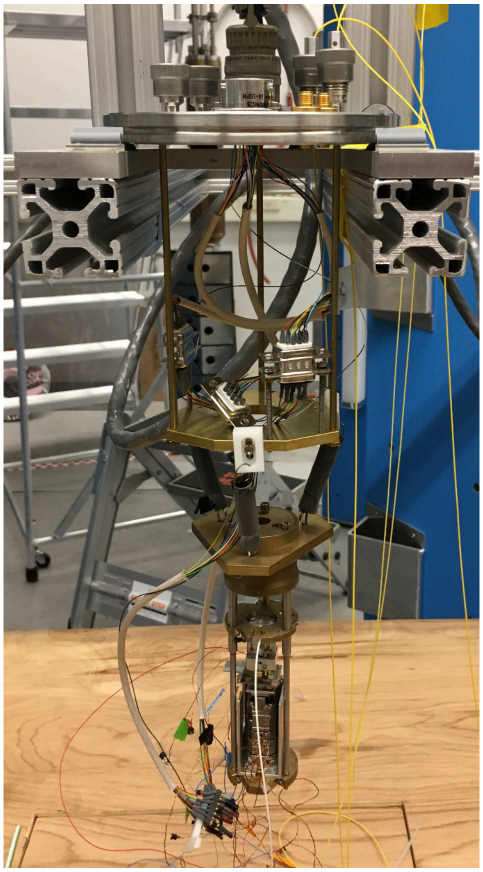

Figure I.1: The new PSB B19 microscope assembly.

- Watch movement in x and y
  - Add little holders for additional fibers watching x and y, pass-throughs in the top plate as well (of the new, larger diameter)
- Other considerations
  - Triangles and hexagons instead of circles
  - Small holes / vented screws to avoid virtual leaks

You can buy well-specified springs from McMasterCarr. The Minus-k vibration isolation is rated for 0.5 Hz, and Seppe Kuehn's thesis (Ref. 183, p. 69) states they measured a resonance frequency of 0.6 Hz laterally and 0.7 Hz vertically. By hanging the middle plate from a tripod of springs, we aim for a resonance frequency as low as possible, practically

2 to 4 Hz. We are limited by the distance the springs expand, which is a function of only the gravitational acceleration g and the resonance frequency f_0:

$$x_{\text{eq}} = \frac{g}{4\pi^2 f_0^2} = \frac{25 \times \mathrm{cm\,Hz}^2}{f_0^2} \tag{I.1}$$

The assembled microscope structure is shown in Fig. I.1. To use the microscope, the wiring from the connectors at the top level to the bottom level of the microscope should be re-wired so the correct pins are adjacent to each other. A current source for the laser diode is also needed, and one of the RHK PLLPro controllers should be brought downstairs as well. The sliding cantilever tray should also be lowered closer to the sample surface, within about $1\,\mathrm{mm}$.

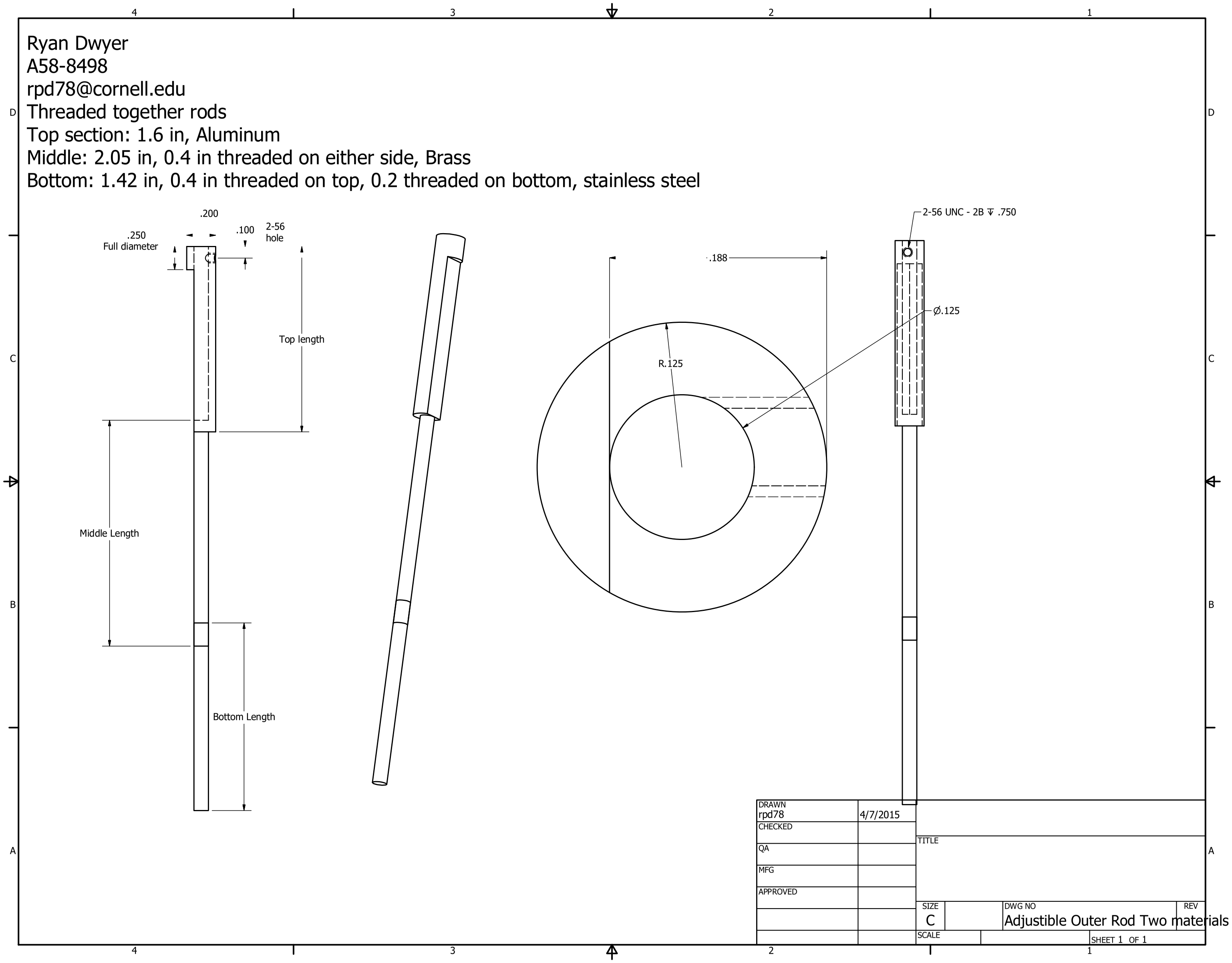

Figure I.2: Adjustable rod made of two materials.

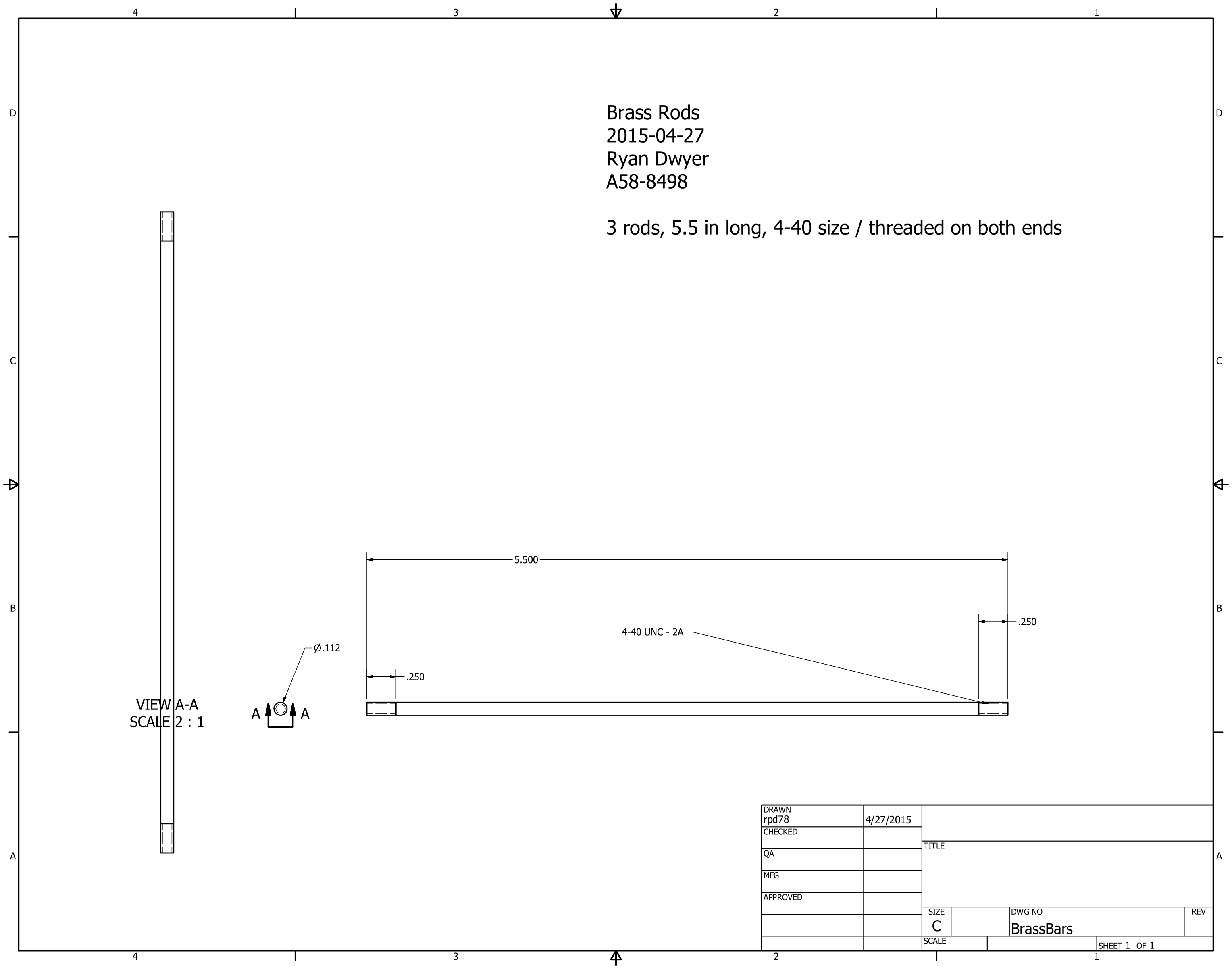

Figure I.3: Brass bar for attaching lid to upper plate.

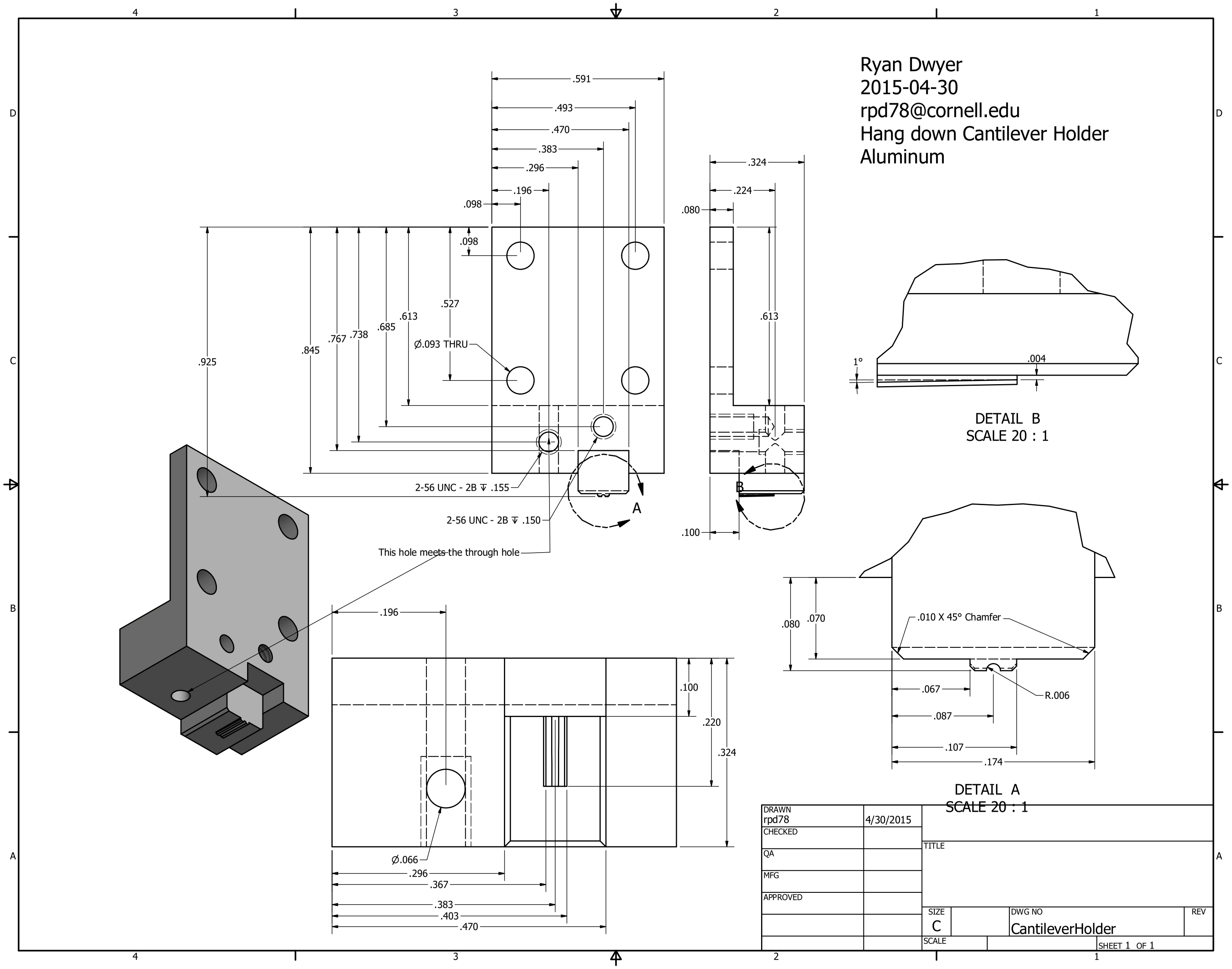

Figure I.4: Cantilever holder for perpendicular geometry (custom, high-sensitivity) cantilevers.

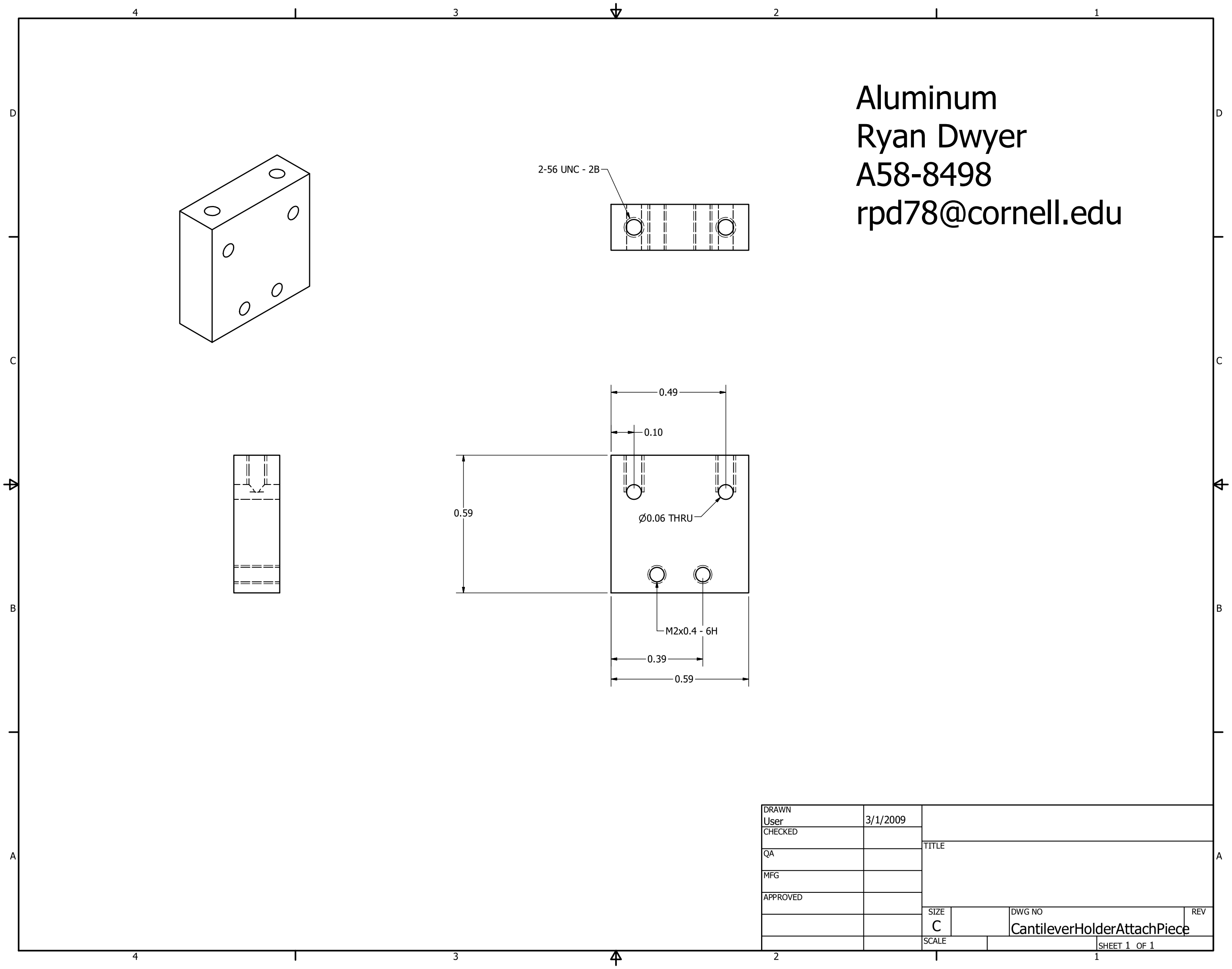

Figure I.5: Perpendicular cantilever holder attachment piece.

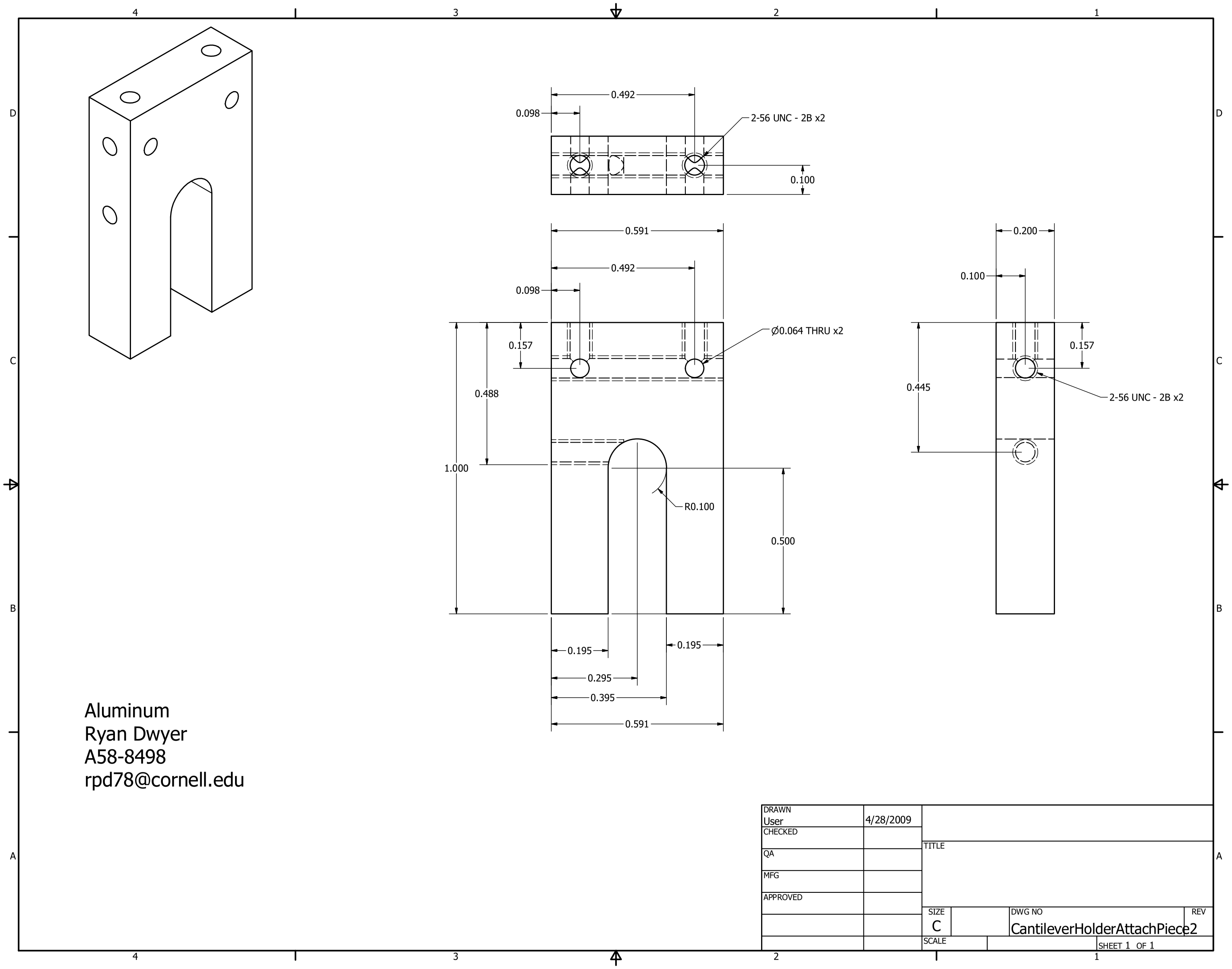

Figure I.6: Perpendicular cantilever holder sliding drawer piece.

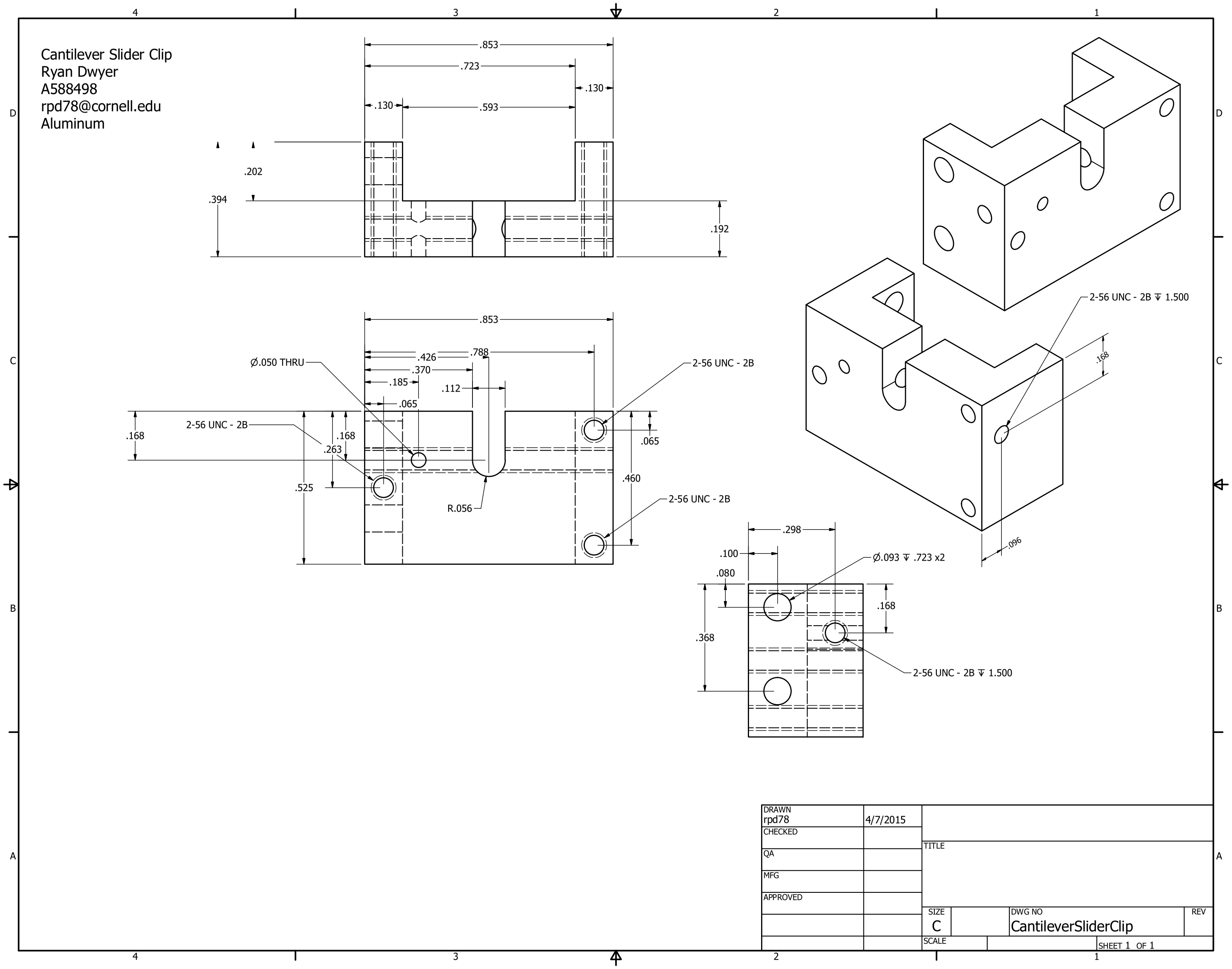

Figure I.7: Perpendicular cantilever holder slider clip.

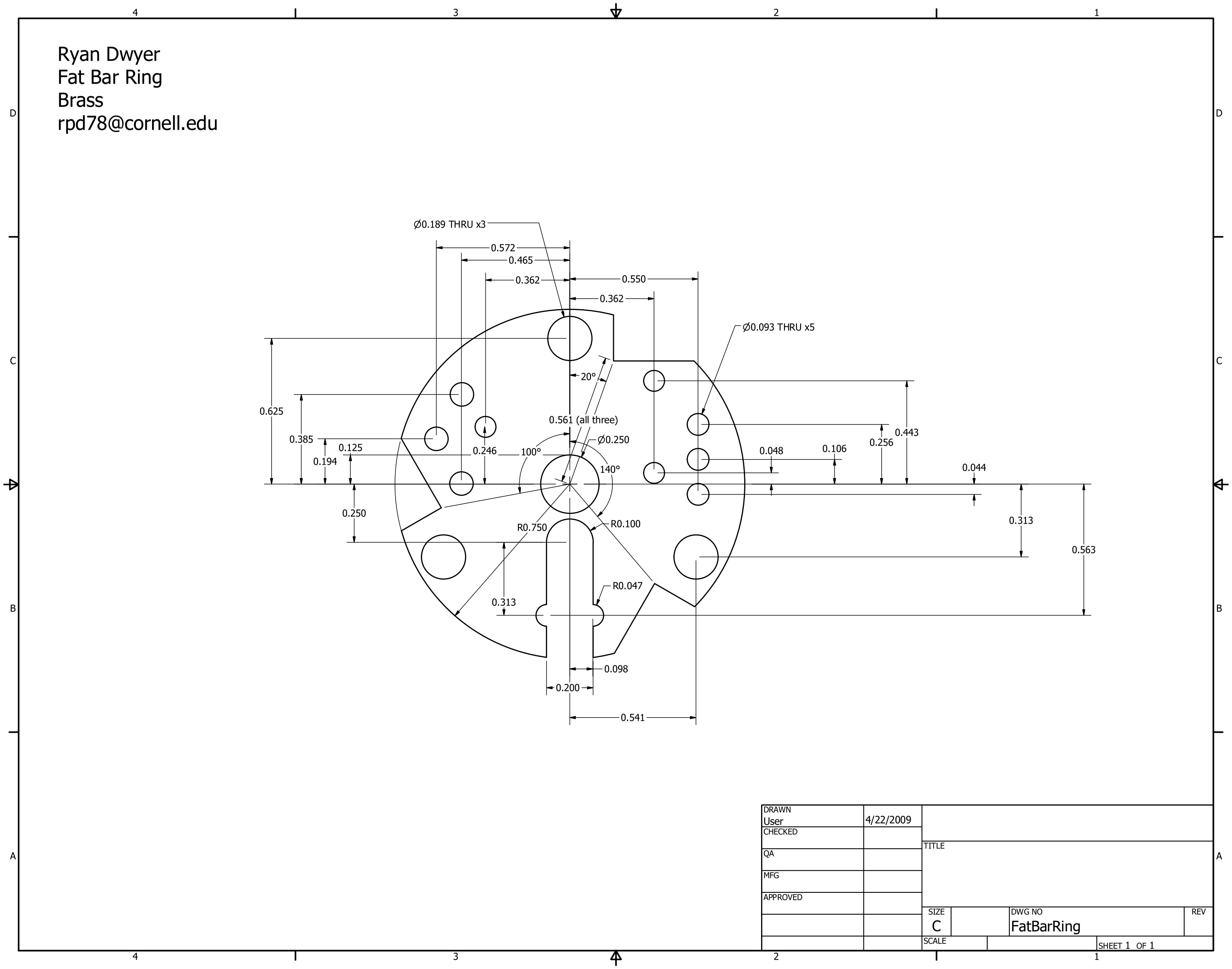

Figure I.8: Brass ring for attaching to thick, adjustable brass bars.

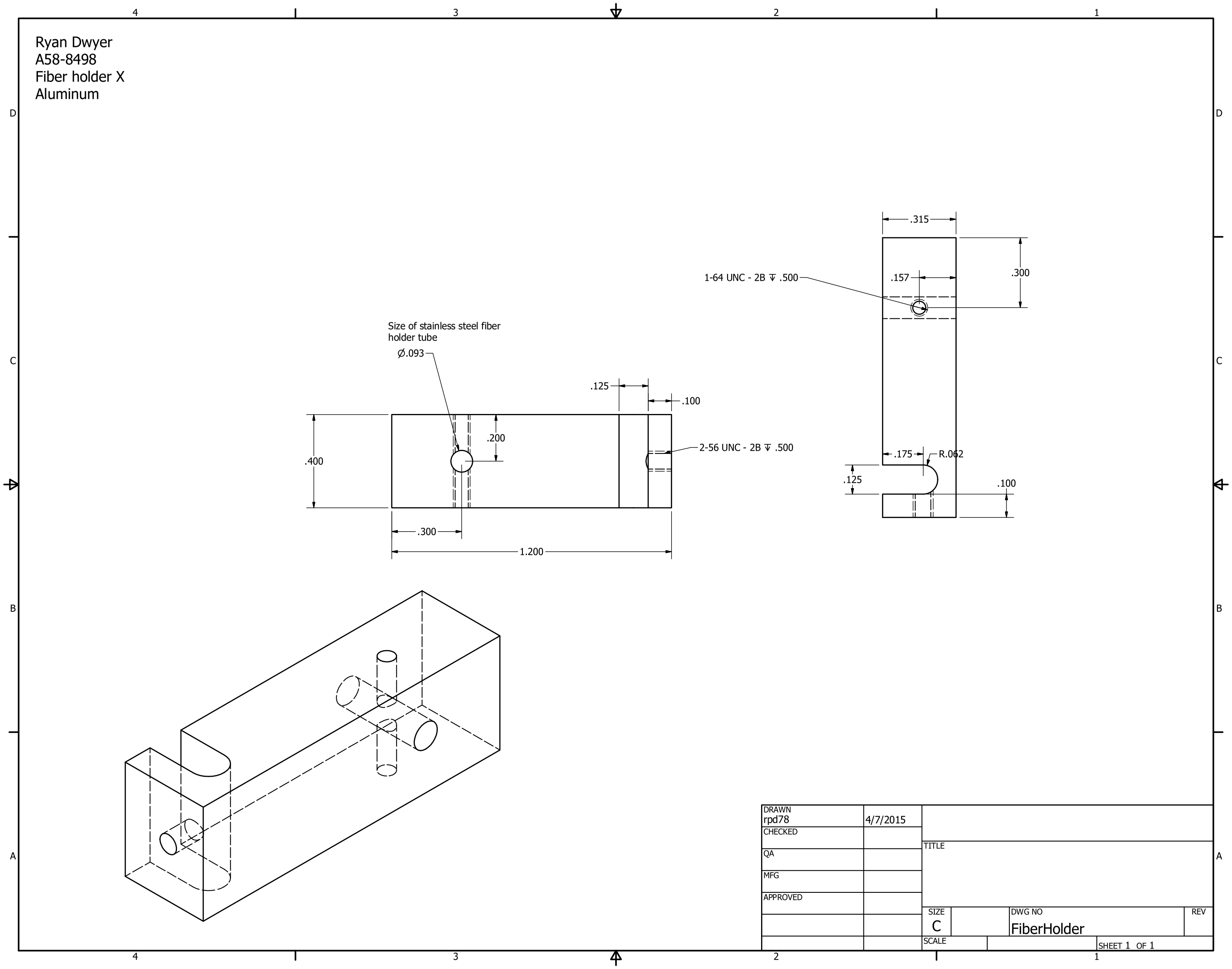

Figure I.9: Aluminum piece for holding an extra fiber optic cable in a metal jacket.

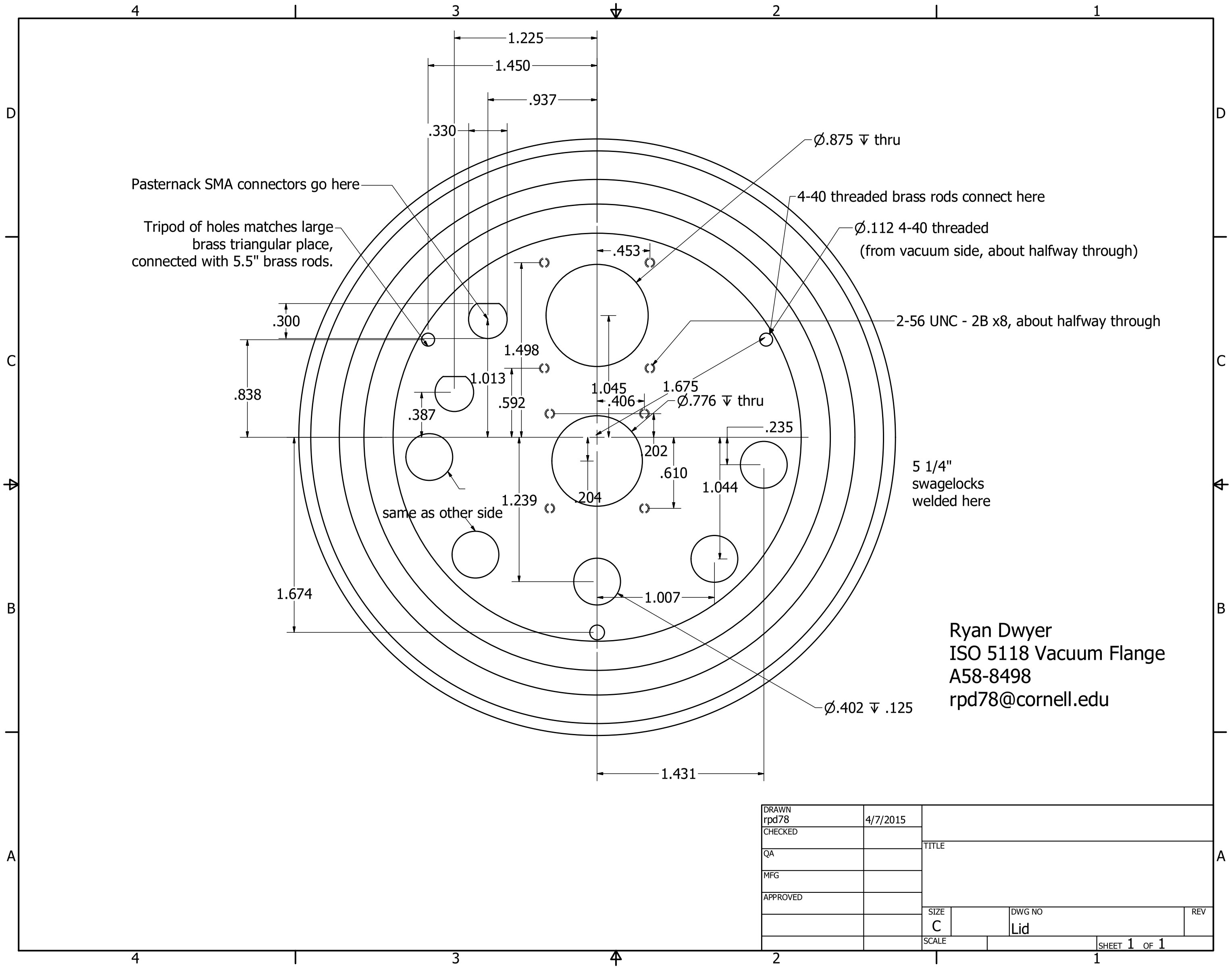

Figure I.10: The re-designed probe lid.

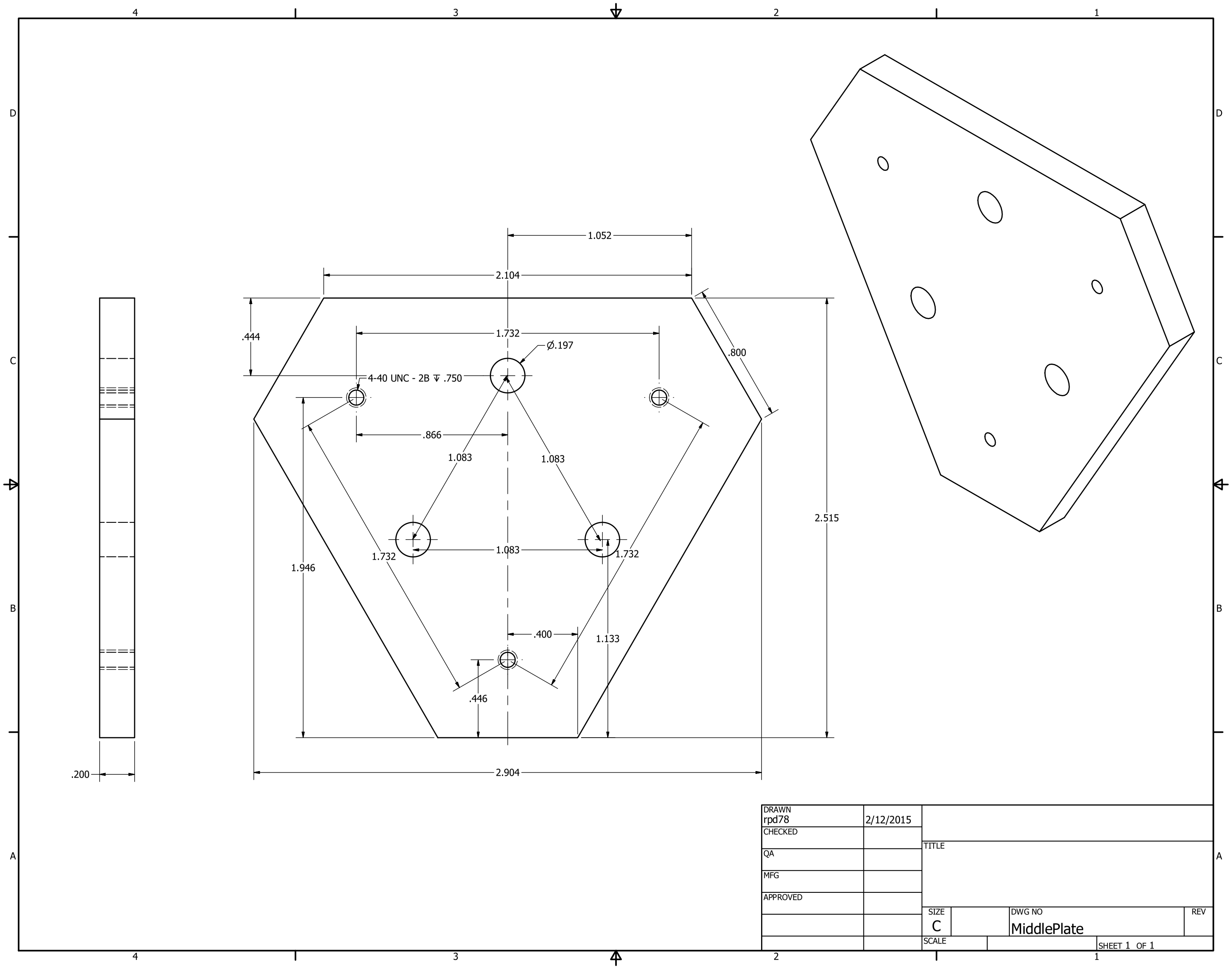

Figure I.11: Caption.

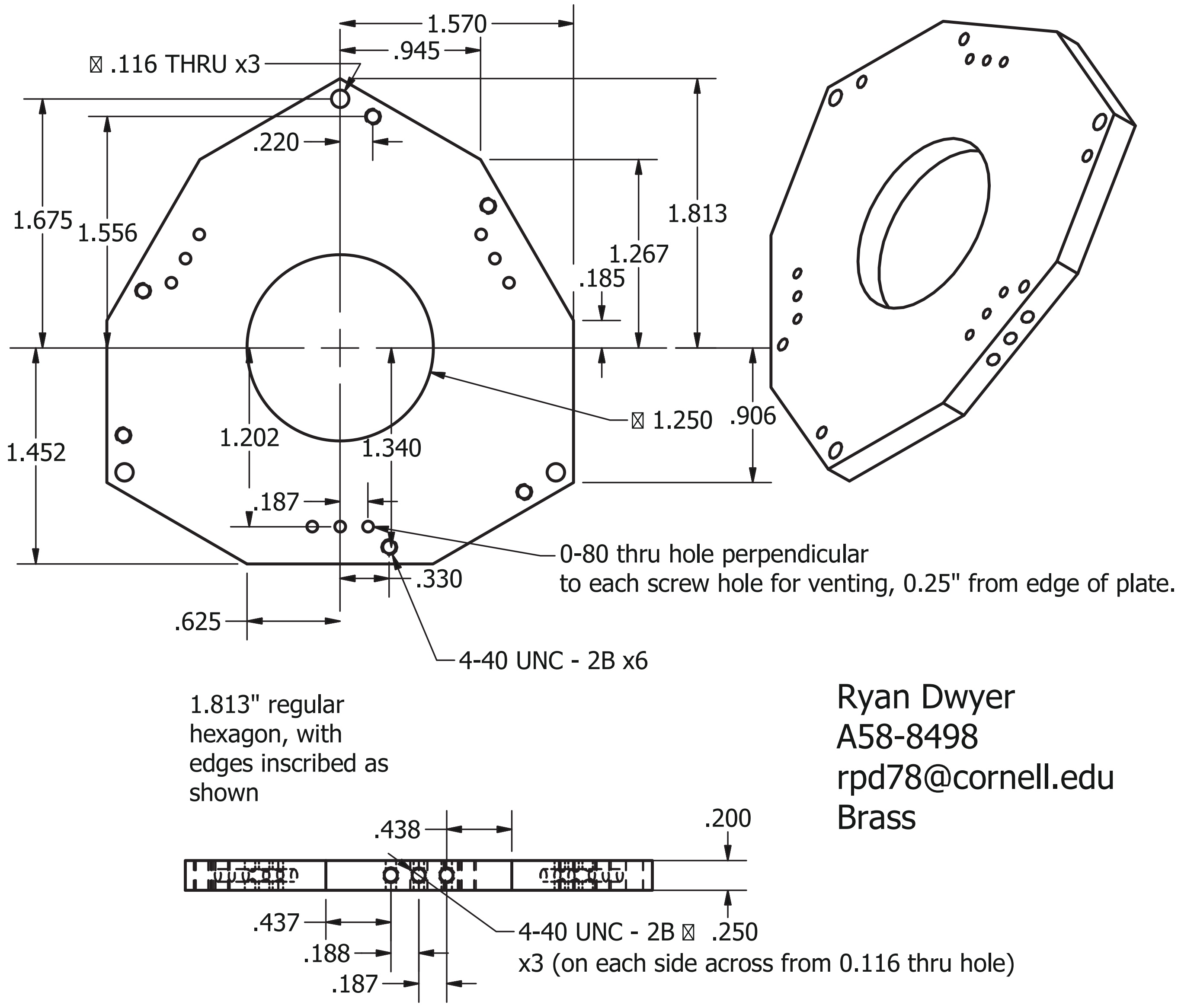

Figure I.12: Attached to the triangular middle plate (Fig. I.11) with springs.

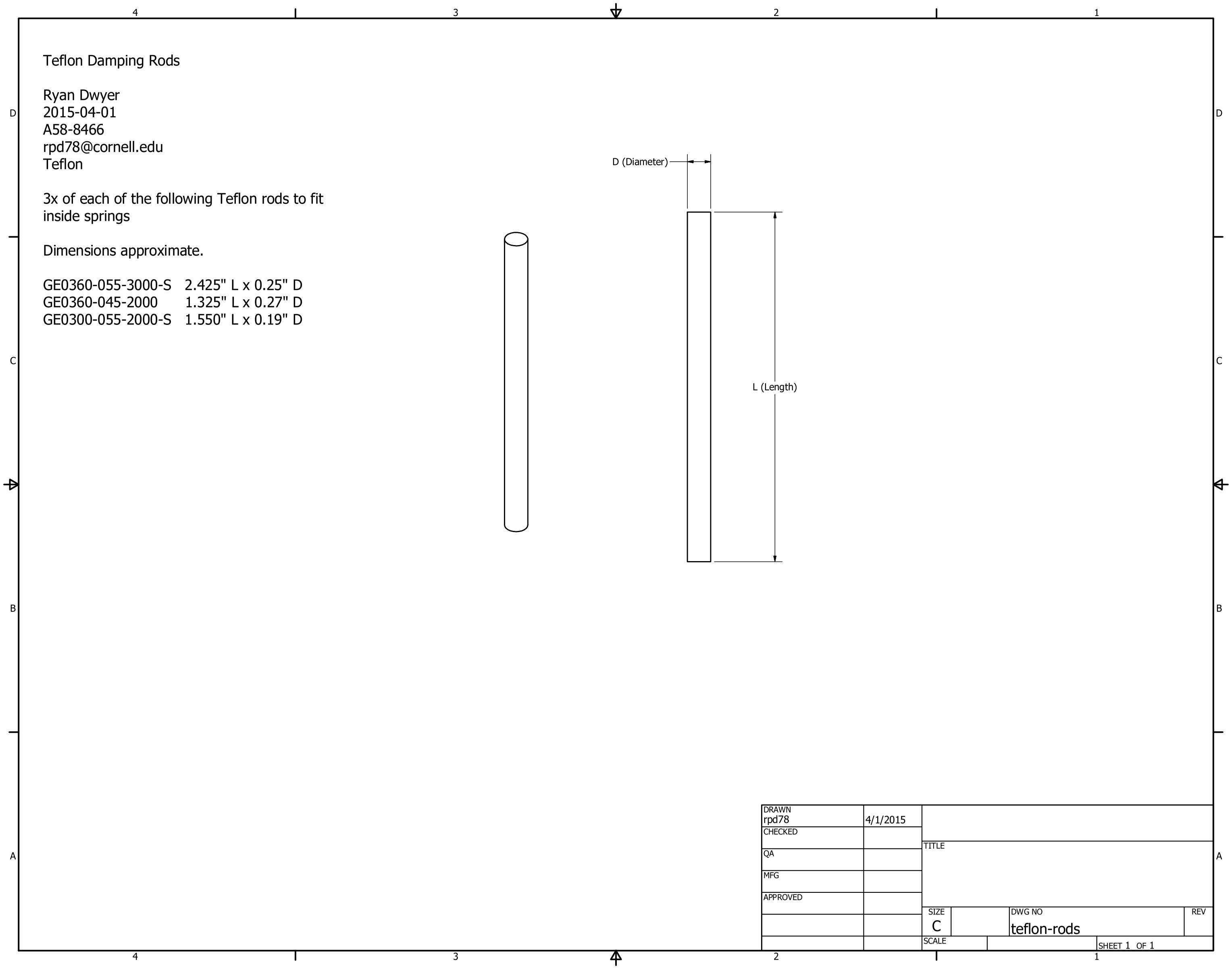

Teflon Damping Rods

Ryan Dwyer
2015-04-01
A58-8466
rpd78@cornell.edu
Teflon

3x of each of the following Teflon rods to fit inside springs

Dimensions approximate.

GE0360-055-3000-S	2.425" L x 0.25" D
GE0360-045-2000	1.325" L x 0.27" D
GE0300-055-2000-S	1.550" L x 0.19" D

Figure I.13: Teflon rods for putting in the middle of springs attaching middle and top triangular plates.

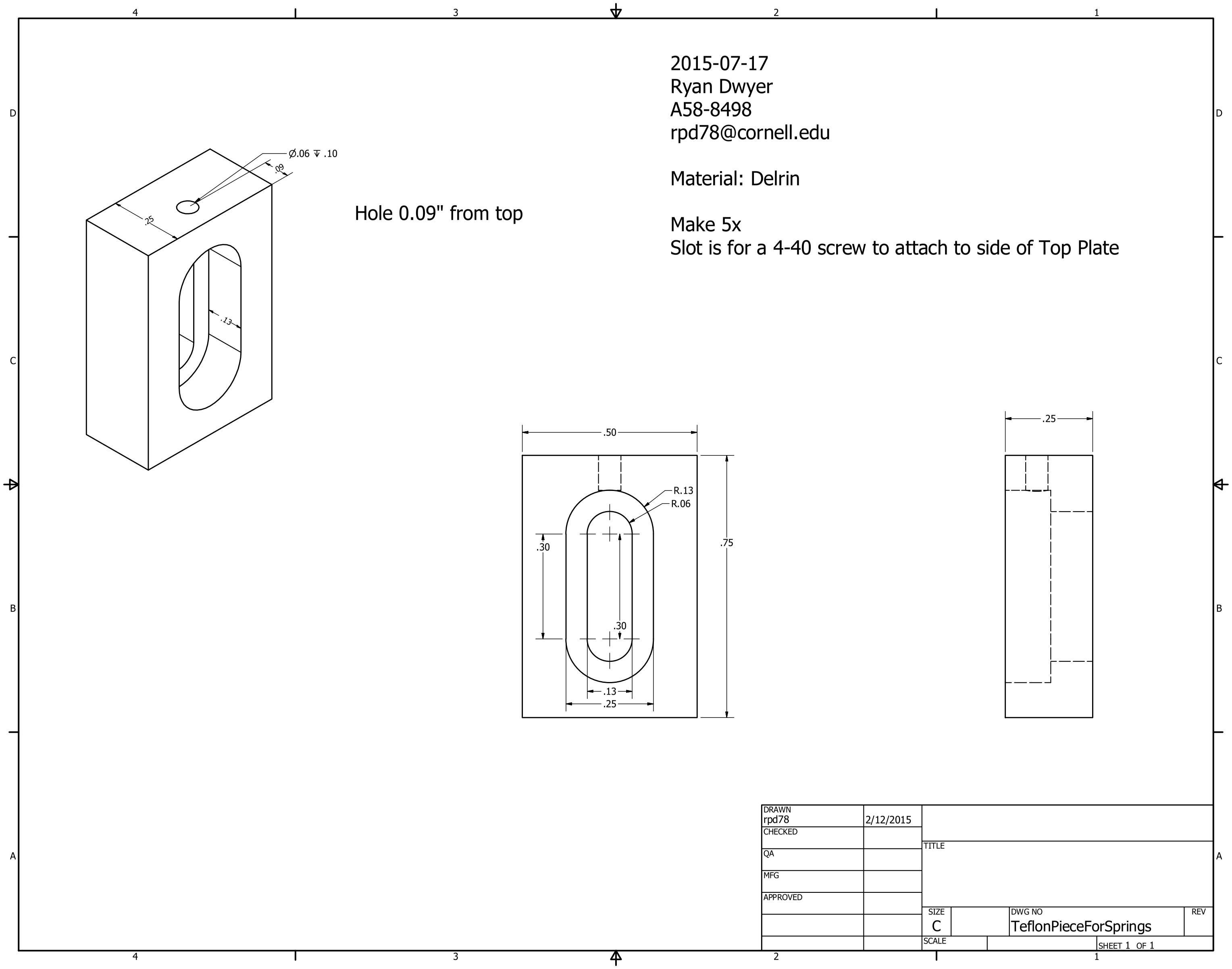
2015-07-17
Ryan Dwyer
A58-8498
rpd78@cornell.edu

Material: Delrin

Make 5x
Slot is for a 4-40 screw to attach to side of Top Plate

Hole 0.09" from top

Figure I.14: Teflon pieces for attaching springs. The spring attaches to the bottom hole.

APPENDIX J

CURRICULUM VITAE

Ryan Dwyer

150 Baker Lab, Ithaca, New York 14853, USA
rpd78@cornell.edu • +1 (262) 506-8712 • ryanpdwyer.github.io

EDUCATION

Cornell University, Ithaca, New York
Doctor of Philosophy (Ph.D.) in Physical Chemistry, 3.8/4.0 Aug 2011 – Jul 2017

- *Advisor:* John Marohn, Ph.D.
- *Thesis:* Probing charge motion in next-generation semiconductors with scanned probe microscopy

University of Notre Dame, South Bend, Indiana
Bachelor of Science (B.S.) in Chemistry, *magna cum laude*, 3.9/4.0 Aug 2007 – May 2011

TEACHING EXPERIENCE

CORNELL UNIVERSITY

Teaching Assistant, Engineering General Chemistry Spring 2017

- Course covered fundamental chemical principles. Supervised laboratory, graded, and held office hours.
- **Academic Excellence Workshop Content Liaison:** Shared lecture notes, common student misconceptions, and course information with undergraduates leading small-group active-learning sessions.

Teaching Assistant, Physical Chemistry Fall 2016

- Graded for Honors Physical Chemistry I and Introductory Physical Chemistry

Workshop Leader, Research Experience for Teachers 2014–2016

- Presented activity on making dye-sensitized solar cells from berry juice to high school teachers
- Recorded a video demonstrating the activity for other interested teachers

Graduate Teaching Assistant Fellow, Cornell Center for Teaching Excellence Aug 2012–Jun 2014

- Led 9 workshops on teaching-related topics, assisted with 4 teaching symposia
- Led international TA training sessions, providing feedback on teaching and communication

Teaching Assistant, Honors Physical Chemistry Fall 2012 – Spring 2013

- Courses covered quantum mechanics (Fall), and thermodynamics, kinetics and elementary statistical mechanics (Spring). Designed problems and worksheets for weekly discussion section; held office hours; graded homework and exams.
- Wrote an introduction to *Mathematica* highlighting common mistakes and errors (still in use).

Teaching Assistant, General Chemistry Fall 2011 – Spring 2012

- Courses covered fundamental chemical principles and the chemical bond. Supervised laboratory, graded, and held office hours.

PRIMARY AND SECONDARY LEVEL

Workshop Leader, Expanding Your Horizons 2013–2017

- Leader for “Juice from Juice,” a 70 minute workshop for seventh and eighth grade girls. Students assembled dye-sensitized solar cells, compared efficiency of cells made with different berry juices and electrodes (2013).
- Developed “Turning on the Lights!”, a 90 minute workshop for ninth grade girls. Guided student assembly and testing of a wind generator; student evaluation of their results and the experimental design; student discussion of key concepts in solar energy transformation.

Volunteer, Community Science Institute 4-H_2O Floating Classroom Partnership 2015 – 2016

- Supervised students age 5 to 16 performing chemical analyses on lake water samples.

Guest Presenter, Elementary and middle school classes Feb 2014, May 2016

- Led students in discussion of states of matter and liquid nitrogen-related activities at Howard University Middle School, Caroline Elementary School.

NSF GK12 Grassroots Fellow Jun 2013 – Jun 2014

- Developed renewable-energy-related modules for high school classes with other fellows and high school teachers.
  - Wrote documents containing background information for teachers, New York State standards covered by the activity, student worksheets, and detailed descriptions and pictures of the activities.
- Led activities related to renewable energy and my research in high school chemistry, physics, and earth science classes.
- Supervised research of a high school teacher in the Marohn laboratory.

RESEARCH EXPERIENCE

Cornell University, with Dr. John Marohn

- Developed new scanned probe microscopy (SPM) methods for studying charge separation, recombination and mobility in organic and perovskite semiconductors
- Supervised two undergraduate students, for 7 semesters and 2 summers
- **Skills:** Scanned probe microscopy; interferometry; photolithography and nanofabrication; electrochemistry; semiconductor device characterization; classical physics; control theory; signal processing, numerical optimization, Bayesian inference, and differential equations.

University of Notre Dame, with Dr. Prashant V. Kamat

- Bound copper (I) sulfide to reduced graphene oxide to improve performance in quantum dot solar cells using polysulfide electrolyte [P1].

PUBLICATIONS

[P3] **R. P. Dwyer**, S. R. Nathan, and J. A. Marohn, Microsecond photocapacitance transients observed using a charged microcantilever as a gated mechanical integrator, accepted to *Science Advances*, [DOI: 10.1126/sciadv.1602951]

[P2] A. M. Tirmzi, **R. P. Dwyer**, T. Hanrath, and J. A. Marohn, Coupled slow and fast charge dynamics in cesium lead bromide perovskite, *ACS Energy Lett.*, **2017**, *2*, 488–496, [DOI: 10.1021/acsenergylett.6b00722]

[P1] J. G. Radich, **R. Dwyer**, and P. V. Kamat, Cu_2S reduced graphene oxide composite for high-efficiency quantum dot solar cells. Overcoming the redox limitations of S_2^-/S_n^{2-} at the counter electrode, *J. Phys. Chem. Lett.*, **2011**, *2*, 2453–2460, [DOI: 10.1021/jz201064k].

PATENTS

[A1] J. A. Marohn, S. R. Nathan, and **R. P. Dwyer**, Atomic Force Microscopy Apparatus, Methods, and Applications, U. S. provisional application filed May 10, 2017, *pending*.

CONFERENCE PRESENTATIONS

EXTERNAL

[C8] **R. P. Dwyer**, S. R. Nathan and J. A. Marohn, M. Talk at *Optical Probes of Organic and Hybrid Semiconductors*, Quebec City, Canada, June 2017.

[C7] **R. P. Dwyer**, S. R. Nathan and J. A. Marohn, Measuring photocapacitance transients in organic semiconductor films with subcycle time resolution. Poster at *Materials Research Society Fall Meeting*, Boston, MA, December 2016.

[C6] **R. P. Dwyer**, S. R. Nathan and J. A. Marohn, Theory and measurements of sub-cycle photo-capacitance dynamics in polymer bulk heterojunction films. Talk at *ACS Northeastern Regional Meeting*, Binghamton, NY, October 2016.

[C5] **R. P. Dwyer**, S. R. Nathan and J. A. Marohn, Measuring Photocapacitance Transients in Organic Semiconductor Films using a Scanned Probe Microscopy Cantilever as a Mechanical Integrator. Talk at *Electronic Materials Conference (EMC)*, Newark, DE, June 2016.

[C4] **R. P. Dwyer**, S. R. Nathan and J. A. Marohn, Light-induced charge transients measured using scanned probe microscopy. Poster at *Materials Research Society Fall Meeting*, Boston, MA, December 2015.

[C3] **R. P. Dwyer**, N. C. Hoepker, R. L. Loring and J. A. Marohn, Charge mobility in organic semiconductors detected using fluctuation microscopy. Talk at *SPM on SPM*, Toronto, ON, Canada, September 2014.

[C2] **R. P. Dwyer**, N. C. Hoepker, and J. A. Marohn, Local mobility measurements in organic films using split-gate transistors and time-resolved electric force microscopy. Poster at *Electronic Materials Conference (EMC)*, Notre Dame, IN, June 2013.

[C1] **R. P. Dwyer**, N. C. Hoepker, and J. A. Marohn, Time-resolved electric force microscopy simulations over split-gate transistors to infer local charge mobility. Poster at *Organic Field Effect Transistor (OFET) Conference*, Princeton, NJ, October 2012.

INTERNAL

[I6] **R. P. Dwyer**, S. R. Nathan and J. A. Marohn, Light-induced charge transients measured using scanned probe microscopy. Poster for *Department of Chemistry and Chemical Biology Graduate Recruiting*, February 2016.

[I5] **R. P. Dwyer**, L. M. Smieska, S. R. Nathan and J. A. Marohn, Imaging surface potential and electric fields in organic semiconductors via Kelvin probe microscopy. Poster for *Department of Chemistry and Chemical Biology Graduate Recruiting*, March 2015.

[I4] **R. P. Dwyer**, N. C. Hoepker, and J. A. Marohn, Detecting charge carrier interactions in organic semiconductors using fluctuation microscopy, Talk for *Department of Chemistry and Chemical Biology Grad and Postdoc Seminar*, October 2015.

[I3] **R. P. Dwyer**, Studying organic solar cell materials using electric force microscopy. Talk at *NSF Grassroots GK12 program*, July 2013.

[I2] **R. P. Dwyer**, J. G. Radich and P. V. Kamat, Strategies for Improving the Performance of Quantum Dot Solar Cells. Talk for *University of Notre Dame College of Science Joint Annual Meeting*, May 2011.

[I1] **R. P. Dwyer**, J. G. Radich and P. V. Kamat, Copper (I) sulfide-reduced graphene oxide composites: A better counter electrode for quantum dot solar cells," *University of Notre Dame Undergraduate Research Symposium*, August 2010.

EDUCATION AND OUTREACH PRESENTATIONS

[E10] **R. P. Dwyer** and G. A. Aguirre, Turning on the lights: A simple, student-assembled wind generator. Workshop at *Science Teachers Association of New York State (STANYS) Conference*, Rochester, NY, November 2014.

[E9] **R. P. Dwyer** and G. Park, Strategies for effective team-based learning. Workshop for *Cornell Center for Teaching Excellence*, March 2014.

[E8] **R. P. Dwyer**, Strategies for teaching laboratories. Workshop for *Cornell Center for Teaching Excellence*, October 2013.

[E7] **R. P. Dwyer** and C. Hale, Utilizing informal classroom assessment techniques to evaluate student learning. Workshop for *Cornell Center for Teaching Excellence*, October 2013.

[E6] **R. P. Dwyer** and C. Browning, "Flipping the classroom" as a TA. Workshop for *Cornell Center for Teaching Excellence*, March 2013.

[E5] **R. P. Dwyer** and B. Condon, Creating effective questions for i>clickers and online quizzes. Workshop for *Cornell Center for Teaching Excellence*, March 2013.

[E4] **R. P. Dwyer** and M. Gough, Concept, inquiry, and problem based learning approaches. Workshop for *Cornell Center for Teaching Excellence*, February 2013.

[E3] **R. P. Dwyer** and C. Hale, How to get started: Teaching models and approaches. Workshop for *Cornell Center for Teaching Excellence*, November 2012.

[E2] **R. P. Dwyer**, A. Birson, and B. Brown, Deepening student learning through research assignments. Workshop for *Cornell Center for Teaching Excellence*, October 2012.

[E1] **R. P. Dwyer** and I. Gruss, Reflective course development: Learning-centered syllabus. Workshop for *Cornell Center for Teaching Excellence*, September 2012.

SOFTWARE AND DATASETS

[S2] **R. P. Dwyer**, S. R. Nathan and J. A. Marohn, Data and workup for "Microsecond photocapacitance transients observed using a charged microcantilever as a gated mechanical integrator." Available at http://github.com/ryanpdwyer/1605-phasekick, 2016.

[S1] **R. P. Dwyer** and J. A. Marohn, The FreqDemod Python package. Available at https://github.com/JohnMarohn/FreqDemod, 2015.

FELLOWSHIPS AND AWARDS

NSF Grassroots GK12 Graduate Student Fellowship Jun 2013 – Jun 2014
Department of Chemistry and Chemical Biology Teaching Assistant Award, Cornell University 2012
University of Notre Dame Chemistry Research Award 2011
University of Notre Dame William R. Wischerath Outstanding Major Award 2011

COMPUTER AND TECHNICAL SKILLS

Numerical computing

- Wrote Python signal processing modules to analyze data from new SPM experiments
- Improved inference from poorly conditioned microscopy data using PyStan Bayesian model
- Eliminated systematic bias in probe characterization using maximum likelihood, Bayesian model
- Formulated experiments and noise as ordinary differential equations and simulated in Python and Julia

Open source contributions

- Contributed documentation and a new feature to Pint, a popular Python units package
- Contributed bug fix to Julia ordinary differential equations (ODE) package

Electronics

- Redesigned analog and digital circuity to implement new scanned probe experiments
- Circuit layout using EAGLE, circuit simulation using LTSpice

Languages: Python, LabVIEW, Mathematica, Julia, Matlab, C, Unix scripting

Other computer: Adobe Illustrator, Autodesk Inventor (CAD) Word, Excel, PowerPoint

MEMBERSHIPS

American Chemical Society
Materials Research Society
Society of Industrial and Applied Mathematics
American Association of Physics Teachers

REFERENCES

[1] C. Tang, *Appl. Phys. Lett.*, **1986**, *48*, 183 – 185, [url]. 1

[2] D. P. McMahon, D. L. Cheung, and A. Troisi, *J. Phys. Chem. Lett.*, **2011**, *2*, 2737 – 2741, [url]. 1, 2.1

[3] A. A. Bakulin, A. Rao, V. G. Pavelyev, P. H. M. Van Loosdrecht, M. S. Pshenichnikov, D. Niedzialek, J. Cornil, D. Beljonne, and R. H. Friend, *Science*, **2012**, *335*, 1340 – 1344, [url]. 1, 2.1

[4] T. J. Savenije, A. J. Ferguson, N. Kopidakis, and G. Rumbles, *J. Phys. Chem. C*, **2013**, *117*, 24085 – 24103, [url]. 1, 2.1

[5] K. Vandewal, S. Albrecht, E. T. Hoke, K. R. Graham, J. Widmer, J. D. Douglas, M. Schubert, W. R. Mateker, J. T. Bloking, G. F. Burkhard, A. Sellinger, J. M. J. Fréchet, A. Amassian, M. K. Riede, M. D. McGehee, D. Neher, and A. Salleo, *Nat. Mater.*, **2013**, *13*, 63 – 68, [url]. 1, 2.1

[6] B. M. Savoie, N. E. Jackson, L. X. Chen, T. J. Marks, and M. A. Ratner, *Acc. Chem. Res.*, **2014**, *47*, 3385 – 3394, [url]. 1, 2.1

[7] S. D. Dimitrov and J. R. Durrant, *Chem. Mater.*, **2014**, *26*, 616–630, [url]. 1, 2.1

[8] S. Albrecht, K. Vandewal, J. R. Tumbleston, F. S. U. Fischer, J. D. Douglas, J. M. J. Fréchet, S. Ludwigs, H. Ade, A. Salleo, and D. Neher, *Adv. Mater.*, **2014**, *26*, 2533 – 2539, [url]. 1, 2.1

[9] N. E. Jackson, B. M. Savoie, T. J. Marks, L. X. Chen, and M. A. Ratner, *J. Phys. Chem. Lett.*, **2015**, *6*, 77 – 84, [url]. 1, 2.1

[10] T. M. Burke, S. Sweetnam, K. Vandewal, and M. D. McGehee, *Adv. Energy Mater.*, **2015**, *5*, 1500123, [url]. 1, 2.1

[11] H. M. Feier, O. G. Reid, N. A. Pace, J. Park, J. J. Bergkamp, A. Sellinger, D. Gust, and G. Rumbles, *Adv. Energy Mater.*, **2016**, *6*, 1502176, [url]. 1, 2.1

[12] M. Causá, J. De Jonghe-Risse, M. Scarongella, J. C. Brauer, E. Buchaca-Domingo, J.-E. Moser, N. Stingelin, and N. Banerji, *Nat. Comms.*, **2016**, *7*, 12556, [url]. 1, 2.1

[13] B. W. Larson, O. G. Reid, D. C. Coffey, S. M. Avdoshenko, A. A. Popov, O. V. Boltalina, S. H. Strauss, N. Kopidakis, and G. Rumbles, *Adv. Energy Mater.*, **2016**, p. 1601427, [url]. 1, 2.1

[14] C. Deibel, A. Wagenpfahl, and V. Dyakonov, *Phys. Rev. B*, **2009**, *80*, 075203, [url]. 1, 2.1

[15] A. J. Ferguson, N. Kopidakis, S. E. Shaheen, and G. Rumbles, *J. Phys. Chem. C*, **2011**, *115*, 23134 – 23148, [url]. 1, 2.1

[16] G. Rumbles, Excited State Processes in Electronic and Bio Nanomaterials (ESP-2014); Santa Fe, New Mexico; June 9 – 12, **2014**. 1

[17] D. C. Coffey, B. W. Larson, A. W. Hains, J. B. Whitaker, N. Kopidakis, O. V. Boltalina, S. H. Strauss, and G. Rumbles, *J. Phys. Chem. C*, **2012**, *116*, 8916–8923, [url]. 1, 2.1, 2.3

[18] G. Binnig, C. Quate, and C. Gerber, *Phys. Rev. Lett.*, **1986**, *56*, 930 – 933, [url]. 1

[19] Y. Martin, D. Abraham, and H. Wickramasinghe, *Appl. Phys. Lett.*, **1988**, *52*, 1103 – 1105, [url]. 1

[20] D. Rugar, C. S. Yannoni, and J. A. Sidles, *Nature*, **1992**, *360*, 563 – 566, [url]. 1

[21] M. Nonnenmacher, M. O'Boyle, and H. Wickramasinghe, *Appl. Phys. Lett.*, **1991**, *58*, 2921 – 2923, [url]. 1, 6.2.2

[22] A. Kikukawa, S. Hosaka, and R. Imura, *Appl. Phys. Lett.*, **1995**, *66*, 3510 – 3512, [url]. 1, 3.1, 4, 5.1, 6.2.2

[23] W. R. Silveira, E. M. Muller, T. N. Ng, D. H. Dunlap, and J. A. Marohn in *Scanning Probe Microscopy: Electrical and Electromechanical Phenomena at the Nanoscale*, ed. S. V. Kalinin and A. Gruverman, Vol. II; Springer Verlag, New York, 2007; pp. 788 – 830. 1, 4

[24] S. Hudlet, M. Saint Jean, B. Roulet, J. Berger, and C. Guthmann, *J. Appl. Phys.*, **1995**, *77*, 3308, [url]. 1

[25] A. S. Grove, B. E. Deal, E. H. Snow, and C. T. Sah, *Solid-State Electronics*, **1965**, *8*, 145–163, [url]. 1

[26] J. Grosvalet, C. Jund, C. Motsch, and R. Poirier, *Surf. Sci.*, **1966**, *5*, 49–80, [url]. 1

[27] J. Grosvalet and C. Jund, *IEEE Trans. Electron Devices*, **1967**, *14*, 777–780. 1

[28] E. H. Nicollian and A. Goetzberger, *Bell Syst. Tech. J.*, **1967**, *46*, 1055–1133, [url]. 1

[29] D. C. Coffey and D. S. Ginger, *Nat. Mater.*, **2006**, *5*, 735 – 740, [url]. 1, 2.1, 2.1, 2.2

[30] R. Giridharagopal, G. E. Rayermann, G. Shao, D. T. Moore, O. G. Reid, A. F. Tillack, D. J. Masiello, and D. S. Ginger, *Nano Lett.*, **2012**, *12*, 893 – 898, [url]. 1, 2.1, 2.1, 2.4.2, 3, 3.3, A.6

[31] P. A. Cox, M. S. Glaz, J. S. Harrison, S. R. Peurifoy, D. C. Coffey, and D. S. Ginger, *J. Phys. Chem. Lett.*, **2015**, *6*, 2852 – 2858, [url]. 1, 2.1, 3, 3.3

[32] D. U. Karatay, J. S. Harrison, M. S. Glaz, R. Giridharagopal, and D. S. Ginger, *Rev. Sci. Instrum.*, **2016**, *87*, 053702, [url]. 1, 2.1, 2.1, 3, 3.1, 3.3, 3.3.3, 3.3.4

[33] A. M. Tirmzi, R. P. Dwyer, T. Hanrath, and J. A. Marohn, *ACS Energy Lett.*, **2017**, pp. 488–496, [url]. 1, 2.3, 6, 6.1, 6.2, 6.2.1, 6.4

[34] R. P. Dwyer, S. R. Nathan, and J. A. Marohn, *Sci. Adv.*, **2017**, [url]. 2, 2.1, 2.2, 2.4, 2.5, 2.6, 2.7, 2.8, 2.9, 2.10, 2.11, 2.12, 3, 3.1, A.1, A.2, A.3, A.4, A.5, A.6, A.7, A.8, A.9

[35] R. Giridharagopal, G. Shao, C. Groves, and D. S. Ginger, *Mater. Today*, **2010**, *13*, 50 – 56, [url]. 2.1

[36] X.-D. Dang, A. B. Tamayo, J. Seo, C. V. Hoven, B. Walker, and T.-Q. Nguyen, *Adv. Funct. Mater.*, **2010**, *20*, 3314 – 3321, [url]. 2.1

[37] J. R. O'Dea, L. M. Brown, N. Hoepker, J. A. Marohn, and S. Sadewasser, *MRS Bull.*, **2012**, *37*, 642 – 650, [url]. 2.1

[38] J. L. Luria, N. Hoepker, R. Bruce, A. R. Jacobs, C. Groves, and J. A. Marohn, *ACS Nano*, **2012**, *6*, 9392 – 9401, [url]. 2.1, D

[39] E. J. Spadafora, R. Demadrille, B. Ratier, and B. Grevin, *Nano Letters*, **2010**, *10*, 3337 – 3342, [url]. 2.1, 6.2.2

[40] R. J. Hamers and D. G. Cahill, *Appl. Phys. Lett.*, **1990**, *57*, 2031, [url]. 2.1

[41] S. Weiss, D. F. Ogletree, D. Botkin, M. Salmeron, and D. S. Chemla, *Appl. Phys. Lett.*, **1993**, *63*, 2567, [url]. 2.1

[42] G. Nunes and M. R. Freeman, *Science*, **1993**, *262*, 1029–1032, [url]. 2.1

[43] S. Grafström, *J. Appl. Phys.*, **2002**, *91*, 1717, [url]. 2.1

[44] O. Takeuchi, R. Morita, M. Yamashita, and H. Shigekawa, *Jap. J. Appl. Phys.*, **2002**, *41*, 4994–4997, [url]. 2.1

[45] O. Takeuchi, M. Aoyama, R. Oshima, Y. Okada, H. Oigawa, N. Sano, H. Shigekawa, R. Morita, and M. Yamashita, *Appl. Phys. Lett.*, **2004**, *85*, 3268, [url]. 2.1

[46] T. L. Cocker, V. Jelic, M. Gupta, S. J. Molesky, J. A. J. Burgess, G. D. L. Reyes, L. V. Titova, Y. Y. Tsui, M. R. Freeman, and F. A. Hegmann, *Nat. Photon.*, **2013**, *7*, 620–625, [url]. 2.1

[47] M. Eisele, T. L. Cocker, M. A. Huber, M. Plankl, L. Viti, D. Ercolani, L. Sorba, M. S. Vitiello, and R. Huber, *Nat. Photon.*, **2014**, *8*, 841–845, [url]. 2.1

[48] M. Takihara, T. Takahashi, and T. Ujihara, *Appl. Phys. Lett.*, **2008**, *93*, 021902, [url]. 2.1, 6.2.4

[49] G. Shao, M. S. Glaz, F. Ma, H. Ju, and D. S. Ginger, *ACS Nano*, **2014**, *8*, 10799–0807, [url]. 2.1, 6.2.4, D.2

[50] J. Murawski, T. Graupner, P. Milde, R. Raupach, U. Zerweck-Trogisch, and L. M. Eng, *J. Appl. Phys.*, **2015**, *118*, 154302, [url]. 2.1

[51] J. Murawski, T. Mönch, P. Milde, M. P. Hein, S. Nicht, U. Zerweck-Trogisch, and L. M. Eng, *J. Appl. Phys.*, **2015**, *118*, 244502, [url]. 2.1

[52] Z. Schumacher, Y. Miyahara, A. Spielhofer, and P. Grutter, *Phys. Rev. Appl.*, **2016**, *5*, 044018, [url]. 2.1, 4

[53] D. Coffey *Characterizing the Local Optoelectronic Performance of Organic Solar Cells with Scanning-Probe Microscopy* PhD thesis, University of Washington, Seattle, Washington, **2007**. 2.1

[54] A. Hou, F. Ho, and D. Bloom, *Electron. Lett.*, **1992**, *28*, 2302 – 2303, [url]. 2.1

[55] A. Leyk, C. Bo?hm, D. Van der weide, and E. Kubalek, *Electron. Lett.*, **1995**, *31*, 1046 – 1047, [url]. 2.1

[56] B. T. Rosner and D. W. van der Weide, *Rev. Sci. Instrum.*, **2002**, *73*, 2505, [url]. 2.1

[57] W. Magnus, *Comm. Pure Appl. Math.*, **1954**, *7*, 649 – 673, [url]. 2.1.1, 3

[58] S. Blanes, F. Casas, J. Oteo, and J. Ros, *Phys. Rep.*, **2009**, *470*, 151–238, [url]. 2.1.1, 3

[59] S. Kuehn, R. Loring, and J. Marohn, *Phys. Rev. Lett.*, **2006**, *96*, 156103, [url]. 2.2

[60] S. Yazdanian, J. Marohn, and R. Loring, *J. Chem. Phys.*, **2008**, *128*, 224706, [url]. 2.2, E.1

[61] N. Hoepker, S. Lekkala, R. F. Loring, and J. A. Marohn, *J. Phys. Chem. B*, **2011**, *115*, 14493–14500, [url]. 2.2, 4, C.6, E.1

[62] J. L. Hutter and J. Bechhoefer, *Rev. Sci. Instrum.*, **1993**, *64*, 1868 – 1873, [url]. 2.2

[63] J. L. Luria *Spectroscopic Characterization of Charge Generation and Trapping in Third-Generation Solar Cell Materials Using Wavelength- and Time-Resolved Electric Force Microscopy* PhD thesis, Cornell University, Ithaca, New York, **2011**. 2.4.2

[64] D. Rugar, H. Mamin, and P. Guethner, *Appl. Phys. Lett.*, **1989**, *55*, 2588 – 2590, [url]. 2.4.2, C.1

[65] L. M. Smieska, V. A. Pozdin, J. L. Luria, R. G. Hennig, M. A. Hines, C. A. Lewis, and J. A. Marohn, *Adv. Funct. Mater.*, **2012**, *22*, 5096 – 5106, [url]. 2.4.2

[66] E. Jones, T. Oliphant, P. Peterson, et al., SciPy: Open source scientific tools for Python, 2001–. 2.4.3

[67] F. T. Krogh, *Math. Comp.*, **1970**, *24*, 185–190, [url]. 2.4.3

[68] S. D. Team, Pystan: the Python interface to Stan, version 2.8.0, 2015. 2.4.4, H

[69] R. P. Dwyer, S. R. Nathan, and J. A. Marohn, Data and workup for “Microsecond photocapacitance transients observed using a charged microcantilever as a gated mechanical integrator.” Available from http://github.com/ryanpdwyer/1605-phasekick, 2016. 2.4.4

[70] R. P. Dwyer and J. A. Marohn, The FreqDemod 0.2.1 Python package Available for installation at https://pypi.python.org/pypi/FreqDemod. Documentation available at http://freqdemod.readthedocs.org. Source code available at https://github.com/JohnMarohn/FreqDemod., 2015. 2.4.4

[71] D. U. Karatay, J. S. Harrison, and R. Giridharagopal, 2015. 3.3, 3.3.4

[72] L. Burgi, H. Sirringhaus, and R. Friend, *Appl. Phys. Lett.*, **2002**, *80*, 2913 – 2915, [url]. 4, 5.1

[73] W. Silveira and J. Marohn, *Phys. Rev. Lett.*, **2004**, *93*, 116104, [url]. 4, 5.1

[74] T. N. Ng, W. R. Silveira, and J. A. Marohn, *Phys. Rev. Lett.*, **2007**, *98*, 066101, [url]. 4, 5.1, E.2

[75] J. D. Slinker, J. A. DeFranco, M. J. Jaquith, W. R. Silveira, Y.-W. Zhong, J. M. Moran-Mirabal, H. G. Craighead, H. D. Abrua, J. A. Marohn, and G. G. Malliaras, *Nat. Mater.*, **2007**, *6*, 894 – 899, [url]. 4, 5.1

[76] L. S. C. Pingree, D. B. Rodovsky, D. C. Coffey, G. P. Bartholomew, and D. S. Ginger, *J. Am. Chem. Soc.*, **2007**, *129*, 15903–15910, [url]. 4, 5.1

[77] L. Burgi, T. Richards, R. Friend, and H. Sirringhaus, *J. Appl. Phys.*, **2003**, *94*, 6129 – 6137, [url]. 4, 5.1

[78] T. N. Ng, W. R. Silveira, and J. A. Marohn, *Proc. SPIE*, **2006**, *6336*, 63360A, [url]. 4, 5.1

[79] K. Takimiya, H. Ebata, K. Sakamoto, T. Izawa, T. Otsubo, and Y. Kunugi, *J. Am. Chem. Soc.*, **2006**, *128*, 12604–12605, [url]. 4, 5.1

[80] S. Lekkala, N. Hoepker, J. A. Marohn, and R. F. Loring, *J. Chem. Phys.*, **2012**, *137*, 124701, [url]. 4, E.1, E.1.1

[81] S. Lekkala, J. A. Marohn, and R. F. Loring, *J. Chem. Phys.*, **2013**, *139*, 184702, [url]. 4, E.1, E.3

[82] J. L. Garrett and J. N. Munday, *Nanotechnology*, **2016**, *27*, 245705, [url]. 4, 5.4, 6.3.1

[83] T. Manaka, M. Nakao, D. Yamada, E. Lim, and M. Iwamoto, *Opt. Express, OE*, **2007**, *15*, 15964–15971, [url]. 5.1

[84] M. Celebrano, C. Sciascia, G. Cerullo, M. Zavelani-Rossi, G. Lanzani, and J. Cabanillas-Gonzalez, *Adv. Func. Mater.*, **2009**, *19*, 1180–1185, [url]. 5.1

[85] J. D. Morris, T. L. Atallah, C. J. Lombardo, H. Park, A. Dodabalapur, and X.-Y. Zhu, *Appl. Phys. Lett.*, **2013**, *102*, 033301, [url]. 5.1

[86] S. Bain, D. C. Smith, N. R. Wilson, and M. Carrasco-Orozco, *Appl. Phys. Lett.*, **2009**, *95*, 143304, [url]. 5.1

[87] C. Melzer, C. Siol, and H. von Seggern, *Adv. Mater.*, **2013**, *25*, 4315–4319, [url]. 5.1

[88] G. de Tournadre, F. Reisdorffer, R. Rödel, O. Simonetti, H. Klauk, and L. Giraudet, *J. Appl. Phys.*, **2016**, *119*, 125501, [url]. 5.1

[89] B. M. Dhar, G. S. Kini, G. Xia, B. J. Jung, N. Markovic, and H. E. Katz, *Proc. Natl. Acad. Sci. U.S.A.*, **2010**, *107*, 3972 – 3976, [url]. 5.1

[90] J. Lee, J. Kong, H. Kim, S.-O. Kang, and K. Lee, *Appl. Phys. Lett.*, **2011**, *99*, 243301, [url]. 5.1

[91] J. Drijkoningen, J. Kesters, T. Vangerven, E. Bourgeois, L. Lutsen, D. Vanderzande, W. Maes, J. D'Haen, and J. Manca, *Org. Electron.*, **2014**, *15*, 1282–1289, [url]. 5.1

[92] V. W. Bergmann, S. A. L. Weber, F. Javier Ramos, M. K. Nazeeruddin, M. Grätzel, D. Li, A. L. Domanski, I. Lieberwirth, S. Ahmad, and R. Berger, *Nat. Comms.*, **2014**, *5*, 5001, [url]. 5.1

[93] Q. Chen, L. Mao, Y. Li, T. Kong, N. Wu, C. Ma, S. Bai, Y. Jin, D. Wu, W. Lu, B. Wang, and L. Chen, *Nat. Comms.*, **2015**, *6*, 7745, [url]. 5.1

[94] V. W. Bergmann, Y. Guo, H. Tanaka, I. M. Hermes, D. Li, A. Klasen, S. A. Bretschneider, E. Nakamura, R. Berger, and S. A. L. Weber, *ACS Appl. Mater. Interfaces*, **2016**, *8*, 19402–19409, [url]. 5.1

[95] R. P. Dwyer, L. M. Smieska, A. M. Tirmzi, and J. A. Marohn, **2017**. 5.1, 5.1, 5.2.3

[96] U. Zerweck, C. Loppacher, T. Otto, S. Grafstrom, and L. Eng, *Phys. Rev. B*, **2005**, *71*, 125424, [url]. 5.4, 6.2.2

[97] S. A. Burke, J. M. LeDue, Y. Miyahara, J. M. Topple, S. Fostner, and P. Grütter, *Nanotechnology*, **2009**, *20*, 264012, [url]. 5.4, 6.2.2

[98] Y. Sugawara, L. Kou, Z. Ma, T. Kamijo, Y. Naitoh, and Y. Jun Li, *Appl. Phys. Lett.*, **2012**, *100*, 223104, [url]. 5.4

[99] Y. Miyahara, J. Topple, Z. Schumacher, and P. Grutter, *Phys. Rev. Appl.*, **2015**, *4*, [url]. 5.4, 6.3.1

[100] Y. Miyahara and P. Grutter, *Appl. Phys. Lett.*, **2017**, *110*, 163103, [url]. 5.4, 6.3.1

[101] R. Bracewell, *The Fourier Transform and Its Applications*, McGraw-Hill international editions, McGraw Hill, 3st ed., 2000. 6.1, H

[102] W. Melitz, J. Shen, A. C. Kummel, and S. Lee, *Surf. Sci. Rep.*, **2011**, *66*, 1–27, [url]. 6.2.2

[103] E. J. Spadafora, M. Linares, W. Z. Nisa Yahya, F. Lincker, R. Demadrille, and B. Grevin, *Appl. Phys. Lett.*, **2011**, *99*, 233102, [url]. 6.2.2

[104] Y. Leng, C. C. Williams, L. C. Su, and G. B. Stringfellow, *Appl. Phys. Lett.*, **1995**, *66*, 1264–1266, [url]. 6.2.2

[105] L. Collins, J. I. Kilpatrick, S. a. L. Weber, A. Tselev, I. V. Vlassiouk, I. N. Ivanov, S. Jesse, S. V. Kalinin, and B. J. Rodriguez, *Nanotechnology*, **2013**, *24*, 475702. 6.2.2

[106] Z. Schumacher, A. Spielhofer, Y. Miyahara, and P. Grutter, **2016**, [url]. 6.2.4

[107] Z. Schumacher, A. Spielhofer, Y. Miyahara, and P. Grutter, *Appl. Phys. Lett.*, **2017**, *110*, 053111, [url]. 6.2.4

[108] P. Horowitz and W. Hill, *The Art of Electronics*, Cambridge University Press, New York, NY, 3rd ed., 2015. 6.3.2, 6.3.3, B.1, H

[109] P. Hobbs, *Building Electro-Optical Systems: Making It all Work*, Wiley Series in Pure and Applied Optics, Wiley, 2000. 6.3.3, H

[110] J. G. Longenecker *High-Gradient Nanomagnet-on-Cantilever Fabrication for Scanned Probe Detection of Magnetic Resonance* PhD thesis, Cornell University, Ithaca, New York, **2013**. 6.4, I

[111] M. Roseman and P. Grütter, *Rev. Sci. Instrum.*, **2000**, *71*, 3782, [url]. 6.4

[112] R. P. Dwyer, A. M. Tirmzi, and J. A. Marohn, The KPFM python package, 2017. 6.4

[113] L. Collins, A. Belianinov, S. Somnath, N. Balke, S. V. Kalinin, and S. Jesse, *Scientific Reports*, **2016**, *6*, srep30557, [url]. 6.4

[114] M. Bussonnier, Release of IPython 6.0, 2017. 6.4

[115] C. Turner, **2008**, *25*, 159–163, [url]. A.1

[116] D. G. Cahill, *Rev. Sci. Instrum.*, **2004**, *75*, 5119–5122, [url]. A.3

[117] J. Luria, Y. Kutes, A. Moore, L. Zhang, E. A. Stach, and B. D. Huey, *Nat. Energy*, **2016**, *1*, 16150, [url]. A.3

[118] A. Gelman and D. B. Rubin, *Statist. Sci.*, **1992**, *7*, 457–472, [url]. A.7

[119] M. Waskom, O. Botvinnik, drewokane, P. Hobson, Y. Halchenko, S. Lukauskas, J. Warmenhoven, J. B. Cole, S. Hoyer, J. Vanderplas, and et al., seaborn: v0.7.0, 2016. A.7

[120] J. L. Luria *Spectroscopic Characterization of Charge Generation and Trapping in Third-Generation Solar Cell Materials Using Wavelength- and Time-Resolved Electric Force Microscopy* PhD thesis, Cornell University, **2011**. C.1

[121] L. M. Smieska *Microscopic Studies of the Fate of Charges in Organic Semiconductors: Scanning Kelvin Probe Measurements of Charge Trapping, Transport, and Electric Fields in p- and n-type Devices* PhD thesis, Cornell University, **2015**. C.1, C.1

[122] X. Li, Spectroscopic study of electrochemically doped PEDOT:ClO_4 with tunable workfunction, 2015. D, D.3, D.4, D.5

[123] K. Maturova, M. Kemerink, M. Wienk, D. Charrier, and R. Janssen, *Adv. Funct. Mater.*, **2009**, *19*, 1379 – 1386, [url]. D

[124] H. Frohne, D. C. Müller, and K. Meerholz, *ChemPhysChem*, **2002**, *3*, 707 – 711, [url]. D

[125] A. Petr, F. Zhang, H. Peisert, M. Knupfer, and L. Dunsch, *Chem. Phys. Lett.*, **2004**, *385*, 140 – 143, [url]. D, D.1

[126] P. Damlin, C. Kvarnström, and A. Ivaska, *J. Electroanal. Chem.*, **2004**, *570*, 113–122, [url]. D

[127] H. J. Snaith, H. Kenrick, M. Chiesa, and R. H. Friend, *Polymer*, **2005**, *46*, 2573 – 2578, [url]. D

[128] W. E. McClain, P. R. Florence, A. Shu, A. Kahn, and J. Schwartz, *Organic Electronics*, **2013**, *14*, 411–415, [url]. D

[129] G. A. MacDonald, P. A. Veneman, D. Placencia, and N. R. Armstrong, *ACS Nano*, **2012**, *6*, 9623–9636, [url]. D

[130] C. Kvarnström, H. Neugebauer, S. Blomquist, H. Ahonen, J. Kankare, and A. Ivaska, *Electrochim. Acta*, **1999**, *44*, 2739–2750, [url]. D

[131] D. Boudinet, M. Benwadih, Y. Qi, S. Altazin, J.-M. Verilhac, M. Kroger, C. Serbutoviez, R. Gwoziecki, R. Coppard, G. L. Blevennec, A. Kahn, and G. Horowitz, *Organic Electronics*, **2010**, *11*, 227–237, [url]. D.2

[132] A. Liscio, E. Orgiu, J. M. Mativetsky, V. Palermo, and P. Samorí, *Adv. Mater.*, **2010**, *22*, 5018–5023, [url]. D.2

[133] K. M. Knesting, P. J. Hotchkiss, B. A. MacLeod, S. R. Marder, and D. S. Ginger, *Adv. Mater.*, **2012**, *24*, 642–646, [url]. D.2

[134] B. A. MacLeod, N. E. Horwitz, E. L. Ratcliff, J. L. Jenkins, N. R. Armstrong, A. J. Giordano, P. J. Hotchkiss, S. R. Marder, C. T. Campbell, and D. S. Ginger, *J. Phys. Chem. Lett.*, **2012**, *3*, 1202–1207, [url]. D.2

[135] E. L. Ratcliff, A. Garcia, S. A. Paniagua, S. R. Cowan, A. J. Giordano, D. S. Ginley, S. R. Marder, J. J. Berry, and D. C. Olson, *Adv. Energy Mater.*, **2013**, *3*, 647 – 656, [url]. D.2

[136] P. B. Hoffmann, A. G. Gagorik, X. Chen, and G. R. Hutchison, *J. Phys. Chem. C*, **2013**, p. 130828063532001, [url]. D.2

[137] A. Risteska, S. Steudel, M. Nakamura, and D. Knipp, *Org. Electron.*, **2014**, *15*, 3723–3728, [url]. D.2

[138] M. Jesper, M. Alt, J. Schinke, S. Hillebrandt, I. Angelova, V. Rohnacher, A. Pucci, U. Lemmer, W. Jaegermann, W. Kowalsky, T. Glaser, E. Mankel, R. Lovrincic, F. Golling, M. Hamburger, and U. H. F. Bunz, *Langmuir*, **2015**, *31*, 10303–10309, [url]. D.2

[139] W. Denk and D. W. Pohl, *Appl. Phys. Lett.*, **1991**, *59*, 2171 – 2173, [url]. E.1

[140] H. Callen and T. Welton, *Phys. Rev.*, **1951**, *83*, 34 – 40, [url]. E.1

[141] B. C. Stipe, H. J. Mamin, T. D. Stowe, T. W. Kenny, and D. Rugar, *Phys. Rev. Lett.*, **2001**, *86*, 2874 – 2877, [url]. E.1

[142] B. C. Stipe, H. J. Mamin, C. S. Yannoni, T. D. Stowe, T. W. Kenny, and D. Rugar, *Phys. Rev. Lett.*, **2001**, *87*, 277602, [url]. E.1

[143] T. D. Stowe, T. W. Kenny, D. J. Thomson, and D. Rugar, *Appl. Phys. Lett.*, **1999**, *75*, 2785 – 2787, [url]. E.1

[144] M. Bouhassoune, S. v. Mensfoort, P. Bobbert, and R. Coehoorn, *Organic Electronics*, **2009**, *10*, 437–445, [url]. E.1

[145] S. V. Novikov, D. H. Dunlap, V. M. Kenkre, P. E. Parris, and A. V. Vannikov, *Phys. Rev. Lett.*, **1998**, *81*, 4472 – 4475, [url]. E.1

[146] C. Tanase, E. Meijer, P. Blom, and D. De Leeuw, *Phys. Rev. Lett.*, **2003**, *91*, 216601, [url]. E.1

[147] N. Craciun, J. Wildeman, and P. Blom, *Physical Review Letters*, **2008**, *100*, [url]. E.1

[148] S. Tiwari and N. Greenham, *Opt. Quantum. Electron.*, **2009**, *41*, 69–89, [url]. E.1

[149] R. Kepler, *Physical Review*, **1960**, *119*, 1226–1229, [url]. E.1

[150] P. G. Schouten, J. M. Warman, and M. P. de Haas, *The Journal of Physical Chemistry*, **1993**, *97*, 9863–9870, [url]. E.1

[151] S. M. Yazdanian, N. Hoepker, S. Kuehn, R. F. Loring, and J. A. Marohn, *Nano Lett.*, **2009**, *9*, 2273 – 2279, [url]. E.1

[152] E. M. Roeling, W. C. Germs, B. Smalbrugge, E. J. Geluk, T. de Vries, R. A. J. Janssen, and M. Kemerink, *AIP Advances*, **2012**, *2*, 012106, [url]. E.1

[153] E. M. Roeling, W. C. Germs, B. Smalbrugge, E. J. Geluk, T. de Vries, R. A. J. Janssen, and M. Kemerink, *Nat. Mater.*, **2011**, *10*, 51–55, [url]. E.1

[154] D. F. S. Petri, *J. Braz. Chem. Soc.*, **2002**, *13*, 695 – 699, [url]. E.1.1

[155] P. Borsenberger and D. Weiss, *Organic Photoreceptors for Xerography*, Optical Science and Engineering Series, CRC Press LLC, 1998. E.2

[156] R. Ruiz, A. Papadimitratos, A. C. Mayer, and G. G. Malliaras, *Adv. Mater.*, **2005**, *17*, 1795 – 1798, [url]. E.2

[157] M. Kiguchi, M. Nakayama, T. Shimada, and K. Saiki, *Phys. Rev. B*, **2005**, *71*, 035332, [url]. E.2

[158] H.-J. Yuh and D. M. Pai, *Philos. Mag. Lett.*, **1990**, *62*, 61 – 66, [url]. E.3

[159] Y. Shen, M. Klein, D. Jacobs, J. Campbell Scott, and G. Malliaras, *Phys. Rev. Lett.*, **2001**, *86*, 3867 – 3870, [url]. E.3

[160] A. Morozovska, E. Eliseev, and S. Kalinin, *Appl. Phys. Lett.*, **2010**, *96*, 222906, [url]. E.5

[161] A. N. Morozovska, E. A. Eliseev, S. L. Bravina, F. Ciucci, G. S. Svechnikov, L.-Q. Chen, and S. V. Kalinin, *J. Appl. Phys.*, **2012**, *111*, 014107, [url]. E.5

[162] J. H. Moore, C. C. Davis, M. A. Coplan, and S. C. Greer, *Building Scientific Apparatus*, Cambridge University Press, Cambridge, UK ; New York, 4 edition ed., 2009. H

[163] J. Bechhoefer, *Rev. Mod. Phys.*, **2005**, *77*, 783–836, [url]. H

[164] R. Mancini, *Op Amps for Everyone: Design Reference*, Newnes, 2003. H

[165] R. Morrison, *Grounding and shielding techniques*, John Wiley, New York, 1998. H

[166] H. W. Ott, *Noise Reduction Techniques in Electronic Systems*, Wiley-Interscience, New York, 2nd ed., 1988. H

[167] G. Strang, *Linear Algebra and Its Applications*, Cengage Learning, Belmont, CA, 4th ed., 2006. H

[168] D. G. Luenberger, *Introduction to Dynamic Systems: Theory, Models, and Applications*, Wiley, New York, 1st ed., 1979. H

[169] R. G. Lyons, *Understanding Digital Signal Processing*, Prentice Hall, Upper Saddle River, NJ, 3rd ed., 2010. H

[170] S. W. Smith, *The Scientist and Engineer's Guide to Digital Signal Processing*, California Technical Pub, San Diego, Calif, 1st ed., 1997. H

[171] S. J. Farlow, *Partial Differential Equations for Scientists and Engineers*, Dover Publications, New York, reprint ed., 1993. H

[172] D. Simon, *Optimal State Estimation: Kalman, H_∞, and Nonlinear Approaches*, Wiley-Interscience, Hoboken, N.J, 1st ed., 2006. H

[173] F. S. Acton, *Numerical Methods that Work*, The Mathematical Association of America, Washington, D.C, 1st ed., 1990. H

[174] D. G. Luenberger, *Optimization by Vector Space Methods*, Wiley-Interscience, New York, 1969 ed., 1997. H

[175] J. G. Simmonds, J. E. M. Jr, and Physics, *A First Look at Perturbation Theory*, Dover Publications, Mineola, N.Y, revised 2nd ed., 1997. H

[176] Z. Shaw, Learn Python the Hard Way, 2017. H

[177] Z. Shaw, Learn C the Hard Way, 2017. H

[178] H. J. Paarsch and K. Golyaev, *A Gentle Introduction to Effective Computing in Quantitative Research: What Every Research Assistant Should Know*, The MIT Press, Cambridge, Massachusetts, 2016. H

[179] T. J. Sargent and J. Stachurski, Quantitative Economics. H

[180] M. Betancourt, *arXiv*, **2017**, [url]. H

[181] C. Moler and C. Van Loan, *SIAM Rev.*, **2003**, *45*, 3–49, [url]. H

[182] A. Pribram-Jones, D. A. Gross, and K. Burke, *Annu. Rev. Phys. Chem.*, **2015**, *66*, 283–304, [url]. H

[183] S. Kuehn *Force-Gradient Detected Magnetic Resonance and the Origins of Noncontact Friction* PhD thesis, Cornell University, Ithaca, New York, **2007**. I